Scuola Dottorale di Ingegneria
Sezione di Ingegneria dell'Elettronica Biomedica,
dell'Elettromagnetismo e delle Telecomunicazioni

XXVI CICLO DEL CORSO DI DOTTORATO

Analysis and design of scattering cancellation based cloaking devices operating at microwave and optical frequencies

(Analisi e sintesi di dispositivi di occultamento elettromagnetico basati sulla cancellazione dello scattering a microonde e frequenze ottiche)

Dottorando: Ing. Alessio Monti

Docente-Guida: Prof. Filiberto Bilotti

There is nothing new under the sun,

but there are lots of old things we don't know

Ambrose Bierce

Acknowledgements

My research project was carried out at the Department of Electronics Engineering of the "RomaTre" University, Rome, Italy, from January 2011 to December 2014. There are many people that have contributed to transform this period into an amazing and unprecedented experience.

First, I would like to deserve a special thanks to my supervisor Professor Filiberto Bilotti, Head of the Antenna and Special Materials Research Lab. He not only guided and supported me in my research with enthusiasm and expertise, but he represented, and still represents, my professional role model. Prof. Bilotti personally and professionally supported me through these demanding years significantly contributing to my scientific growth and responsibilization. Among other things, he deserves my sincere gratitude for all the opportunities he gave me, as the extraordinary possibility to fruitfully collaborate with top-level scientists all over the world.

An equally authentic thank also go to Professor Alessandro Toscano, Head of the Environmental Electromagnetic Diagnostic Lab, for his invaluable support, his encourage and for having trusting in me for all time. He has been supportive and friendly since the first days I began working with him and his experience and scientific help allowed me to achieve results that I would never expected. Moreover, his exemplar professional conduct will represent for me a model of behavior in all my future experiences.

Moreover, I would like to thank all the Professors and the staff of the Electronics Engineering Department of the Roma Tre University for the excellent work environment and for the courtesy revealed in these years.

In addition, I desire to thank Prof. Andrea Alù, Professor at the Department of Electrical and Computer Engineering at The University of Texas at Austin, and Jason C. Soric, PhD student at the same University. The collaboration with them has represented for me an extraordinary occasion of scientific and personal growth. Andrea deserves my special gratitude for his unquestioningly trust and for having given me the opportunity to perform positions of responsibility in an international context. These opportunities meant a lot to me.

I would also like to sincerely thank my research mates at the Engineering Department, Dr. Mirko Barbuto, Dr. Davide Ramaccia and Dr. Claudia Guattari for the pleasing time spent inside and outside the Department between hard work, enjoyments and relax.

Last, but certainly not least, I reserve an immeasurable thanks to my parents, my brother and my girlfriend Francesca. Literally, nothing would be possible for me without them.

Contents

Sommario (Italiano) **8**

Introduction **14**

1 Microwave mantle cloaking **18**

1.1 Introduction to electromagnetic cloaking 18

1.2 Analytical formulation of the mantle cloaking for a cylindrical geometry 23

1.2.1 TM-polarization 25

1.2.2 TE-polarization 29

1.2.3 Multilayered mantle cloaks 31

1.3 Metasurface analytical models 35

1.3.1 Single-polarized metasurfaces 36

1.3.2 Dual-polarized metasurfaces 38

1.3.3 Examples of dual-polarized cloaking devices 44

1.4 References 56

2 Antennas application of mantle cloaking **61**

2.1 Increasing the absorption efficiency of the receiving antennas 62

2.1.1 Mantle cloaking for receiving dipole antennas 62

2.1.2 A practical design 67

2.2 Reduction of the mutual blockage effect among close antennas 70

2.2.1 An operative scenario 71

2.3 Dual-polarization reduction of the blockage effect 76

2.3.1 Experimental verification 77

2.4 Design of invisible Yagi-Uda antennas..... 80

2.4.1 Design guidelines 81

2.4.2 Cloaks design 87

2.4.3 Use of the cloaked Yagi-Uda antennas in realistic scenarios 90

2.5 References 94

3 Scattering cancellation at optical frequencies 98

3.1 Optical epsilon-near-zero materials 99

3.1.1 Analytical models 100

3.1.2 Application of optical ENZ materials 105

3.2 Optical mantle cloaking..... 110

3.2.1 Optical metasurfaces 111

3.2.2 Optical metasurfaces and mantle cloaking 119

3.2.3 Mantle cloaking with nanorods 126

3.3 References 128

4 Other research activities 131

4.1 Design of broadband actively loaded MTM-inspired components .. 132

4.1.1 Design of a broadband split-ring-resonator (SRR) 134

4.1.2 Design of a broadband miniaturized monopole antennas 139

4.1.3 Stability issues 146

4.2 Fabrication and characterization of resistive sheets..... 149

4.2.1 Realization of graphite-based resistive sheets 149

4.2.2 Realization of a MTM-inspired electromagnetic absorber without a metallic backing 153

4.3 References 158

List of Figures and Tables **163**

Publications **173**

Ph.D. candidate profile **178**

Sommario (Italiano)

Introduzione

Lo studio sistematico dei materiali e delle superfici artificiali in grado di esibire proprietà non convenzionali ha una storia relativamente recente. Sebbene esso possa essere fatto risalire all'inizio degli anni '90, con le prime conferenze internazionali sui materiali chirali, non reciproci e bianisotropi, è con l'avvento del nuovo millennio che i materiali elettromagnetici artificiali e i metamateriali sono diventati un campo di ricerca consolidato, in costante sviluppo e caratterizzato da un approccio marcatamente multidisciplinare. Negli ultimi 15 anni, lo studio dei materiali artificiali ha consentito un importante progresso teorico nell'ambito dell'elettromagnetismo e dell'ottica portando alla ribalta nuovi fenomeni fisici non osservabili nei materiali naturali e consentendo la definizione di tecnologie innovative. Recentemente, inoltre, si è assistito ad una diffusione dei principi dei materiali elettromagnetici artificiali anche in altri settori della scienza applicata, quali l'acustica e la termodinamica, i quali stanno andando incontro ad una significativa rivoluzione.

Tra le varie possibilità offerte dai metamateriali, una delle più interessanti è senza dubbio quella in italiano potremmo definire scienza dell'occultamento ("*cloaking science*"). Con tale termine si intende la possibilità di ridurre la visibilità elettromagnetica di un oggetto all'interno di un desiderato intervallo di frequenze. In termini più rigorosi, possiamo affermare che un dispositivo di cloaking (o di occultamento) è un dispositivo che permette di ridurre in maniera significativa il campo elettromagnetico complessivo diffuso da un oggetto quando questo è illuminato da un campo elettromagnetico esterno. A differenza di altri dispositivi di riduzione dello scattering noti da decenni, come i materiali radar assorbenti, un dispositivo di cloaking è in grado di ridurre il campo *totale* diffuso dall'oggetto rendendolo sostanzialmente non rilevabile da qualsiasi sensore che operi all'interno della banda di funzionamento del dispositivo di cloaking. Le possibili applicazioni delle tecniche di cloaking sono tuttora in fase di studio e spaziano dall'ingegneria delle telecomunicazioni a quella biomedica, dalle tecnologie militari a quelle satellitari, dalla manipolazione delle forze ottiche alla riduzione

dell'effetto di Casimir.

Nel corso dell'ultimo decennio sono state proposte diverse tecniche per la realizzazione di un dispositivo di cloaking. Tra di esse, la cosiddetta "*scattering cancellation*" è senza dubbio la più versatile per numerose applicazioni ingegneristiche, soprattutto quelle relative alla teoria delle antenne e alla sensoristica. Infatti, tale tecnica consente una riduzione dello scattering dell'oggetto senza che venga inibita l'interazione tra il campo elettromagnetico esterno e l'oggetto da occultare.

La realizzazione di un dispositivo di occultamento basato sullo cancellazione dello scattering è stata per diversi anni un compito relativamente complesso, poiché richiedeva l'utilizzo di metamateriali volumetrici di tipo *epsilon-near-zero* (ENZ) caratterizzati da un certo ingombro, nonché da notevoli perdite elettromagnetiche in grado di degradarne significativamente le prestazioni. Negli ultimi anni, tuttavia, si sta assistendo ad un importante evoluzione nello studio delle cosiddette metasuperfici. Tali strutture, costituite da superfici periodiche strutturate su scala piccola rispetto alla lunghezza d'onda incidente, sono caratterizzate da perdite limitate, ridotto peso e ingombro e, infine, da notevole semplicità realizzativa. Anche la scienza dell'occultamento ha tratto notevoli vantaggi dallo sviluppo delle metasuperfici. In particolare, è stato introdotto una variante della cancellazione dello scattering basata sull'utilizzo di metasuperfici. Tale variante, nota come il nome di "*mantle cloaking*", è stata l'oggetto principale delle mie ricerche, come dettagliato nel seguito.

1. Mantle cloaking alle frequenze delle microonde

Il primo filone di ricerca ha riguardato l'analisi teorica delle tecnologie di occultamento elettromagnetico alle frequenze delle microonde basate su metasuperfici. Una metasuperficie operante alle frequenze delle microonde è costituita da una superficie metallica patternata in modo opportuno. Mediante lo studio sistematico e la generalizzazione dei modelli analitici usati per descrivere le metasuperfici alle frequenze delle microonde, è stato possibile definire una procedura di sintesi per metasuperfici anisotrope che consente il progetto analitico di dispositivi di occultamento a doppia polarizzazione. Tale risultato ha rappresentato un avanzamento dello stato dell'arte della tecnologia del cloaking elettromagnetico poiché ha consentito il progetto di

dispositivo di occultamento per oggetti elettricamente piccoli e di forma arbitraria indipendentemente dalla particolare tipologia di campo elettromagnetico incidente.

Un secondo aspetto delle attività di ricerca sul cloaking a microonde ha riguardato lo studio e il progetto di dispositivi di cloaking multistrato basati su metasuperfici. L'utilizzo di rivestimenti multistrato introduce delle complicazioni di carattere teorico che devono essere tenute in debita considerazione, ma consente di estendere il fenomeno di cloaking su bande operative più ampie (cloaking a larga banda) e per oggetti le cui dimensioni non soddisfano il limite quasi-statico (cloaking di oggetti elettricamente non piccoli). Queste estensioni hanno consentito di aumentare la diffusione delle tecnologie di cloaking elettromagnetico in un numero sempre maggiore di scenari operativi realistici.

2. Applicazioni del mantle cloaking in scenari d'antenna

Il secondo filone, strettamente connesso al precedente, ha riguardato l'applicazione dei dispositivi di occultamento sopra descritti a scenari applicativi di interesse nell'ambito della teoria delle antenne. In particolare, è stato dimostrato che i dispositivi di occultamento consentono di superare i problemi dovuti agli effetti di bloccaggio mutuo tra le antenne senza modificare in modo sostanziale le prestazioni dei dispositivi radianti cui sono stati applicati. Tale aspetto consente un significativo miglioramento ed ampliamento delle tecniche di co-siting, ovvero di condivisione delle strutture supporto da parte di diversi dispositivi radianti, che rappresentano oggi un elemento caratterizzante il progetto delle infrastrutture di telecomunicazione.

Inoltre, le tecnologie di occultamento a microonde si sono rivelate anche utili nella realizzazione di dispositivi di nuova concezione quali, ad esempio, antenne riceventi sintonizzabili su diverse modalità operative (massima potenza ricevuta, minimo scattering, massimo scattering, ecc.) e caratterizzate da un funzionamento prossimo a quello definito dai limiti teorici esistenti.

3. Cancellazione dello scattering a frequenze ottiche

Il terzo filone di ricerca ha riguardato il progetto di materiali artificiali in grado di realizzare un effetto cloaking alle frequenze ottiche. Dapprima, ci si è concentrati sul

progetto di metamateriali in grado di esibire un comportamento ENZ nello spettro visibile. Nonostante le loro innumerevoli applicazioni descritte nelle recente letteratura, l'implementazione effettiva di tali materiali alle frequenze ottiche ha sempre rappresentato una sfida non semplice. Generalizzando le formule di omogeneizzazione classiche, si è dimostrato teoricamente e con simulazioni full-wave che opportuni allineamenti di nanosfere core-shell immerse in una matrice dielettrica sono in grado di manifestare il comportamento ENZ desiderato nella parte superiore dello spettro visibile (regione del blu-violetto). Tali misture sono state usate con successo per realizzare dispositivi di occultamento elettromagnetico e filtri ottici angolari.

Successivamente, ci si è concentrati più nel dettaglio sugli aspetti di modellazione degli allineamenti di nanoparticelle plasmoniche. In modo alternativo e complementare a quanto sviluppato in precedenza, la generalizzazione dei risultati presenti letteratura ha consentito di dimostrare che gli allineamenti di nanoparticelle possono essere caratterizzati mediante la definizione di un'opportuna reattanza superficiale. L'utilizzo del modello bidimensionale basato sulla reattanza superficiale si è dimostrato più adeguato rispetto a quello tridimensionale della permittività efficace utilizzato in precedenza, soprattutto in virtù delle ridotte dimensioni elettriche delle nanoparticelle. Tale analisi ha consentito di estendere i fenomeni di cloaking basati su metasuperfici a tutto lo spettro del visibile. La disponibilità di un modello teorico, inoltre, ha permesso di ingegnerizzare le proprietà plasmoniche delle nanoparticelle migliorando in modo drammatico le prestazioni di occultamento ottico degli allineamenti di nanoparticelle proposti in precedenza.

4. Altre attività di ricerca

Tra le altri attività di ricerca condotte vi è l'indagine relativa all'utilizzo dei circuiti attivi per incrementare la larghezza di banda delle inclusioni risonanti. Tali inclusioni sono comunemente utilizzate per il progetto di metamateriali volumetrici e per particolari applicazioni innovative (dispositivi per l'aumento della trasmissione da apertura sottile, assorbitori elettromagnetici miniaturizzati, filtri in microstriscia, ecc.). In particolare, è stato investigato nel dettaglio l'utilizzo di circuiti attivi non-Foster per aumentare la banda operativa di funzionamento di dispositivi basati su split-ring-

resonator (SRR). Gli aspetti teorici (topologie circuitali necessarie, calcolo dei valori ideali di capacità e induttanza negativa, ecc.) e quelli applicativi (implementazione del circuito non-Foster con elementi reali che tengano in considerazioni gli effetti parassiti, problemi di stabilità del circuito, ecc.) sono stati entrambi tenuti in debita considerazione in fase di analisi e progetto. L'attività di ricerca ha permesso di dimostrare che i circuiti non-Foster consentono di incrementare drammaticamente la banda operativa dei dispositivi ispirati ai metamateriali e di ridurre significativamente le distorsioni che tali dispositivi possono introdurre nei segnali a banda larga.

In secondo luogo, mi sono anche occupato della realizzazione di assorbiti elettromagnetici a banda larga mediante fogli resistivi realizzati con materiali economici e facili da reperire. Tale studio, che ha previsto anche una fase di caratterizzazione dei fogli resistivi, ha permesso la realizzazione di un assorbitore ispirato ai metamateriali composto da una superficie selettiva in frequenza in grado di emulare il comportamento di una parete elettrica perfetta e un foglio resistivo di grafite spray. La sostituzione del piano metallico con la superficie selettiva in frequenza, ha consentito di ottenere un assorbitore più leggero rispetto alle soluzioni tradizionali e, inoltre, in grado di limitare l'incremento della segnatura radar al di fuori della banda di funzionamento.

Introduction

The systematic study of the artificial materials and surfaces able to exhibit unusual properties has a relatively recent history. Although it can be traced back in the early 90s, with the first international conference on chiral, non-reciprocal and bianisotropic materials, is with the advent of the new millennium that the artificial materials become a consolidated research field of the applied electromagnetics characterized by a markedly multidisciplinary approach. Over the past 15 years, the artificial materials have allowed a major theoretical advance in electromagnetism and optics bringing to the fore new physical phenomena that cannot be observed in natural materials. Recently, moreover, there has been a spread of the basic principles of metamaterials in other areas of applied science, such as acoustics and thermodynamics which are experiencing a significant revolution.

Among the various possibilities offered by metamaterials, one of the most interesting is undoubtedly the so-called "cloaking science". This term generally refers to the ability to reduce the electromagnetic visibility of an object within a desired range of frequencies. In more rigorous terms, we can say that a cloaking device is a device allowing to dramatically reduce the overall electromagnetic field scattered by an object when it is illuminated by an external electromagnetic field. Unlike other known scattering reduction devices, such as the radar-absorbing materials, a cloaking device is able to reduce the total field scattered by the object making it substantially undetectable to any external sensor that operates within the band of operation of the device cloaking. The possible applications of the cloaking techniques are still being studied and ranges from the telecommunications engineering to the biomedical one, from the military field to the satellite one, from the control of the optical forces to the reduction of the Casimir effect.

During the last decade several techniques have been proposed for the realization of a cloaking device. Among them, the so-called "scattering cancellation" is undoubtedly the most versatile for many engineering applications, especially those related to the antenna and sensor theory. This technique, in fact, allows a reduction of the object scattering without inhibiting the interaction between the external electromagnetic field and the object itself.

The realization of a cloaking device based on the cancellation of scattering has been for many years a relatively complex task, since it required the use of volumetric epsilon-near-zero metamaterials characterized by a non- negligible size and significant electromagnetic losses degrading the cloaking performance. In recent years, however, we are witnessing to an important evolution in the study of so-called metasurfaces. These structures, formed by periodic surfaces structured on a scale smaller compared to the incident wavelength, are characterized by very low losses, a minimal amount of space and weight and, finally, by a significant constructive simplicity. The cloaking science has greatly benefited from the development of metasurfaces. In particular, it was introduced a variant of the scattering cancellation in which the volumetric metamaterials are replaced by the metasurfaces. This variant, known as the name of "*mantle cloaking*", has been the main object of my researches, whose final results are collected in this thesis.

Chapter 1 is focused on the theoretical basis of the mantle cloaking at microwave frequencies. The main innovative results achieved in this context are: 1) the definition of a general procedure to design anisotropic mantle cloaks operating, at the same frequency, for both TM and TE incident polarizations. In particular, starting from the analytical model of metasurfaces available in the literature, I have first explored the potentials and limitations of the most common metasurface geometries for their application as mantle cloaks. Then, I have introduced new types of patterned surfaces aimed at improving their polarization response. It has been demonstrated that, only by using four metasurface topologies, it is possible to obtain all the required combinations of positive and negative reactance values in order to design effective mantle cloaks for planar, cylindrical and 3D objects; 2) The study of the interesting features of multilayered mantle cloaking devices, including, for instance, significant broadband and/or dual-band scattering reduction.

Chapter 2 focus on the application of the cloaking technologies both in the transmitting and the in receiving operation mode of antenna systems. My results in this field can be summarized as follows: 1) definition of new-conception optimized receiving sensors with the desired level of absorption efficiency, being able to minimize the electrical presence of a receiving antenna for a chosen level of overall absorption; 2) use of the mantle cloaking to overcome the blockage effect affecting the over-crowed

communication platforms, both for passive obstacle (*e.g.,* the support structure of the platforms) and among different antennas; 3) definition of a procedure to design new-conception linear antennas and arrays specifically designed to properly work in a frequencies range and to be electromagnetically invisible in another one. These radiative systems provide a new degree of freedom in the design of modern communication platforms hosting an increasing number of radiators. In fact, the possibility to use invisible antenna systems that can be successfully placed in close proximity will allow to reduce both the space occupancy and the weight of the civil and military platforms as well as on of the satellite systems.

Chapter 3 dealt with the topic of optical cloaking. The following results has been obtained: 1) possible implementation of optical epsilon-near-zero (ENZ) metamaterials based on the employment of an array of core-shell nano-spheres embedded in a dielectric medium. The core of the nano-spheres and the host medium are both made of silica whereas the shell is formed by a plasmonic material (*i.e.*, silver). Using classical homogenization formulas, I show that it is possible to design the array in such a way to exhibit near-zero values of the effective real permittivity with relatively low-losses in the upper part of the optical spectrum; 2) investigation of the application of the mantle cloaking technique to near-infrared and visible frequencies, using thin covers consisting of 2D arrays of plasmonic non-spherical nanoparticles. Here, I focused in more detail in the plasmonic nanoparticles modeling and I generalized the literature results to demonstrate that the nanoparticles arrays can be characterized by a suitable average surface reactance. Then, I show that the use of two-dimensional model is more appropriate than the one based on the effective permittivity. This analysis has allowed to extend the metasurfaces-based cloaking up to optical frequencies and to engineer the shape of the plasmonic nanoparticles in order to dramatically improve the performance of the optical cloaking devices previously proposed.

Finally, Chapter 4 collects my results in other research fields: 1) investigation of the use of non-Foster active circuits to increase the operation bandwidth of a split-ring resonator (SRR) for possible application in metamaterial-inspired components, In particular, I propose a possible realistic implementation of the active load, based on the employment of commercially available circuit elements. The obtained results (seven

times improvement of the impedance bandwidth of the SRR-based monopole antenna) prove that non-Foster active loads can be successfully used to overcome the inherent narrow-band operation of SRR-based passive metamaterials and metamaterial-inspired components.; 2) definition of a simple and low-cost technique for realizing resistive sheets. This approach, requiring only easy-to-find and inexpensive materials, consists in the deposition of graphite powder on ultrathin plastic sheet substrates. I show that, by controlling the deposition time and the mass of the deposited powder, it is possible to realize resistive sheets exhibiting a desired surface resistance in a wide range of values.

All chapters are preceded by a short introduction describing my publications related to that specific topic and summarizing the content of the various Section. In each Section, I have reported the state-of-the-art about the topic and my main findings, that are supported by a combination of theoretical, numerical, and, where available, experimental results.

1 Microwave mantle cloaking

This Chapter is focused on the theoretical basis of the electromagnetic cloaking. My contribution to this topic is available in the publications [J02]-[J03], [C01], [C08]-[C08], [C14]-[C15]. The first Section (Section 1.1) provides a brief overview of the cloaking technologies and clarify the novelty of these approaches compared to other well-established scattering control techniques. The second Section (Section 1.2) illustrates the mantle cloaking analytical formulation. The attention is focused on the cylindrical geometry since it be considered as the reference one to design the mantle cloaking devices used in the antenna systems described in the next Chapter. Finally, in the third Section (Section 1.3), it is described the analytical models that can be used to design the microwave surfaces needed to realize a cloaking devices operating for any incidence polarization of the electromagnetic field.

1.1 Introduction to electromagnetic cloaking

The possibility of making an object electromagnetically less visible to an external observer or to a detection device has attracted the attention of the scientific community since the ancient times. Starting from the second world-war, scientists and engineers have focused their attention on the reduction of the radar signature of an object proposing different techniques, as the passive and the active cancellation, the shaping and the use of lossy materials act as electromagnetic absorbers [1]. In the last ten years, instead, a new scattering reduction technique under the name of *electromagnetic cloaking* has been widely investigated [2]-[9] . Since both the reduction of the object radar signature and the cloaking are focused on the control of the object scattering, it is important to clarify what are the differences between them.

It is well known from the basic electromagnetic theory that the object visibility towards a radar system is expressed by an equivalent physical quantity known as *radar cross section*. Following the accepted formalism adopted by Knott, Tuley and Shaeffer [1], the radar cross section of a target is defined as 4π times the limit for $r \to \infty$ of the ratio between the power per unit solid angle scattered in a *specified direction* and the power per unit area in a plane wave incident on the scatterer from a specified direction, *i.e.,*

$$\sigma_{RCS} = \lim_{r\to\infty} 4\pi r^2 \frac{\left|\mathbf{E}^{scat}\right|^2}{\left|\mathbf{E}^{inc}\right|^2}, \tag{1.1}$$

being $\mathbf{E}^{scat}$ the scattered electric field, $\mathbf{E}^{inc}$ the incident electric field on the target and r the distance between the object and the measurement point. From (1.1), it is evident that the radar cross section of an object is related to the power density scattered by the target in a *given direction* and it represents the power that may be radiated back to a radar receiving antenna for possible detection. Therefore, it is also referred to as *differential scattering cross section* since it gives the angular distribution of the scattered power.

A related, but conceptually different, quantity is the so-called *total scattering cross section* (SCS) that is defined as a measure of the total power scattered by a target over all the spatial directions, *i.e.,*

$$\sigma_T = \frac{\text{total scattered power } (W)}{\text{incident power density } (W/m^2)}, \quad m^2. \tag{1.2}$$

It is easy to understand that the total scattering cross section is formally defined as *the integral of the radar cross section over all spatial directions*, *i.e.,*

$$\sigma_T = \frac{1}{4\pi}\int \sigma_{RCS}\, d\Omega. \tag{1.3}$$

Thanks to the above definitions, it is now very easy to explain why the RCS reduction (RCSR) and the cloaking are distinct techniques. The RCSR, developed prior to the

introduction of cloaking technologies, allows the scattering reduction *in a specific direction* (*i.e.*, function of the impinging radar signal direction and of the observer position in the case of bistatic measurements). On the contrary, cloaking is focused on the reduction of the SCS allowing achieving minimal scattering in all possible directions. The minimization of the total scattering cross section also involves a minimization of all the reflections, as well as of shadowing effects and, therefore, cloaking allows making the object completely invisible to an external detector independently from the mutual position between the object and the detector itself.

I also observe that the amount of the total SCS reduction has been established as the best figure of merit to quantify the performances of a cloaking device. The *scattering cross section gain* is defined as the ratio between the SCSs of the cloaked and of the uncloaked object, respectively. If we express the total SCS in *dB*, the scattering gain becomes:

$$\text{SCS gain} = \sigma_{T,dB}^{cloaked} - \sigma_{T,dB}^{uncloaked} \tag{1.4}$$

From a physical point of view, the SCS gain is simply the amount of the total SCS reduction that has been allowed thanks to the use of the cloaking devices.

In the last ten years, several conceptually different cloaking techniques have been proposed [2]-[9]. A first approach, named *transformation electromagnetic* and originally introduced in [2]-[3], consists of covering the object with a properly engineered metamaterial cover that is able to guide the impinging field around the object itself, avoiding, in this way, any interaction of the external field with the object. This approach, schematized in Fig. 1, in principle works for any shape, dimension and constitutive material of the object, and it has also been verified experimentally in several configurations, see, e.g., [10]. Nevertheless, the design of such covers, as well as their practical realization, remains a non-trivial task since it requires the use of thick anisotropic and inhomogeneous artificial materials.

Another proposed general approach is the so-called *scattering cancellation* technique [6]. This approach is based on a different physical principle that has been schematized in Fig. 2: in this case, the cover surrounding the object does not inhibit the interaction of the external field with the object, but is instead designed such that the field scattered by the

object can be compensated by the field scattered by the cloak, leading, thus, to a significant reduction of total scattering. It is important to underline that the fact that the cloaked object is not "isolated" from the external electromagnetic field is not a weakness but, conversely, can be considered as an advantage of the scattering cancellation cloaking compared to the other techniques since, as discussed in the next Chapter, it has allowed to propose some unprecedented applications of cloaking technologies in both the antenna and sensor theory. Several practical realizations of this cloaking technique have been proposed over the years at microwave [11]-[12] and optical [13]-[17] frequencies and some sensor applications [18]-[20] have also been suggested.

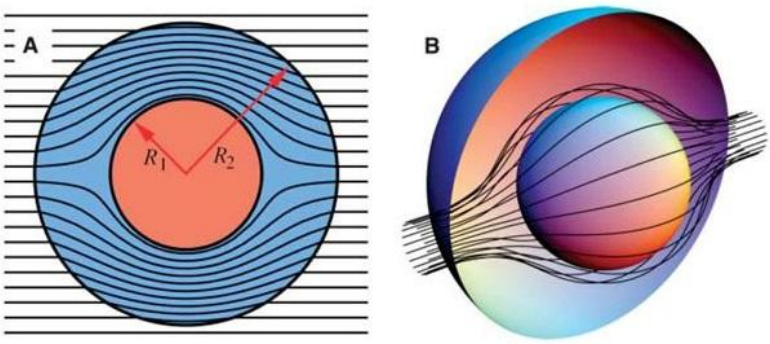

Fig. 1: Schematic representation of the operation of a transformation electromagnetic-based cloaking device [2].

As a first limitation of this cloaking approach, it is possible to point out that single-layer scattering cancellation is effective in the scattering reduction of objects whose characteristic size is small comparable to the operational wavelength. This limitation is due to the fact that the scattering from an object is the result of the superimposition of different modes, whose number and amplitude is directly related to the object size. Since a single layer cloaking cover is only able to properly compensate the field of the dominant scattering mode, the use of mono-layer cloaks necessarily involves a limitation in the maximum size of the object to hide. Unfortunately, such restriction limits the application of cloaking technology in many scenarios where it is required to reduce the scattering of objects whose dimensions are comparable to or even larger than the wavelength. However, as I am going to show below, it is possible to generalize the scattering cancellation cloaking approach to multi-layer covers working for non-electrically small objects.

Secondly, since scattering cancellation cloaking is based on the destructive interference between the field scattered by the object and the one scattered by the cloak, the cloak design is strongly dependent on the shape and on the electromagnetic properties of the object to hide. However, this does not imply that the scattering cancellation cloaking of irregularly shaped object cannot be achieved. As far as the object dimensions are small compared to the operative wavelength (*i.e.*, the quasi-static condition is satisfied), it is always possible to cancel the first scattering mode of the object through a scattering cancellation-based cloak. In the case of a regular geometry, as the 1D slab, the 2D cylinder, the 3D sphere, etc., it is possible achieving a closed form solution of the Mie scattering problem and, therefore, simplifying the cloak design. However, a numerical general solution can be easily found also for objects with arbitrary geometries, as have been proven in [21],[22].

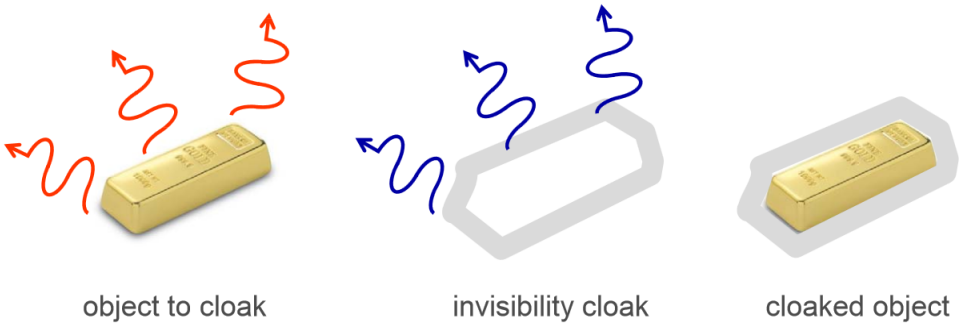

Fig. 2: Schematic representation of the operation of a scattering cancellation-based cloaking device.

The first implementation of the scattering cancellation cloak foresaw the use of bulky volumetric epsilon-near-zero (ENZ) or epsilon-negative (ENG) metamaterials [11],[12]. However, recently, it has been proven that the scattering cancellation approach can be obtained by using covers made of thin metasurfaces such as the ones shown in Fig. 3. This approach, known as *mantle cloaking* [7],[8] is particularly promising especially at microwave frequencies due to its straightforward implementation [23] and to the availability of accurate analytical models [24]-[27] allowing to quickly achieve a working design. Moreover, since it is a scattering cancellation cloaking approach and, therefore, it does not electromagnetically isolate the hidden object, mantle cloaking can be successfully applied in different antenna scenarios, with substantial advantages both in the transmitting [28] and in the receiving [29] operation mode of an antenna.

In this Chapter I focus my attention of the theory beyond the mantle cloaking. First, in the nest Section it is investigate the analytical formulation of the mantle cloaking approach for a cylindrical geometry, which can be considered as the reference one for the design of cloaking devices for antenna applications. Finally, in the third Section it is derived the analytical models used to characterize and to design the metasurfaces required by the mantle cloaking.

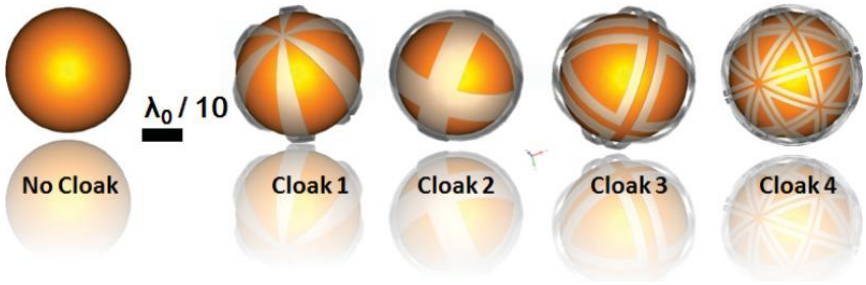

Fig. 3: Some examples of mantle cloaking devices for a spherical object [8].

1.2 Analytical formulation of the mantle cloaking for a cylindrical geometry

Let us to considerer the generic scenario depicted in Fig. 4 in which an infinitely long cylinder composed by a generic material (ε, μ) and surrounded by a conformal metasurface is illuminated by an external normal incident electromagnetic plane wave $\mathbf{E}_i = \mathbf{E}_0 e^{jkx}$ (*i.e.*, whose wave vector is perpendicular to the axis of the cylinder). The radius of the cylinder is equal to a whereas the one of the metasurface is $a_c = \gamma a$. A metasurface is typically composed of deeply subwavelength elements and may be described by an averaged surface impedance, related to the tangential electric field $\mathbf{E}_{\tan} = Z_S^{TM} \mathbf{J}_s$, where $\mathbf{J}_s$ is the induced average surface current density.

My aim is to find a closed-form formula to evaluate the total scattering cross section of the cylinder in function of the electromagnetic parameters of the structure. For this purpose, I follow the analytical procedure described in [7],[30]. The starting point is the scalar wave equation $\nabla^2 \psi + k^2 \psi = 0$, which in cylindrical polar coordinates r, ϕ, z reads as

$$\frac{1}{r}\frac{\partial}{\partial r}\left(r\frac{\partial \psi}{\partial r}\right)+\frac{1}{r^2}\frac{\partial^2 \psi}{\partial \phi^2}+\frac{\partial^2 \psi}{\partial z^2}+k^2\psi=0. \tag{1.5}$$

Separable solutions of (1.5) that are single-valued functions of φ are of the form

$$\psi_n(r,\phi,z)=Z_n(\rho)e^{jn\phi}e^{jhz} \qquad (n=0,\pm1,\ldots), \tag{1.6}$$

where $\rho=r\sqrt{k^2-h^2}$ and Z_n is a solution to the Bessel equation, *i.e.,* the Bessel functions of first and second kind, J_n and Y_n, of order n. The vector harmonics generated by (1.6) are the following:

$$\mathbf{M}_n=\sqrt{k^2-h^2}\left(in\frac{Z_n(\rho)}{\rho}\hat{\mathbf{r}}-Z_n'(\rho)\hat{\boldsymbol{\varphi}}\right)e^{j(n\phi+hz)}, \tag{1.7}$$

$$\mathbf{N}_n=\frac{\sqrt{k^2-h^2}}{k}\left(inZ_n'(\rho)\hat{\mathbf{r}}-hn\frac{Z_n(\rho)}{\rho}\hat{\boldsymbol{\varphi}}+\sqrt{k^2-h^2}Z_n(\rho)\hat{\mathbf{z}}\right)e^{j(n\phi+hz)}, \tag{1.8}$$

where h is the separation constant whose value is dictated by the form of the incident field and the necessity of satisfying the boundary conditions at the boundaries between the cylinders and the surrounding medium.

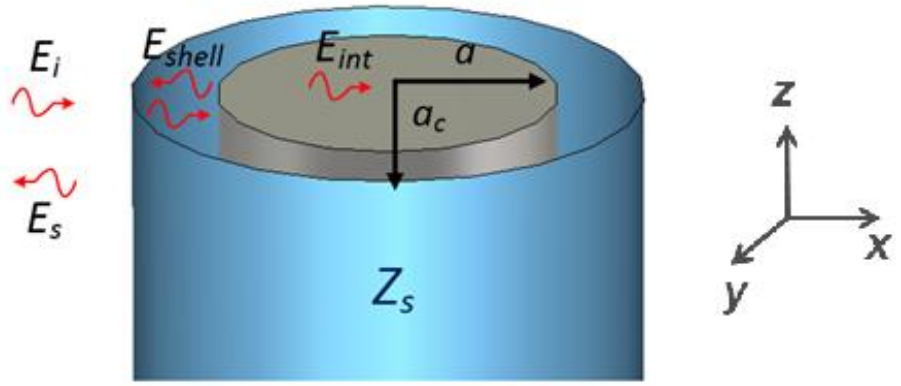

Fig. 4: Infinitely long cylinder surrounded by a conformal metasurface.

There are two possible orthogonal polarization states of the incident wave: electric field polarized parallel to the z axis and electric field polarized perpendicular to the z axis. I shall consider each of these polarizations in turn.

1.2.1 TM-polarization

I consider there the case in which the electric field of the incident plane wave is parallel to the axis of the cylinder, *i.e.,* $\mathbf{E}_i = \hat{\mathbf{z}} E_0 e^{jkx}$. The first step consists in the expansions of the incident electric field in vector cylindrical harmonics. In order for the expansion to be finite at $r = 0$ I must exclude the Bessel function Y_n as the radially dependent part of the generating function. Moreover, it is easy to understand from the form of $\mathbf{E}_i$ that $h = -k$. Therefore, the expansion of the incidence field is:

$$\mathbf{E}_i = \sum_{n=-\infty}^{+\infty} \left[A_n \mathbf{M}_n^{(1)} + B_n \mathbf{N}_n^{(1)} \right], \tag{1.9}$$

where the superscript (1) denotes the Bessel function of the first kind. By exploiting the orthogonality of the vector harmonics, it is easy to verify that

$$A_n = 0, \qquad B_n = \frac{E_0 (-j)^n}{k} = E_n, \tag{1.10}$$

with $k = k_0$ if the incidence medium is the vacuum. Therefore, the expansion the incident electromagnetic field reads as follow

$$\mathbf{E}_i = \sum_{n=-\infty}^{\infty} E_n \mathbf{N}_n^{(1)} (\rho, \varphi, z), \tag{1.11}$$

Following a similar procedure, it is possible to expand into cylindrical vector harmonics also the electric field $\mathbf{E}_s$ scattered by the overall system, the electric field $\mathbf{E}_{shell}$ comprised between the metasurface and the cylinder and the electric field $\mathbf{E}_{\text{int}}$

inside the cylinder. In particular, the field $\mathbf{E}_{shell}$ is the superposition of an incoming and an outgoing cylindrical wave whereas the fields $\mathbf{E}_{\text{int}}$ and $\mathbf{E}_s$ are an incoming and an outgoing cylindrical wave, respectively. In formulas, I can write:

$$\mathbf{E}_s = -\sum_{n=-\infty}^{\infty} E_n \left(b_n \mathbf{N}_n^{(3)} + i a_n \mathbf{M}_n^{(3)} \right), \tag{1.12}$$

$$\mathbf{E}_{\text{int}} = \sum_{n=-\infty}^{\infty} E_n \left(c_n \mathbf{N}_n^{(1)} + d_n \mathbf{M}_n^{(1)} \right), \tag{1.13}$$

$$\mathbf{E}_{shell} = \sum_{n=-\infty}^{\infty} E_n \left(i e_n^1 \mathbf{N}_n^{(3)} + i e_n^2 \mathbf{N}_n^{(1)} - f_n^1 \mathbf{M}_n^{(3)} - f_n^2 \mathbf{M}_n^{(1)} \right), \tag{1.14}$$

where the superscript $^{(3)}$ denotes the Hankel function H_n. The eight terms $a_n \ldots f_n^2$ are unknown expansion coefficients that can be calculated by imposing the proper boundary conditions. The first four of these equations arise from the continuity of the tangential components of both electric and magnetic field at the interface $r = a$ (Fig. 5 - left):

$$\begin{cases} E_{\text{int}}^{\varphi}(r=a) = E_{shell}^{\varphi}(r=a) \\ E_{\text{int}}^{z}(r=a) = E_{shell}^{z}(r=a) \\ H_{\text{int}}^{\varphi}(r=a) = H_{shell}^{\varphi}(r=a) \\ H_{\text{int}}^{z}(r=a) = H_{shell}^{z}(r=a) \end{cases}. \tag{1.15}$$

The remaining four equations can be derived imposing the double-boundary condition characterizing the metasurfaces at the second interface of the structure (Fig. 5 – right), *i.e.*,

$$\begin{cases} E_{shell}^{\varphi}(r=a_c) = Z_s \left[\hat{\mathbf{r}} \times \left(H_i^{\varphi}(r=a_c) + H_s^{\varphi}(r=a_c) - H_{shell}^{\varphi}(r=a_c) \right) \right] \\ E_{shell}^{z}(r=a_c) = Z_s \left[\hat{\mathbf{r}} \times \left(H_i^{z}(r=a_c) + H_s^{z}(r=a_c) - H_{shell}^{z}(r=a_c) \right) \right] \\ E_i^{\varphi}(r=a_c) + E_s^{\varphi}(r=a_c) = Z_s \left[\hat{\mathbf{r}} \times \left(H_i^{\varphi}(r=a_c) + H_s^{\varphi}(r=a_c) \right) \right] \\ E_i^{z}(r=a_c) + E_s^{z}(r=a_c) = Z_s \left[\hat{\mathbf{r}} \times \left(H_i^{z}(r=a_c) + H_s^{z}(r=a_c) \right) \right] \end{cases}. \tag{1.16}$$

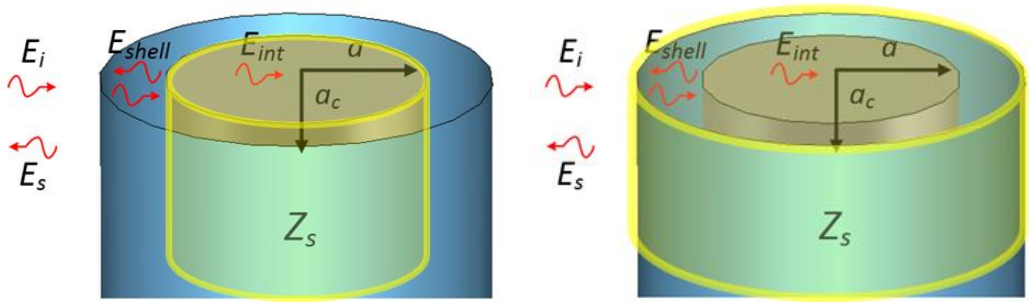

Fig. 5: (left) First and (right) second interface of the coated cylinder.

By solving the 8×8 systems returned by (1.15)-(1.16), it is possible to achieve an analytical expressions of the terms $a_n \ldots f_n^2$. Among them, I are interested in the expressions of a_n and b_n since they are directly related to the scattered field (1.12). In particular, the total scattering width (SW) of the coated cylinder (*i.e.*, the scattering cross section per unit of length) can be evaluated as follows

$$Q_{sca} = \frac{2}{k_0 a}\left[|b_0|^2 + 2\sum_{n=1}^{\infty}\left(|b_n|^2 + |a_n|^2 \right) \right]. \tag{1.17}$$

Formula (1.17) shows that the overall scattering of an object is the superposition of different scattering modes each of them identified by a proper value of the integer index *n*. As an example, in Fig. 6, it is reported the contribution to the total scattering cross-section at $f_0 = 3\ GHz$ of the first five scattering modes of an uncoated dielectric cylinder (*i.e.*, $X_s \to \infty$) with relative permittivity equal to ε = 4 and ε = 10, respectively, as the cylinder radius changes. As can be appreciated, as far the cylinder radius is small compared to the operative wavelength the only non-negligible contribution to the overall scattering is provided by the zeroth scattering mode. Since a metasurface can tailor a single scattering mode, it possible to obtain a cloaking phenomenon for objects that satisfy the so-called quasi-static condition, *i.e.*, $r \le \lambda_0/10$.

As an evidence, in Fig. 7 it is reported the variation of scattering width gain with the surface reactance of a mantle cloak for an infinitely long dielectric cylinder with relative permittivity $\varepsilon = 10$ and radius $a = \lambda_0/10$. As it can be appreciated, depending on the cover radius, it is ever possible to observe a minimum of the SW for a cylinder for a specific

value of the cloak surface reactance X_s. This SW minimum is related to a dramatic reduction of the object electromagnetic visibility and identifies a cloaking phenomenon. Please note that, for dielectric objects, the required surface reactance value is positive (*i.e.*, inductive) whereas for metallic object a capacitive reactive sheet is required.

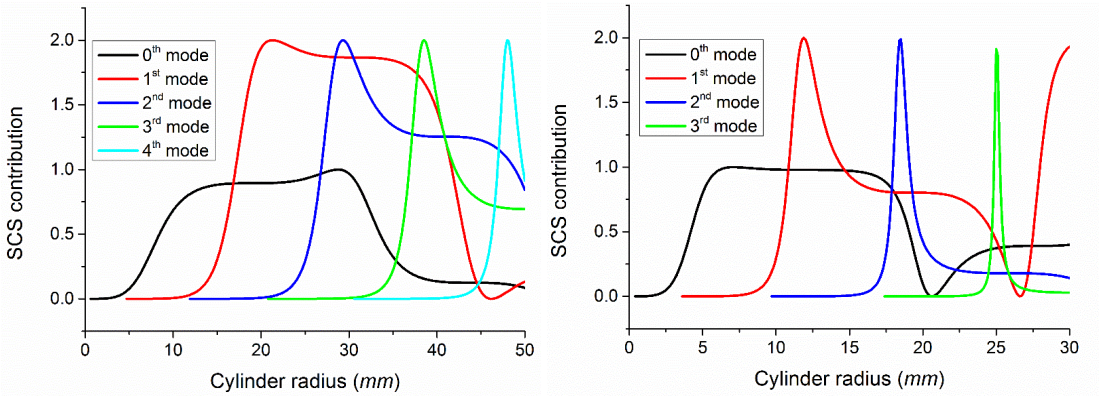

Fig. 6: SCS contribution of several scattering modes of a dielectric cylinder with relative permittivity equal to $\varepsilon = 4$ and $\varepsilon = 10$, respectively, as the cylinder radius changes. The operation frequency is $f_0 = 3$ GHz.

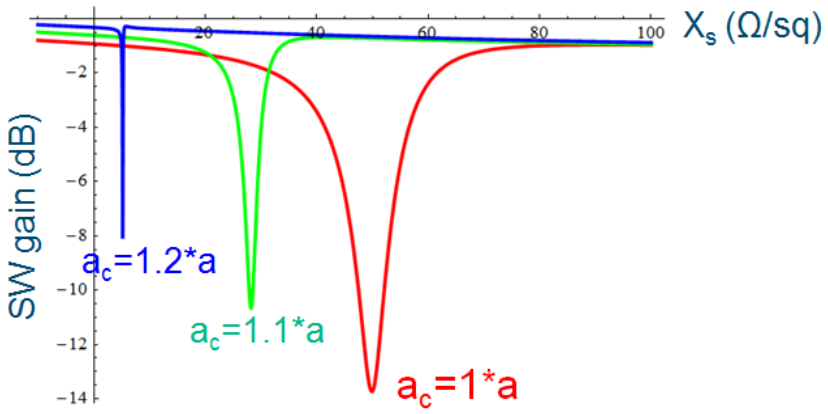

Fig. 7: Variation of the scattering width gain with the surface reactance of a mantle cloak for an infinitely long dielectric cylinder with permittivity $\varepsilon = 10$ and radius $a = \lambda_0/10$.

For sub-wavelength dielectric cylinders, the ideal cloaking value of the cloak surface reactance can be calculated with the following expression [8]:

$$X_s^{ideal} = \frac{2}{\omega a \gamma \varepsilon_0 (\varepsilon - 1)}. \tag{1.18}$$

Differently from the dielectric case, instead, in the metallic one the cloaking effect is generally quite narrowband and a more refined analytical approximation is required in order to avoid a gross evaluation of the ideal surface impedance. By expanding the Bessel and the Hankel functions describing the zeroth TM scattering mode contribution to the total SCS with proper Taylor series, I can derive the following formula for the case of TM incidence [24]:

$$X_s^{ideal} = -\frac{16\mu_0\omega a_c\left(a_c^2k_0^2-4\right)\ln\left(a/a_c\right)}{\left(a^2k_0^2-4\right)\left(256-4a_c^4k_0^4+a_c^6k_0^6\right)}\times \\ \times\left[4\left(a^2-a_c^2\right)k_0^2+\left(a^2k_0^2-4\right)\left(a_c^2k_0^2-4\right)\right]. \tag{1.19}$$

1.2.2 TE-polarization

I consider there the case in which the electric field of the incident plane wave is perpendicular to the axis of the cylinder, *i.e.*, $\mathbf{E}_i=\hat{\mathbf{y}}E_0e^{jkx}$. The main difference compared to the TM incidence regards the field expansion. For what concerns the incidence field, in this case it reads as follow:

$$\mathbf{E}_i=\sum_{n=-\infty}^{\infty}-iE_n\mathbf{M}_n^{(1)}\left(\rho,\varphi,z\right), \tag{1.20}$$

Also in this case, the field $\mathbf{E}_{shell}$ is the superposition of an incoming and an outgoing cylindrical wave whereas the fields $\mathbf{E}_{\text{int}}$ and $\mathbf{E}_s$ are an incoming and an outgoing cylindrical wave, respectively. Exploiting the expansion (1.20), I can write:

$$\mathbf{E}_{\text{int}}=\sum_{n=-\infty}^{\infty}E_n\left(c_n\mathbf{M}_n^{(1)}+d_n\mathbf{N}_n^{(1)}\right) \tag{1.21}$$

$$\mathbf{E}_s=-\sum_{n=-\infty}^{\infty}E_n\left(b_n\mathbf{M}_n^{(3)}+ia_n\mathbf{N}_n^{(3)}\right) \tag{1.22}$$

$$\mathbf{E}_{shell}=\sum_{n=-\infty}^{\infty}E_n\left(ie_n^1\mathbf{M}_n^{(3)}+ie_n^2\mathbf{M}_n^{(1)}-f_n^1\mathbf{N}_n^{(3)}-f_n^2\mathbf{N}_n^{(1)}\right) \tag{1.23}$$

Similarly to the TM-case, by imposing the proper boundary conditions and solving the 8×8 systems, I can achieve the analytical expressions of the unknown coefficients. Then, by proper expanding the scattering coefficients a_n and b_n in Taylor series, it is possible to obtain the closed-form formulas to evaluate the ideal surface reactance able to suppress the first scattering mode under a TE incidence for both a dielectric and a metallic cylinder. However, the relative expressions are quite cumbersome and they are here omitted.

I conclude this Subsection with some observations: first, I underline that, for a cylindrical geometry, the TE scattering is generally significantly lower than TM, so the design of a cloak able to tailor also the scattering of this polarization may not necessarily be essential for all applications. However, it is equally important to note that the analysis developed here also apply to the case of electrically large objects, for which TE scattering may became stronger, as evident in Fig. 8. In these cases, multilayered mantle cloaks, described in the next Subsection, provide the necessary degrees of freedom to suppress higher-order TM and TE scattering harmonics.

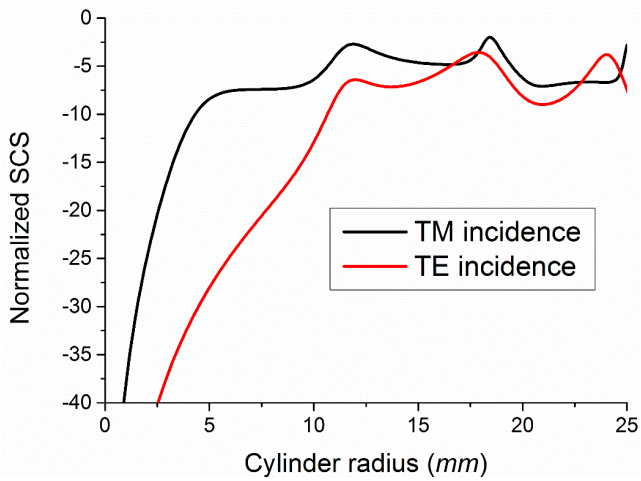

Fig. 8: Normalized SCS of a dielectric cylinder with relative permittivity $\varepsilon = 10$ at 3 GHz for both TM and TE incidence as the cylinder radius changes.

Second, it is important to point out that TE scattering is usually the combination of several scattering orders with similar amplitudes, differently from what happens in the TM case for which it is possible to recognize a dominant contribution from the lower scattering harmonic. With a single-layer cover I can typically suppress one or two scattering orders and, therefore, the SCS gain in the TE case is inevitably lower

compared to the TM case. Also in this case, multilayered mantle cloaks may help achieving further total SCS reductions, since they allow the suppression of multiple scattering orders concurring to the overall TE scattering.

1.2.3 Multilayered mantle cloaks

As evident from the discussion of the previous Subsection, single-layer mantle cloaking devices are effective in the scattering reduction of objects whose characteristic size is small compared to the operational wavelength and for moderately narrow frequency range.

In this Subsection, it is proposed a generalization of the mantle cloaking approach to multi-layer covers working for non-electrically small objects and/or for broader frequency range. Here, it is considered the structure shown in Fig. 9, where an infinitely long cylinder with radius a and electromagnetic parameters (ε, μ) is surrounded by two conformal anisotropic metasurfaces with effective surface impedance tensor equal to $\underline{\underline{Z}}_s^1$ and $\underline{\underline{Z}}_s^2$, where:

$$\underline{\underline{Z}}_s^i = \begin{pmatrix} Z_s^{TM,i} & 0 \\ 0 & Z_s^{TE,i} \end{pmatrix}, \qquad i = 1, 2. \tag{1.24}$$

The radius of the metasurfaces are $a_c^1 = \gamma_1 a$ and $a_c^2 = \gamma_2 a$, respectively, and the object is illuminated by an external plane wave with electric field parallel (TM incidence) or perpendicular (TE incidence) to the cylinder axis.

The electromagnetic analysis is analogous to the one developed for a single layer mantle cloak device. The only difference is related to the existence of another space region (the one comprised between the two metasurfaces) in which the electric field $\mathbf{E}_{shell,2}^{TM}$ needs to be defined. The following expressions can be used:

$$\mathbf{E}_s^{TM} = \sum_{n=-\infty}^{+\infty} E_n \left[-b_n \mathbf{N}_n^{(3)}(r, \varphi, z) - j a_n \mathbf{M}_n^{(3)}(r, \varphi, z) \right] \tag{1.25}$$

$$\mathbf{E}_{shell,1}^{TM} = \sum_{n=-\infty}^{+\infty} E_n \begin{bmatrix} -f_{n,1}\mathbf{N}_n^{(3)}(r,\varphi,z) - je_{n,1}\mathbf{M}_n^{(3)}(r,\varphi,z) + \\ +f_{n,2}\mathbf{N}_n^{(1)}(r,\varphi,z) + e_{n,2}\mathbf{M}_n^{(1)}(r,\varphi,z) \end{bmatrix} \tag{1.26}$$

$$\mathbf{E}_{shell,2}^{TM} = \sum_{n=-\infty}^{+\infty} E_n \begin{bmatrix} -h_{n,1}\mathbf{N}_n^{(3)}(r,\varphi,z) - jg_{n,1}\mathbf{M}_n^{(3)}(r,\varphi,z) + \\ +h_{n,2}\mathbf{N}_n^{(1)}(r,\varphi,z) + g_{n,2}\mathbf{M}_n^{(1)}(r,\varphi,z) \end{bmatrix} \tag{1.27}$$

$$\mathbf{E}_{int}^{TM} = \sum_{n=-\infty}^{+\infty} E_n \left[c_n\mathbf{M}_n^{(1)}(r,\varphi,z) + d_n\mathbf{N}_n^{(1)}(r,\varphi,z) \right] \tag{1.28}$$

Please note that, for the reader convenience, the incoming cylindrical waves have been highlighted using a blue font, whereas the outgoing cylindrical wave are written in red. Analogous expressions can be easily derived for the TE polarization.

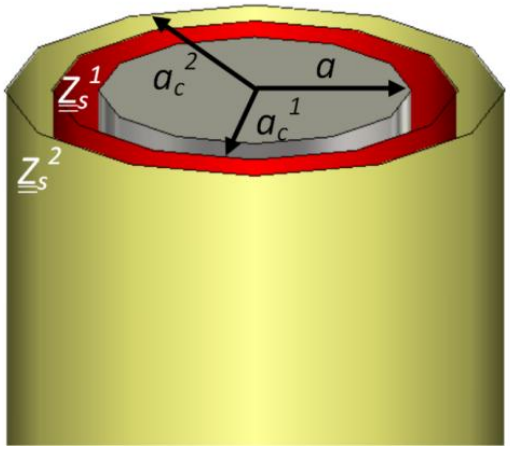

Fig. 9: Section of a multilayer mantle cloaking in the cylindrical geometry.

The 12×12 analytical systems whose solutions return the scattering coefficients can be easily obtained using expressions (1.15)-(1.16). In particular, equations (1.16) need to be applied both the first (*i.e.*, $r = a_c^1$) and to the second (*i.e.*, $r = a_c^2$) interface of the coated object. The generalization of this electromagnetic analysis to a generic *N*-layer cloak device is straightforward.

MULTIBAND AND BROADBAND CLOAKING

Multiband cloaking is naturally enabled using bilayer cloaks. In this Subsection, I consider a conductive target of cross-section $2a = \lambda_0/5$, where λ_0 is the wavelength a 3 GHz, as this represents a target of practical interest. Using the analytical formulation

developed above it is possible to calculate the required surface impedance values to simultaneously reduce the scattering at 2 GHz and 3 GHz for conformal aspect ratios $\gamma_1 \equiv a_c^1/a = 1.01$ and $\gamma_2 \equiv a_c^2/a = 1.50$, such that the overall covered object is still $2a_c^2 = 0.3\lambda_0$. In Fig. 10, the scattering characteristics are shown for this example, targeting the two dominant scattering modes at the two design frequencies. In the top panel, the surface impedances ($X_{s,1} = -1.5\ \Omega$, $X_{s,2} = -184.2\ \Omega$) are properly selected to suppress the monopolar and the dipolar scattering mode at 2 and 3 GHz, respectively. As expected, I see strong scattering suppression at 2 GHz, where the monopolar term is dominant. Targeting the dipolar term at 3 GHz, a more broadband suppression is achieved at higher frequencies where it becomes more relevant. Here I see a strong suppression of -10.2 dB at 2 GHz with a wide 3 dB bandwidth between 3.3-4.3 GHz.

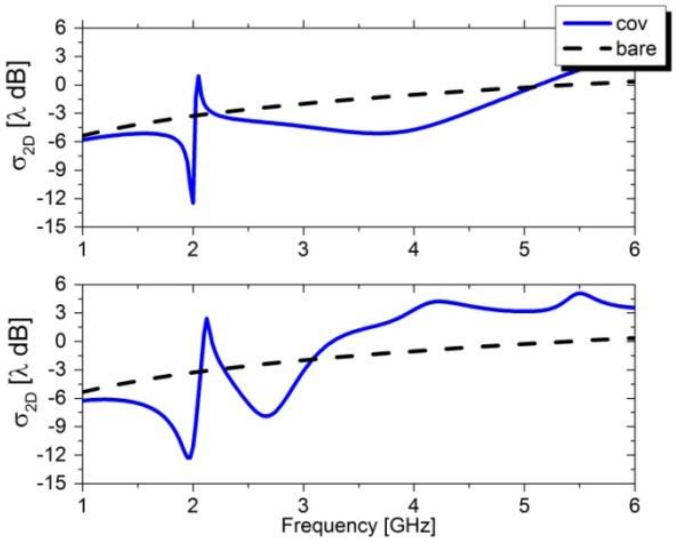

Fig. 10: (Top panel) Scattering profile targeting the monopolar mode at 2 GHz and the dipolar at 3 GHz. (Bottom panel) Scattering profile targeting the monopolar mode at 2 and 3 GHz.

In the bottom panel of Fig. 10, it is next show the effect of cancelling the monopolar term at both frequencies with the same aspect ratios. The required surface impedances ($X_{s,1} = -1.6\ \Omega$, $X_{s,2} = -113.7\ \Omega$) now have a tighter dual-band operation of -9.1 dB at 2 GHz and -5.6 dB at 2.7 GHz. Fig. 10 demonstrates two significant applications for cloaking designs under the cancellation condition for the chosen scattering modes. It should be emphasized here that I selected these two modes because they dominate the scattering at the two target frequencies, but in general they may not always be the best

choice, as the interactions between the chosen surfaces may enhance other higher-order modes (HOM), especially for larger targets. The effect of the coupling interactions between these residual in-band modes is seen in Fig. 10, which either slightly detunes the minimum SW, or limits the scattering suppression or overall bandwidth.

CLOAKING OF NON-ELECTRICALLY SMALL OBJECTS

I consider here the possibility to exploit the multilayered mantle cloaking devices to suppress more than one scattering order at the same frequency and, therefore, cloaking non-electrically objects. As an example, in Fig. 11 I report the SCS contribution of the first three scattering modes of a dielectric cylinder with permittivity $\varepsilon = 10$ at a frequency $f_0 = 3\ GHz$ as the cylinder radius changes for both TM and TE polarization.

For $a = \lambda_0 / 2.85 = 35\ mm$ the total SCS for both the polarizations is the superposition of three scattering modes. As can be appreciated in Fig. 12, with a properly designed bi-layer anisotropic mantle cloak device ($a_c^1 = 1.04 \times a$, $a_c^2 = 1.06 \times a_c^1$, $X_s^{TM,1} = -37.6\ \Omega$, $X_s^{TE,1} = -11.8\ \Omega / sq$, $X_{s,TM}^2 = 272.4\ \Omega$, $X_{s,TE}^2 = -19\ \Omega$) it is possible to reduce the object SCS of 6 *dB* for the TM polarization and 10 *dB* for the TE polarization. The use of a tri-layer mantle cloaking device (Fig. 13) allows to achieve a bigger reduction equal to 12 *dB* and 9 *dB* of the TM and TE scattering, respectively. Please note that, the geometrical and electromagnetic values of the cloaks has been obtained with a numerical minimization of the analytical formulas expressing the scattering of a cylinder cloaked with a *N*-layered cover.

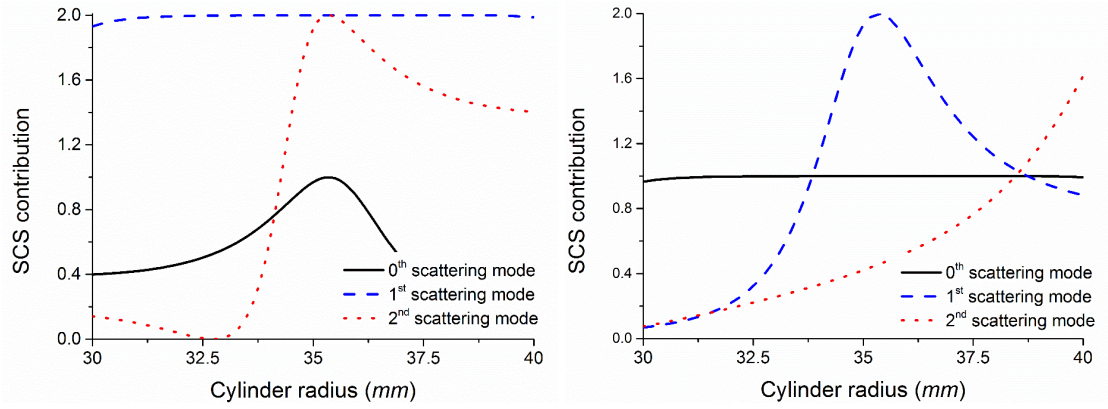

Fig. 11: SCS contribution of the first three scattering modes for a dielectric cylinder with relative permittivity $\varepsilon = 10$ at a frequency $f_0 = 3\ GHz$ for both TM (left) and TE (right) incidence.

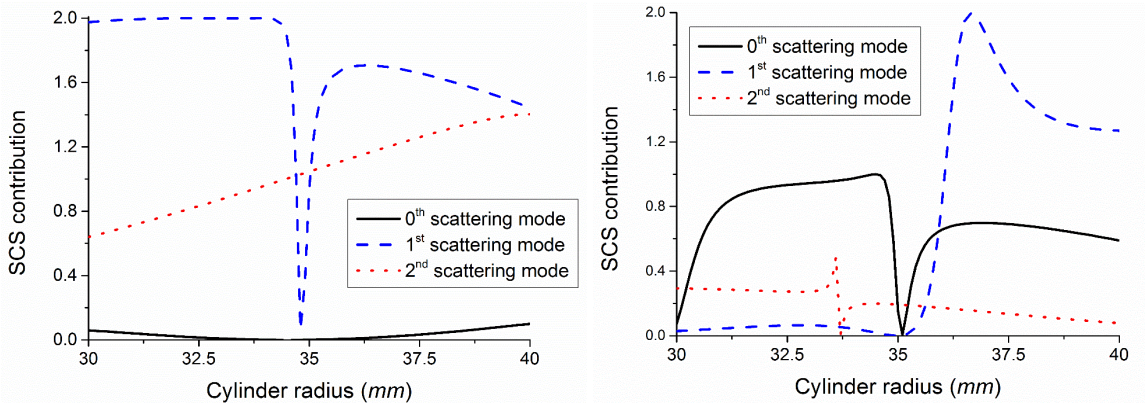

Fig. 12: SCS contribution of the first three scattering modes for a dielectric cylinder with relative permittivity $\varepsilon = 10$ at a frequency $f_0 = 3$ GHz coated with a bi-layer mantle cloak device as the cylinder radius changes for both TM (left picture) and TE (right picture) incidence.

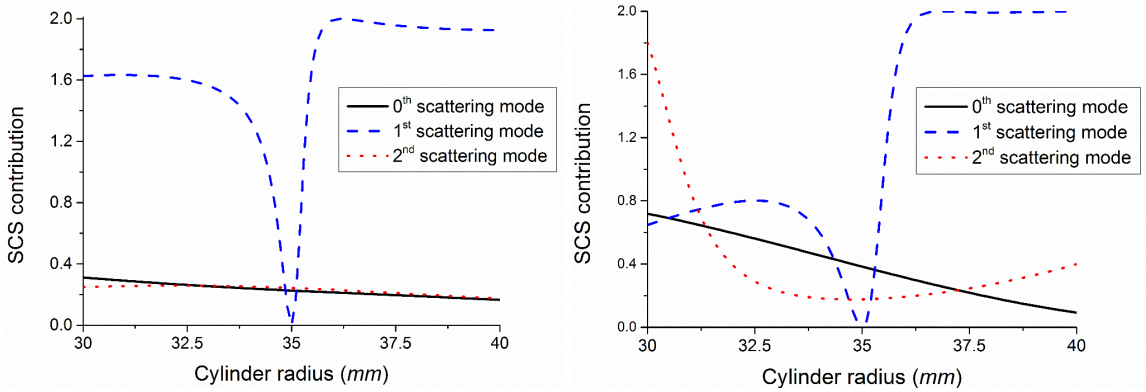

Fig. 13: SCS contribution of the first three scattering modes for a dielectric cylinder with relative permittivity $\varepsilon = 10$ at a frequency $f_0 = 3$ GHz coated with a tri-layer mantle cloak device as the cylinder radius changes for both TM (left picture) and TE (right picture) incidence.

1.3 Metasurface analytical models

In the previous Section, I have investigated the theoretical basis of the mantle cloaking approach. In particular, it has been proven that the use of one or more metasurfaces exhibiting a desired value of their own intrinsic surface reactance is able to provide a cloaking effect, *i.e.*, a nullification of the object scattering. At microwave frequencies, a metasurface can be realized simply using a patterned metallic surface. In this Section, I summarize the results of [24]-[27] in which the design of microwave metasurfaces for cloaking applications for both TM and TE incidence polarization has been deeply investigated.

1.3.1 Single-polarized metasurfaces

This Subsection is focused on the analytical models that are used to describe the electromagnetic behavior of the metasurface working for the sole TM polarization of the incident field.

Let us consider a patterned metallic surface with unit-cell depicted in Fig. 14. The structure consists of an array of thin metallic strips printed on a dielectric substrate with relative permittivity ε_r. The equivalent surface reactance of the infinite periodic structure has been studied by various authors employing different approaches [32]-[40]. The first model was presented in [32] and generalized, in a semi-empirical way, by Ulrich [33]. More accurate results have been obtained in [37], where a transmission-line model was used to obtain the equivalent circuit of the grid. The same expression has been later obtained in [38] by using the average boundary approach.

In the general case, without any additional assumption on the strip periodicity, beyond being electrically small, the surface impedance exhibited by the structure when illuminated by a TM (*i.e.*, electric field parallel to the strips) normally-incident plane wave can be expressed by the following closed-form formula [38]:

$$Z_s^{grid,TM} = jX_s^{grid,TM} = j\frac{\eta_{eff}}{2}\alpha = j\sqrt{\frac{\mu_0}{\varepsilon_0\varepsilon_{eff}}}\frac{\alpha}{2}, \tag{1.29}$$

where η_{eff} is the effective wave impedance and α is the so-called grid parameter, whose complete expression can be found in [39]. Note that the effective permittivity can be expressed as $\varepsilon_{eff} = (\varepsilon_r + 1)/2$, assuming that the background medium of the impinging wave is vacuum. For electrically dense arrays ($k_{eff}\, a \ll 2\pi$), the grid parameter has the simple expression

$$\alpha = \frac{k_{eff}\, a}{\pi}\ln\left[\csc\left(\frac{\pi w_1}{2a}\right)\right]. \tag{1.30}$$

In order to study the response of the structure of Fig. 14 to a TE (*i.e.*, electric field perpendicular to strips) normally-incident plane wave, I can apply the formulas of the complementary structure, obtained using Babinet's principle in its modified form to take into account the presence of a dielectric discontinuity at the interface [34]. Therefore, the surface impedance of the grid for TE incidence is

$$Z_s^{grid,TE} = jX_s^{grid,TE} = \frac{2}{(\varepsilon_r + 1)} \frac{\eta_0^2}{4Z_s^{grid,TM}} \tag{1.31}$$

It is worth noticing that for TE incidence the term w_1 in the expression of $Z_s^{grid,TM}$ in (1.31) is now replaced by a-w_1. To summarize, I can state that, if the incident electric field is parallel to the strips, the impedance exhibited by the metasurface is inductive, while for orthogonal excitation the response of the structure is purely capacitive.

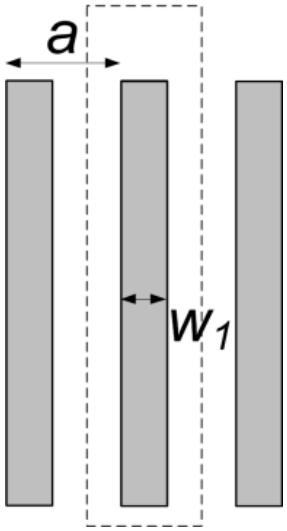

Fig. 14: Unit-cell (inside the dashed line) of an array of metallic strips (grid).

The proper working of these design formulas for mantle cloaking applications has been extensively investigated in [24]. I do report here the relative results since, in the next Subsection, it is shown the derivation and on the proper working of more elaborate formulas working for both TM and TE polarization of the impinging plane wave.

1.3.2 Dual-polarized metasurfaces

In the previous Section, it has been described the analytical model of some inductive or capacitive isotropic metasurfaces able to provide a mantle cloaking effect. Given the strong anisotropy of the considered objects, such covers work for a single polarization of the impinging field, *i.e.*, the one parallel to the cylinder axis that typically represents the strongest contribution to the overall scattering in the long-wavelength limit.

However, in practical situations, especially for cylinders of thickness comparable to the wavelength, it is desirable to reduce the field scattered by an object under the assumption of a more general illumination. Any impinging wave, in fact, can be decomposed into orthogonally polarized TE and TM waves, and cloaks able to suppress the scattering for both polarizations may be able to fully conceal the object, independent of the excitation. The aim of this Section is to generalize the mantle cloaking design to the case of covers operating, at the same frequencies, for both orthogonal polarizations of the incidence field.

I start by considering a metasurface with a rectangular unit-cell, like the one shown in Fig. 15(a). The widths of the vertical and horizontal strips, as well as their lengths, can vary independently. Thanks to the structure anisotropy, it is possible to obtain different surface reactance values for orthogonal polarizations. As shown in the following, this feature opens the possibility to design mantle cloaks effective for all polarizations of the incident plane wave, and for objects made of anisotropic materials and/or with an anisotropic shape. The transition from the array of metallic strips (Fig. 14) to the rectangular unit-cell metasurface (Fig. 15(a)) introduces a resonant response, since a rectangular unit-cell is characterized by an inductance, associated to the vertical or the horizontal strips (depending on the incidence polarization), and a capacitance, associated to the orthogonal strips (Fig. 15(b) and Fig. 15(c)). However, for subwavelength dimensions, the self-resonant frequency (SRF) will be much higher than the cloaking band. Therefore, such a structure can be analytically studied using the conventional grid model, whose details were given in previous Section. In particular, it is easy to verify that, if an external plane wave with electric field parallel to the vertical strips (TM incidence), is applied the overall surface impedance is given by the parallel

combination of the effective inductance associated with the parallel strips (1.29) and the effective capacitance of the orthogonal ones (1.31), *i.e.*,

$$Z_s^{rect,TM} = \frac{-j\eta_0 \left(ac_0 f\right) \ln\left[\csc^2\left(\frac{\pi w_1}{2a}\right)\right]}{abf\left(1+\varepsilon_r\right)\ln\left[\csc^2\left(\frac{\pi w_1}{2a}\right)\right]\ln\left[\sec^2\left(\frac{\pi w_2}{2b}\right)\right] - 2c_0^2}, \tag{1.32}$$

where η_0 is the free space impedance, c_0 is the speed of light in vacuum and f is the frequency. Similarly, if the external plane wave has an electric field parallel to the horizontal strips (TE incidence), the surface impedance $Z_s^{rect,TE}$ can be simply obtained from (1.32) by replacing a with b and w_1 with w_2.

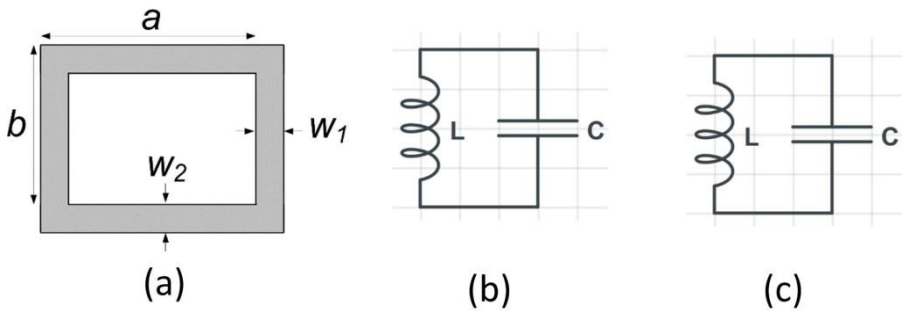

Fig. 15: (a) Unit-cell of a rectangular metasurface. w_1 and w_2 are the widths of each parallel segment of the metasurface. (b)-(c) Its equivalent circuit model for the TM and TE polarization, respectively.

Varying the values of a, b, w_1 and w_2, the metasurface exhibits different values of effective reactance for the two orthogonal polarizations. Even though the metasurface model (1.32) is a parallel combination of a capacitive and an inductive impedance, it is easy to verify that the effective surface reactance exhibited by the metasurface is always positive (*i.e.*, inductive), independent of the incidence polarization. From an analytical point of view, this is due to the large value of shunt capacitance in (1.32). For this reason, as I will show later, this type of metasurface is useful to design cloaks for objects requiring positive values of surface reactance for both polarizations. Another important observation arising from formula (1.32) is that the values of $Z_s^{rect,TM}$ and $Z_s^{rect,TE}$ are only slightly affected by the relative permittivity of the dielectric substrate ε_r. In fact, as it is

evident from the model of the grid metasurface, the relative permittivity plays a relevant role only for the capacitive part of the surface impedance, whereas it does not contribute to the inductance of the strips parallel to the impinging electric field. Since the strip capacitance assumes a very large value and can be neglected in the parallel combination (1.32), the contribution of a non-extreme permittivity to the overall impedance (1.32) is generally negligible.

In some practical cases it is required that the surface reactance exhibits different signs for TE and TM polarizations. Metasurface geometries able to synthesize different combinations of surface reactance signs for the two orthogonal polarizations are, therefore, necessary. To achieve this goal, the easiest choice is to add small modifications to the rectangular unit-cell geometry, as shown in Fig. 16(a)-Fig. 18(a). By introducing horizontal and/or vertical slits in the rectangular unit-cell I provide additional capacitance for TM and/or TE polarization (depending on necessity), without changing the sign for the other polarization. Polarization coupling will be present, but it only slightly de-tunes the operating frequency for each polarization, especially at oblique angles of incidence. These small modifications keep the overall design simple and provide additional degrees of freedom for the effective design of metasurface-based mantle cloaks.

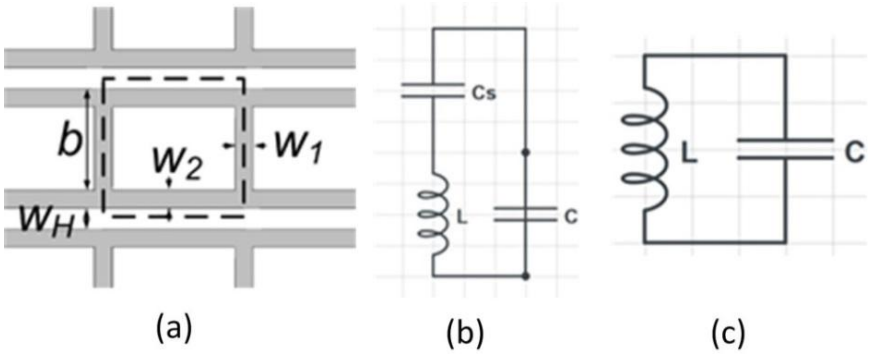

Fig. 16: (a) Metasurface characterized by a rectangular unit-cell with horizontal slits able to exhibit a negative and a positive value of surface reactance for TM and TE polarization, respectively; (b)-(c) Its equivalent circuit model for the TM and TE polarization, respectively.

It is possible to develop a proper circuital representation of the horizontal and/or vertical cut metasurfaces in the limit of small slits by extending the results of [41] where a model of isotropic squared metasurfaces with both vertical and horizontal slits has been proposed. I describe here the steps to derive the circuit model of the structure

depicted in Fig. 16(a). As a first observation, it is possible to note that, for TM incidence, the vertical slits introduce an additional capacitance *C* connected in series to the inductance *L* of the vertical strips. This LC series circuit (whose impedance is denoted as $Z_s^{V,TM}$) is then connected in parallel to the capacitance of the horizontal strips (with impedance $Z_s^{H,TM}$). Therefore, the overall surface impedance $Z_s^{H-\text{slits},TM}$ of the rectangular horizontal-cut metasurface can be expressed as:

$$Z_s^{H-slits,TM} = \frac{Z_s^{V,TM} Z_s^{H,TM}}{Z_s^{V,TM} + Z_s^{H,TM}}. \tag{1.33}$$

Since $Z_s^{V,TM}$ is the series between an inductance and a capacitance, its expression is equal to:

$$Z_s^{V,TM} = Z_L^{V,TM} + Z_C^{V,TM}, \tag{1.34}$$

being $Z_L^{V,\text{TM}}$ and $Z_C^{V,\text{TM}}$ the impedance associated to *L* and *C*, respectively. The expression of $Z_L^{V,\text{TM}}$ can be easily obtained using the expression of $Z_s^{grid,TM}$. The expression of $Z_C^{V,\text{TM}}$, instead, can be derived adjusting the results of [41] to the geometry under consideration. After some trivial calculations and setting $\varepsilon_r = 1$, it is possible to obtain:

$$Z_L^{V,TM} = jX_L^{V,TM} = j\frac{ak_0\eta_0 \ln\left[\csc\left(\frac{\pi w_1}{2a}\right)\right]}{2\pi}, \tag{1.35}$$

$$Z_C^{V,TM} = -jX_L^{V,TM} = -j\frac{2\pi\eta_0}{4(b+w_2)k_0 \ln\left[\csc\left(\frac{\pi w_V}{2(b+w_V+w_2)}\right)\right]}. \tag{1.36}$$

It is interesting to note that the expression of $Z_C^{V,\text{TM}}$ can be derived from the one of $Z_s^{grid,TE}$ considering a capacitive strip effect given by an equivalent strip with width w_V

and separation distance equal to $b + w_V + w_2$ and multiplying the result by a geometrical factor due to the fact that the conductor is not continuous [40].

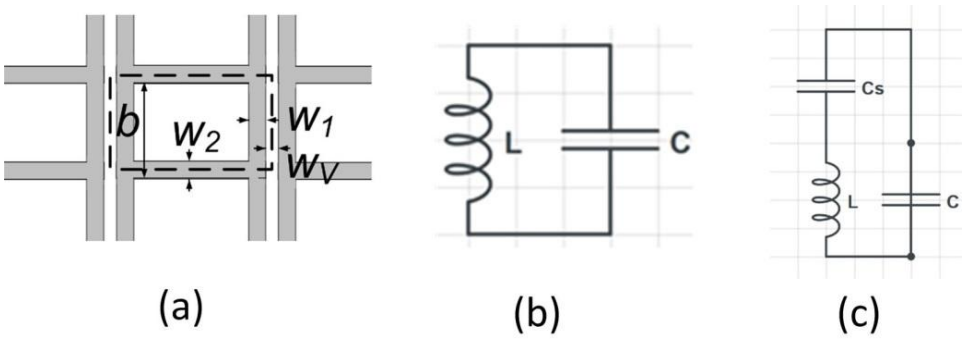

Fig. 17: (a) Metasurface characterized by a rectangular unit-cell with vertical slits able to exhibit a positive and a negative value of surface reactance for TM and TE polarization, respectively; (b)-(c) Its equivalent circuit model for the TM and TE polarization, respectively.

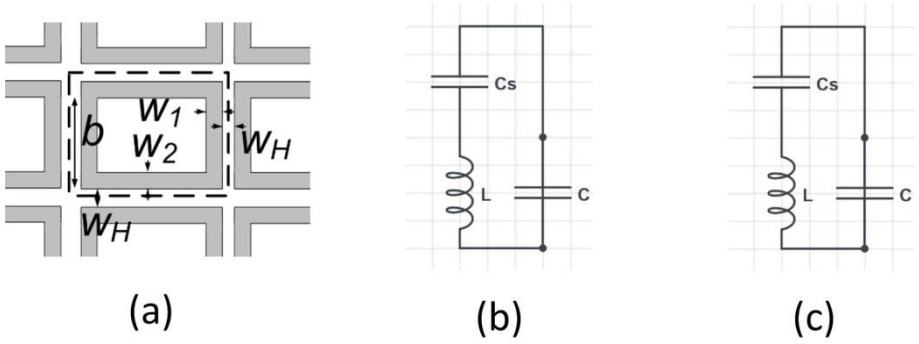

Fig. 18: (a) Metasurface characterized by a rectangular unit-cell with both horizontal and vertical slits able to exhibit a negative value of surface reactance for both TM and TE polarization; (b)-(c) Its equivalent circuit model for the TM and TE polarization, respectively.

The only other unknown quantity in (1.33) is $Z_s^{H,TM}$. Since it represents the capacitive effect of the horizontal strips perpendicular to the incidence electric field, its expression can be easily derived directly applying the formula (1.31). Therefore, all the quantities in (1.33) have been defined and it is possible to numerically compute the value of $Z_s^{H-\text{slits},TM}$ through a numerical code.

It is worth noting that the introduction of the vertical slits also produces a variation in the TE surface impedance of the structure. The TE surface impedance is still expressed by the dual of (1.32) but, in the horizontal-cut rectangular unit-cell metasurface, it is required to consider equivalent strips with width equal to $2w_2 + w_V$ and separation distance equal to $b + 2w_2 + w_V$. As already mentioned and as it is clear from the

electromagnetic analysis developed so far, these variations do not change the sign of the TE surface impedance that still remains inductive, but they produce a lowering of $Z_s^{H-\text{slits},TE}$ compared to $Z_s^{rect,TE}$ that needs to be taken into account in the metasurface design.

Following the described procedure I can easily obtain the analytical models of the structures of Fig. 17(a) and Fig. 18(a). For the first structure it is possible to obtain:

$$Z_s^{V-slit,TM} = Z_s^{\text{rect},TM}\Big|_{\substack{a\to a+2w_1+w_V \\ w_1\to 2w_1+w_V}}, \tag{1.37}$$

$$Z_s^{V-slits,TE} = \frac{Z_s^{V,TE} Z_s^{H,TE}}{Z_s^{V,TE} + Z_s^{H,TE}}, \quad Z_s^{H,TE} = Z_L^{H,TE} + Z_C^{H,TE}, \tag{1.38}$$

with

$$Z_C^{H,TE} = -\frac{j(2\pi\eta_0)}{4(a+w_1)k_0 \ln\left[\csc\left(\dfrac{\pi w_H}{2(a+w_H+w_1)}\right)\right]}. \tag{1.39}$$

For the structure of Fig. 18(a), it is possible to write

$$Z_s^{H-slits,TM} = \frac{Z_s^{V,TM} Z_s^{H,TM}}{Z_s^{V,TM} + Z_s^{H,TM}}, \quad Z_s^{V,TM} = Z_L^{V,TM} + Z_C^{V,TM}, \tag{1.40}$$

$$Z_s^{V-slits,TE} = \frac{Z_s^{V,TE} Z_s^{H,TE}}{Z_s^{V,TE} + Z_s^{H,TE}}, \quad Z_s^{H,TE} = Z_L^{H,TE} + Z_C^{H,TE} \tag{1.41}$$

with

$$Z_C^{V,TM} = -\frac{j(2\pi\eta_0)}{4(b+w_2)k_0 \ln\left[\csc\left(\dfrac{\pi w_H}{2(b+w_H+w_2)}\right)\right]}, \tag{1.42}$$

$$Z_C^{H,TE} = -\frac{j(2\pi\eta_0)}{4(a+w_1)k_0 \ln\left[\csc\left(\dfrac{\pi w_H}{2(a+w_H+w_1)}\right)\right]}. \tag{1.43}$$

1.3.3 Examples of dual-polarized cloaking devices

1D OBJECTS

In order to show the potential of the proposed model, I start by considering a 1D (planar) slab made of a dielectric bi-axial anisotropic material and thickness t. Such anisotropy arises in many realistic dielectric substrates, such as woven glass. This object can be considered as the natural generalization of the 1D isotropic dielectric slab used as a case-study in [7], but here extended to an anisotropic material. The lossless bi-axial anisotropic material is characterized by the following relative permittivity tensor:

$$\underline{\underline{\varepsilon}} = \begin{bmatrix} \varepsilon_x & 0 & 0 \\ 0 & \varepsilon_y & 0 \\ 0 & 0 & \varepsilon_z \end{bmatrix} \tag{1.44}$$

Due to its anisotropy, I expect that the required surface reactance needed to obtain a cloaking effect at the same frequency are different for TM and TE incident polarizations. The first step of my design procedure is to identify the required values of the surface impedance and the optimal distance between the metasurface and the object. Such values can be easily derived using a transmission model of the coated structure and imposing the nullification of the reflection coefficient at the metasurface branch [7]. Since I are considering a normally incidence plane wave, I can neglect the polarization conversion phenomena and I can deal separately with the TM polarization and the TE one. With reference to the coordinate system shown in Fig. 19, I use the term TM polarization to denote a normally incident plane wave with propagation vector directed along $-\hat{\mathbf{z}}$ and electric field parallel to the $y-$axis and, similarly, the term TE polarization to denote a normally incident plane wave with electric field parallel to the $x-$axis. For electrically thin slab $k_0 t\sqrt{\varepsilon_i} << \lambda_0$ (with $i = x, y$) and for small separation distance $k_0 d << \lambda_0$, the optimal surface impedance and the optimal separation distance between the slab and the metasurface can be expressed as follows:

$$X_s^{ideal,TM} = \frac{\eta_0\sqrt{1+t^2k_0^2\varepsilon_y}}{k_0\left(\varepsilon_y-1\right)t},$$
$$d^{TM} = \frac{\sqrt{1+t^2k_0^2\varepsilon_y}-1}{t\varepsilon_y k_0^2}, \tag{1.45}$$

being $k_0 = 2\pi/\lambda_0$ the free-space propagation constant. For the case of TE incidence, results can be easily obtained by (1.45) substituting ε_y with ε_x. It is important to note that, since in the general case $\varepsilon_x \neq \varepsilon_y$, the optimal values d^{TM} and d^{TE} are different. This means that, in the 1D case, an anisotropic metasurface placed at a fixed distance from the object cannot hit the optimal design values for both TM and TE polarization. However, for small value of t and weak anisotropy the difference between the two distances is negligible as I are going to show below.

As an example, I have considered an electrically small anisotropic slab with thickness $t = \lambda_0/50$ and permittivity tensor elements equal to $\varepsilon_x = 10, \varepsilon_y = 8, \varepsilon_z = 12$. Using formulas (1.45) I can determine the optimal value of the surface impedance and the separation distance that are, for TM and TE incidence, $\left\{X_s^{TM},\ d^{TM}\right\} = \left\{870\ \Omega,\ \lambda_0/201.5\right\}$ and $\left\{X_s^{TE},\ d^{TE}\right\} = \left\{680\ \Omega,\ \lambda_0/202\right\}$. The optimal separation distance for TM and TE incidence are very similar and, therefore, it is possible to fix $d = d^{TM}$ without affecting the cover performances for the TE incidence in a significant way. As it is clear from the discussion of the previous section, it is possible to achieve such surface impedance values using a rectangular unit-cell metasurface. Once fixed the values of w_1 and w_2, it is possible to use formula (1.32) and its dual for TE incidence to write a 2×2 system whose solution provide the values of a and b. The achieved analytical geometrical values need to be slightly improved with the numerical procedure described in [27]. The final design is characterized by the following values: $w_1 = w_2 = \lambda_0/795$, $a = \lambda_0/2.49$ and $b = \lambda_0/3.07$. The full-wave results for the reflection coefficient of the coated structure for both the incidence polarizations are shown in Fig. 19. The slight shift in the reflection coefficient minimum with respect to the cloaking frequency f_0 is due to the

approximations used to derive formula (1.45) from the rigorous transmission-line model and it is confirmed by the rigorous analytical results.

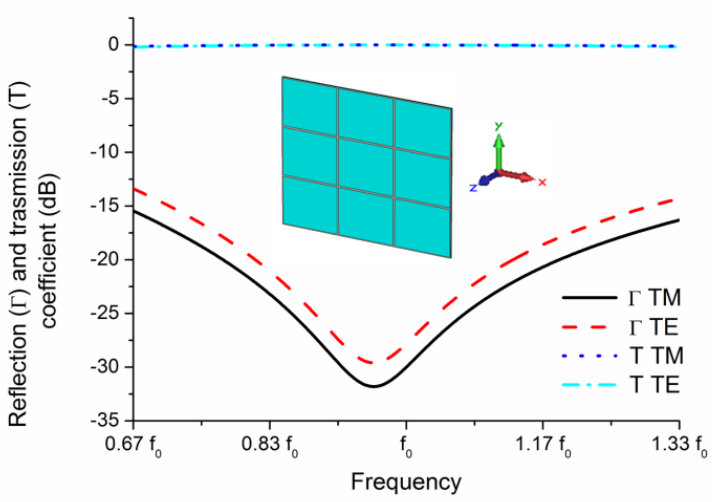

Fig. 19: Magnitude of the reflection and transmission coefficients for a cloaked slab with thickness $t = \lambda_0/100$ (shown in the inset) in the case of TM and TE incident polarizations. The mantle cloaking cover is realized with the rectangular unit cell metasurface.

Now, I focus my attention to non-electrically thin anisotropic slabs. In particular, I consider an anisotropic slab with the same permittivity of the previous example but with a thickness $t = \lambda_0 / 10$. Due to the moderately high value of the permittivity tensor elements, such a slab does not satisfy the conditions under which (1.45) have been obtained. For these reasons, the ideal surface impedance values for TE and TM polarization need to be computed numerically starting from the rigorous expression of the reflection coefficient at the metasurface branch. Moreover, in this case, the optimal distances d^{TM} and d^{TE} are significantly different between them. However, as I are going to show below, it is still possible to achieve high performances of the cover for both polarizations by choosing a sub-optimal value of X_s^{TE}. From the rigorous analytical model, it is possible to obtain that the optimal separation distance for the TM incidence is equal to $d^{TM} = \lambda_0 / 22.45$ and the relative reactance is equal to $X_s^{TM} = -155.6\ \Omega$. For the same value of the separation distance the sub-optimal value of the reactance for the TE polarization is equal to $X_s^{TE} = -190\ \Omega$.

As mentioned before, I can get the required values of surface reactance using a metasurface characterized by a rectangular unit-cell, with horizontal and vertical slits

able to add a capacitive effect for TM and TE polarizations. The design of such metasurface is rather straightforward and can be obtained by using the analytical model described previously together with the numerical procedure [27]. As an example of final design, I choose the one consisting of the following geometrical parameters: $a = \lambda_0 / 8.3$, $b = \lambda_0 / 6.68$, $w_1 = \lambda_0 / 340$, and $w_2 = \lambda_0 / 363$. The dimensions of the vertical and horizontal slits are equal to $\lambda_0 / 190$ and $\lambda_0 / 195$, respectively. The magnitude of the reflection and transmission coefficients for both TM and TE polarizations are shown in Fig. 20. A cloaking effect for both polarizations at the design frequency f_0 is obtained. Moreover, the amplitude of the reflection coefficients are the same as obtained when assuming an ideal anisotropic surface reactance, confirming that the patterned surface actually exhibits the required surface reactance values for both polarizations.

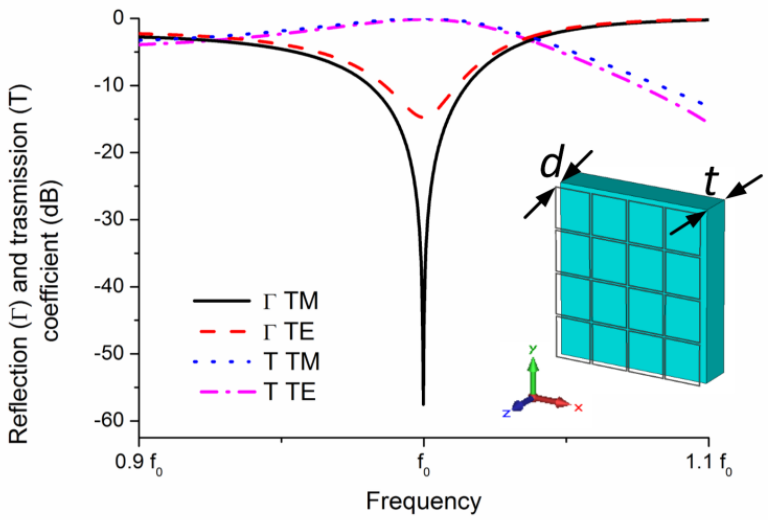

Fig. 20: Magnitude of the reflection and transmission coefficients for a cloaked slab with thickness $t = \lambda_0/10$ (shown in the inset) in the case of TM and TE incident polarizations. The mantle cloaking cover is realized with the rectangular unit cell metasurface with both horizontal and vertical slits.

Finally, I show the performance of the $t = \lambda_0 / 10$ cloaked slab for different incidence angles. With reference to the inset of Fig. 19, I denote with ϑ the angle between the propagation vector $\mathbf{k}$ and the z-axis measured on the $x-z$ plane starting from the z-axis. Full-wave results for different values of ϑ and for both the incidence polarizations are shown in Fig. 21. Due to the polarization coupling caused by the anisotropic material [43], the surface impedance values used to achieve cloaking for a normally incidence plane wave are not yet the optimal ones for a different incidence angle. This effect is

additional to the angle dependence of the rectangular unit-cell surface impedances producing an increasing shift in the cloaking frequency compared to the original frequency. However, due to the moderate large bandwidth of the 1D mantle cloaking effect, it is possible to finally observe that the designed metasurface is able to guarantee a significant cloaking effect for a moderately large angular range.

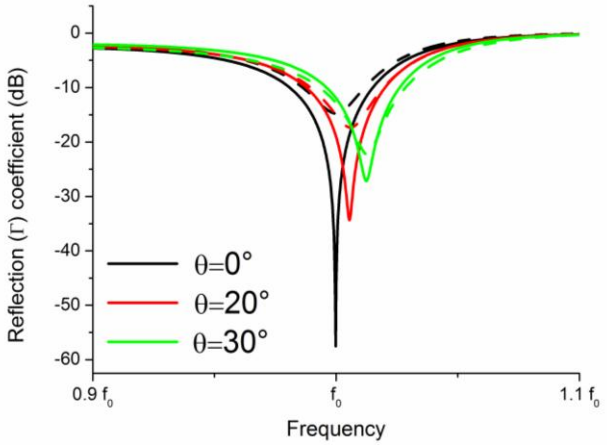

Fig. 21: Reflection coefficient of the cloaked slab for different incidence angles. Solid lines refer to TM polarization whereas dashed lines are obtained for TE polarization.

2D OBJECTS

The procedure outlined for a 1D object can be extended also to 2D geometries, such as circular cylinders. As already mentioned, for 2D and 3D geometries, the figure of merit to quantify the performance of a cloaking device is the so-called scattering cross section gain (or scattering width gain in 2D), that is simply the ratio between the total SCS (total SW) of the cloaked object and the one of an uncloaked object.

Differently from the 1D case, for 2D geometries there is an inherent geometrical anisotropy leading to different cloaking scenarios for TM (electric field parallel to the cylinder axis) and TE (magnetic field parallel to the cylinder axis) incident polarizations, even when the considered materials are isotropic. As a general consideration, I remember that, in the case of TE incidence, the overall scattering of an electrically small cylinder cannot be reduced to a single scattering mode as in the case of TM incidence. By using the rigorous analytic approach described in the previous Section of this Chapter, it is easy to verify that the dominant scattering contribution of a metallic cylinder with $r = \lambda_0 / 10$, being λ_0 the free-space cloaking wavelength, is represented by the first

scattering order. However, a non-negligible contribution is also given by the zeroth scattering mode of the object. Fig. 22 shows the theoretical performances of a mantle cloak for a metallic cylinder under TE incidence in terms of the SW gain. I observe two cloaking effects associated to the suppression of the zeroth and of the first scattering mode, respectively. The best performances (about $4\,dB$ of total SW reduction) can be achieved when the cover is designed to cancel the first scattering order.

In order to apply the analytical models previously derived, it is required to retrieve the values of the ideal surface impedance able to provide cloaking effects for both TM and TE incidence. Formula (1.19) can be used for TM incidence and a similar expression can be also derived for the TE one. Thanks to these design formulas, it is possible to compute the ideal cloaking values needed to reduce the scattering cross section of an infinitely long metallic cylinder for both TM and TE polarizations. For example, by choosing a metallic cylinder with $r = \lambda_0 / 10$ and a cloak radius $r_c = 1.2 \times r$, the cloaking conditions become $X_s^{ideal,TM} = -48\,\Omega$ (capacitive reactance) and $X_s^{ideal,TE} = 61\,\Omega$ (inductive reactance).

From the discussion in the previous Subsection, it is evident that, in order to design a realistic sheet exhibiting such surface reactance values, it is needed to use a metasurface characterized by rectangular unit-cells with vertical slits. Also in this case, the analytical models in combination with the retrieval procedure allow us to quickly obtain a working design that can be conformally applied to the cylinder. The final design is characterized by the following geometrical parameters: $a = \lambda_0 / 5.5$, $b = \lambda_0 / 2.97$, $w_1 = \lambda_0 / 5.82$, and $w_2 = \lambda_0 / 56.4$; the slit width is equal to $\lambda_0 / 126$. The performance of the cloak in terms of the SW gain, is shown in Fig. 22. The obtained SCS reduction is close to *9 dB* (suppression of 87% of the scattered signal integrated all around the object) for TM incidence and equal to *4 dB* (suppression of 60% of the scattered signal) for TE incidence.

I stress that the achieved SW gain at the design frequency f_0 is very similar to the theoretical one predicted by the Mie theory, confirming the effectiveness of the proposed design. In Fig. 23, please note that moving away from the cloaking frequency, it is possible to appreciate an increasing mismatch between the full-wave results and the theoretical ones. Such disagreement can be easily attributed to the fact that the

theoretical results have been obtained by considering an ideal metasurface exhibiting a constant value of its surface reactance. Conversely, full-wave results take into account the inherent frequency dispersion that affects any real metasurface.

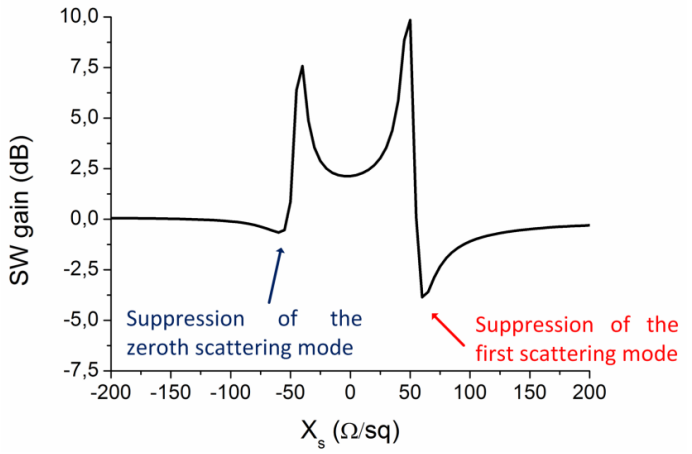

Fig. 22: Theoretical SW gain as the surface impedance of the cover changed for the case of TE incidence on a 2D metallic cylinder.

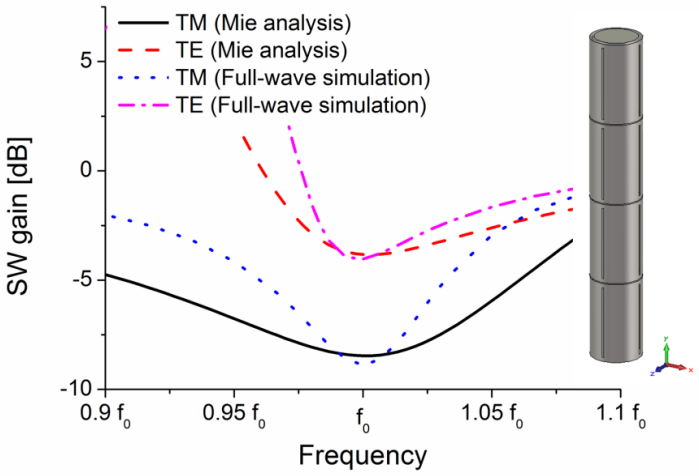

Fig. 23: Simulated SW gain for both TM and TE polarization compared to the one derived from Mie theory for a cloaked infinitely long metallic cylinder.

3D OBJECTS

In this Subsection, I consider 3D anisotropic structures and prove that the proposed design procedure can be also applied to these more complex geometries. As a first example, I consider a 3D electrically short dielectric cylinder, with permittivity $\varepsilon_d = 10$. The cylinder length is $L = \lambda_0 / 2$ and its radius $r = \lambda_0 / 10$. From a geometric point of view, this structure is again largely anisotropic and, therefore, different values of surface

reactance are required to obtain cloaking effects for both polarizations. Different from the 2D infinitely long cylinder, closed-formulas to compute the ideal cloaking surface impedance values do not exist for these structures. Therefore, such values must be estimated by means of full-wave simulations in which the surface reactance of the ideal cover is varied to numerically find the required values to achieve cloaking for both TM and TE polarizations. My full-wave simulations suggest that, for a cover radius $r_c = 1.1 \times r$, the scattering minima are obtained for $X_s^{ideal,TM} = 58\ \Omega$ and $X_s^{ideal,TE} = 110\ \Omega$. Since two different inductive values are required for the two polarizations, it is possible to use the metasurface characterized by a rectangular unit-cell, without any slit. Considering that the actual physical metasurface should exhibit these required values and must be applied conformally to the dielectric cylinder, I obtain a 4×4 equation system, whose solutions return the geometry of the metasurface unit-cell:

$$\begin{cases} X_s^{rect,TM} = X_s^{ideal,TM} \\ X_s^{rect,TE} = X_s^{ideal,TE} \\ \left(N_{rows} - 1\right) b + w_2 = L_{cylinder} \\ \dfrac{2\pi r}{N_{columns}} = a \end{cases}, \tag{1.46}$$

where the expression for $X_s^{rect,TE/TM}$ are given by (1.32). It is important to remark that system (1.46) still applies until the values of N_{rows} and $N_{columns}$ are able to provide metasurface geometrical values that do not break the metasurface homogenization requirements. The values of N_{rows} and $N_{columns}$ that satisfy these requirements depend on different parameters, such as the object and the cover radius and the permittivity of the object to hide. In addition, the curvature of the metasurface reduces the validity range of the geometrical parameters, since the local planarity of the curved metasurface has to be guaranteed. For the case under examination, full-wave simulations prove that the analytical system (1.46) has effective solutions for $N_{rows} \geq 3$ and $N_{columns} \geq 3$. Of course, by increasing the values of N_{rows} and $N_{columns}$ the analytically designed geometries will be more accurate due to the reduction of dimensions of the metasurface unit cell. However, it is important to point out that the maximum values of N_{rows} and $N_{columns}$

depend on the electrical size of the objects to hide, as well as on the desired working frequency. Too large values, in fact, may result in extremely thin vertical and/or horizontal strips difficult to produce with PCB technologies. Therefore, the choice of the values to be attributed to N_{rows} and $N_{columns}$ is a trade-off between these different aspects.

The final geometry, obtained by solving (1.46) for $\varepsilon_r = 1$ and applying the refinement procedure described in [27], is characterized by the following geometrical parameters: $a = \lambda_0 / 11.85$, $b = \lambda_0 / 8.04$, $w_1 = \lambda_0 / 500$ and $w_2 = \lambda_0 / 333$. The total SCS reduction for TM incidence can be quantified in *19 dB*, whereas a *11 dB* reduction has been obtained for TE incidence. In order to show the effectiveness of the designed cloak, in Fig. 24 it is compared its performance with the one of an optimized single polarization mantle cloaking cover. The structures have been excited by a normally incident circularly polarized plane wave. As it is evident from the picture, the dual-polarized mantle cloak yields a dramatic additional SCS reduction in the circularly polarized case compared to the single polarization device. In fact, a single polarization cover is only able to reduce the TM scattering, keeping unaffected or even increasing the TE one. Therefore, under circularly polarized plane wave excitation, the residual unsuppressed TE scattering becomes the dominant scattering contribution of the structure that can be suppressed only by using a dual-polarized mantle cloak.

Finally, as an additional 3D example, I consider a metallic prolate ellipsoid with principal semi-axes $a = b = \lambda_0 / 10$, $c = \lambda_0 / 4$. Also in this case, using full-wave simulations I computed the ideal cloaking reactance values for $r_c = 1.18 \times r$: $X_s^{ideal,TM} = 21\,\Omega$ (electric field parallel to the major axis), $X_s^{ideal,TE} = 103\,\Omega$ (electric field orthogonal to the major axis). I can write again a linear system similar to (1.46) obtaining an initial design of the cloak that, after refinement, brings us to the final design providing *12 dB* reduction for TM polarization and *5 dB* for TE. Again, these values are in a good agreement with the reduction expected in the ideal case. The 3D SCS reduction for both incident polarizations is shown in Fig. 25 for an impinging wave directed along the *z*-axis.

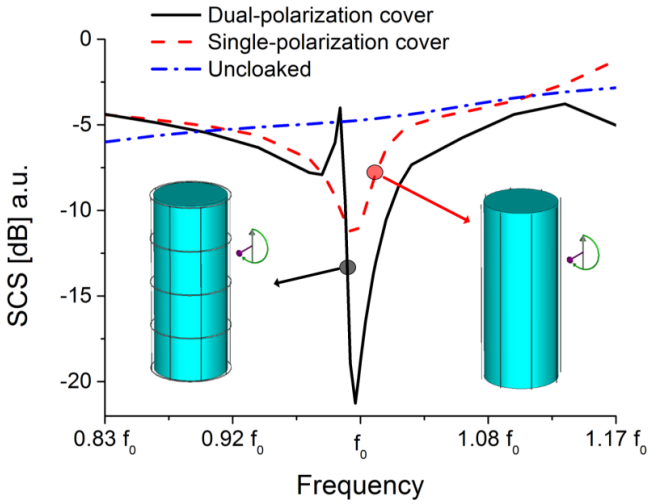

Fig. 24: Comparison between the SCS suppression performance of a dual polarized mantle cloak (solid line) and a single polarized mantle cloak (dashed line) in the case of normally incident left-handed circularly polarized plane wave. The scattering of the bare cylinder is represented using the dot-dashed line.

MULTILAYER MANTLE CLOAKING DEVICES

In this Section, I show that the metasurfaces design formulas developed previously can be successfully applied also for multilayered mantle cloaking devices.

I start by considering a finite length metallic cylinder. 3D conductive cylindrical rods present a more difficult task than those of 2D structures analytically studied previously. This is due to well-known axial resonances and edge effects, which introduce more complex HOMs interactions than those of 2D structures. Building on the theoretical results presented in the previous Section, I now consider realistic bilayer mantle cloaks to suppress the scattering from the finite-length conductive rod in Fig. 14, with length $L = 180mm$ and cross-section $2a = 19.05mm$. The rod is covered by two ultrathin patterned surfaces tailored to suppress the scattering signature of the object in different frequency bands. Each cover is separated from the rod by air. The typical design process starts from the analytical designs developed in the previous Subsection for infinite cylinders, and then consists in optimizing the effective surface impedance around the analytical design to minimize the total scattering cross-section (SCS) either in terms of maximum bandwidth below a certain acceptable scattering level, or to achieve the maximum scattering suppression at a single frequency. The two objectives are generally mutually exclusive [44].

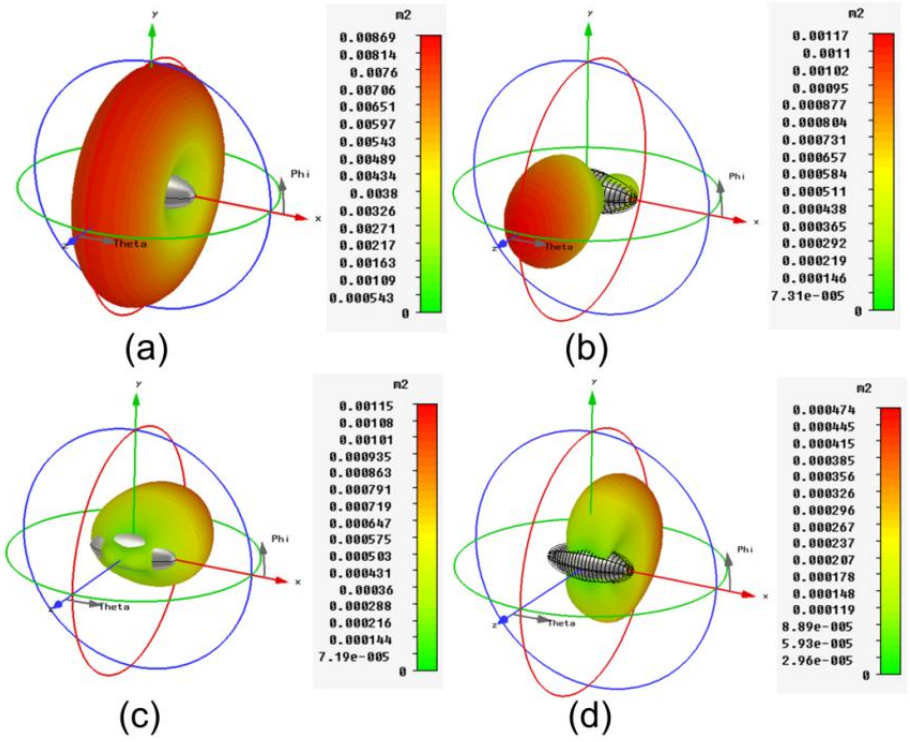

Fig. 25: 3D SCS at the cloaking frequency for TM polarization in the (a) uncloaked and (b) cloaked case. Picture (c) and (d) represents the same quantities for TE polarization.

Using horizontal strip metasurfaces shown in the inset of Fig. 26 and calculated by (1.29), dual-band operation is shown across a large band with $a_1 = 37mm$, $w_1 = 0.8mm$ $\left(X_{s,1} = -72.1\Omega\right)$; $a_2 = 36.2mm$, $w_2 = 10mm$ $\left(X_{s,2} = -185.7\Omega\right)$. In Fig. 26 it is possible to observe a scattering suppression of approximately 76% at frequencies $f_1 = 3.13$ GHz and $f_2 = 4.85$ GHz, with moderate bandwidths. The bandwidth at each design frequency is below 6%, measured at a 5 dB total scattering suppression level, which is competitive compared to other passive 3D cloaking strategies.

By optimizing the cloaks, I can realize the response shown in the bottom panel of Fig. 26, for which I find 87% total SCS suppression at 3.3 GHz and a 5 dB fractional bandwidth of over 30%. The period and gap of the innermost cloak are $a_1 = 45.4mm$ and $w_1 = 19.3mm$ $\left(X_{s,1} = -393.4\ \Omega\right)$, while the second layer has $a_2 = 41.2mm$ and $w_2 = 10.9mm$ $\left(X_{s,1} = -229.1\ \Omega\right)$. In Fig. 27 I show the electric field amplitude on a plane orthogonal to the cylinder axis at different frequencies for both the uncloaked and the cloaked scenario. The cloaking effect is evident within all the cloaking bandwidth.

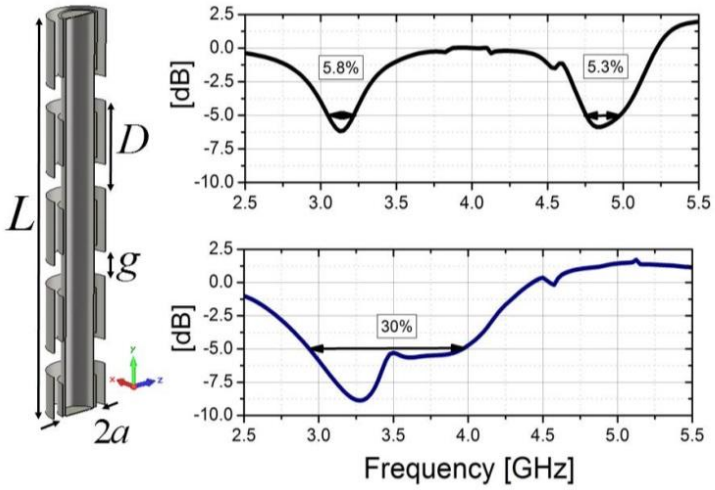

Fig. 26: (Left) Geometry of a conducting cylinder covered by a bilayer mantle cloak under a TM plane wave illumination. (Top) dual band operation and (bottom) wideband.

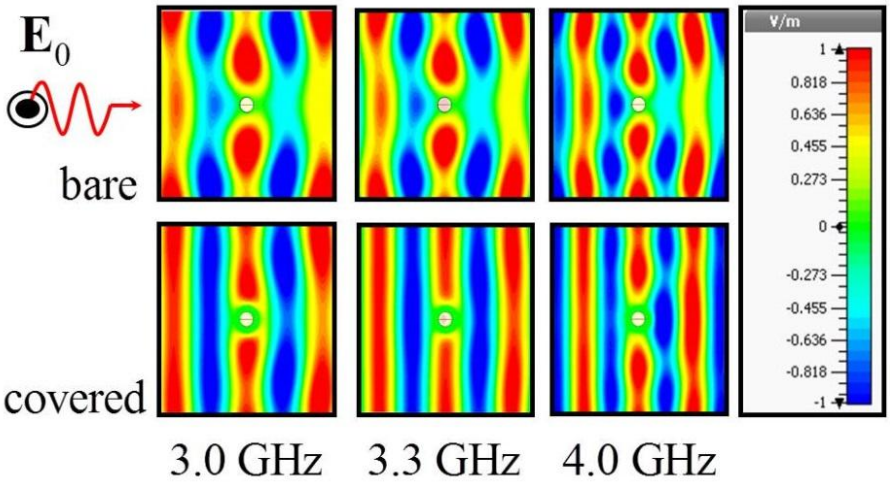

Fig. 27: Bilayer cloak for broadband operation as in Fig. 26.

Finally, I show that the analytical design formulas also works in a bilayer cloak used to reduce the scattering of a non-electrically thin cylinder. I consider the case theoretically described in the previous Section, in which dielectric cylinder with permittivity $\varepsilon = 10$ at a frequency $f_0 = 3\ GHz$ with radius $a = \lambda_0 / 2.85 = 35\ mm$. As can be appreciated in Fig. 12, with a properly designed bi-layer anisotropic mantle cloak device ($a_c^1 = 1.04 \times a$, $a_c^2 = 1.06 \times a_c^1$, $X_s^{TM,1} = -37.6\ \Omega$, $X_s^{TE,1} = -11.8\ \Omega / sq$, $X_{s,TM}^2 = 272.4\ \Omega$, $X_{s,TE}^2 = -19\ \Omega$) it is possible to reduce the object SCS of 6 *dB* for the TM polarization and 10 *dB* for the TE polarization. These metasurfaces can be designed using the analytical models (1.32)-(1.43). The unit cells of the two dual-polarized metasurface are shown in

Fig. 28 and the performance for a circular polarized incident plane wave of the relative mantle cloaking device is shown in Fig. 29. The total SCS reduction of about 6 *dB* is totally consistent with the theoretical findings of the previous Section.

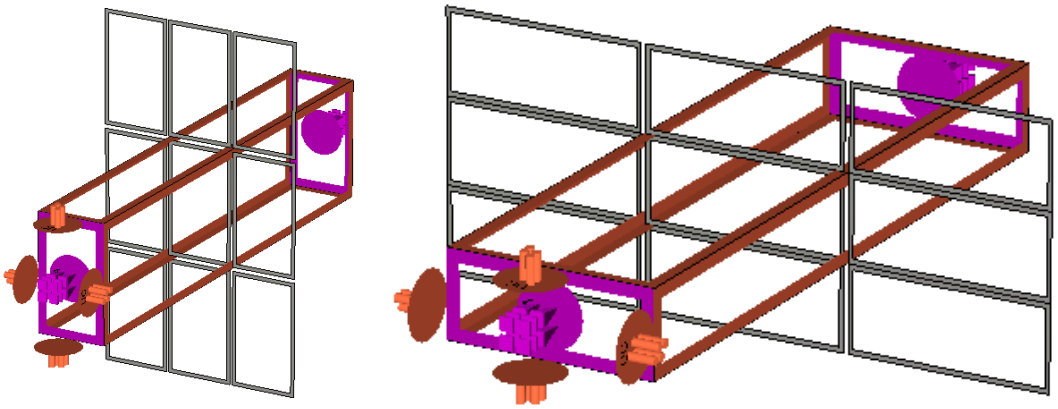

Fig. 28: Unit cells of the two designed dual-polarized metasurface working for a non-electrically small dielectric cylinder.

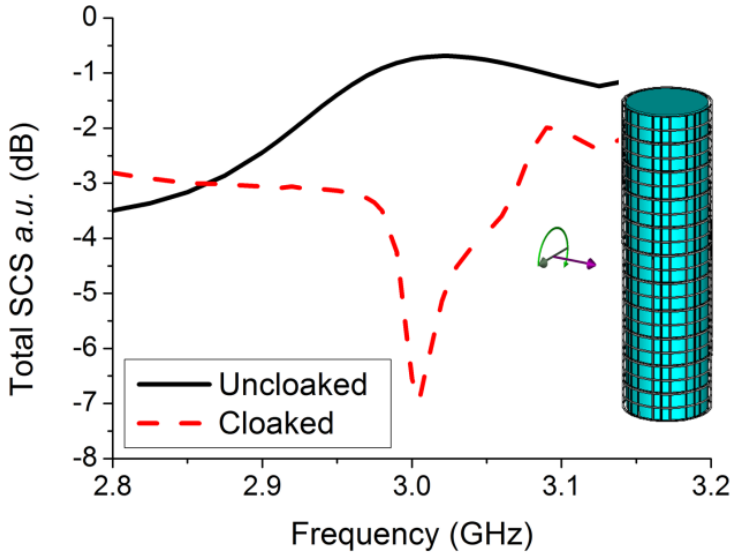

Fig. 29: Performance of the by-layer dual-polarized mantle cloaking device working for a non-electrically small dielectric cylinder.

1.4 References

[1] E. Knott M.T. Tuley and J.F. Shaeffer, *Radar Cross Section Second Edition*, Boston, United State of America, Artech House Publishers, 1993.

[2] J. B. Pendry, D. Schurig, and D. R. Smith, "Controlling electromagnetic fields," *Sci.*, vol. 312, pp. 1780-1782, 2006.

[3] U. Leonhard, "Optical conformal mapping," *Sci.*, vol. 312, pp. 1777-1780, 2006.

[4] P. Alitalo, O. Luukkonen, L. Jylha, J. Venermo, and S.A. Tretyakov, "Transmission-line networks cloaking objects from electromagnetic fields," *IEEE Trans. Antennas Propagat.*, vol. 56, pp. 416-424, Feb. 2008.

[5] P.-S. Kildal, A. A. Kishk, and A. Tengs, "Reduction of forward scattering from cylindrical objects using hard surfaces," *IEEE Trans. Antennas Propag.*, vol. 44, no. 11, pp. 1509–1520, Nov. 1996.

[6] A. Alù, and N. Engheta, "Achieving transparency with plasmonic and Metamaterial Coatings," *Phys. Rev. E*, vol. 72, 016623, 2005.

[7] P. Y. Chen, and A. Alù, "Mantle cloaking using thin patterned metasurfaces," *Phys. Rev. B*, vol. 84, 205110, 2011.

[8] A. Alù, "Mantle cloak: invisibility induced by a surface," *Phys. Rev. B*, vol. 80, 24115, 2009.

[9] M. Selvanayagam, and G. V. Eleftheriades, "An active electromagnetic cloak using the equivalence principle," *IEEE Antennas Wireless Propag. Lett.*, vol. 11, pp.1226-1229, 2012.

[10] D. Schurig, J. J. Mock, B. J. Justice, S. A. Cummer, J. B. Pendry, A. F. Starr, and D. R. Smith, "Metamaterial electromagnetic cloak at microwave frequencies," *Sci.*, vol. 314, pp. 977-980, 2006.

[11] B. Edwards, A. Alù, M.G. Silveirinha, and N. Engheta, "Experimental verification of plasmonic cloaking at microwave frequencies with metamaterials," *Phys. Rev. Lett.*, vol. 103, no. 15, pp. 153901, 2009.

[12] F. Bilotti, S. Tricarico, and L. Vegni, "Electromagnetic cloaking devices for TE and TM polarizations," *New J. of Physics*, vol. 10, 115035, 2008.

[13] S. Mühlig, M. Farhat, C. Rockstuhl, and F. Lederer, "Cloaking dielectric spherical objects by a shell of metallic nanoparticles," *Phys. Rev. B*, vol. 83, 195116, 2011.

[14] A. Monti, F. Bilotti, and A. Toscano, "Optical cloaking of cylindrical objects by using covers made of core–shell nanoparticles," *Opt. Lett.*, vol. 36, pp. 4479-4481, 2011.

[15] M. Farhat, S. Mühlig, C. Rockstuhl, and F. Lederer, "Scattering cancellation of the magnetic dipole field from macroscopic spheres," *Opt. Expr.*, vol. 20, pp. 13896-13906, 2012.

[16] A. Monti, F. Bilotti, A. Toscano, and L. Vegni, "Possible implementation of epsilon-near-zero metamaterials working at optical frequencies," *Opt. Commun.*, vol. 285, pp. 3412–3418, 2012.

[17] S. Mühlig, A. Cunningham, J. Dintinger, M. Farhat, S. B. Hasan, T. Scharf, T. Bürgi, F. Lederer, and C. Rockstuhl, "A self-assembled three-dimensional cloak in the visible," *Sci. Rep.*, vol. 3, 2328, 2013.

[18] A. Alù and N. Engheta, "Cloaking a receiving antenna or a sensor with plasmonic metamaterials," *Metamaterials*, vol. 4, no. 4, pp. 153–159, 2010.

[19] A. Alù and N. Engheta, "Cloaked near-field scanning optical microscope tip for noninvasive near-field imaging," *Phys. Rev. Lett.*, vol. 105, no. 26, pp. 263906, 2010.

[20] F. Bilotti, S. Tricarico, F. Pierini, and L. Vegni "Cloaking apertureless near-field scanning optical microscopy tips," *Opt. Lett.*, vol. 36, no. 26, pp. 211–213, 2011.

[21] S. Tricarico, F. Bilotti, A. Alù, and L. Vegni, "Plasmonic cloaking for irregular objects with anisotropic scattering properties," *Phys. Rev. B*, vol. 81, 026602, 2010.

[22] C. Forestiere, L. D. Negro, and G. Miano, "Cloaking of arbitrarily shaped objects with homogeneous coatings," *Phys. Rev. B*, vol. 89, 205120, 2014.

[23] J. C. Soric, P. Y. Chen, A. Kerkhoff, D. Rainwater, K. Melin, and A. Alù, "Demonstration of an ultralow profile cloak for scattering suppression of a finite-length rod in free space," *New. J. Phys.*, vol. 15, 033037, 2013.

[24] Y. R. Padooru, A. B. Yakovlev, P. Y. Chen, and A. Alù, "Analytical modeling of conformal mantle cloaks for cylindrical objects using sub-wavelength printed and slotted arrays," *J. Appl. Phys.*, vol. 11, 034907, 2012.

[25] A. Monti, F. Bilotti, A. Toscano, J. Soric, and A. Alù, "Mantle cloak devices for TE and TM polarizations," *Proceedings of the Antennas and Propagation Society International Symposium*, Orlando, USA, 7-13 July 2013, pp. 324-325.

[26] A. Monti, L. Tenuti, G. OIiveri, A. Alù, A. Massa, A. Toscano, and F. Bilotti "Design of multi-layer mantle cloaks," *Proc. of Metamaterials 2013*, Bordeaux, France, 16-19 September 2013.

[27] A. Monti, J. Soric, A. Alù, A. Toscano, and F. Bilotti, "Anisotropic Mantle Cloaks for TM and TE Scattering Reduction," *IEEE Trans. Antennas Propagat.*, in press. DOI: 10.1109/TAP.2015.2396532.

[28] A. Monti, J. Soric, A. Alù, F. Bilotti, A. Toscano, and L. Vegni, "Overcoming mutual blockage between neighboring dipole antennas using a low-profile patterned metasurface," *IEEE Antennas Wireless Propag. Lett.*, vol.11, pp.1414, 2012.

[29] J. C. Soric, R. Fluery, A. Monti, A. Toscano, F. Bilotti, and A. Alù, "Controlling scattering and absorption with metamaterial covers," *IEEE Trans. Antennas Propag.*, vol. 62, pp. 4220-4229, 2014.

[30] C. F. Bohren and D.R. Huffman, *Absorption and Scattering of Light by Small Particles*, New York, United States of America: Wiley-Interscience, 1998.

[31] A. Monti, A. Alù, A. Toscano, and F. Bilotti "Design and simulations of dual-polarized mantle cloaking devices," in *Proc. of Metamaterials 2013*, Bordeaux, France, 16-19 September 2013, pp. 391-393.

[32] N. Marcuvitz, *Waveguide handbook*, New York, NY: McGraw-Hill, 1951.

[33] R. Ulrich, "Far infrared properties of metallic mesh and its complementary structure," *Infrared Phys.*, vol. 7, pp. 37-55, 1967.

[34] R. Ulrich, "Effective low-pass filters for far-infrared frequencies," *Infrared Phys.*, vol. 7, pp. 65-74, 1967.

[35] R. C. Compton, L. B. Whitbourn, and R. C. McPhedran, "Strip gratings at a dielectric interface and application of Babinet's principle," *Appl. Optics*, vol. 23, pp. 3236-3242, 1984.

[36] R. C. Compton, L. B. Whitbourn, and R. C. McPhedran, "Simple formulae for the transmittance of strip gratings," *Int. J. Infrared Milli.*, vol. 4, pp. 901-912, 1983.

[37] L. B. Whitbourn, and R. C. Compton, "Equivalent-circuit formulas for metal grid reflectors at a dielectric boundary," *Appl. Optics*, vol. 24, pp. 217-220, 1985.

[38] S. Tretyakov, *Analytical modeling in applied electromagnetics*, Norwood, MA: Artech House, 2003.

[39] O. Luukkonen, C. Simovski, G. Granet, G. Goussetis, D. Lioubtchenko, A. V. Raisanen, and S. A. Tretyakov, "Simple and accurate analytical model of planar grids and high-impedance surfaces comprising metal strips or patches," *IEEE Trans. Antennas Propagat.*, vol. 56, pp. 1624-1632, 2008.

[40] V. V. Yatsenko, S. A: Tretyakov, S. I. Maslovski, A. A Sochava, "Higher order impedance boundary conditions for sparse wire grids," *IEEE Trans. Antennas Propagat.*, vol. 48, pp. 720-727, 2000.

[41] R. J. Langley, E. A. Parker, "Equivalent circuit model for arrays of square loops," *Electron. Lett.*, vol. 18, pp. 294-296, 1982.

[42] R. J. Langley, and A. J. Drinkwater, "An improved empirical model for the Jerusalem cross," *IEE Proc. H Microwaves: Opt. & Antennas,* vol. 129, pp. 1-6, 1982.

[43] J. Hao, and L. Zhou, "Electromagnetic wave scatterings by anisotropic metamaterials: Generalized 4×4 transfer-matrix method," *Phys. Rev. B.*, vol. 77, 094201, 2008.

[44] F. Monticone, and A. Alù, "Do Cloaked Objects Really Scatter Less?," *Phys. Rev. X*, Vol. 3, 041005, 2013.

2 *Antennas application of mantle cloaking*

In this Chapter, I present some of the antenna applications of the mantle cloaking that I have proposed with my co-authors over the last years ([J01]-[J02], [J04]-[J05], [J08], [C01]-[C02], [C06]-[C08], [C09]-[C09], [C14]-[C16], [C19]). In fact, since it is a scattering cancellation cloaking approach and, therefore, it does not electromagnetically isolate the hidden object, mantle cloaking can be successfully applied in different antenna scenarios, with unprecedented advantages both and in the receiving and in the transmitting operation mode of an antenna.

The first Section (Section 2.1) is focused on the advantages provided by the mantle cloaking in the receiving regime of an antenna. It will be shown that a properly designed cloak allows to manage the balance between the absorbed and the scattered power of a receiving antenna in an unpreceded way. The other Sections focus on the application of the mantle cloaking to transmitting antennas. In particular, I first show (Section 2.2 and 2.3) how it is possible to exploit mantle cloaking to reduce the blockage effect between different antennas or between passive objects and antennas. Then (Section 2.4), I describe some new-conception radiative systems that are specifically designed to work in a frequencies range and to be electromagnetically invisible in another one. This innovative typology of radiative systems may play an important role in the modern communication platforms that host an increasing number of antennas operating for the different TLC services. The possibility to use invisible antenna systems that does not affect the performances of the other radiators, in fact, will allow to dramatically reduce both the space occupancy and the weight of the platforms mounted on civil and military vehicles as well as on satellite systems.

2.1 Increasing the absorption efficiency of the receiving antennas

The quest for reliable low interference/low observability measurement and communication systems has a long tradition [1]-[6], which dates back to the concept of minimum-scattering receiving antennas [2]. These ideas have been interestingly revived in recent years by new theoretical findings and recent needs for novel applications [7]-[18]. Proposed in 2009, the concept of "cloaking a sensor" to maintain its ability to absorb power while significantly reducing its scattering was originally based on a low-permittivity, epsilon-near-zero plasmonic cover [11]. The reduction of interference and mutual coupling of co-located antennas using cloaks has been proposed also using transformation-optics cloaks [19], transmission-line cloaks [20], hard-soft boundaries [21]-[22], metascreen covers [23]-[24]. Even more exotic solutions, such as the combination of cloaks and *anti-cloaks*, have been suggested to extract a portion of the impinging signal inside transformation-based cloaks, while at the same time minimizing their scattering [25]-[26]. Some of the limitations and potentials of these approaches in comparison to more conventional minimum-scattering antennas has been in part discussed in [12]. Related to these efforts, the general physical bounds on absorption and scattering from arbitrary passive absorptive objects have been derived and discussed in [27]. In the following, it is explored in detail the fundamental potential of cloaked receiving antennas. The attention is focused on the mantle cloaking technique that, as described in the previous chapter, can be ideally suited for radio-frequency applications.

2.1.1 Mantle cloaking for receiving dipole antennas

Consider the geometries in Fig. 30, in which a loaded dipole oriented along $\hat{\mathbf{x}}$ is excited by a plane wave with electric field $\mathbf{E}_0$ polarized in the same direction, traveling along $\hat{\mathbf{z}}$ in free-space, with permeability and permittivity (μ_0, ε_0). When the antenna is not covered, the absorbed and scattered powers are fully determined by the current

distribution induced along the antenna, which may be controlled to a large degree by the antenna load Z_L, as rigorously modeled in [12].

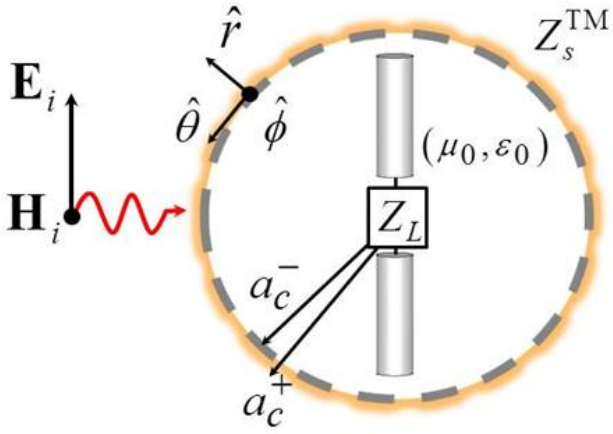

Fig. 30: Geometry of interest: a loaded dipole antenna coated with a mantle cloak.

For wire antennas with length $2l < \lambda/2$ I may safely consider only the electric dipole contribution to the total scattering. I further assume the quasi-static condition $k_0 a_c < 1$. In this limit the dipolar scattering coefficient reduces to

$$c_1^{TM} = -\frac{1}{1 - \frac{18\pi}{l^2 k_0^2 \eta_0} \frac{X_{in}\left(X_{in} + X_L - jR_L\right)}{\left[R_L + j\left(4X_{in} + X_L\right)\right]}}. \tag{2.1}$$

Analyzing (2.1) for fixed R_L, I notice that it is possible to minimize the scattering for $Z_L = -j4X_{in}$, an anti-resonance condition originally envisioned in [28], while absorption is maximized for $Z_L = -jX_{in}$, i.e., at resonance. This is also consistent with the results derived in [12],[27]. It may also be easily shown that maximum power absorption is obtained under conjugate matching ($Z_L = R_{in} - jX_{in}$), and in this case necessarily $\sigma_1^{scat} = \sigma_1^{abs} = 3\lambda_0^2/8\pi$. As discussed in [27], scattering and absorption features of an arbitrary passive scatterer, for any harmonic n, are fundamentally bounded. If I define the absorption efficiency as the ratio $\eta_{abs} = \sigma^{abs}/\sigma^{scat}$, this bound may be easily represented in the efficiency versus total absorption plane shown in Fig. 31. The shaded

region of the plot is forbidden for any passive dipolar scatterer, while any point inside the white area is allowed. It is particularly instructive to look at the conditions under which a loaded dipole antenna may reach the physical bound, *i.e.*, the boundary between the grey and white regions. These are the most interesting operating points for a receiving antenna, as they ensure maximized absorption, and/or maximum or minimum absorption efficiency for a given absorption level. It is easy to show that I lie on the boundary line under the condition $\mathrm{Im}\left\{2c_n^{TM/TE}+1\right\}=0$ [27]. Applying this condition to (2.1), I obtain two distinct solutions provided that the load resistance is within

$$0<R_L<1.5\left|X_{in}\right|, \tag{2.2}$$

and, assuming $R_L<<\left|X_{in}\right|$, these solutions simplify into

$$\begin{aligned} X_L^+ &= -4X_{in}+\frac{R_L^2}{3\left|X_{in}\right|}+O\left(R_L\right)^3, \\ X_L^- &= -X_{in}-\frac{R_L^2}{3\left|X_{in}\right|}+O\left(R_L\right)^3. \end{aligned} \tag{2.3}$$

Interestingly, these conditions are precisely the ones discussed above for minimizing scattering and maximizing absorption. This means that, close to its resonance or anti-resonance, the antenna reaches the physical bound.

As a practical example, consider a bare dipole with dimensions $2l=\lambda/4$, where $\lambda=30$ cm, a feed-gap $g=2.34$ mm and diameter $d=0.47$ mm, yielding an input impedance $Z_{in}=14.6-j454.8\,\Omega$, calculated by the finite-element method (FEM). Several key contours are plotted and compared against full-wave simulations in Fig. 31. Consider first the *high* and *low* absorption efficiency regions, which are reached by the outermost black dashed and solid lines, respectively. The dashed black line is generated by sweeping R_L while $X_L=X_L^+=-4X_{in}$, and the solid black line is generated by sweeping R_L while $X_L=X_L^-=-X_{in}$. All the X_L-constant contours tend to the same asymptote when $R_L\to\infty$ [27], which corresponds to the open-circuit asymptote. This

inevitable asymptotic behavior prevents the $X_L = X_L^-$ contour to reach the high efficiency or low-visibility region, inherently forbidding a resonant antenna to scatter little. Indeed, it is observed that this contour falls off the fundamental bound when $R_L \approx 1.5|X_{in}|$. In addition, in the limit $R_L \to 0$, I obtain different behavior depending on the chosen reactive loading, spanning the high-visibility, or nearly invisible response.

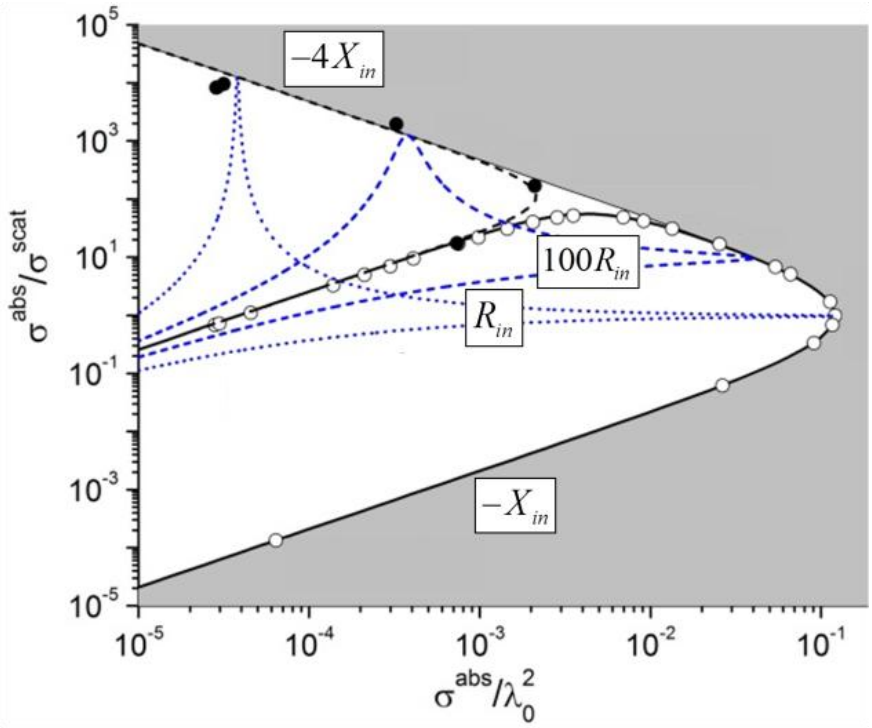

Fig. 31: Absorption efficiency versus absorption for a bare $\lambda/4$ receiving dipole antenna loaded by an impedance $Z_L = R_L + jX_L$. The black (darker) contours are generated keeping X_L constant while sweeping R_L over all positive values (solid black: $X_L = -X_{in}$; dashed black: $X_L = -4X_{in}$). The blue (lighter) contours are generated keeping R_L constant and sweeping X_L over all real values (blue dots: $R_L = R_{in}$; dashed blue: $R_L = 100R_{in}$). The grey shaded area is forbidden to passive dipolar scatterers. Full-wave simulations are shown in circles.

In the figure, the circular markers represent the result of full-wave simulations changing the load resistance for X_L^-, while the solid circles correspond to X_L^+. The agreement with the analytical contours is excellent, validating the quasistatic model. Also shown in the figure are dashed blue (lighter) curves generated keeping R_L constant, while sweeping the load reactance. For $R_L = R_{in}$, two clear points hit the bound, one when $X_L = -X_{in}$ and the other for $X_L = -4X_{in}$, obtaining a conjugate match and an anti-resonant peak in efficiency, respectively. The other constant load resistance

curve is shown for $R_L = 100R_{in}$, obtaining similar behavior and also hitting the bound twice under resonant and anti-resonant conditions, but at different locations. As predicted by my quasistatic considerations, by sweeping the load resistance, the bound is reached for two load reactances, corresponding to the conditions for minimizing scattering and maximizing absorption.

I now consider the possibility of modifying the dispersion of the curves in Fig. 2 by using a properly designed mantle cloaking device. It is obvious from the previous discussion that the way to yield a high absorption efficiency from a resonant antenna is to shift up the open-circuit asymptote. I achieve this effect with a microwave metasurface designed to cloak the open-circuit antenna.

Consider again the $2l = \lambda/4$ antenna described previously. I choose a small spherical metasurface shell with $a = 1.25l = 4.68$ cm to maintain a small dimension of the overall structure, reducing the influence of higher-order scattering harmonics. The theoretical analysis shows that a metasurface with $X_s^{open} = 11.7$ kΩ may be able to suppress the c_1^{TM} scattering coefficient for an open-circuit load. In my full-wave model, the quarter-wavelength dipole is surrounded by a mathematical sphere with boundary condition $J_s = E_{\tan} / jX_s^{open}$, where $E_{\tan}$ is the tangential electric field. I have solved the problem using [29]. Fig. 32 shows the absorption efficiency dispersion varying the load resistance at resonance, as calculated by my analytical formulas (solid lines), which agree well with full-wave simulations (dots). The resistance is swept over all positive values for each curve using the load reactance $X_L = -X_{in}$. This is done for the bare case (white dots and black line) and repeated for the covered case (blue dots and blue line). In the inset I show the same curves in the absorption efficiency vs. absorption plot, consistent with Fig. 31.

It is seen that the mantle cloak is able to reduce by over 10 dB the structural scattering of the bare dipole for large load resistance values, and push the oblique asymptote to large absorption efficiencies. This is reflected in a significantly larger absorption efficiency along the tail of the cloaked geometry, and a significant increase in peak absorption efficiency for $R_L = 5$ kΩ. It is remarkable how the cloaked sensor may boost the absorption efficiency at resonance up to a value of 200 for the proper value of load

resistance. Similar efficiency values may be achieved in the bare case only off-resonance by suitably mismatching X_L.

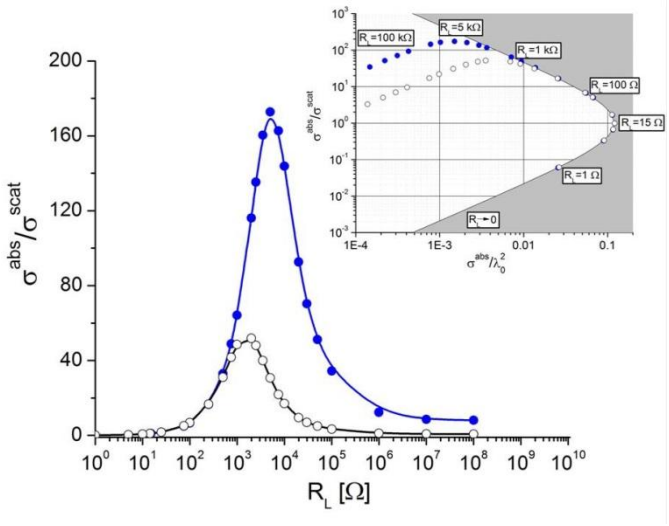

Fig. 32: Variation of the absorption efficiency at resonance with the load resistance, comparing the bare (black line, white dots) and cloaked (blue line, blue dots) $\lambda/4$ sensor of Fig. 31. Solid lines show the analytical results, dots indicate full-wave simulations. The inset shows the corresponding dispersion on a plot consistent with Fig. 31.

2.1.2 A practical design

An example of special interest is represented by half-wavelength dipole antennas, which are widely used due to their self-resonant nature and low input reactance. In receiving mode, these antennas are known to generally scatter more than they receive [30], regardless of their resistive loading. I now apply my cloaking technique to a half-wavelength wire antenna to increase its absorption efficiency at resonance. The low input reactance can greatly facilitate the mantle cloak design, and therefore in this section I explore a realistic mantle cloak applicable to half-wavelength dipoles. In this regard, instead of considering a spherical shape, which was a preferred geometry to analytically solve the problem, here I consider a conformal cylindrical geometry ideal to suppress the scattering for the polarization of interest, consistent with the design and the theoretical analysis developed in the previous Chapter.

Fig. 33 illustrates the schematic of my designed mantle cloak, applied to an open-circuit half-wavelength dipole. The bare antenna of length $2l \approx \lambda/2 = 43.8$ mm and diameter $d = 4$ mm is loaded by a small inductor $L = 28$ nH to tune it at its resonance,

and a variable resistor at its feed-gap $g = 1\ \text{mm}$. The inductive surface is realized using thin conductive vertical strips over a dielectric cover of relative permittivity $\varepsilon_c = 6$ (Rogers TMM6) and thickness $a_c - a = 400\ \mu\text{m}$. Here, a trace period $D = 1.426\ \text{mm}$ and width $w = 606\ \mu\text{m}$ is chosen to realize an inductive surface with $X_s^{open} = 11\ \Omega$. Obviously this metasurface design is not isotropic, but it is sufficient to provide the desired reactive impedance for the polarization of interest (parallel to the wires and the dipole). I have checked using full-wave simulations that indeed this realized cover can significantly suppress the open-circuit dipole antenna scattering by 18.5 dB at 3 GHz. I stress here that, while my analytical model assumes a homogeneous surface impedance, in realizing these structures the near-field interactions with the dipole antenna can introduce significant effects associated with higher-order Floquet harmonics. Yet, it is possible to fine tune my designs based on the analytical model to take these corrections into account and, as shown in the following figures, my full-wave simulations considering all near-field effects agree well with the analytical model.

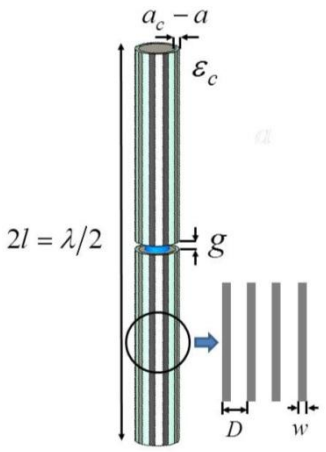

Fig. 33: Geometry of the proposed inductive metascreen over the two arms of the dipole antenna, leaving the small gap open to free space.

The reduction of structural scattering is evident in the far-field scattering patterns shown in Fig. 34. The cover almost completely cancels the dipolar scattering contribution from the open-circuit antenna, leaving only a forward, highly directive scattering pattern, due to higher-order modes. It is important to stress the scale difference in Fig. 34 to see how strongly the scattering of the open-circuit antenna is reduced by the metascreen.

Next in Fig. 35 I sweep the load resistance for the bare and cloaked antennas to demonstrate how the metascreen enables much larger absorption efficiencies, lying on the optimal bound, whereas the bare antenna intrinsically limits the absorption efficiency to values below $\eta_{abs}=1$. A significant increase in absorption efficiency is accomplished using a simple metascreen cover with moderate values of surface reactance.

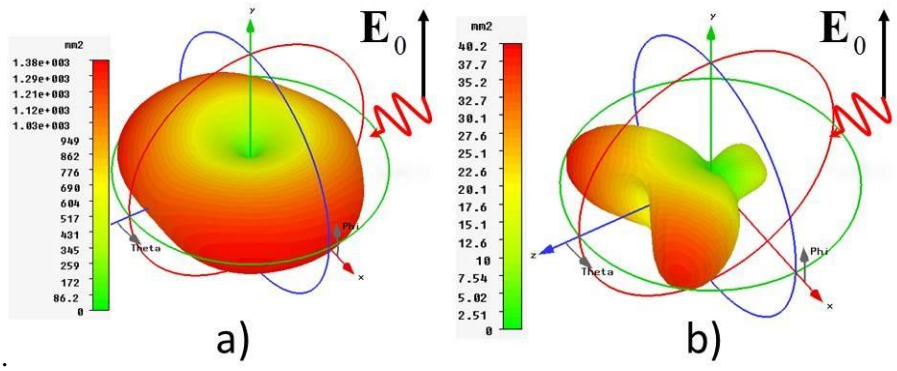

Fig. 34: Comparison of the open circuit far-field scattering of the bare (a) and covered dipole (b).

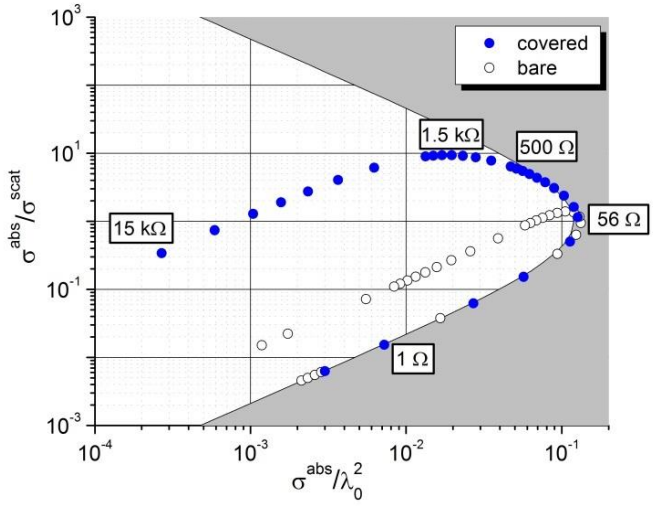

Fig. 35: Absorption efficiencies versus absorption of the bare and covered $\lambda/2$ dipole antennas at 3 GHz.

As a final step in my analysis, I consider the effects of realistic losses that can arise in the mantle cloak. A self-resonant dipole similar to Fig. 33, but now with a dielectric spacer $\varepsilon_r=4$ is considered for operation at $f_0=3.51$ GHz. Fig. 10 shows the effects of realistic losses in the metasurface substrate on the scattering suppression of the open-circuit dipole antenna, varying the loss-tangent of the considered material as indicated in

the legend. In particular, I show the scattering gain, defined as the total scattering cross-section of the covered open-circuit antenna normalized to that of the uncovered object. It is seen that a low-loss dielectric material like HiK only slightly affects the cloak performance, while a lossier material like Neoprene may substantially lower the overall performance. I have verified in my simulations that the finite conductivity of metals at radio-frequencies is negligible, ensuring that my proposed designs are realistically achievable in practice using low-loss dielectric substrates.

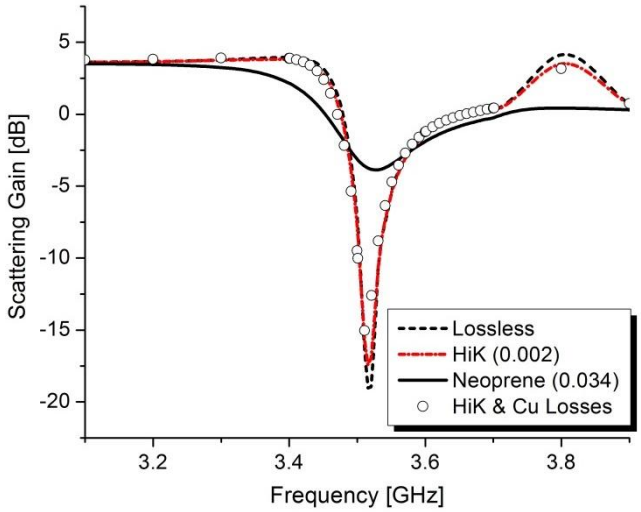

Fig. 36: Open-circuit scattering suppression considering several realistic material covers, including dielectric and metal losses.

2.2 Reduction of the mutual blockage effect among close antennas

I put forward here an interesting antenna application of cloaking, consisting in the reduction of the blockage effect between closely spaced antennas. It is well known that the presence of an obstacle in the near-field of an antenna appreciably modifies its radiating (e.g., the radiation pattern shape) and electrical (e.g., the impedance matching) features. Several papers concerning the reduction of the blockage effect caused by passive objects have been proposed. For example, in [30]-[31], soft and hard surfaces have been shown to reduce the scattering of a cylindrical object (e.g. a strut or the feed) part of a parabolic antenna. More recently, in [32]-[33] metal-plate and transmission-line cloaks were shown to reduce the blockage effect of a passive object placed directly in

front of a horn antenna. However, there are very few studies about the reduction of the mutual blockage effect between two antennas that are designed in free-space but are forced, for space constraints, to stay in close electrical proximity. In this situation, that is ever more common in modern crowded electromagnetic environments, the obstacle placed in the proximity of the antenna is another antenna, usually operating at a different frequency. Here, the performance degradation of both antennas can become dramatic, affecting antenna coverage as well as their resonant properties.

The reduction of mutual blockage is not a straightforward task, due to the fact that the object to hide is not passive, and owns an electromagnetic functionality. The cloak, thus, must not affect excessively the antenna performance at its operating frequency. In order to overcome this issue, in [34] the authors proposed the employment of an eccentric elliptical transformation-based cloak to restore the parameters of a two-dimensional (2D), infinitely long (i.e., nonresonant) electrical source, whose radiation is blocked by an identical scatterer placed in its neighborhood. This solution, though fascinating, is difficult to realize experimentally and it is based on a variety of ideal assumptions hardly met in realistic antenna configurations, which are commonly formed by three-dimensional (3D) resonating elements. Here, I show that the mantle cloaking technique may be very suitable for the same purpose in realistic configurations.

2.2.1 An operative scenario

I consider as my reference scenario the situation in which two transmitting dipole antennas, resonating at slightly different frequencies, are placed in very close electrical proximity of each other. The two dipoles are designed in free-space to operate for different services (e.g., two dipoles of different mobile network operators hosted by the same telecommunication strut). The shorter dipole is designed to resonate in free-space at $f_{0,1} = 3.33$ GHz, while the longer one resonates at $f_{0,2} = 3.07$ GHz. Both antennas were optimized to be matched to a 75 Ω feed. When placed in close proximity, in particular with a separation of just $d = \lambda_0/10$ at 3 GHz, their radiation performance is largely compromised due to mutual blockage. This is shown in Fig. 37, where the antenna system has been characterized using the full-wave numerical simulator. The radiation patterns of the two isolated dipoles at their respective resonance frequencies fed by 75 Ω

ports are shown in Fig. 37(a) and Fig. 37(b), respectively, while in Fig. 37(c) and Fig. 37(d) I show the same patterns when the dipoles are placed in close proximity to each other and separately driven. As expected, the radiation pattern of each antenna is dramatically affected by the presence of a closely spaced metallic scatterer (i.e., the other dipole) in its near-field region. In Fig. 38, I show the reflection coefficient at the input ports in the isolated and coupled scenarios. In this latter case, the two dipoles are no longer matched to the source, again due to mutual coupling. The presence of the other dipole, in fact, drastically affects the near-field distribution and, thus, the input reactance of both antennas.

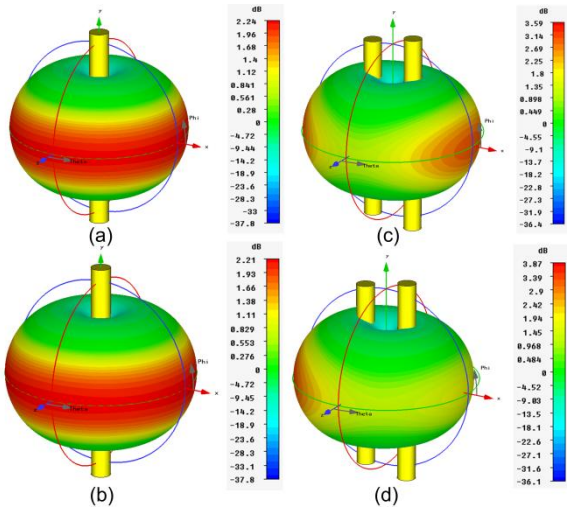

Fig. 37: 3D gain patterns of (a) the isolated first dipole at f_{01}, (b) the isolated second dipole at f_{02}, (c) the first dipole at f_{01} in presence of the second dipole, and (d) the second dipole at f_{02} in presence of the first dipole.

In order to reduce the coupling effects, I cover each dipole with a mantle cloak capable of preserving and restoring their isolated radiation characteristics and canceling their mutual coupling. The first antenna is covered with a mantle cloak working at f_{02}, while the second dipole is cloaked at f_{01}. The conformal mantle cloaks have been designed over a flexible dielectric substrate, whose external face is suitably patterned with a metallic surface, as shown in Fig. 39. The patterns of the metasurfaces have been chosen designed using the analytical models presented in the previous Chapter. Considering the specific field polarization, vertical metallic strips are the most suitable geometry to affect the local averaged reactance, and I have performed a proper optimization to minimize the total scattering cross section (SCS) of each 3D dipole at the

resonance frequency of the other dipole under transverse magnetic (TM) plane-wave excitation. The geometrical parameters of the two metasurfaces are reported in the caption of Fig. 39.

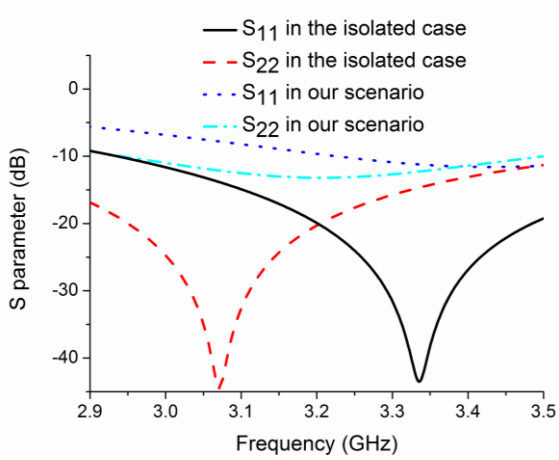

Fig. 38: Amplitude of the reflection coefficient at the input port of the first and second dipole in the isolated case (continuous and dashed line, respectively) and in the reference scenario (dotted line and dash-dotted line, respectively).

I calculated an overall SCS reduction of nearly *15 dB* for both cloaked antennas under ideal TM plane-wave excitation. In my reference scenario, however, each dipole is excited by the near-field of the other antenna, which is markedly different from a plane-wave. Still, the scattering cancellation effect is very robust to different excitations [35], and it works also in the very near-field of the object [36]. Therefore, I expect a large scattering reduction even in this extreme excitation scenario in which the two antennas are closely coupled and surrounded by a thin patterned conformal surface.

The radiation and matching properties of the two cloaked antennas are shown in Fig. 40, where I show the gain patterns (dotted line) on the H- and E-plane compared to the uncloaked (dashed line) and isolated (continuous line) cases. It is evident that, by applying the patterned metasurface covers, I obtain a significant restoration of the original patterns, despite the very small distance between them. The two antennas are effectively invisible to each other at their respective operating frequencies. Furthermore, in Fig. 41, I show the amplitude of the reflection coefficient at the input ports of the two antennas in the cloaked case. As expected, around the resonant frequency of each isolated dipole, I obtain a significant improvement of the impedance matching of the two antennas compared to the uncloaked case.

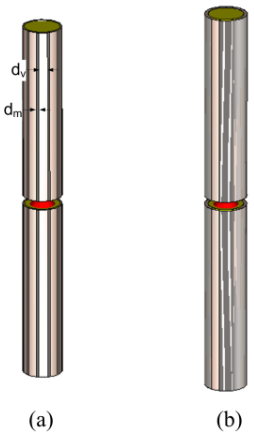

Fig. 39: The two dipole antennas cloaked with two metasurfaces consisting of N vertical metallic strips printed on thin, flexible, commercial substrates (DuPont 951 with $\varepsilon_r = 7.8$, $tan\delta = 0.0015$ at 2 GHz and Roger TMM4 with $\varepsilon_r = 4.5$, $tan\delta = 0.002$ at 10 GHz, respectively). The geometrical parameters are: (a) N = 11, $d_v = 1.07$ mm, $d_m = 0.3$ mm and (b) N = 3, $d_v = 0.99$ mm and $d_m = 4$ mm. The cover radii are $a_c = 1.2a$ and $a_c = 1.2a$, respectively, a being the antenna radius.

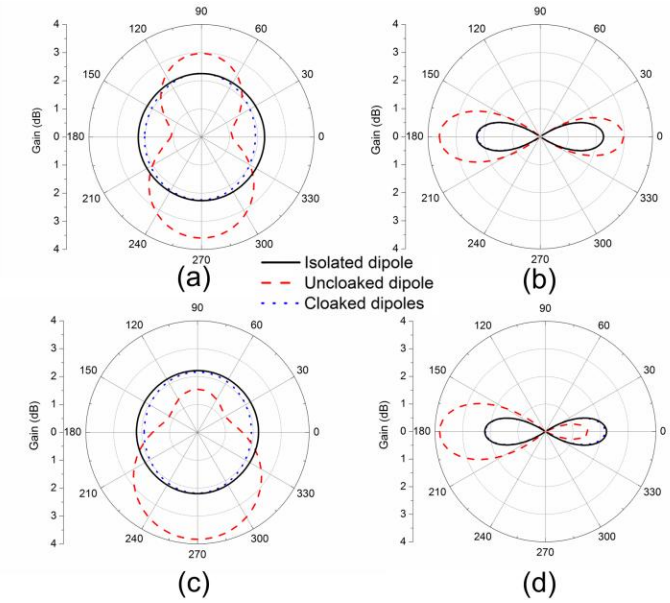

Fig. 40: Gain patterns of the first antenna at 3.298 GHz on the (a) H-plane and (b) E-plane in the case of isolated dipoles (continuous line), the uncloaked scenario (dashed line), and the cloaked one (dotted line). Figures (c) and (d) show the same quantities for the second antenna at 2.970 GHz.

I have also considered the performance of the designed cloaks for different separation distances, and particularly when the two dipoles further approach each other. In Fig. 42 I show the gain patterns on the H-plane for a separation distance between dipole centers equal to $\lambda/15$ at *3 GHz* (the gain patterns on the E-plane are omitted for brevity). Please note that the covers are unchanged, and are the same as in the previous example. The cloak performance, in terms of restoration of original gain pattern and impedance

matching, are essentially unchanged. These results are further evidence of the robustness of the mantle cloak against different excitations, including those in the very near-field.

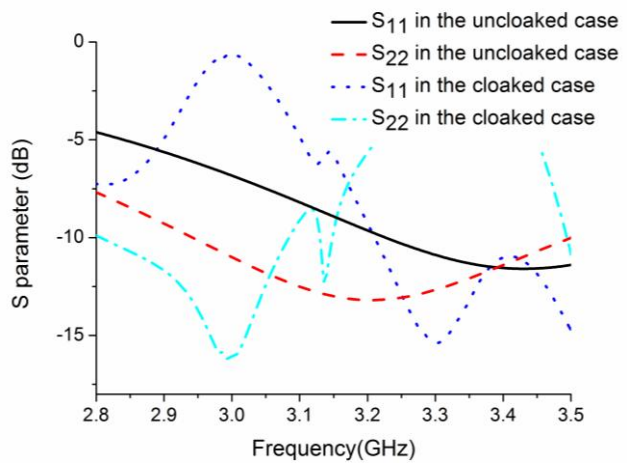

Fig. 41: Amplitude of the reflection coefficient at the input port of the first and second dipole in the uncloaked case (continuous and dashed lines, respectively) and of the first and second dipole in the cloaked case (dotted and dash-dotted lines, respectively).

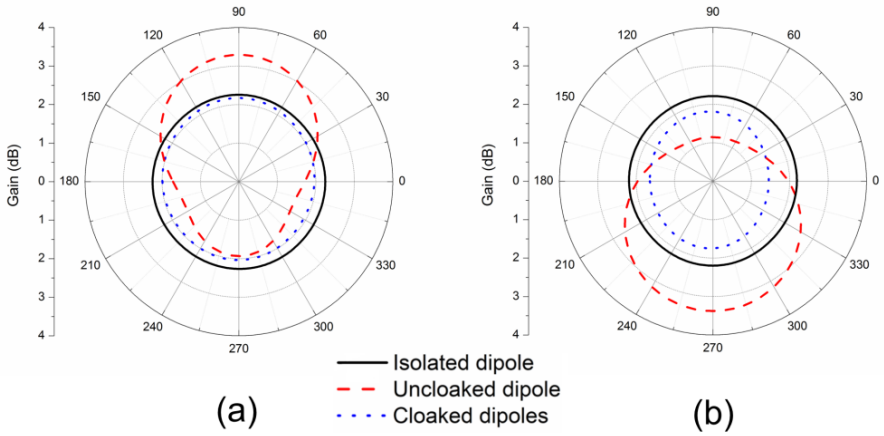

Fig. 42: (a) Gain pattern of the first antenna at 3.298 GHz on the H-plane and (b) gain pattern of the second antenna at 2.970 GHz in the isolated, uncloaked and cloaked scenario for a separation distance equal to $\lambda/15$.

I also analyze the operational bandwidth of the designed cloaks in terms of far-field radiation. For this purpose, in Fig. 43 I show the radiation patterns (on the H-plane) of the two dipoles in the neighborhood of the cloaking frequencies. It is clear that the obtained cloaking effect and the respective mutual blockage reduction is rather narrowband, due to the different frequency dispersion of the cloak and the antenna itself. With proper optimization, it may be possible to obtain a more broadband effect, in particular if the operating frequency of the two antennas is not so close in frequency.

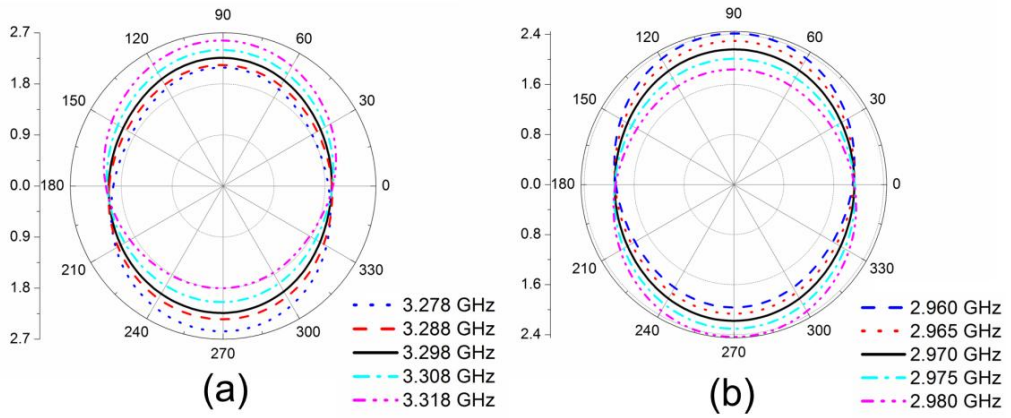

Fig. 43: Gain patterns on the H-plane of the (a) first and (b) second dipole around their respective resonance frequencies.

2.3 Dual-polarization reduction of the blockage effect

In this Section, I show that it is possible to improve the results of the previous Section by using the dual-polarized metasurfaces described in the previous Chapter. As an example, I consider an array of metallic cylinders aligned along the x-axis and placed in front of a pyramidal horn antenna. For sake of simplicity, the array is formed by equal cylinders with length $L = \lambda_0 / 2.2$ and radius $r = \lambda_0 / 11.1$. The presence of an obstacle in the near-field region of the antenna dramatically affects its electrical (impedance matching) and radiative (side lobe level and gain) performances. The amplitude of the reflection coefficient at the input port of the obstructed horn antenna is shown in Fig. 44 (continuous line). As expected, the scatterers placed in front of the antenna introduce high reflections, worsening the antenna impedance matching and strongly affecting its radiation.

In order to reduce the antenna blockage, different cloaking solutions can be used [32]-[35],[38]-[39]. For example, in [39] the authors considered a horn antenna obstructed by a metallic cylinder properly cloaked by using the transmission-line approach. However, such cloak would work only for a single polarization of the incidence field and the reduction of blockage is achieved by positioning the short side of the horn parallel to the cylinder axis (TM incidence on the cylinders). Additionally, my proposed design is more conformal, and can be simply and cheaply constructed on flexible PCB technologies. In contrast, my proposed dual-polarized mantle cloaks are able to reduce the blockage for

whatever orientation of the horn. Due to the geometry and coupling in the array, TE scattering may actually be quite strong and, depending on the number of elements, may even be dominant. For these reasons, I show the results for the case in which the antenna is placed with the longer side parallel to the cylinder axis. As well known, the field emerging from such antenna is polarized along the x-axis, and corresponds to TE incidence on the array elements. I cloaked the individual cylinders with a proper dual polarized cover, and simulated the antenna reflection coefficient for different separations between elements (d_{array}) and for different distances between the horn aperture and the array (d_{horn}).

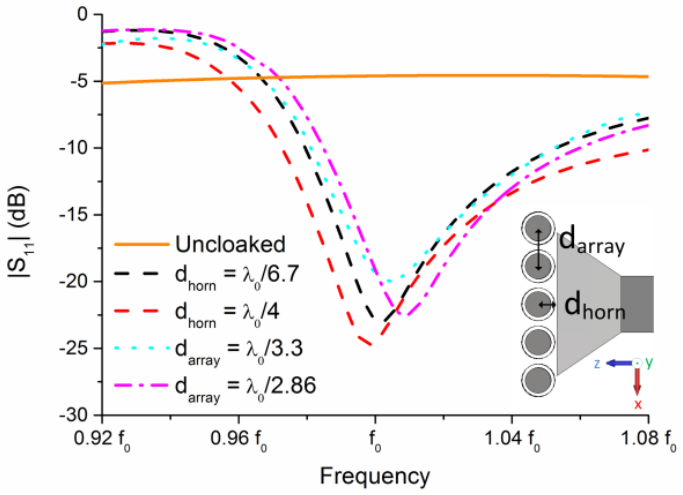

Fig. 44: Magnitude of S_{11} of a horn antenna in presence of bare and cloaked array of cylinders for different values of d_{horn} (with $d_{array} = \lambda_0/3$) and d_{array} (with $d_{horn} = \lambda_0/5$).

As seen in Fig. 44, the dual polarized cover is able to largely suppress the scattering from the array, in such a way that the cylinders presence does not affect the horn antenna at its operating frequency band, dramatically improving its matching properties. This is achieved despite the array is placed right in front the antenna aperture. I also observe that the TE scattering suppression generally exhibits a broader operating bandwidth compared to the TM case, resulting in a larger blockage reduction bandwidth.

2.3.1 *Experimental verification*

In the following, I experimentally demonstrate in three different geometries the concepts presented in previous Section. Fig. 45 shows my experiments on an array of

dual-polarized cloaked cylinders in three different scenarios, with results shown in the following figures for: TM-polarized excitation (Fig. 46), TE-polarized excitation (Fig. 47) and a TM-polarized triangular array (Fig. 48). The arrays are formed by optimized individual cloaks covering finite length conductive rods. In this case, I built each of the covers using a vinyl cutter with conventional 1 oz. copper foil with a non-conductive adhesive. The copper foil is attached to ultrathin polycarbonate sheets using transfer tape, which adds more structural stability to the cloaks. The optimized cloaks have TM-polarized gaps of 0.7 mm and TE-polarized gaps of 0.4 mm to operate at 3 GHz, with an air gap separation between the cover and conductive rod of 1.905 mm.

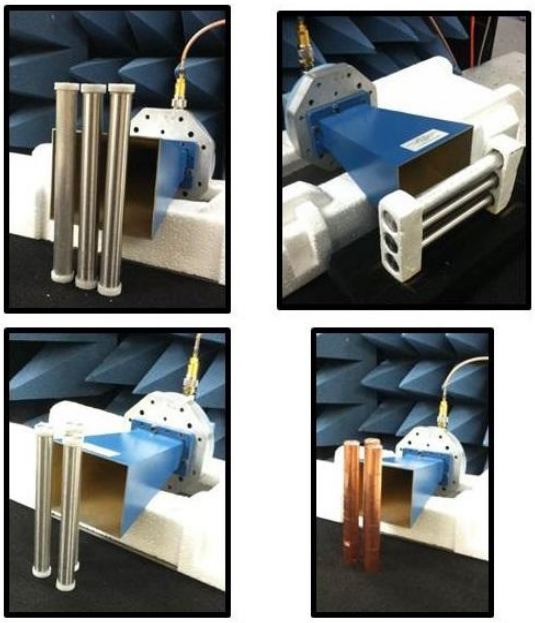

Fig. 45: Testing scenarios: (Top left: TM-pol array), (Top right: TE-pol array), (Bottom left: TM-pol triangle), and (Bottom right: ultraconformal cover).

First, I consider the most challenging case in Fig. 46, where a densely packed array of finite length cylinders is aligned with the incoming electric field and placed directly in front of the microwave horn. The field distribution (first column image) and antenna mismatch (bottom row) antenna blockage for this polarization is dramatic. By applying simple passive covers to each of the rods (second column), I see that, quite astonishingly, the radiation pattern is nearly restored to the one of the horn radiating in free space (last column). I show the measured near field at 3.1 GHz. Not shown here for brevity, the field was shown to be restored across the entire antenna band between 2.6-3.95 GHz. I

also show here the matching at the microwave horn feed, and its improvement is apparent and centered in the same frequency range. Excellent nearfield restoration is clearly seen in the measurements, and the deployment of these ultrathin cloaks is easily foreseen in many practical antenna configurations.

Next, I consider an array of finite length rods aligned to the incoming TE polarization in Fig. 47. Even for an array of three rods the near field is shown to be nearly identical in all three cases (bare, covered, and free space), expected due to the moderate cross section of each of the rods. However, here the antenna matching improvement is clearly seen between 3.0-3.4 GHz. It should be noted that the slight detuning can be decreased by simply making the TE slits slightly larger. This has not been experimentally verified, but confirmed with numerical simulation.

As a final example, in Fig. 48 I show the field restoration and matching improvement for other conducting finite length blocking geometries. As it can be seen in the figure, the field restoration is clear even in the very nearfield of the array configuration shown in the inset, indicating that the cloaking performance is highly resilient to non-uniform field excitations.

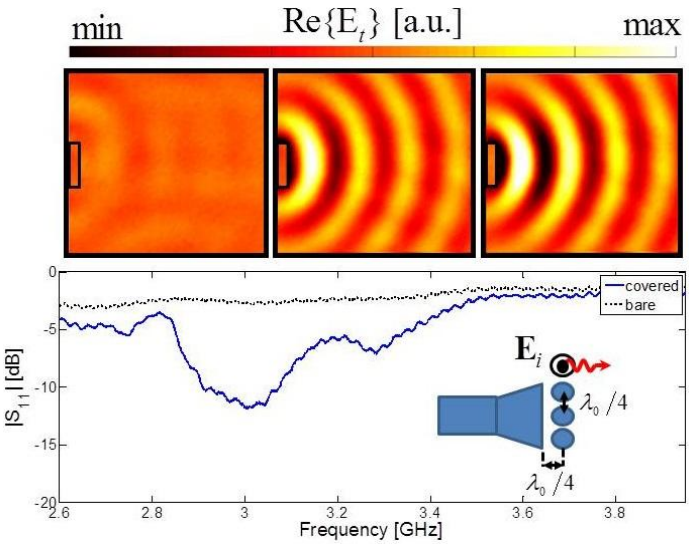

Fig. 46: A dense TM-polarized array. (Top) Snapshot in time of the transverse electric field distribution (bare, covered, free-space) at 3.1 GHz. (Bottom) Input impedance improvement as seen by the S-band microwave horn used in the near field images. The inset also shows the polarization and testing geometry in the measurements.

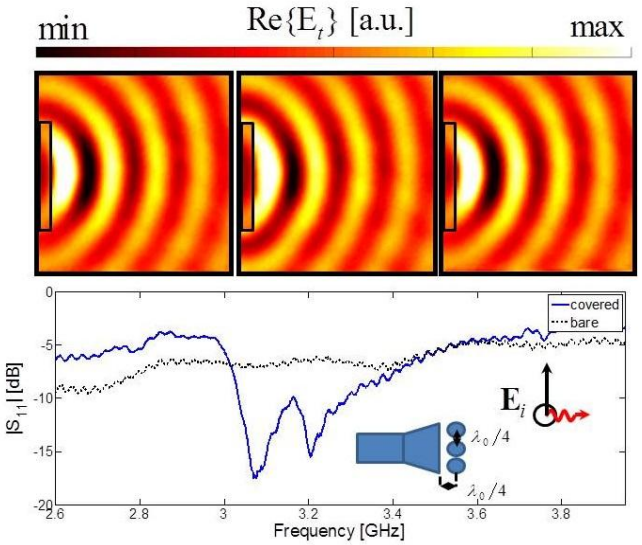

Fig. 47: A dense TE-pol array. (Top) Snapshot in time of the transverse electric field distribution (bare, covered, free-space) at 3.2 GHz. (Bottom) Input impedance improvement as seen by the S-band microwave horn used in the near field images.

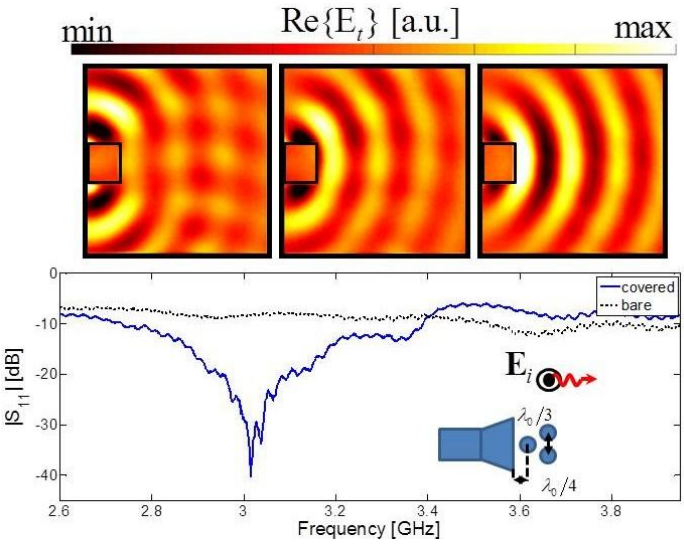

Fig. 48: A dense TM-polarized triangular array. (Top) Snapshot in time of the transverse electric field distribution (bare, covered, free-space) at 3.0 GHz. (Bottom) Input impedance improvement as seen by the S-band microwave horn used in the near field images.

2.4 Design of invisible Yagi-Uda antennas

In this Section, I exploit the peculiarities of mantle cloaking to propose the first new-conception antenna system that is specifically designed to work in a frequencies range and to be electromagnetically invisible in another one. This innovative typology of radiative systems may play an important role in the modern communication platforms

that host an increasing number of antennas operating for the different TLC services. The possibility to use invisible antenna systems that does not affect the performances of the other radiators, in fact, will allow to dramatically reduce both the space occupancy and the weight of the platforms mounted on civil and military vehicles as well as on satellite systems.

Here, I focus my attention on a very popular and widely used antenna, *i.e.*, the Yagi-Uda radiator, and I show how it is possible to design a Yagi-Uda antenna operating, for instance, at UHF frequencies and invisible within a wide range of the S band. The proposed design guidelines take into account all the numerous issues that arise in a realistic design, as the complex scattering effects affecting the finite-length metallic cylinders composing the Yagi-Uda and the needed trade-offs between cloaking and antenna performances.

2.4.1 Design guidelines

In this Subsection, I outline the guidelines for the design of a cloaked Yagi-Uda antenna. Hereinafter, I denote with BW_a the operation frequencies range (f_{1a} - f_{2a}) of the Yagi-Uda antenna and with BW_b the frequency range (f_{1b} - f_{2b}) in which I desire to make the Yagi-Uda invisible. In my design, I choose the commonly used range [896 - 970] *MHz* [40] as BW_a and the range [2.6 - 3.9] *GHz* as BW_b but I emphasize that the procedure that I will outline below is effective for any desired frequency range. As it will be clear later on, my choice is motivated by the fact that these ranges constitute a particular case in which the achievement of a final design is particularly challenging.

The first step to design an invisible Yagi-Uda consists in the design a traditional 3-elements Yagi-Uda antenna, whose geometry is reported in Fig. 49(a). Following the design recommendations of [41], I have fixed the following initial geometrical parameters: $L_r = 0.52\lambda_{0a}$, $L_c = 0.47\lambda_{0a}$, $L_d = 0.43\lambda_{0a}$, $d_{cd} = 0.35\lambda_{0a}$ and $d_{cr} = 0.25\lambda_{0a}$. In these expressions, λ_{0a} represents the wavelength at the center frequency of BW_a. The choice of the radii of the three cylinders requires a particular attention since it represents the first trade-off between the Yagi-Uda performances (in particular its bandwidth) and the cloaking one. A single layer scattering cancellation-based cloaking device, in fact, can effectively nullify the SCS of an object only if its scattering is mainly due to the first

scattering mode. As it is well known, this occurs when the quasi-static condition, *i.e.*, $r_r, r_c, r_d << \lambda_{0b}$ [42] being λ_{0b} the wavelength at the center frequency of cloaking bandwidth BW_b, is satisfied. In my design, for which $\lambda_{0a} = 3.5\ \lambda_{0b}$, I have safely fixed all the radii equal to $\lambda_{0a} / 107 = \lambda_{0a} / 31$. As I are going to show below, this choice allows achieving both the desired antenna bandwidth BW_a and significant cloaking performances in BW_b. I emphasize that if a broader antenna bandwidth would be required, it is possible to increase the radii of the three elements even beyond the quasi-static condition and dealt with the enhanced cylinders scattering recurring to multilayer mantle cloaking devices.

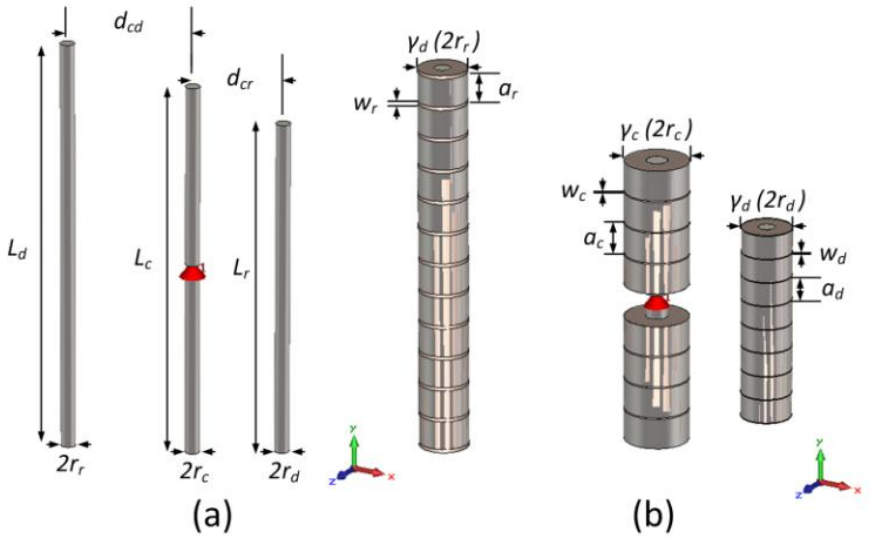

Fig. 49: (a) Geometry of a traditional Yagi-Uda antenna; (b) Geometry of a cloaked Yagi-Uda antenna in which the three metallic rods are surrounded by as many generic mantle cloaking devices. γ is the ratio between the cover and the cylinder radius.

After a brief optimization with a full-wave simulator, I achieve the final antenna design whose electrical and radiative characteristics are shown in Fig. 50 and Fig. 51, respectively. The antenna is matched in BW_a and exhibits a front-to-back ratio approximately equal to 11.5 *dB* at its center frequency.

The second step of the design consists in covering the three elements composing the Yagi-Uda with as many *generic* mantle cloak devices. As well known, a mantle cloak device is composed by a properly patterned metallic surface (also known as *metasurface*) supported by a dielectric and exhibiting a desired value of its intrinsic surface reactance

X_s (Ω/sq). Since the cloaking of a metallic cylinder requires a capacitive metasurface, the cloaks, shown in Fig. 49(b), are simply composed by thin vertical metallic strips.

The cloaks radii and the choice of the supporting dielectric both represent two design critical elements. These parameters, in fact, affect both the Yagi-Uda and the cloaking performances. According to the results achieved in [43], I can state, as general rules, that the use of a dielectric with high permittivity increases the cloaking performance but it is related to a reduction of both the cloaking bandwidth and of the input resistance of the Yagi-Uda antenna. Secondly, the use of large radii increases the cloaking performance but reduces the input resistance of the Yagi-Uda and, depending on the electrical length of the cylinders at λ_{0b}, may introduce complex scattering phenomena that avoid the achievement of a cloaking effect within BW_b. A good trade-off among these different requirements can be found by using a substrate made of Teflon, a low-loss and easily machinable material with a moderate permittivity value $\varepsilon_r = 2.1$, and fixing γ_r, γ_c and γ_d equal to 3.

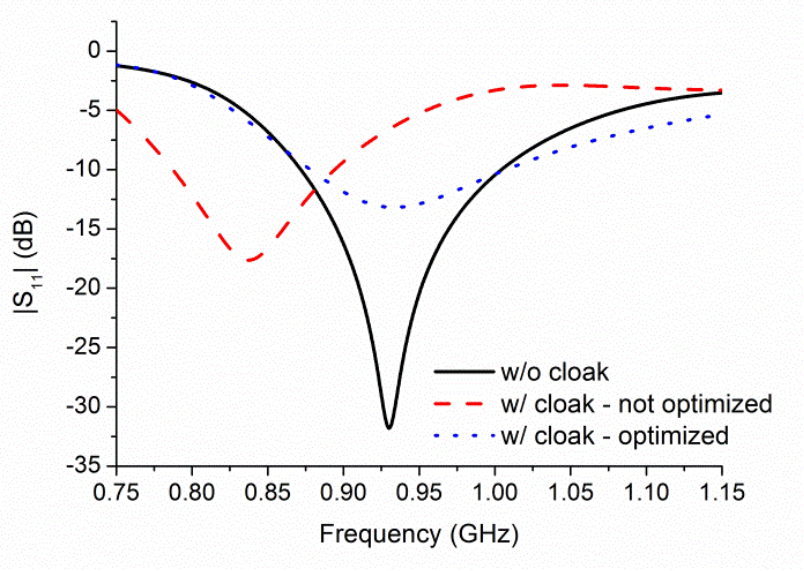

Fig. 50: Magnitude of the reflection coefficient of the bare Yagi-Uda antenna (continuous line), of the not optimized cloaked Yagi-Uda antenna (dashed line) and of the optimized cloaked Yagi-Uda antenna (dotted line).

It is important to underline that, in this step of the design, it is not possible to known the exact periodicity of the metallic strips (denoted with a in Fig. 49(b)), the strips separation (denoted with w) and the strips number. As explained in the previous Chapter, in fact, these values affect the surface reactance X_s exhibited by the metasurface.

Since the required surface reactance values depend on the length of each cylinder and such lengths will be optimization parameters in the next step, now I can only take into account the presence of the cloaks on the Yagi-Uda performances using a generic metasurface printed on a dielectric substrate. However, please note that since the cloaks are designed to work in BW_b, a can be safely considered electrically small in BW_a. Therefore, the generic cloaks shown in Fig. 49(b) can be later replaced by optimized cloaks without affecting the antenna behavior.

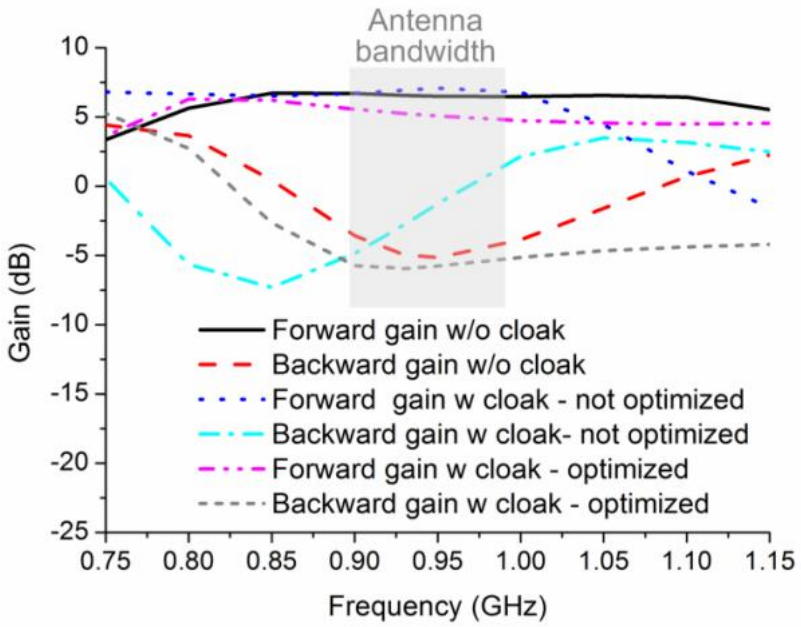

Fig. 51: Forward and backward gain of the bare Yagi-Uda antenna compared to the ones achieved with a not optimized and an optimized cloaked Yagi-Uda antenna.

As it is possible to appreciate in Fig. 50 and Fig. 51, the application of the generic cloaks around the Yagi-Uda elements introduce a frequency downshift of both the electrical and the radiative antenna characteristics. It is easy to understand that this effect is mainly due to the dielectric used to support the metasurfaces placed around the cylinders. A first solution to restore the proper operation of the Yagi-Uda is to scale all the antenna dimensions by a proper factor. Despite its simplicity, this solution may represent the best one in many scenarios. However, there are a few cases, as the one that I choose here, in which the antenna scaling cannot be applied. As already mentioned above, in fact, the finite length of the cylinders is related to complex scattering effects that the Mie theory, developed for infinitely-length cylinders, does not take into account.

These effects cannot be compensated by a mantle cloaking device and their presence would make not possible to make the Yagi-Uda antenna invisible. It is easy to verify that it is possible to avoid these effects if the length of the cloaked parasitic elements does not excessively approach the wavelengths of the cloaking range BW_b. For our design, in particular, the critical element is the length of the director that needs to be less than λ_{2b}, being f_{2b} the higher frequency of BW_b. A simple antenna scaling would not allow satisfying this condition and, therefore, a further optimization is required.

The first step of the new optimization consists in the restoration of the antenna resonance. It is easy to understand that it is possible upshifting the antenna resonance by reducing the length of the three cylinders of a proper quantity. Then, it is necessary to optimize the length of the parasitic elements (L_d and L_r) and their separation from the driven one (d_{cd} and d_{cr}) taking into account the previously defined bound ($L_d < \lambda_{2b}$). The effects of the different geometrical parameters on the antenna characteristics are shown in Fig. 51-Fig. 54. As evident, the main issue is to approach to the antenna input resistance to the required 50 Ω. The numerical optimization led to the geometrical parameters reported in Table 1. As can be appreciated from Fig. 50 and Fig. 51, the optimized cloaked antenna is matched in BW_a and exhibits a front-to-back ratio equal to 11.2 *dB*.

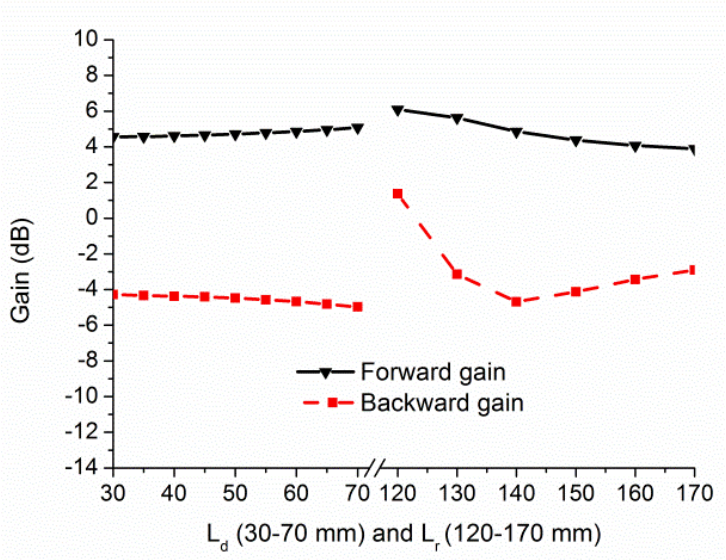

Fig. 52: Forward and backward gain of the cloaked Yagi-Uda antenna at the center frequency of BW_a as the director and reflector lengths change (once fixed L_r=*140 mm* and L_d= *60 mm*, respectively.

It is worth noticing that, being the front-to-back ratio almost equal in the two cases, the forward gain of the cloaked Yagi-Uda antenna is slightly smaller compared to the one achieved in the uncloaked case. However, I point out that if it would be possible to exploit an external device to achieve the impedance matching with a 50 Ω source and, so, to neglect the value of the input resistance in the optimization of the cloaked Yagi-Uda antenna, a higher forward gain might be achieved even in the cloaked case.

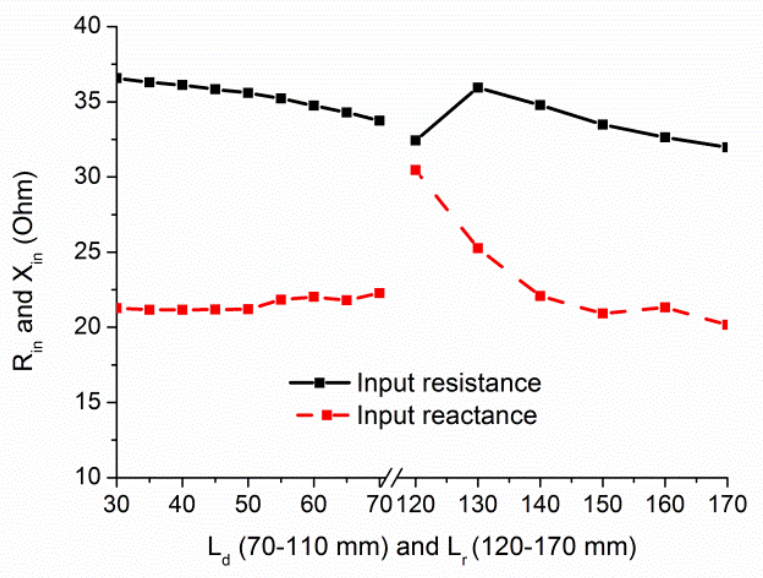

Fig. 53: Input resistance and reactance of the cloaked Yagi-Uda antenna at the center frequency of BW_a as the director and reflector lengths change (once fixed $L_r = 140\ mm$ and $L_d = 60\ mm$, respectively).

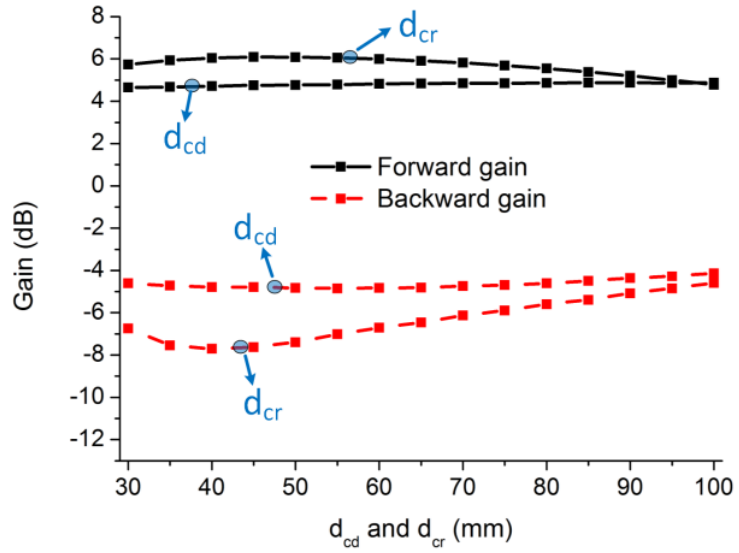

Fig. 54: Forward and backward gain of the cloaked Yagi-Uda antenna at the center frequency of BW_a as the distances d_{cd} and d_{cr} change (once fixed $d_{cr} = 98\ mm$ and $d_{cd} = 74\ mm$, respectively).

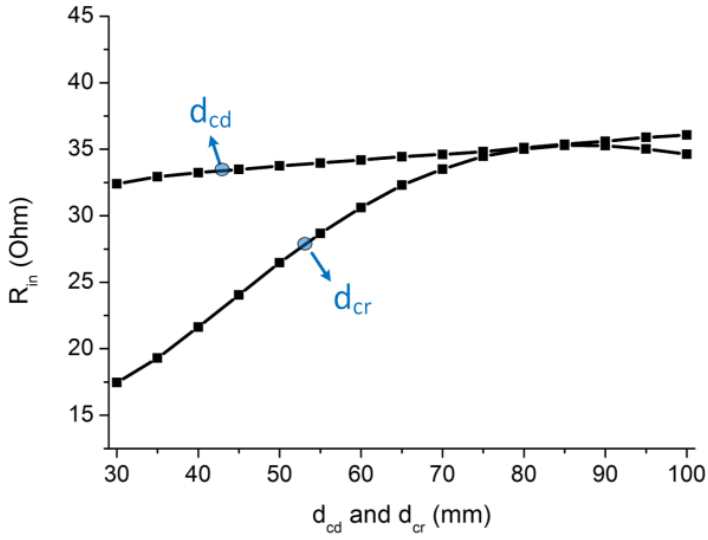

Fig. 55: Input resistance of the cloaked Yagi-Uda antenna at the center frequency of BW_a as the distances d_{cd} and d_{cr} change (once fixed $d_{cr} = 98\ mm$ and $d_{cd} = 74\ mm$, respectively).

Table 1: Geometrical parameters of the cloaked Yagi-Uda antenna.

Geometrical parameter	Value
L_r	λ_{0a} / 2.28
L_c	λ_{0a} / 3.13
L_d	λ_{0a} / 4.63
d_{cr}	λ_{0a} / 3.72
d_{cd}	λ_{0a} / 7.33
r_r	λ_{0a} / 107
r_c	λ_{0a} / 83
r_d	λ_{0a} / 107

2.4.2 *Cloaks design*

In this Subsection, I focus my attention on the design of the cloaks applied around the three elements of the Yagi-Uda. As already mentioned in the previous Subsection, these capacitive cloaks are simply composed by vertical metallic strips engraved on a dielectric support. The periodicity a and the separation among the strips w strongly affect the surface reactance exhibited by the cloaks at λ_{0b} but does not affect the performances of

the Yagi-Uda in BW_a. As discussed in the previous Chapter, the formula used to design the cloaks is the following:

$$X_s = -j \frac{\pi}{2\omega\varepsilon_0 a \ln\left[\csc\left(\frac{\pi w}{2a}\right)\right]}, \tag{2.4}$$

where ω is the desired cloaking frequency (*e.g.*, in our case, it corresponds to the central frequency of BW_b).

By using (2.4) it is possible to quickly design three vertical-strips metasurfaces exhibiting the required surface reactances. The geometrical parameters of the final cloaks, composed by $N_r = 12$ and $N_c = N_d = 8$ rows, respectively, are reported in Table 2, whereas in Fig. 56 I show the dispersive behavior of the designed metasurfaces, retrieved using a simple full-wave procedure based on a transmission-line model. As already discussed in the previous Subsection, the designed cloaks can replace the generic ones used during the Yagi-Uda optimization without affecting the antenna performances. This aspect has been properly checked with full-wave simulations but it is not here reported for the sake of brevity.

Table 2: Geometrical parameters of the designed metasurfaces.

Geometrical parameter	Value
a_r	λ_{0b} / 7.9
a_c	λ_{0b} / 8.0
a_d	λ_{0b} / 11.1
w_r	λ_{0b} / 73.8
w_c	λ_{0b} / 185.5
w_d	λ_{0b} / 307.5

In Fig. 57 I report the total SCS (*i.e.*, the scattering cross section of the object integrated all around the object itself) of both the uncloaked and cloaked Yagi-Uda antenna when it is illuminated by an external plane wave whose electric field is parallel to the axis of the

cylinders. I have achieved a 14.6 *dB* reduction of the total SCS around the central frequency of BW_b with a -10 *dB* fractional bandwidth of about 400 *MHz*.

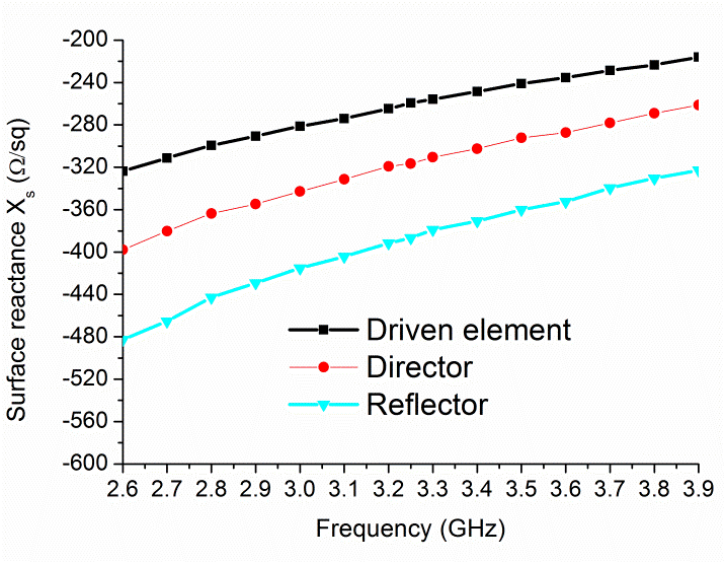

Fig. 56: Retrieved surface reactance as the frequency changes of the three designed vertical strips metasurfaces.

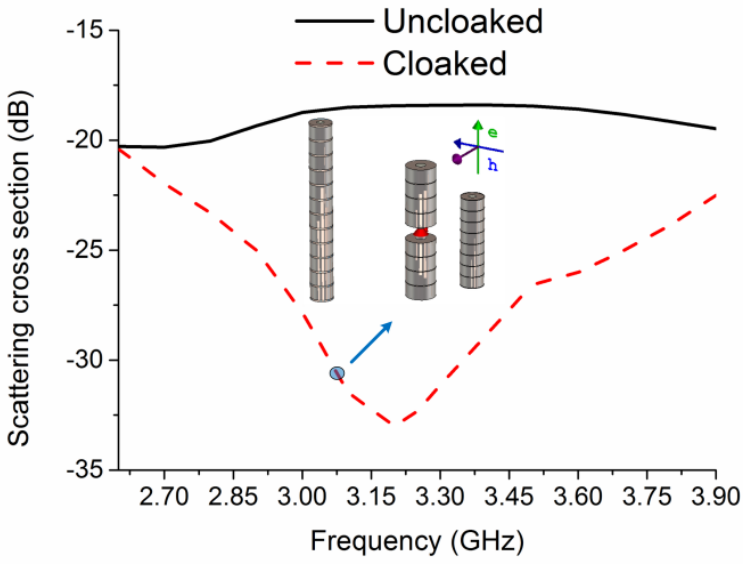

Fig. 57: Total scattering cross section of the Yagi-Uda antenna in the uncloaked case (continuous line) and in the cloaked one (dashed line) under a TM plane wave illumination.

I conclude this Subsection by stating that, thanks to the application of the designed cloaks, the Yagi-Uda antenna designed in the previous Subsection is effectively invisible in BW_b while it keeps it ability to properly operate as an efficient radiator in BW_a.

2.4.3 Use of the cloaked Yagi-Uda antennas in realistic scenarios

In this Subsection, I check the capability of the designed cloaked Yagi-Uda antenna to be electromagnetically invisible to other radiators. As a first example, I consider the scenario depicted in the insets of Fig. 58, in which a Yagi-Uda radiator obstructs an 11 *dB* WR-284 horn antenna whose mono-modal band coincides with the range BW_b adopted here [40]. The distance between the two antennas is equal to $\lambda_{0b}/2$. In Fig. 58, I show the comparison between the magnitude of the reflection coefficient of the horn antenna in three cases: the isolated one (*i.e.*, unobstructed horn antenna), the uncloaked one (*i.e.*, horn antenna obstructed by an uncloaked Yagi-Uda radiator) and the cloaked one (*i.e.*, horn antenna obstructed by a cloaked Yagi-Uda radiator designed with the outlined procedure). As expected, the horn impedance matching in the uncloaked case is very poor due to the presence of the Yagi-Uda antenna that introduces a significant perturbation in the horn near field. Instead, in the cloaked case, the horn impedance matching is dramatically improved, especially within the cloaking bandwidth in which the horn does not experience the presence of the Yagi-Uda despite its very close proximity. In the insets of the same picture, it is also shown the comparison between the 3D horn radiation pattern in the uncloaked and cloaked case at the central frequency of BW_b. While a dramatic deterioration of the horn radiation pattern can be observed in the uncloaked case, the original horn pattern is totally restored in the cloaked one, confirming the effectiveness of the proposed device.

In Fig. 59-Fig. 60, I compare the horn radiation pattern on the horizontal plane at the frequencies 3.1 *GHz* and 3.6 *GHz*, respectively. From these pictures, it is evident that the restoration of the original horn radiative characteristics is obtained in a wide range of frequencies and not only at the cloaking frequency. Outside this range, the horn pattern is progressively deteriorated due to the reduction in the cloaking performances of the designed cloaks (see Fig. 57).

It is worth to noticing that in the scenario depicted in the insets of Fig. 58 and depending on the relative distance, the designed cloaked Yagi-Uda antenna may not properly work due to the interaction with the horn antenna that represents an obstacle placed in the Yagi-Uda near field region. However, this issue can be overcome by using

Yagi-Uda antenna with a higher number of directors. My simulations, in fact, confirm that by increasing the director elements, the Yagi-Uda antenna progressively recovers its free-space characteristics. The procedure for design *N*-elements Yagi-Uda antenna can be easily generalized by the one outlined here. I also underline that the presence of a thin horizontal metallic structure supporting the elements of the Yagi-Uda would not affect the cloaking performances due to its very moderate scattering for a vertical incidence polarization (as the one emerging from the horn antenna aperture).

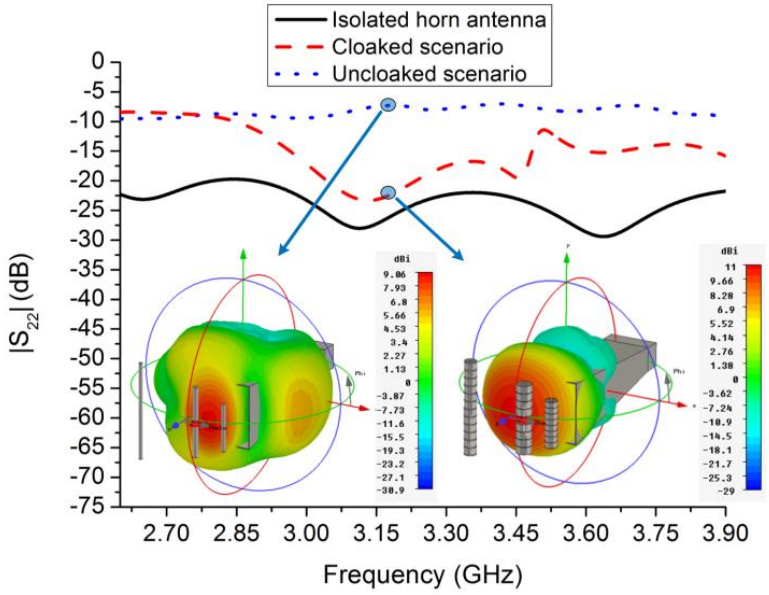

Fig. 58: Magnitude of the reflection coefficient of the horn antenna in the isolated case (continuous line), in the uncloaked one (dotted line) and in the cloaked one (dashed line).

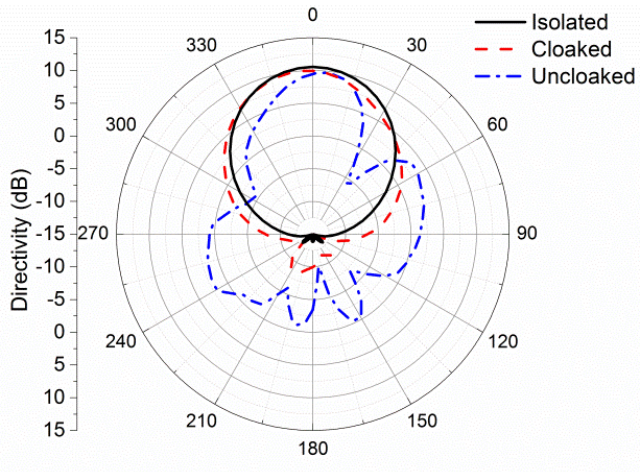

Fig. 59: Radiation pattern of the horn antenna on the horizontal plane at 3.1 *GHz* in the isolated (continuous line), in the uncloaked (dotted line) and in the cloaked case (dashed line).

Finally, as a further evidence of the advantages provided by the invisible Yagi-Uda antennas, I investigate the challenging scenario depicted in Fig. 61. In this case, a Yagi-Uda antenna optimized to work in a subrange of the cloaking band BW_b (denoted with the term "second Yagi-Uda") is placed between the driven element and the reflector one of the cloaked Yagi-Uda antenna that operates at BW_a ("first Yagi-Uda"). The second Yagi-Uda is intentionally oriented to radiate in an opposite direction compared to the first one. As expected and reported in Fig. 62, in an uncloaked scenario the presence of the first Yagi-Uda dramatically deteriorates the performances of the second one. In the cloaked scenario, instead, the second Yagi-Uda antenna correctly radiates in opposite direction compared to the first one and operates as the first Yagi-Uda was not present (Fig. 62). In the same picture, moreover, please note that the first Yagi-Uda is not affected by the presence of the second one due its reduced electrical dimensions in BW_a. Therefore, the antenna system shown in Fig. 61 acts as a high-directivity and extremely compact dual-band radiator with opposite main lobe directions for its two resonance frequencies.

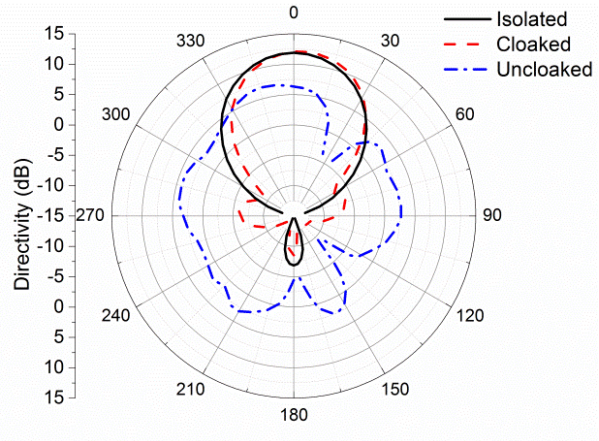

Fig. 60: Radiation pattern of the horn antenna on the horizontal plane at 3.6 *GHz* in the isolated (continuous line), in the uncloaked (dotted line) and in the cloaked case (dashed line).

In Fig. 63, I report the forward and backward gain of the two Yagi-Uda antennas as the frequency changes. The insets of the same picture show the 3D radiation pattern at the central frequency of BW_a and BW_b, respectively. As can be appreciated, each Yagi-Uda antenna properly operates in its own bandwidth without affecting the performances of the other antenna.

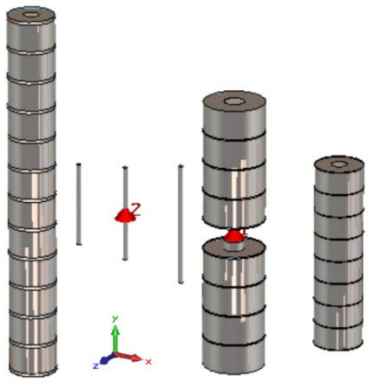

Fig. 61: Antenna scenario in which a Yagi-Uda antenna operating at *3.2 GHz* is placed between the director and the driven element of the cloaked Yagi-Uda antenna (that operates a 0.93 *GHz*).

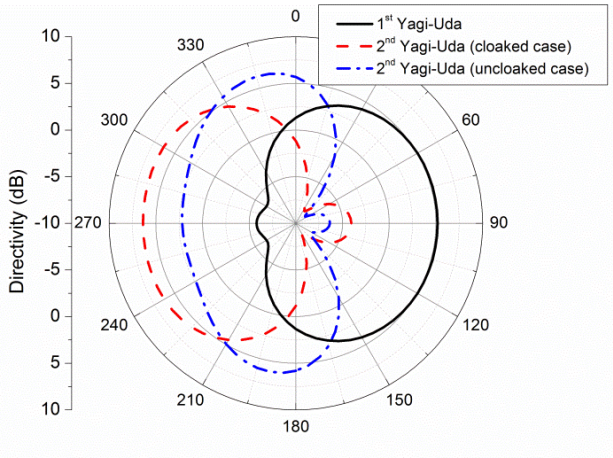

Fig. 62: Directivity on the *x-z* plane of the two Yagi-Uda antennas system shown in Fig. 61. The directivity of the second Yagi-Uda is shown both in the uncloaked and in the cloaked scenario.

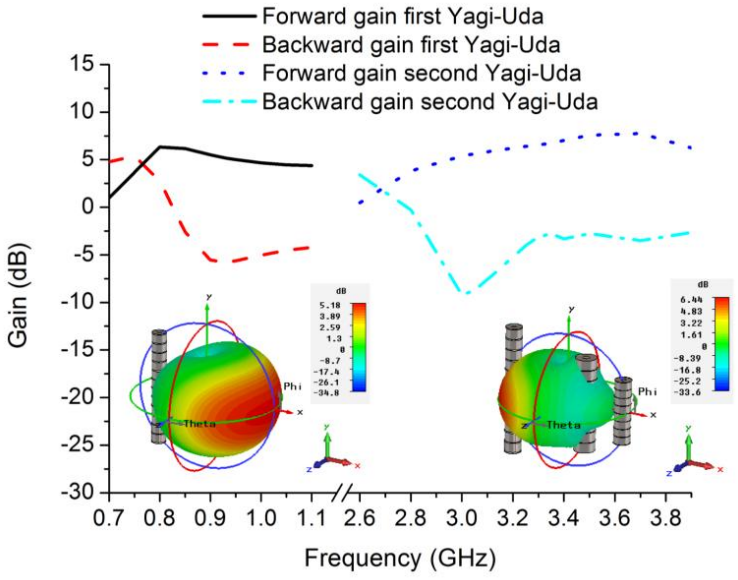

Fig. 63: Forward and backward gain of the two Yagi-Uda antennas shown in Fig. 61.

2.5 References

[1] R.F. Harrington, "Theory of loaded scatterers," Proc. IEEE, vol. 3, no. 4, pp. 617–623, April 1964.

[2] W.K. Kahn, and H. Kurss, "Minimum-scattering antennas," IEEE Trans. Antenna Prop., vol. 13, no. 5, pp. 671–675, Sept. 1965.

[3] J.K. Schindler, R.B. Mack, and P. Blacksmith, "The control of electromagnetic scattering by impedance loading," Proc. IEEE, vol. 53, no. 8, pp. 993–1004, Aug. 1965.

[4] R.B. Green, "Scattering from conjugate-matched antennas," IEEE Trans. Antenna Prop., vol. 14, no. 1, pp 17–21, Jan. 1966.

[5] R.C. Hansen, "Relationships between antennas as scatters and as radiators," Proc. IEEE, vol. 77, no. 5, pp 659–662, May 1989.

[6] J.B. Andersen and A. Frandsen, "Absorption efficiency of receiving antennas," IEEE Trans. Antenna Prop., vol. 53, no. 9, pp. 2843–2849, Sept. 2005.

[7] D.H. Kwon and D.M. Pozar, "Optimal characteristics of an arbitrary receive antenna," IEEE Trans. Antenna Prop., vol. 57, no. 12, pp. 3720–3727, Dec. 2009.

[8] D.H. Kwon, and D.M. Pozar, "Design of received and scattered powers for dipole arrays using load optimization," Antennas and Propagation Society International Symposium (APSURSI), 2010 IEEE, July 2010.

[9] M. Gusstafsson, C. Sohl, and G. Kristensson, "Illustrations of new physical bounds on linearly polarized antennas," IEEE Trans. Antenna Prop., vol. 57, no. 5, pp. 1319–1327, May 2009.

[10] M. Gusstafsson, J.B. Andersen, G. Kristensson, and G.F. Pedersen, "Forward scattering of loaded and unloaded antennas," IEEE Trans. Antenna Prop., vol. 60, no. 12, pp. 5663–5668, Dec. 2012.

[11] A. Alù, and N. Engheta, "Cloaking a sensor," Phys. Rev. Lett., vol. 102, pp. 233901, June 2009.

[12] A. Alù and S. Maslovski, "Power relations and a consistent analytical model for receiving wire antennas," IEEE Trans. Antenna Prop., vol. 58, no. 5, pp. 1436–1448, May 2010.

[13] A.O. Karilainen and S.A. Tretyakov, "Circularly polarized receiving antenna incorporating two helices to achieve low backscattering," IEEE Trans. Antenna Prop., vol. 60, no. 7, pp. 3471–3475, July 2012.

[14] C.A. Valagiannopoulos and N.L. Tsitsas, "Integral equation analysis of a low-profile receiving planar microstrip antenna with a cloaking substrate," Radio Sci., vol. 47, RS004878, April 2012.

[15] N. L. Swanson and B. D. Billard, "Electively maximizing and minimizing the scattering and absorption of electromagnetic waves," US patent 6842242 B2, Jan 11, 2005.

[16] A. T. de Hoop, "Theorem on the maximum absorption of electromagnetic radiation by a scattering object of bounded extent," Radio Science, vol. 16, no. 6, pp. 971–974, 1981.

[17] C. A. Valagiannopoulos, "A miniature inhomogeneous cloak following a power law," International Journal of Applied Electromagnetics and Mechanics, vol. 42, no. 1, pp. 63–71, Jan. 2013.

[18] T. Chaigne, O. Katz, A. C. Boccara, M. Fink, E. Bossy, and S. Gigan, "Controlling light in scattering media non-invasively using the photoacoustic transmission matrix," Nat Photon, vol. 8, no. 1, pp. 58–64, Jan. 2014.

[19] D.H. Kwon and D.H. Werner, "Restoration of antenna parameters in scattering environments using electromagnetic cloaking," Appl. Phys. Lett., vol. 92, no. 11, pp. 113507, March 2008.

[20] J. Vehmas, P. Alitalo, and S. Tretyakov, "Experimental demonstration of antenna blockage reduction with a transmission-line cloak," IET Microw. Antennas Propag., vol. 6, no. 7, pp. 830–834, Jan. 2012.

[21] P.-S. Kildal, A. A. Kishk, and A. Tengs, "Reduction of forward scattering from cylindrical objects using hard surfaces," IEEE Trans. Antennas Propag., vol. 44, no. 11, pp. 1509–1520, Nov. 1996.

[22] M. Riel, Y. Brand, Y. Demers, and P.E. Maagt, "Performance improvements of center-fed reflector antennas using low scattering struts," IEEE Trans. Antenna Prop., vol. 60, no. 3, pp. 1269–1280, March 2012.

[23] A. Monti, A. Toscano, and F. Bilotti, "Metasurface mantle cloak for antenna applications," Antennas and Propagation Society International Symposium (APSURSI), 2012 IEEE, July 2012.

[24] A. Monti, J. Soric, A. Alù, F. Bilotti, A. Toscano, and L. Vegni, "Overcoming mutual blockage between neighboring dipole antennas using a low-profile patterned metasurface," IEEE Antennas and Wireless Propagation Letters, vol.11, pp.1414, 2012.

[25] H. Chen, X. Luo, H. Ma, and C.T. Chen, "The anti-cloak," Optics Express, vol. 16, pp. 14603, Sep. 2008.

[26] T. Xu, X.F. Zhu, B. Liang, Y. Li, X.Y. Zou, and J.C. Cheng, "Scattering reduction for an acoustic sensor using a multilayer shell comprising a pair of homogenous isotropic single-negative media," Appl. Phys. Lett., vol. 101, pp. 033509, July 2012.

[27] R. Fleury, J. C. Soric, and A. Alù, "Physical Bounds on Absorption and Scattering for Cloaked Sensors," online at: http://arxiv.org.

[28] S.A. Tretyakov, S. Maslovski, and P.A. Belov, "An analytical model of metamaterials based on loaded wire dipoles," IEEE Trans. Antenna Prop., vol. 51, no. 19, pp. 2652, Oct. 2003.

[29] Comsol Multiphysics, 4.3a, www.comsol.com.

[30] C.F. Balanis, Antenna Theory, 3rd Ed. New Jersey: Wiley, 2012.

[31] P. S. Kildal, A. A. Kishk, and A. Tengs, "Reduction of forward scattering from cylindrical objects using hard surfaces," *IEEE Trans. Antennas Propag.*, vol. 44, pp. 1509-1520, 1996.

[32] M. Riel, Y. Brand, Y. Demers, and P.D. Maagt, "Performance improvements of center-fed reflector antennas using low scattering struts," *IEEE Trans. Antennas Propag.*, vol. 60, pp. 1269-1280, 2012.

[33] P. Alitalo, C. Valagiannopoulos, and S. A. Tretyakov, "Simple cloak for antenna blockage reduction," *2011 IEEE APS Int. Sym.*, pp. 669-672, 2011.

[34] P. Alitalo, J. Vehmas, and S. A. Tretyakov, "Reduction of antenna blockage with a transmission-line cloak," *Antennas Propag. (EUCAP), Proceedings of the 5th European Conference on*, pp. 2399-2402, 2011.

[35] D. H. Know and D. H. Werner, "Restoration of antenna parameters in scattering environments using electromagnetic cloaking," *Appl. Phys. Lett.*, vol. 92, 113507, 2008.

[36] A. Alù and N. Engheta, "Plasmonic materials in transparency and cloaking problems: mechanism, robustness, and physical insights," *Opt. Expr.*, vol. 15, 3318, 2007.

[37] A. Alù and N. Engheta, "Cloaking and transparency for collections of particles with metamaterial and plasmonic covers," *Opt. Expr.*, vol. 15, 7578, 2007.

[38] P.S. Kildal, and R. Rajo-Iglesias, "Mushroom surface cloaks for making struts invisible," *IEEE APS Int. Symp.*, pp. 869-872, 2007.

[39] J. Vehmans, P. Alitalo, S. A. Tretyakov, "Experimental demonstration of antenna blockage reduction with a transmission-line cloak," *IET Microw. Antennas Propag.*, vol. 6, pp. 830-834, 2012.

[40] Pasternack®, www.pasternack.com/directional-antennas-category.aspx.

[41] C.A. Balanis, *Antenna theory: Analysis and Design*, Hoboken, United State of America, John Wiley & Sons, 2005, pp. 577-600.

[42] C. F. Bohren and D.R. Huffman, *Absorption and Scattering of Light by Small Particles*, New York, United States of America, Wiley-Interscience, 1998.

[43] J. C. Soric, P. Y. Chen, A. Kerkhoff, D. Rainwater, K. Melin, and A. Alù, "Demonstration of an ultralow profile cloak for scattering suppression of a finite-length rod in free space," *New. J. Phys.*, vol. 15, 033037, 2013.

3 Scattering cancellation at optical frequencies

In this Chapter, I present the results that I have obtained with my co-authors about the possibility to extend the scattering cancellation, both the plasmonic and the mantle cloaking, at optical frequencies ([J03], [J09]-[J10], [C10], [C12]).

The first Section (Section 3.1) is focused on the design of optical epsilon-near-zero (ENZ) metamaterials (MTMs) based on the employment of an array of core-shell nano-spheres embedded in a dielectric medium. The core of the nano-spheres and the host medium are both made of silica, while the shell is formed by a plasmonic material. Using classical homogenization formulas, I show that it is possible to design the array in such a way to exhibit near-zero values of the effective real permittivity with relatively low-losses at optical frequencies. Finally, I show that this kind of materials find application in the optical plasmonic cloaking and in the design of angular filter.

The second Sections (Section 3.2) dealt with the modeling of the nanoparticles array using a different paradigm. In particular, it is first validated and generalized an analytical model recently appeared in the literature to describe a 2D array of plasmonic nanoparticles as a metasurface characterized by its homogenized surface reactance. It is proven that the proposed model allows to efficiently design 2D mantle cloaks with an assigned surface reactance, enabling, thus, the extension of the mantle cloaking technique to optical frequencies. Then, I show that thanks to this model it is possible to design realistic optical mantle cloaks made of 2D arrays of spheroidal plasmonic nanoparticles with a high eccentricity. The proposed cloaks allow significant, moderately broadband cloaking effects at visible frequencies. In these designs, I consider realistic losses and non-critical nanoparticle dimensions to envision their practical realization.

3.1 Optical epsilon-near-zero materials

An important class of MTMs that have found interesting applications in different scientific areas, including field localization and sub-wavelength focusing, is represented by the so-called epsilon-near-zero (ENZ) MTMs [1]. Such materials, characterized by low-positive (i.e. between 0 and 1) or low-negative values (i.e. between – 1 and 0) of the real part of the relative permittivity, in fact, have been used to tailor the phase-front of light [2], to obtain very directive electromagnetic beams [3]-[4], to implement the optical nano-circuit concepts [5], to strongly confine the electromagnetic field [6], to design angular filters [2], to cover apertures and get enhanced transmission [7], to obtain anomalous tunnelling effects [8]-[10], to design innovative lenses with enhanced focusing properties [11]-[12] and, as explained in the first Chapter, to obtain cloaking devices based on the scattering cancellation approach [13]-[15].

For what concerns, in particular, field localization and focusing effects, ENZ materials allow for several interesting electromagnetic properties. Going back to basic physics, in fact, the boundary condition for the normal component of the electric displacement vector at the interface between a regular material and an ENZ one reveals the potential of ENZ materials in field confinement and localization. Being the permittivity inside the ENZ material close to zero, in fact, the normal component of the electric field should be dramatically high in order to match the required boundary condition. This effect has been exploited in a number of components and setups for different applications. ENZ materials have shown their potential also to improve the resolution of imaging systems (such as near-field optical microscopes - NSOMs) and tailor the field localization around a sensing probe [16]-[20]. By partially covering either aperture or aperture-less NSOM tips with ENZ materials, in fact, it is has been demonstrated that the undesired scattering from the tip can be cancelled out, improving, thus, the quality of the image with sub-wavelength resolution obtained from the system.

While the actual implementation of ENZ materials is rather straightforward at microwave frequencies by using the wire-medium or the parallel-plate-medium [13],[21], a few solutions have been proposed at higher frequencies. Besides a couple of

materials (i.e. silicon carbide and silicon nitride) [22] exhibiting a plasma frequency and, thus, an ENZ behaviour in the mid-infrared, the implementation of ENZ materials at higher frequencies requires the design of an artificial material. Noble metals (e.g. gold and silver), in fact, exhibit their plasma frequencies in the ultra-violet regime and, thus, are not appropriate for obtaining ENZ materials in the visible range. An extension of the wire- and parallel-plate-media has been proposed at far- and mid-infrared frequencies [23], but it can be hardly extended at optical frequencies. An alternative solution consists in creating an effective medium mixing a plasmonic material and a regular dielectric in such a way to shift the plasma frequency towards the visible [24],[25]. Such an approach, however, as demonstrated in [24], leads to extreme dimensions (*1-2 nm*) for the plasmonic layers, which are not compatible with current technologies. In addition, even if technologies would be appropriate for such realizations, I would have new modelling issues concerning the evaluation (if not the definition) of the permittivity function of the plasmonic materials in such thin nanometric layers.

Recently, the idea to mix together plasmonic and non-plasmonic materials came again into play. If mixing non-resonant material layers did not lead to viable solutions, the employment of resonating plasmonic particles in a host dielectric, instead, shows some potentials. In [26], for instance, a new implementation scheme has been considered, exploiting the possibility of realizing ENZ covers through amorphous arrangements of silver nano-spheres in air. Such a design successfully works beyond the optical frequencies, at around *900 THz* with moderate low losses. In this Section, I first discuss the latter solution in order to check if it is possible to make it working at optical frequencies, as well, by using proper arrangements of silver or gold nano-spheres. Then, I propose an alternative solution, consisting in arrangements of core-shell nano-particles embedded in a dielectric host.

3.1.1 Analytical models

As previously anticipated, it is possible to lower the plasma frequency of a plasmonic material by designing an artificial mixture constituted by metallic inclusions (*e.g.*, spheres) embedded in a dielectric host medium. If the inclusion dimensions are small

compared to the wavelength inside the host medium, the effective permittivity of the artificial material can be written by using Maxwell-Garnett homogenization formula [27] as:

$$\varepsilon_e(\omega) = n_m^2 \frac{\varepsilon(1+2f)+2n_m^2(1-f)}{\varepsilon(1-f)+n_m^2(2+f)}, \tag{3.1}$$

where $n_m = \sqrt{\varepsilon_m}$ is the refractive index of the non-absorbing and non-magnetic background medium, ε the dispersive permittivity of the sphere material, f the filling volume fraction of the inclusions, and ω the angular frequency. The measured dispersive permittivity of the metallic nano-spheres for some common noble metals can be found in [28]and are used throughout this Section.

The complex effective permittivities of arrays of *gold* nano-spheres with different values of the filling volume fraction and embedded in a silica matrix are shown in Fig. 64 and Fig. 65. With the indicated filling volume fractions (compatible with the limitations presented in [29]), it is possible to bring the ENZ behaviour down to optical frequencies. Losses, however, are clearly too much high to guarantee good performances of the devices realized through such an artificial material and, thus, the proposed solution is to be discarded. This exercise, however, tells us about the role of the filling volume fraction. Higher values of f are, in fact, not compatible with the limitations reported in [29] and lead to an ENZ behaviour at higher frequencies. Lower values of f, instead, reduce the resonance effect of the plasmonic spheres and, consequently, the values of the real part of the effective permittivity are not in the ENZ range anymore. Therefore, the values of the filling volume fraction here considered are the ones optimizing the two opposite trends now described and keeping the required ENZ behaviour at optical frequencies.

As documented in [28], a way to reduce the losses at optical frequencies is to replace gold with *silver*. The results presented in Fig. 66 and Fig. 67confirm that losses are significantly reduced but the ENZ frequency band is now shifted towards the near-UV. Please note that, due to the different plasma frequencies of gold and silver, the values of the filling volume fraction required to have an ENZ behaviour at optical frequencies are now rather low compared to the ones required in the case of gold nano-spheres.

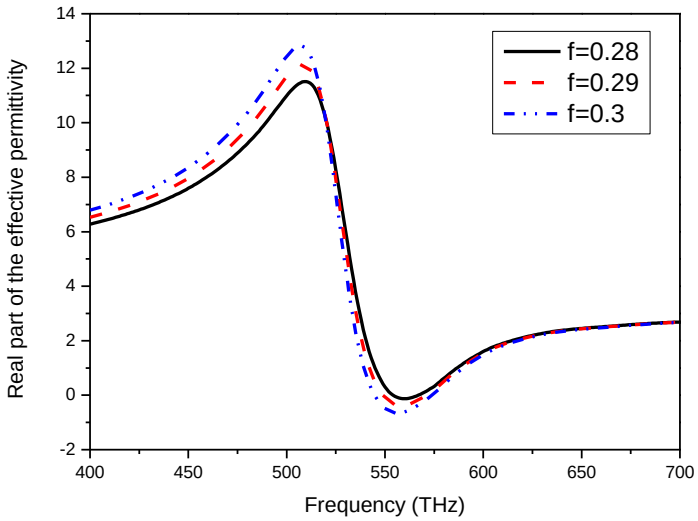

Fig. 64: Real part of the effective permittivity for an array of gold nano-spheres embedded in a silica matrix for different values of the filling volume fraction.

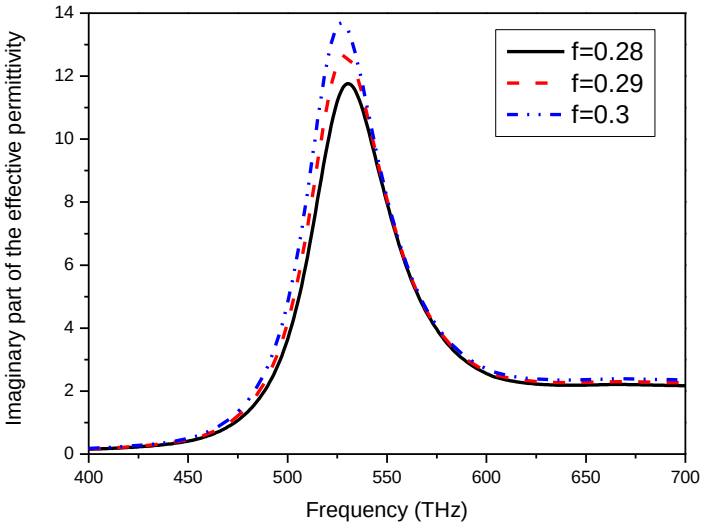

Fig. 65: Imaginary part of the effective permittivity for an array of gold nano-spheres embedded in a silica matrix for different values of the filling volume fraction.

A possible solution I propose here to bring the required ENZ behaviour to optical frequencies with a reasonable level of losses is shown in the following. I propose to use an array of core-shell nano-spheres with a plasmonic shell and a dielectric core. Such a structure allows lowering the ENZ frequency range, due to the hybridization of the two plasmons arising at the two metal-dielectric interfaces. This phenomenon leads, in fact, to two new resonances of the particle, one of which is at a lower frequency compared to that of the plasmonic material itself [30]. The core-shell resonances can be tuned varying the shell thickness, as well as changing the material of the core (and of the shell).

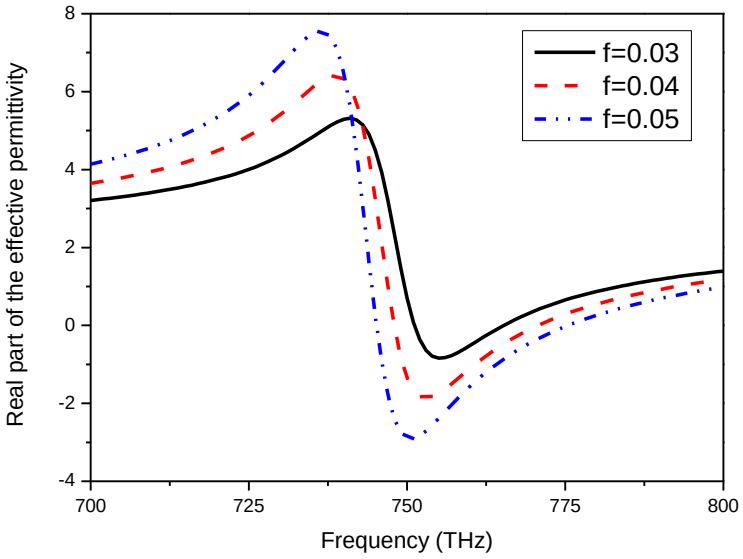

Fig. 66: Real part of the effective permittivity for an array of silver nano-spheres embedded in a silica matrix for different values of the filling volume fraction.

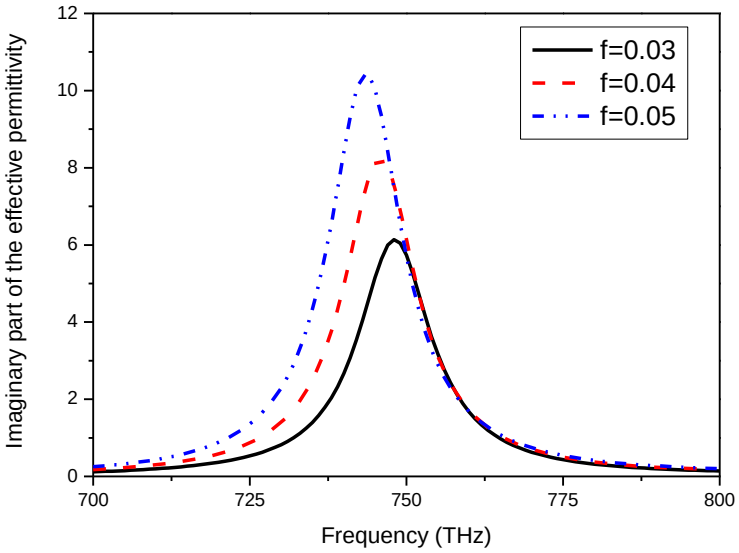

Fig. 67: Imaginary part of the effective permittivity for an array of silver nano-spheres embedded in a silica matrix for different values of the filling volume fraction.

The complex effective permittivity of the artificial material can be analytically expressed by inserting the polarizability of a single core-shell nano-particle [31] into the Clausius-Mossotti homogenization formula [32] as:

$$\varepsilon_{eff} = -\frac{\varepsilon_m\left\{2(f-1)\varepsilon_m\left[(\beta+2)\varepsilon_{r1}+\varepsilon_{r2}-\beta\varepsilon_{r2}\right]+(2f+1)\varepsilon_{r1}\left[2(\beta-1)\varepsilon_{r1}-(2\beta+1)\varepsilon_{r2}\right]\right\}}{(f+2)\varepsilon_m\left[(\beta+2)\varepsilon_{r1}+\varepsilon_{r2}-\beta\varepsilon_{r2}\right]+(f-1)\varepsilon_{r1}\left[2(\beta-1)\varepsilon_{r1}-(2\beta+1)\varepsilon_{r2}\right]},$$

(3.2)

where ε_{r2} and ε_{r1} are core and shell relative permittivities, respectively, a_2 and a_1 the core and the shell radius, respectively, and $\beta = a_2^3/a_1^3$ (see Fig. 68).

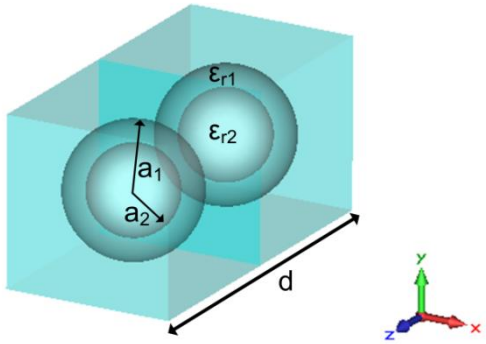

Fig. 68: Unit-cell of the designed artificial material slab. The thickness of the slab along the z-axis is $d = 0.17\ \lambda_0$ at the design frequency.

By suing this formula I have designed an artificial material consisting of an array of nano-spheres formed by a silver shell and a silica core, embedded in a silica matrix. The single nano-particle has an overall radius of *15 nm* and the β factor is assumed equal to *0.296* in order to guarantee a reasonable thickness of the silver shell. Silver is modelled by using its measured bulk permittivity [28], while a constant permittivity equal to *2.137* is assumed for the silica. The resulting complex effective permittivity is shown in Fig. 69.

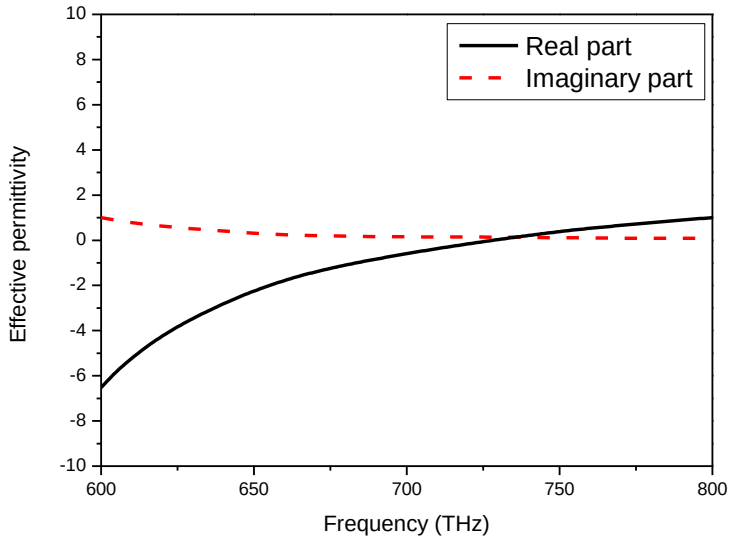

Fig. 69: Real and imaginary part of the effective permittivity for an array of core-shell nano-spheres embedded in a silica matrix with β=*0.296* and f=*0.3*.

3.1.2 Application of optical ENZ materials

In order to test the artificial material model I have developed before, I show in the following a couple of application examples. A straightforward way to test the model is to consider an ENZ planar slab with given thickness and study its electromagnetic properties. As rigorously demonstrated in [2]-[3], an ideal ENZ slab illuminated by a TM-polarized plane-wave behaves as an angular filter. Assuming the magnetic field parallel to the *y*-axis and the electric field in the *xz* plane, the transmission coefficient *T* of the slab is given by [2]:

$$\lim_{\varepsilon \to 0} T(k_x) = \begin{cases} 0 & k_x \neq 0 \\ \dfrac{2e^{idk_0}}{jdk_0 + 2} & k_x = 0 \end{cases} \tag{3.3}$$

where $k_x = k_0 \sin \vartheta_i$, k_0 is the free-space wave-number, and d the thickness of the ENZ slab. The angular filtering properties of the ENZ slab are such that only normal impinging plane-waves are allowed to pass through the slab, while all the other spectral components of the impinging field are reflected back in phase (i.e. the slab behaves as a perfect magnetic conductor for all the oblique-impinging TM plane-waves). In [2] it has been demonstrated also that the angular fractional bandwidth at half power of a lossless ENZ slab can be expressed as:

$$\Delta\theta \approx \frac{\Delta k_x}{k_0} = \frac{2\sqrt{\varepsilon_r}}{k_0 d} \tag{3.4}$$

According to this formula, thus, it is possible increasing the angular selectivity by either reducing the slab permittivity ε_r or increasing the slab thickness. However, according to (3.4) increasing d leads to a reduction of the transmission coefficient amplitude for normal incidence. In addition, as documented in [2], when material losses are introduced in the model, they progressively deteriorate the performance of the filter, especially in the case of narrow angular bandwidths.

By using the artificial material model I have developed in the previous section, I have designed the unit-cell of the ENZ slab (see Fig. 68). I have considered a finite thickness for the slab along the z-axis and imposed periodic boundary conditions along *x*- and *y*-axis. The unit-cell consists of two silica cubes embedding the designed core-shell nano-spheres. I have simulated the electromagnetic behaviour of the slab by using the full-wave numerical software CST Studio Suite, illuminating the slab with a TM plane-wave. The artificial material has been designed to exhibit an ENZ behaviour at around 715 THz and, in order to prove that, I have computed the transmittance spectra at three different frequencies: 600 THz, 715 THz, and 800 THz (see Fig. 70).

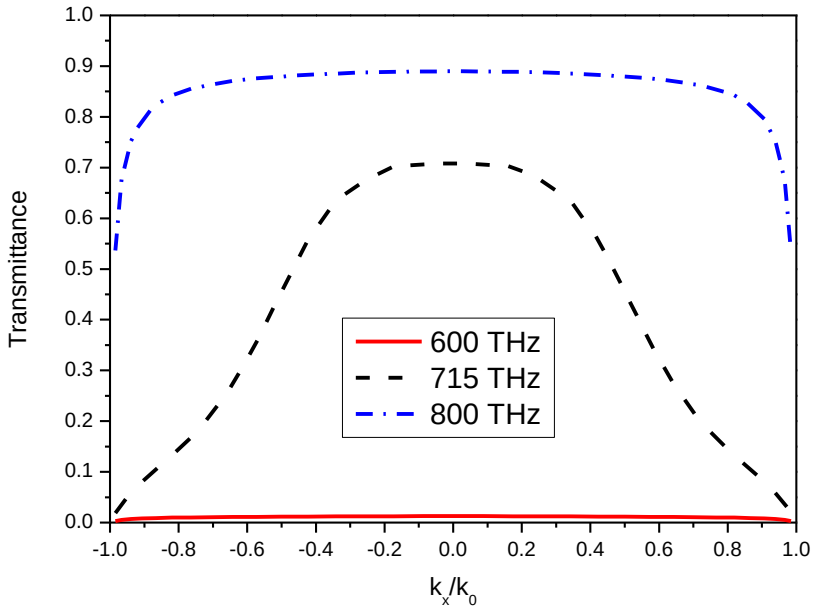

Fig. 70: Transmittance spectrum of the ENZ slab with thickness $d = 0.17\ \lambda_0$ versus the incidence angle at three different frequencies: *600 THz* (red solid line), *715 THz* (black dash line), and *800 THz* (blue dash-dot line).

At *600 THz* the effective permittivity of the artificial material should exhibit negative values of the real permittivity (see Fig. 69) and, thus, an extremely low transmission through the slab is expected. At *800 THz*, according to the permittivity function in Figure 6, the artificial material should act as a standard dielectric and, thus, the transmittance spectrum becomes a regular one. Finally, at *715 THz*, a selective transmission takes place, due to the expected ENZ behaviour of the slab. With a slab thickness of $0.17\ \lambda_0$ (at the frequency of *715 THz*), thus, the *– 3 dB* angular bandwidth is *70°* at *715 THz* against an angular bandwidth of about *160°* at *800 THz*.

I have, then, increased the thickness of the slab, to check the expected reduction of the angular bandwidth (that I pay with a reduction of the normal incidence transmission coefficient amplitude). The corresponding results are presented in Fig. 71.

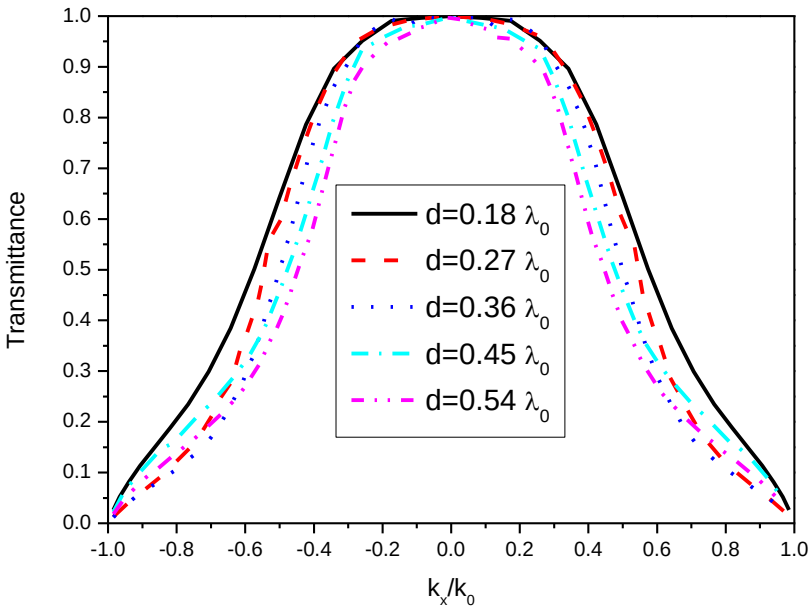

Fig. 71: Transmittance spectrum for different thicknesses *d* of the slab at *715 THz*. Each curve is normalized to the respective normal incidence transmittance value.

In Fig. 72, I show the distribution of the electric field amplitude on a plane parallel to the *xz* plane, placed at the central height of a slab with $d = 0.27\ \lambda_0$. Again, the results are presented for three different frequencies and for different incidence angles. In the first column, I report the data at *600 THz* for normal incidence (θ=0°), θ=30°, and θ=45°, respectively. As expected, whatever the incidence angle is, the transmission above the slab is almost vanishing. The second and the third columns refer to the frequencies of *715 THz* and *800 THz*, respectively. At *715 THz* I find a decreasing of the transmission peak when increasing the incidence angle, while at *800 THz* a regular transmission is observed in accordance with the results of Fig. 70.

The second example I present here refers to a more complex structure exhibiting cloaking properties at optical frequencies. As demonstrated in [15], the scattering cancellation approach can be successfully used to cloak also electrically small or moderate sized objects with anisotropic scattering properties, such as, for instance the dielectric cone ($\varepsilon_r = 2$) reported in Fig. 73(left panel). As reported in [15], such a conical

object can be effectively cloaked by using a conformal cover made of an ENZ material. In [19] the implementation of a conformal conical cover at mid-infrared frequencies by using the natural ENZ behavior of silicon carbide has been presented, but no implementations at optical frequencies have been suggested so far. By using the ENZ artificial material presented in the previous section, I show here that it is possible to design a conformal cloak working in the visible. The artificial material cover is depicted in the right panel of Fig. 73 and the whole structure has been illuminated by a TM plane-wave (i.e. with the electric field parallel to the cone axis). The simulated total scattering cross-sections obtained for different values of the volume filling fraction *f* are reported in Fig. 74.

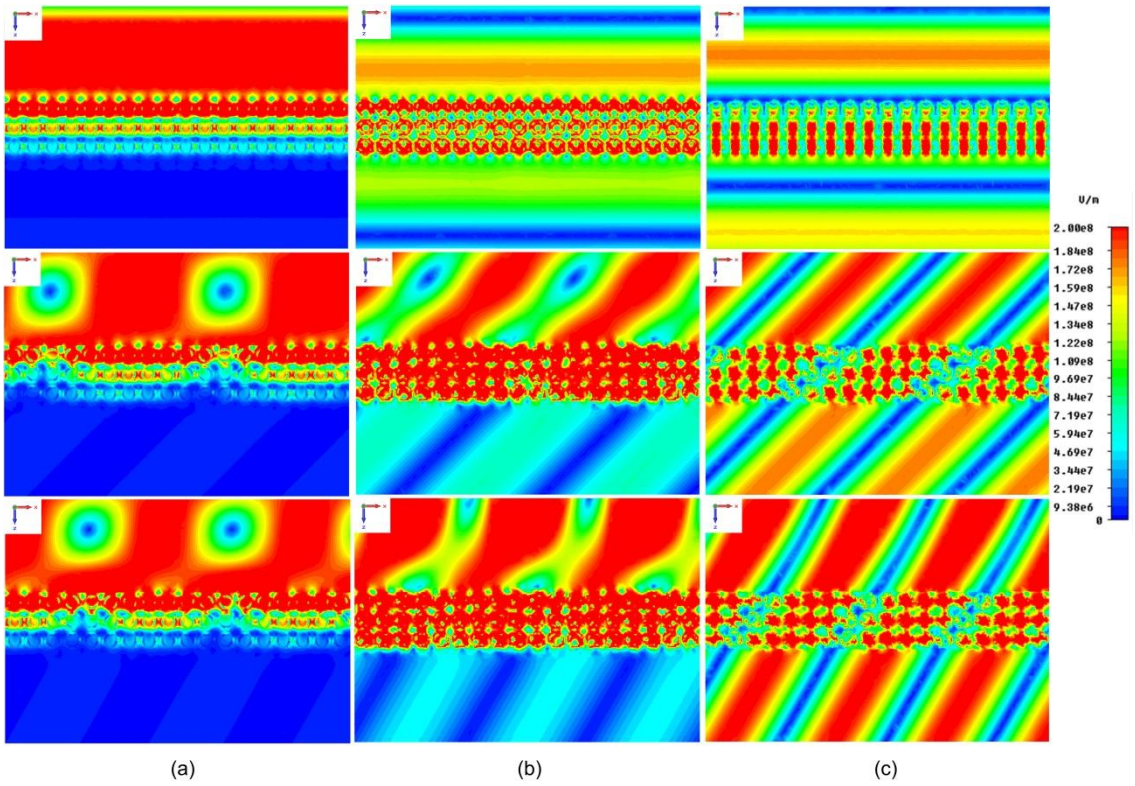

Fig. 72: Distribution of the electric field at (a) *600 THz*, (b) *715 THz*, and (c) *800 THz* for three different incidence angles (*0°*, *30°*, and *45°*) for an ENZ slab with thickness $d = 0.27\ \lambda_0$.

It is worth noticing that the parameter *f* can be used to tune, in a certain range, the operation frequency of the cloak. In particular, with $f = 0.3$ (the same value used for the previous example of the slab), I have obtained the maximum reduction of the total scattering cross-section of the cone at *740 THz*, while with a lower volume filling fraction ($f = 0.2$) the operation frequency of the cloak shifts down to around *685 THz*. Finally, in

Fig. 75, I compare the amplitude and phase distributions of the *y*-component of the electric field at the cloak frequency of *740 THz* (*f = 0.3*) on a plane parallel to the *xz* plane at half height of the cone for the cases of bare and covered objects. The field maps confirm the expected operation of the cloak.

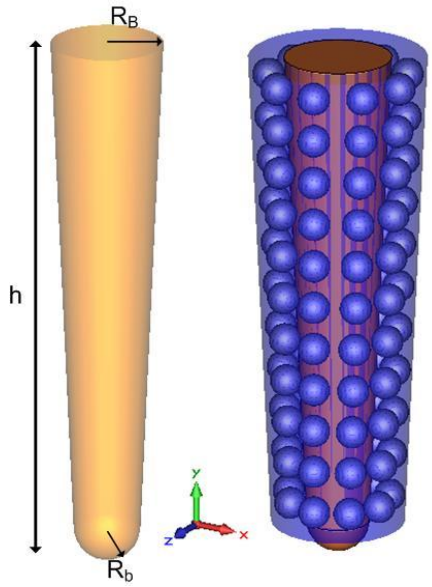

Fig. 73: Bare (left) and cloaked (right) cone. Geometrical parameters: $h = 484\ nm$, $R_B = 50\ nm$ and $R_b = 30\ nm$.

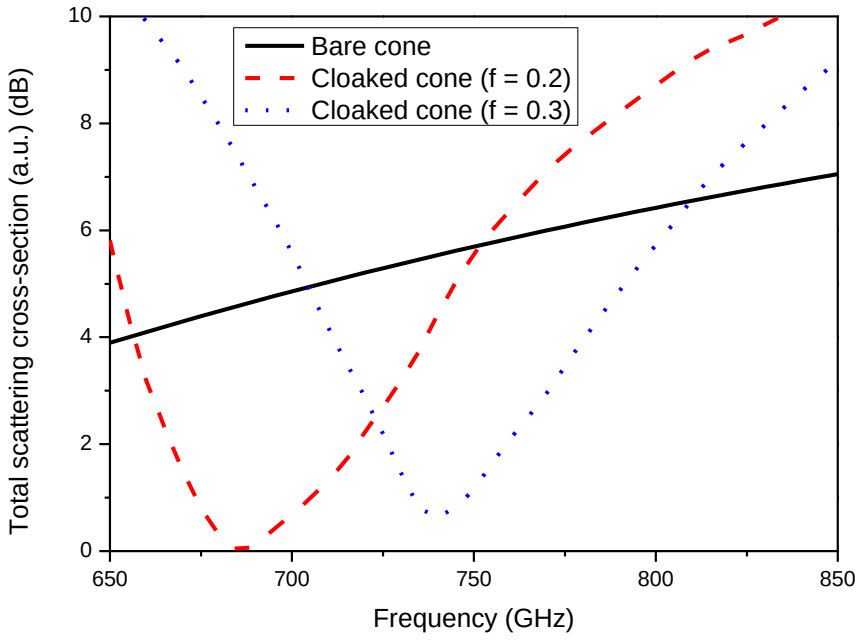

Fig. 74: Total scattering cross-section of the bare cone (black solid line) and of the cloaked one for different values of the volume filling fraction *f*.

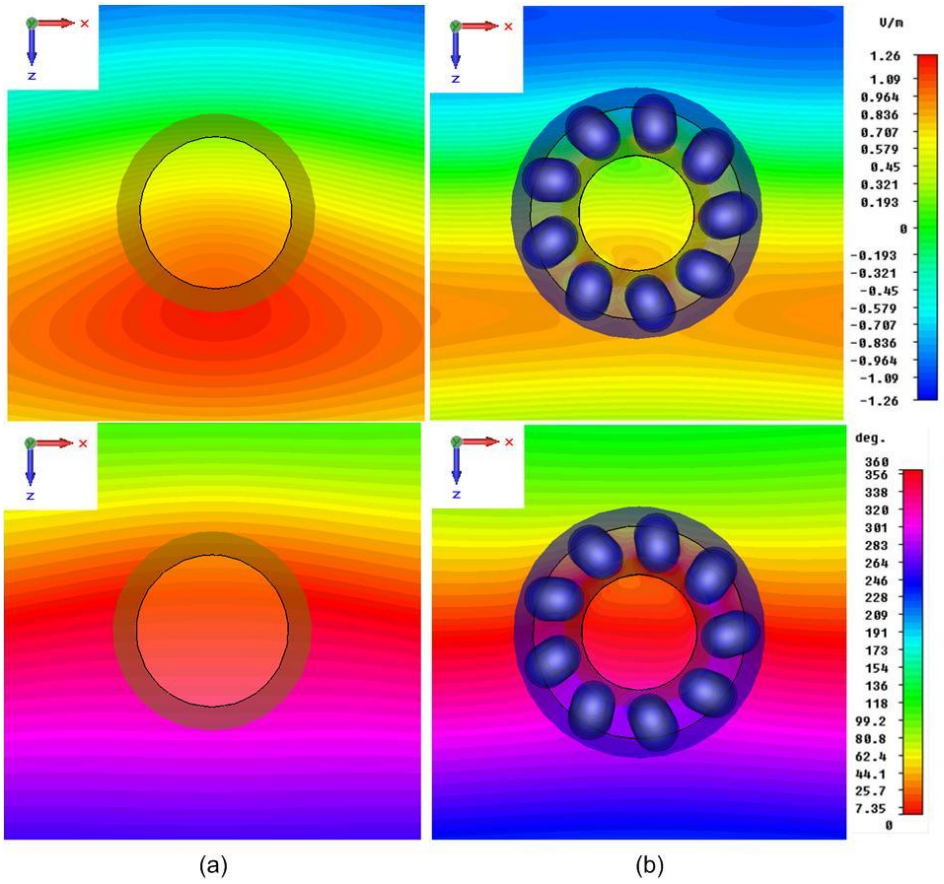

Fig. 75: Amplitude (up) and phase (down) distributions of *y*-component of the electric field for the cases of the bare (a) and cloaked cone (b). The plots show the field distribution at the cloak frequency of *740 THz* on a plane parallel to the *x*-*z* plane placed at the half height of the cone.

3.2 Optical mantle cloaking

As demonstrated in the previous Section, the use of a mixture of core-shell nanoparticles embedded into a dielectric matrix allows to achieve a scattering cancellation effect in the upper part of the optical spectrum. However, smaller silver shell would be required to lower the cloaking frequency below the blue-violet region, with consequent issues in fabrication and in the electromagnetic model used to describe silver and its increased losses. Moreover, the need of a dielectric matrix supporting the nanoparticles array may introduce additional complications in the experimental realization of the cloak. Therefore, the design of cloaking devices based on the scattering cancellation working within the optical range cannot be considered overcame with the findings described in the previous Section.

In this Section, I propose a novel 2D approach for the analysis and design of nanoparticle-based cloaking devices for optical frequencies, showing how this approach allows the design of optical broadband mantle cloaks with robust performance. First, I theoretically show that an array of nanoparticles can be properly modeled using a 2D metasurface model rather than a bulk homogenized material. Then, by integrating the 2D array model within the theoretical formulation of mantle cloaking, I prove that non-spherical nanoparticle arrays may dramatically relax the nanoparticle size requirements and achieve scattering cancellation within the whole visible frequency range. I prove the effectiveness of my approach by using spheroidal nanoparticles and also investigate the performance of simplified structures that may be easier to experimentally realize.

3.2.1 Optical metasurfaces

As described in the previous Chapter, mantle cloaking [44] is a scattering-cancellation cloaking approach based on the use of metasurfaces properly engineered to radiate an electromagnetic field combining out-of-phase with the one scattered by the object. The reference geometry that I consider in this work is shown in the inset of Fig. 1 and consists of a dielectric cylinder of infinite length and sub-wavelength radius surrounded by an ideal 2D reactive sheet modeled through its intrinsic surface reactance X_s $\left(\Omega / sq\right)$. The cloaking condition, for which it is possible to achieve a dramatic cancellation of the overall scattered field under TM plane-wave incidence (*i.e.*, electric field parallel to the cylinder axis), is the following [44]:

$$X_s^{ideal} = \frac{2}{\omega a \gamma \varepsilon_0 \left(\varepsilon_r - 1\right)}, \tag{3.5}$$

being ω the cloaking radial frequency, $\gamma = a / a_c$ the ratio between the radius of the cover a_c and the cylinder radius a, ε_r the relative electric permittivity of the material composing the cylinder and ε_0 the electric permittivity of the vacuum. From (3.5), it is evident that the cloaking surface reactance is inversely proportional to ε_r. Since at optical frequencies the permittivity of dielectric materials is generally quite low, the

required cloaking surface reactance is typically large. This is true also for different canonical geometries, such as the spherical one, as the reader can easily verify from the literature . As an example, I consider an infinite dielectric cylinder with radius $a = 50\ nm$ ($\lambda_0 / 10$ at 600 THz) made of silica (whose optical permittivity is equal to $\varepsilon_r = 2.1$) and covered by an ideal lossless reactive sheet with radius $a_c = 1.2 \times a$. In Fig. 76 I show the required surface reactance (3.5) to achieve cloaking within the range $[400 - 800]\ THz$. From the picture, it is evident that, in order to reach the cloaking condition, I need to design a metasurface exhibiting a strong inductive response within the whole visible frequency range. The slope of the required dispersion is negative, indicating that the condition can be met only over a limited range of frequencies for passive and linear surfaces, as dictated by Foster's reactance theorem.

In this Section I show that it is possible to implement a strongly inductive optical metasurface by using a 2D array of spheroidal plasmonic nanoparticles. At first, it is worth underlining that the possibility to model an array of spherical nanoparticles using a 2D surface impedance model has been recently discussed with reference to the realization of optical filters [46],[47]. Here I briefly revise and generalize this theory and check its effectiveness by using a retrieval model implemented into a full-wave simulator.

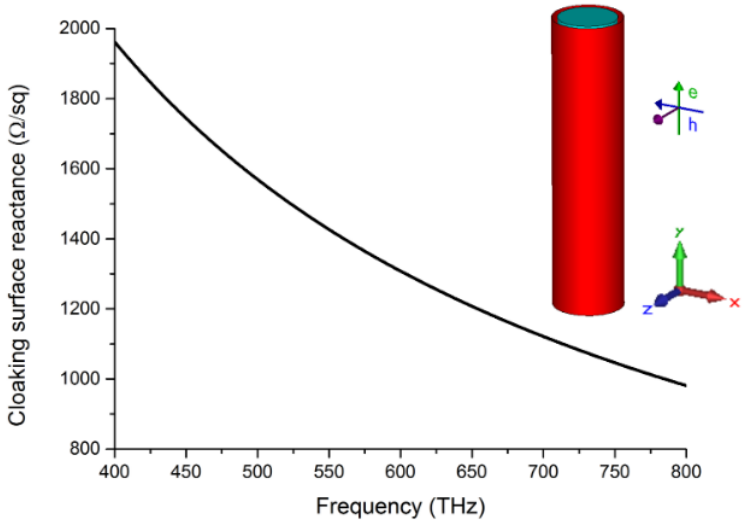

Fig. 76: Required surface reactance within the visible range, calculated using (1) for a cylinder of infinite length made of silica.

I consider an infinitively extended single layer of lossless plasmonic nanoparticles arranged in a square lattice, as shown in Fig. 77. The structure is illuminated by an external TM plane-wave and I assume that the dimensions of the nanoparticles as well as their separations are both much smaller than the operating wavelength. I do not make any assumption, instead, on the nanoparticle shape. It has been proven that this 2D structure exhibits a homogenized surface reactance given by [46]:

$$X_s = -\frac{d^2}{k}\left(\mathrm{Re}\left\{\alpha^{-1}\right\} - \mathrm{Re}\left\{\beta\right\}\right), \tag{3.6}$$

being d the cell size of the square lattice, $k = 2\pi / c$ the wavenumber of the medium hosting the nanoparticle array, α the polarizability of the individual nanoparticle and β the interaction constant among the nanoparticles.

The plasmonic material composing the nanoparticles can be modeled in the first instance using a lossless Drude model:

$$\varepsilon(\omega) = \varepsilon_a - \frac{(\varepsilon_b - \varepsilon_a)\omega_p^2}{\omega^2}, \tag{3.7}$$

where ε_a is the permittivity high-frequency limit, ε_b the static dielectric constant, and ω_p the plasma-frequency of the plasmonic material. As far as silver is concerned, these parameters are: $\varepsilon_a = 5.45$, $\varepsilon_b = 6.18$, and $\omega_p = 1.7\times10^6$ rad/s. It is worth noticing that I neglect losses in silver in this section only for modeling purposes. A more accurate model of the plasmonic material composing the nanoparticles, including intrinsic material losses and additional losses due to the size effect, will be discussed in the next Section in which full-wave simulations of the cloaking devices are presented. After some analytical manipulations, formula (3.6) can be expressed in the following closed form [46]

$$X_s = X^{latttice} + X^{NIA} \approx \frac{c}{4R_0\omega} + \frac{d^2}{V}\frac{\left[\varepsilon_h + L(\varepsilon_a - \varepsilon_h)\right]}{(\varepsilon_h - \varepsilon_a)}\frac{c}{\omega}\frac{\omega_1^2 - \omega^2}{\omega_2^2 - \omega^2}, \tag{3.8}$$

with

$$\omega_1 = \sqrt{\frac{L\left(\varepsilon_b - \varepsilon_a\right)}{\varepsilon_h + L\left(\varepsilon_a - \varepsilon_h\right)}}, \quad \omega_2 = \omega_p \sqrt{\frac{\varepsilon_b - \varepsilon_a}{\varepsilon_a - \varepsilon_h}}, \quad R_0 = \frac{d}{1.438}, \tag{3.9}$$

being L the depolarization factor of the nanoparticle, which depends on its geometry (*e.g.*, $L = 1/3$ for the case of spherical nanoparticles). The term $X^{lattice}$ in (3.8) represents the lattice contribution to the homogenized surface impedance, whereas the term X^{NIA} takes into account for the so-called nanoparticle-in-array impedance.

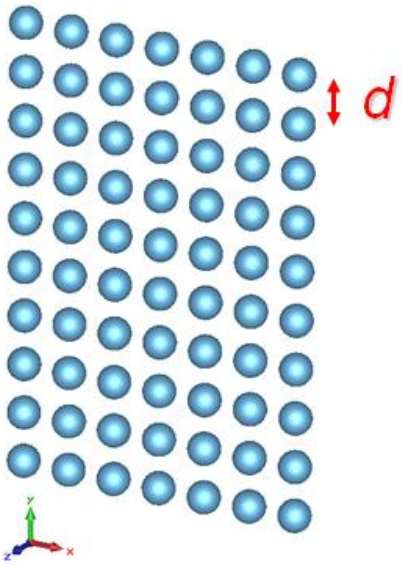

Fig. 77: Single layer of lossless plasmonic nanoparticles arranged in a squared lattice.

In order to check the effectiveness of this model, I have implemented a numerical retrieval procedure based on full-wave simulations. The unit cell of the array has been modeled in a full-wave simulator and two $\lambda/2$ transmission line segments have been introduced before and after the array unit cell, respectively. A picture of the unit cell implemented into the full-wave simulator and the relative circuital representation are shown in Fig. 78. Considering as reference plane the $x-y$ plane passing through the center of the nanosphere, the structure is excited with an external normally incident plane-wave with electric field parallel to the *y*-axis. Once the reflection coefficient Γ is

computed, it is easy to retrieve, frequency by frequency, the effective surface reactance X_s exhibited by the metasurface with the following inversion formula [48]:

$$Z_s = \frac{\eta_0(1+\Gamma)}{-2j\Gamma} = j\frac{\eta_0(1+\Gamma)}{2\Gamma} = jX_s. \tag{3.10}$$

As an example, I consider two arrays of silver nanoparticles with $a = 15\ nm$, $r = 5\ nm$, and $a = 15\ nm$, $r = 6\ nm$, respectively. In Fig. 79, I show the comparison between the surface impedances returned by the analytical model (3.8) and the ones retrieved using the full-wave procedure described above. Two important considerations arise: first, there is excellent agreement between the analytical model and full-wave results, confirming the capability of the 2D model to properly describe the macroscopic behavior of the nanoparticle array. Second, I may not achieve highly-inductive surface reactance values required for the cloaking of a silica cylinder with this geometry. From Fig. 79, it is clear that the array of silver nanoparticles is only able to provide capacitive values or, at most, small inductive values of its intrinsic surface reactance within the visible range. Even by increasing the radius of the spheres (*i.e.*, by reducing the separation distance between adjacent nanoparticles) up to the maximum value allowed by the geometry of the structure, it is not possible to reach the required inductive behavior within the visible range. Using spherical silver nanoparticles, scattering cancellation can be achieved only in the UV range, confirming the results in [26] that were reached using a different homogenization model.

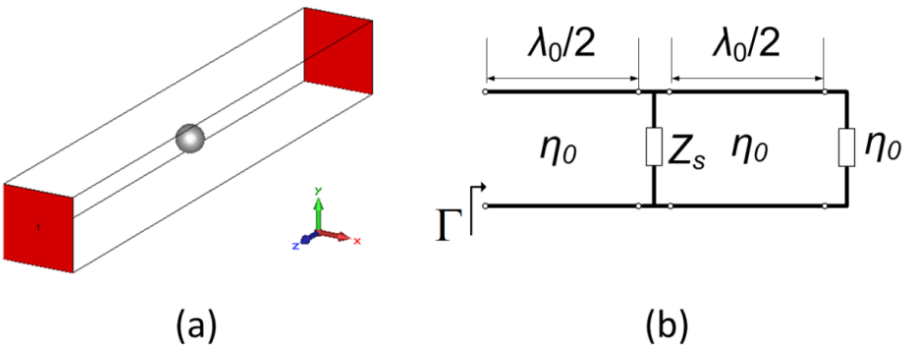

Fig. 78: (a) Unit cell of the optical metasurface implemented in a full-wave simulator; (b) Equivalent circuit model of the structure.

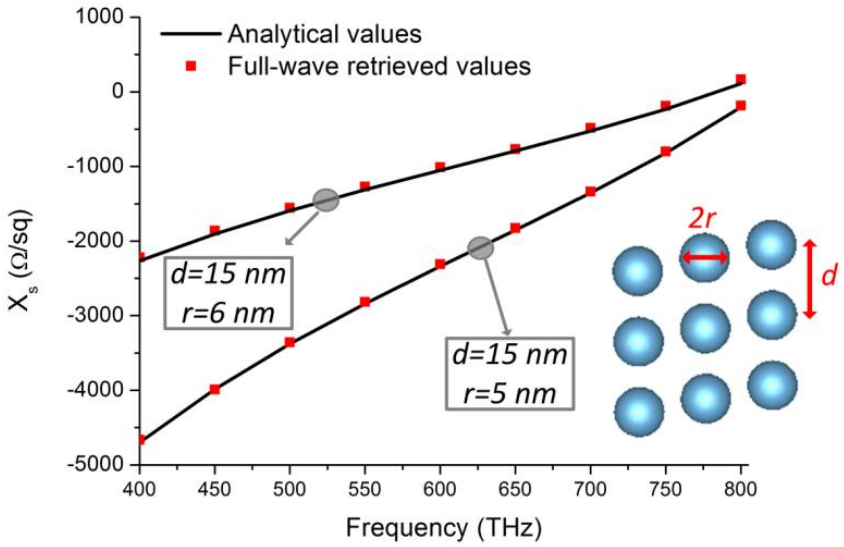

Fig. 79: Comparison between the retrieved values of surface reactance (red scatters) and the ones given by the 2D analytical model (continuous lines) for an array of silver spherical nanoparticles. In the inset the considered array of spherical nanoparticles is shown.

In order to explore the properties of different kinds of optical metasurfaces, I have extended the 2D model to the case of core-shell nanoparticles. A core-shell nanoparticle, depicted in the inset of Fig. 80, is composed by a dielectric core with radius r_2 and permittivity ε_{r2}, and a plasmonic shell with radius r_1 and permittivity ε_{r1}. The generalization of the 2D model to this case is straightforward and can be done by replacing in (3.6) the polarizability α of the nanoparticle with the one of a core-shell structure described in the previous Section:

$$\alpha = 3\varepsilon_m V \frac{(\varepsilon_{r1}-\varepsilon_m)(\varepsilon_{r2}+2\varepsilon_{r1})+\delta(2\varepsilon_{r1}+\varepsilon_m)(\varepsilon_{r2}-\varepsilon_{r1})}{(\varepsilon_{r1}+2\varepsilon_m)(\varepsilon_{r2}+2\varepsilon_{r1})+2\delta(\varepsilon_{r1}-\varepsilon_m)(\varepsilon_{r2}-\varepsilon_{r1})}, \tag{3.11}$$

being ε_m the permittivity of the host medium (vacuum, in our case), V the nanoparticle volume, and $\delta = r_2^3 / r_1^3$.

As an example, I consider an array of core-shell nanoparticles made of a silica core ($\varepsilon_{r2} = 2.1$ and $r_2 = 5\ nm$) and a silver shell with radius $r_1 = 10\ nm$ and permittivity given by the Drude model. The cell size of the square lattice is $d = 30\ nm$. Please note that the nanoparticle dimensions used for this example has been chosen in order to make the silver shell thickness equal to the radius of the first spherical nanoparticle case shown in

Fig. 79. The comparison between the analytical surface reactance values and the ones retrieved through full-wave simulations is shown in Fig. 80 (lower curve). As for the case of spherical nanoparticles, also for the core-shell structures our model is able to accurately describe the surface reactance exhibited by the metasurface. Moreover, it is clear in Fig. 80 that the core-shell nanoparticle array is able to exhibit an inductive surface impedance value comparable to the one required by our previous analysis. However, the inductive value is achieved only in the blue-violet region of the optical range confirming, once again, the results comented in the previous Section and obtained considering a 3D homogenization of the nanoparticle array. I note that, in order to achieve the inductive values of the surface reactance shown in Fig. 76 at lower frequencies, an extremely thin silver shell would be required, as can be appreciated by observing the upper curve depicted in Fig. 80, which refers to the case $r_1 = 10\ nm$ and $r_2 = 7\ nm$ (that corresponds to a $3\ nm$ thick silver shell). This reduction in the nanoparticle size may be responsible for both a dramatic increase in silver losses and theoretical issues in the modeling of the macroscopic properties of silver without considering quantum mechanical effects.

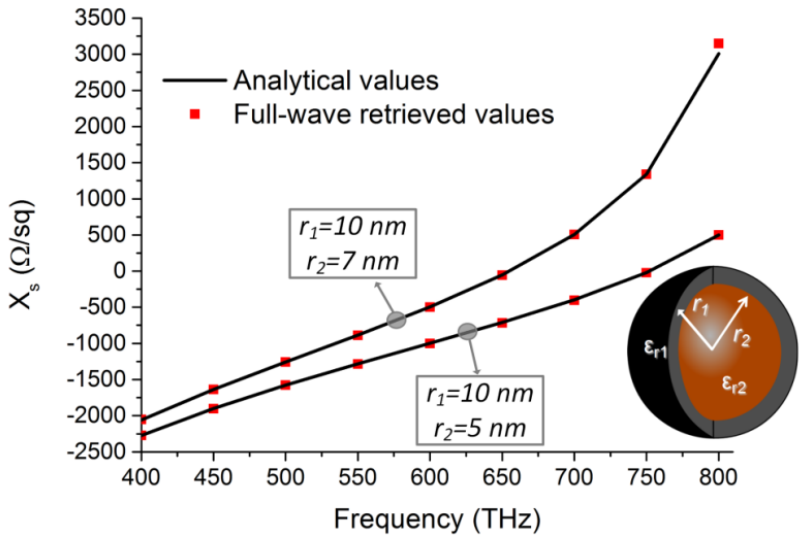

Fig. 80: Comparison between the retrieved values (red scatters) of the surface reactance values and the ones provided by the 2D analytical model (continuous lines) for two arrays of spherical core-shell nanoparticles. In the inset, it is shown a single core-shell nanoparticle.

The mentioned examples demonstrate that a method to increase the optical surface reactance of a 2D array of nanoparticles useful to obtain mantle cloaks working at visible

wavelengths is still missing. In this context, it is interesting to study the behavior of the optical surface reactance with respect to the nanoparticle geometry. Let us consider a prolate spheroid, as the one depicted in the inset of Fig. 81, with $r_y > r_x = r_z$. Due to the geometrical anisotropy of the nanoparticles, the scalar surface reactance needs to be replaced by a tensorial quantity. In fact, the depolarization factor is now a diagonal matrix, whose elements are given by the following expressions [49]:

$$L_x = L_z = \frac{1}{2}, \qquad L_y = \frac{1-e^2}{e^2}\left[-1+\frac{1}{2e}\ln\left(\frac{1+e}{1-e}\right)\right], \tag{3.12}$$

being *e* the nanoparticle eccentricity, whose expression is:

$$e = \sqrt{1-\left(\frac{r_x}{r_y}\right)^2}. \tag{3.13}$$

Since I am interested in cloaking an electrically thin cylinder, the main scattering contribution is expected for TM incidence, *i.e.*, with electric field parallel to the cylinder axis (see the inset of Fig. 76). Therefore, the only component of the surface reactance tensor I am interested in is the one directed along the *y*-axis (denoted with X_s^y). In Fig. 81, the behavior of at the center of the visible spectrum ($f_0 = 600\ THz$) for a 2D array of spheroidal nanoparticles as a function of the eccentricity *e* is shown. The limit $e \to 0$ corresponds to the spherical case previously described. From the picture, it is evident that it is possible to achieve the desired strong inductive values of the *y*-component of the surface reactance by using nanoparticles with high eccentricity, *i.e.*, characterized by a large ratio between r_y and r_x. This means that it is possible to increase the surface reactance of the nanoparticle array without reducing the nanoparticle size below a critical value. This is a key aspect that allows us to realize new scattering-cancellation cloaks able to provide dramatic invisibility effects within the whole visible range, as it will be clear in the next Section.

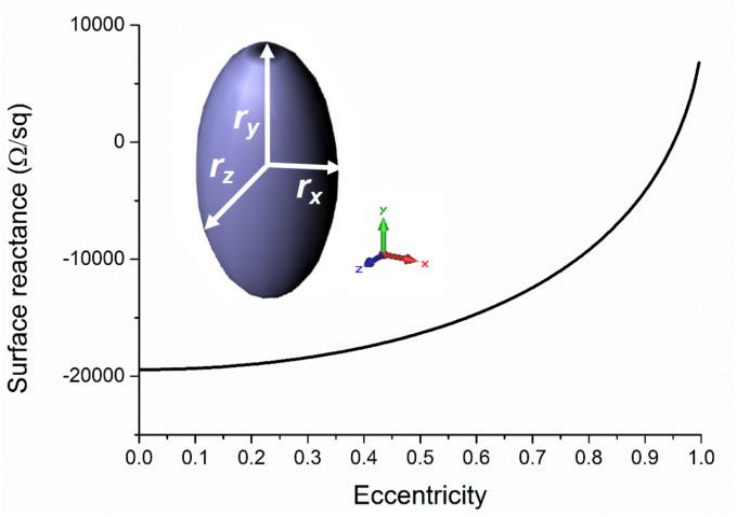

Fig. 81: *y*-component of the surface reactance at f_0 = 600 THz for an array of prolate spheroids as a function of the eccentricity of the nanoparticles. The limit case e = 0 corresponds to spherical nanoparticles.

3.2.2 Optical metasurfaces and mantle cloaking

In the previous Section, I have theoretically proven that the use of non-spherical plasmonic nanoparticles with high eccentricity allows to achieve the surface impedance values required by the mantle cloaking theory to hide an infinite dielectric cylinder. In this Section, I validate the model reporting the results of full-wave simulations for some cloaking structures.

In order to perform realistic full-wave simulations, I need first to replace the lossless Drude model with a more accurate model able to describe the dielectric function of silver for the individual nanoparticles. If the size of the nanoparticle is less than the electron mean free-path of the plasmonic material, the interband contribution to the dielectric function needs to be properly modified to take into account surface dispersion effects. In particular, the so-called size-corrected dielectric function for silver becomes also function of the nanoparticle size *r*, according to the following expression [50]:

$$\varepsilon(\omega,r)=1-\frac{\omega_p^2}{\omega\left(\omega-j\gamma(r)\right)}+\frac{f\,\omega_L^2}{\omega_L^2-\omega^2+j\Gamma_L\omega}, \tag{3.14}$$

with ω_p = 9.17 eV, ω_L = 5.27 eV, f = 2.1, Γ_L = 1.14 *eV* and:

$$\gamma(r) = \gamma_M + \gamma_{size}(r). \tag{3.15}$$

γ_M represents the macroscopic damping constant due to dispersion of the electrons by the ions of the system, whereas the term $\gamma_{size}(r)$ takes into account the contribution to the material losses provided by the finite-size of the nanoparticle. For a spherical nanoparticle, the expression of $\gamma_{size}(r)$ is equal to [49]-[52]:

$$\gamma_{size}(r) = A\frac{v_F}{r}, \tag{3.16}$$

where v_F is the silver Fermi velocity (v_F = 1.39×10^6 m/s) and A is a correction term introduced to fit the experimental data. Even though the value to be attributed to A is currently debated, for our scenario, represented by a spherical nanoparticle cluster deposited on a silica layer, it can be fixed to 0.6 [53].

The last step consists in the generalization of expressions (3.14)-(3.16) to the case of non-spherical nanoparticles. Since the chosen nanoparticles have spheroidal geometry, I can apply the superposition principle [54] and write three different expressions for (3.16) . This means that the dielectric function of silver for such nanoparticles becomes anisotropic and has the following expression:

$$\underline{\underline{\varepsilon}}(\omega, r) = \begin{bmatrix} \varepsilon_x(\omega, r) & 0 & 0 \\ 0 & \varepsilon_y(\omega, r) & 0 \\ 0 & 0 & \varepsilon_z(\omega, r) \end{bmatrix}, \tag{3.17}$$

where

$$\varepsilon_i(\omega, r_i) = 1 - \frac{\omega_p^2}{\omega(\omega - j\gamma(r_i))} + \frac{f\omega_L^2}{\omega_L^2 - \omega^2 + j\Gamma_L\omega}, \quad i = x, y, z. \tag{3.18}$$

To summarize, by introducing the surface dispersion effects in a spheroidal geometry, I need to replace the typical isotropic bulk permittivity of silver with the anisotropic

dielectric function (3.17). The anisotropy is a consequence of the different characteristic dimensions of the spheroidal nanoparticles with respect to the three coordinate axes. In Fig. 82, I report the real and imaginary parts of $\varepsilon_x(\omega,r_x)$ and $\varepsilon_y(\omega,r_x)$, respectively, and compare it to the measured bulk permittivity of silver [28]. The geometrical parameters of the nanoparticles used for this comparison are: $r_x = r_z = 5\ nm$ and $r_y = 20\ nm$ (*i.e.*, $e = 0.968$). $\varepsilon_z(\omega,r_x)$ is not reported here since it is equal to $\varepsilon_x(\omega,r_x)$, being $r_x = r_z$. It is evident that the imaginary part of the permittivity is strongly increased due to the finite-size effect, especially for the components ε_x and ε_z. This is an important aspect because losses may deteriorate the performance of cloaking devices.

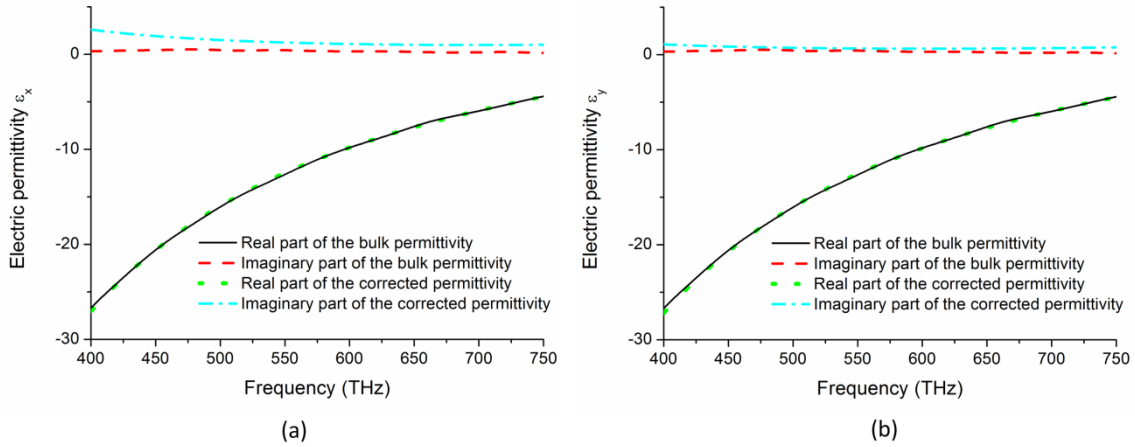

Fig. 82: Pictures (a) and (b) show, respectively, the real and imaginary parts of the *x*- and *y*-components of the silver electric permittivity for an elongated spheroidal nanoparticle taking into account the size-correction term. The corrected permittivity is compared to the bulk one presented in the literature [28].

By using model (3.8) in combination with expressions (3.12)-(3.13), it is now possible to design a realistic cover able to achieve the reactance values shown in Fig. 76 in the visible range. As an example, I consider three different covers that are designed to cloak a silica cylinder at $f_1 = 500\ THz$, $f_2 = 600\ THz$, and $f_3 = 700\ THz$, respectively. Once the separation between nanoparticles is fixed ($d = 60\ nm$), the geometrical parameters of the three covers resulting from the model are the following ones: (1) $r_x = r_z = 4.3\ nm$, $r_y = 28\ nm$ (eccentricity $e = 0.988$); (2) $r_x = r_z = 5.5\ nm$, $r_y = 25\ nm$ (eccentricity $e = 0.976$); (3) $r_x = r_z = 8\ nm$, $r_y = 21\ nm$ (eccentricity $e = 0.943$). The analytical values of the respective surface reactance are: (1) $X_s^y = 1450\ \Omega/sq$; (2) $X_s^y = 1290\ \Omega/sq$; (3) $X_s^y = 1146\ \Omega/sq$. The three covers, wrapped around the silica cylinder, are shown in the insets of Fig. 83 and the relative

performance in terms of total scattering cross section (SCS integrated over all the angles around the object) are shown in Fig. 83. The designed covers are able to dramatically reduce the total scattering of the silica cylinder within the visible frequency range, and the total SCS reduction can be quantified as 13 dB, 13 dB, and 8 dB, respectively. As expected, I observe a worsening in the cloak performance when increasing the cloaking frequency. This fact can be easily attributed to the increase of electrical size of the dielectric cylinder with frequency, and to the consequent increase in the number of scattering modes excited by the cylinder and involved in the scattering phenomena. As it is well-known from the first Chapter, the use of single layer cloaks is typically able to cancel the first scattering mode, which dominates the scattering as far as the cylinder radius is less than $\lambda_0/10$ (corresponding to the frequency $f_2 = 600\ THz$).

I stress here the fact that I achieved a strong cloaking effect in the middle of the visible range (around $f_2 = 600\ THz$) by using nanoparticles whose smallest size is equal to the one used to demonstrate cloaking effects in the UV range with spherical nanoparticles [26]. As clarified in the previous Subsection, this possibility has been enabled by the eccentricity of the nanoparticles used to implement the cloak.

It is worth noticing that the actual cloaking frequencies are slightly different with respect to the design ones. There are many reasons that can explain this minor disagreement: first, I note that the model (3.8) has been developed for a lossless plasmonic material described by the Drude model (3.7). Losses, which have been introduce in the full-wave simulations for a realistic description of the nanoparticles, slightly modify the value of the real part of the dielectric function with a consequent shift in the actual cloaking frequency. In addition, the analytical model has been developed for a planar layer of nanoparticles. Since the nanoparticle array needs to be wrapped around the cylinder to realize the conformal mantle cloak, the curvature is responsible for a change in the actual value of the surface reactance provided by the structure. Finally, the nanoparticle model does not take into account the presence of a dielectric substrate that, in our case, is represented by the cylinder over which the nanoparticles are deposited. Even though a further generalization of the model to take into account some of these effects can be performed, and it is in my plan for the future, its practical utility does not justify the effort. In fact, the shift in the cloaking frequency is

limited to a perceptual error of (10 % or less) and it can be quickly compensated with a full-wave numerical optimization.

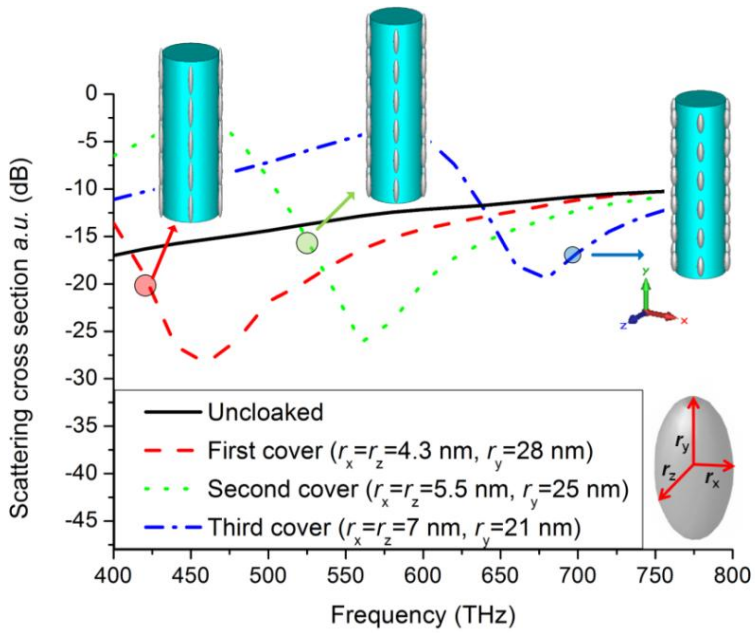

Fig. 83: Performance of the three nanoparticle-based cloaks in terms of minimization of the total scattering cross section.

In Fig. 84, I show the total extinction cross sections (ECS), *i.e.*, the sum between total absorption cross section and the total scattering cross section, of the uncloaked cylinder and of the cloaked ones. For all the designed devices, the extinction cross section at the cloaking frequency is reduced because of the presence of the cover even though, due to losses, the ECS reduction is lower compared to the SCS one. As already clarified in the introduction, for objects with sub-wavelength electrical size, the optical visibility is mainly due to scattering effects rather than to absorption ones [55]. Therefore, the designed covers are indeed able to dramatically reduce the object visibility within the cloaking frequency band. This is confirmed by the results shown in Fig. 85, in which amplitude and phase of the electric field in the uncloaked and cloaked cases for the second designed cloak at 560 *THz* are compared. The restoration of the planar phase fronts achieved in the cloaked structure justifies the effort of designing scattering-cancellation cloaks even though the reduction in the total ECS is not as strong as the SCS one. In the next Subsection I introduce another kind of cloaking structure able to provide a dramatic reduction of both SCS and ACS.

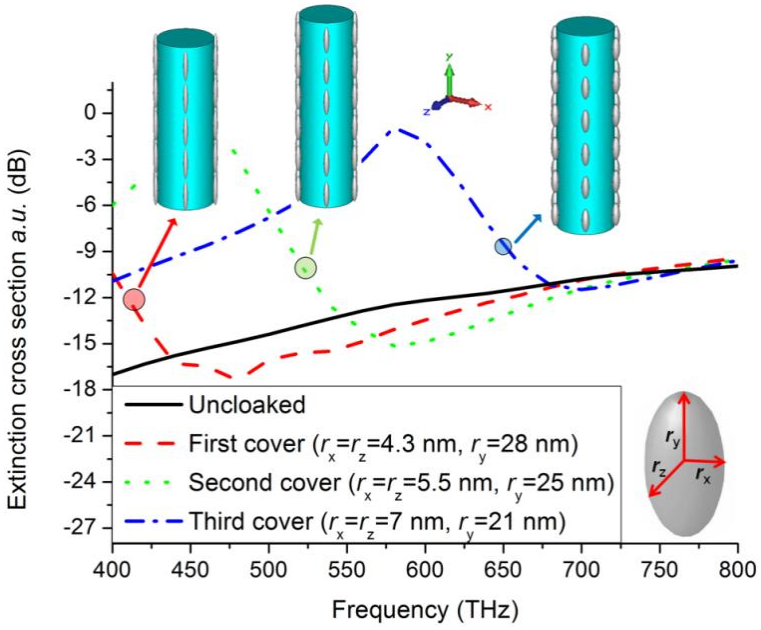

Fig. 84: Performance of the three designed cloaks in terms of minimization of the total extinction cross section.

Before concluding this Section, I investigate the robustness of the cloak performance towards the alignment tolerances expected in practical implementations. For this purpose, I have considered the second structure shown in Fig. 83 whose unit cell is composed by a 360 *nm* long silica cylinder surrounded by 36 ellipsoidal nanoparticles. The nanoparticles have been randomly split into 6 different subsets. The nanoparticles belonging to the first two subsets have been rotated along the *y*-axis by an arc corresponding to a geometrical quantity $\pm\Delta$, respectively. The elements of the third and fourth subsets have been rotated by an arc corresponding to $\pm 1.5\Delta$, respectively. Finally, the elements of the last two subsets have been first rotated by an arc corresponding to $\pm 3\Delta$ and, then, translated by a quantity $\pm\Delta$ along the *y*-axis. The cloak performance for different values of Δ is shown in Fig. 86. As it can be appreciated, the designed cloak is able to properly operate independently from the nanoparticles placement as far as the homogenization requirements are satisfied. These results strongly relax the experimental constraints in view of a fabrication of the proposed devices.

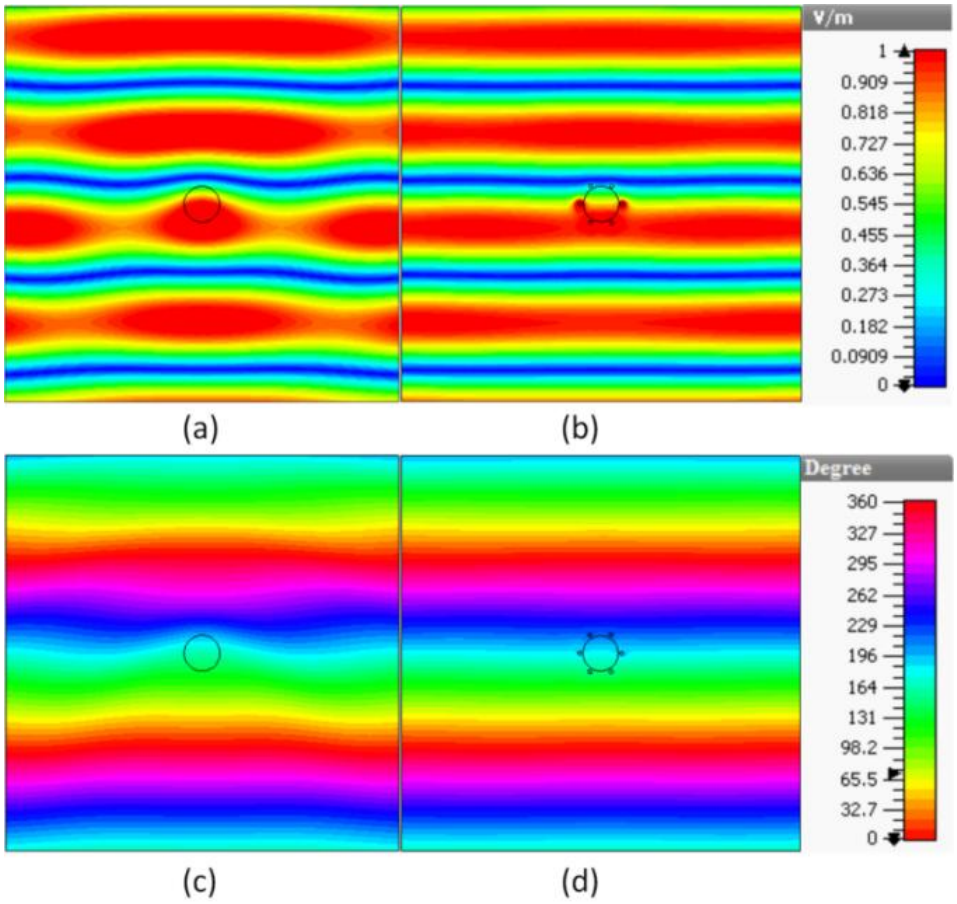

Fig. 85: (a)-(b) Amplitude of the electric field on a plane orthogonal to the cylinder axis and passing through its centre in the uncloaked and cloaked case, respectively; (c)-(d) Phase pattern of the y-component of the electric field on the same plane in the uncloaked and cloaked case.

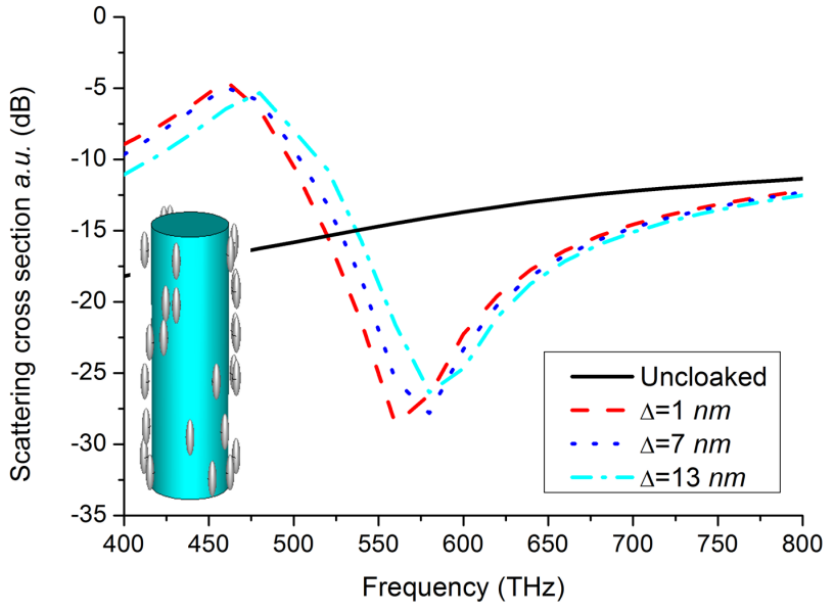

Fig. 86: Performance of the second nanoparticle-based cloak towards the alignment tolerances. In the inset, it is shown the structure for the case Δ=13 *nm*.

3.2.3 Mantle cloaking with nanorods

The structures described in the previous Subsection prove that it is possible to exploit the nanoparticle eccentricity to achieve cloaking effects in the visible using nanoparticles with non-critical size. However, their experimental realization could be rather cumbersome due to the geometry of the individual nanoparticle, as well as to the need of a spacer between the coated cylinder and the nanoparticle array.

Therefore, in this Subsection, I explore the possibility of achieving similar cloaking effects using simplified structures made of silver nanorods with square base directly deposited on the cylinder. Such structures exhibit a strong eccentricity, and may be easier to realize. The cloaking conditions are now different compared to the one depicted in Fig. 76, due to the change of cover radius, but it can be easily verified that strongly inductive surface reactance values are anyway required. A sketch of the cylinder coated with nanorods is shown in Fig. 87. I performed several simulations for different values of the side of the nanorods $2w$. The corresponding results for both total SCS and ECS are shown in Fig. 87 and Fig. 88. The strong eccentricity of the nanorods (ideally $e = 1$ for a cylinder of infinite length) allows to achieve the cloaking requirements. Moreover, since the rod is elongated in the y direction, the electric permittivity $\varepsilon_y(\omega)$ in the direction of applied electric field is not affected by the surface effect, and losses are lower compared to the case of spheroidal nanoparticles. These properties are confirmed by the large cloaking effects demonstrated within the whole visible range using nanorods with non-critical dimensions (the reduction of total SCS equals 23 *dB*, 18 *dB*, and 14 *dB* at 500 *THz*, 620 *THz*, and 700 *THz*, respectively).

Due to the strong SCS reduction and to the lower losses of silver nanorods, also the total ECS of all three cloaked structures is dramatically reduced (10 *dB*, 9 *dB* and 6.2 *dB*, respectively). In other words, the increase in absorption provided by the nanoparticle cover is here rather low compared to the SCS reduction resulting in actual cloaking effects within the visible frequency range. In Fig. 89 and Fig. 90, I show the 3D SCS pattern at $620\ THz$ in the uncloaked and cloaked cases, respectively, for $2w = 14\ nm$. In order to appreciate the cloaking effect, the different scale between the two plots should be noted.

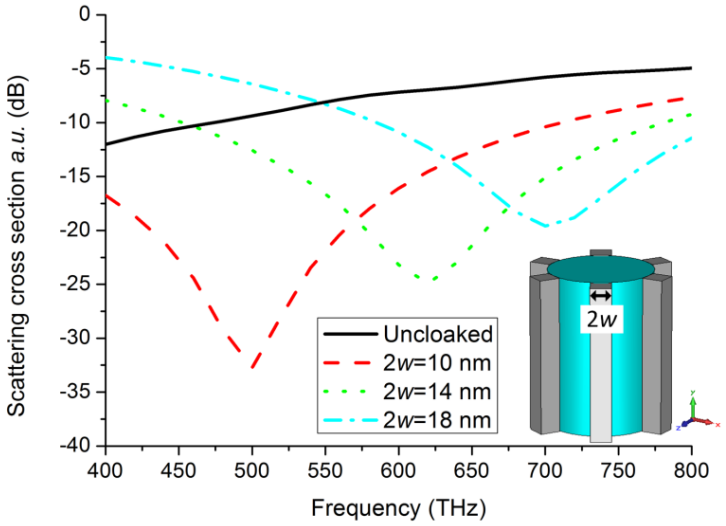

Fig. 87: Total SCS of the cylinder surrounded by the nanorods for different values of the rod side.

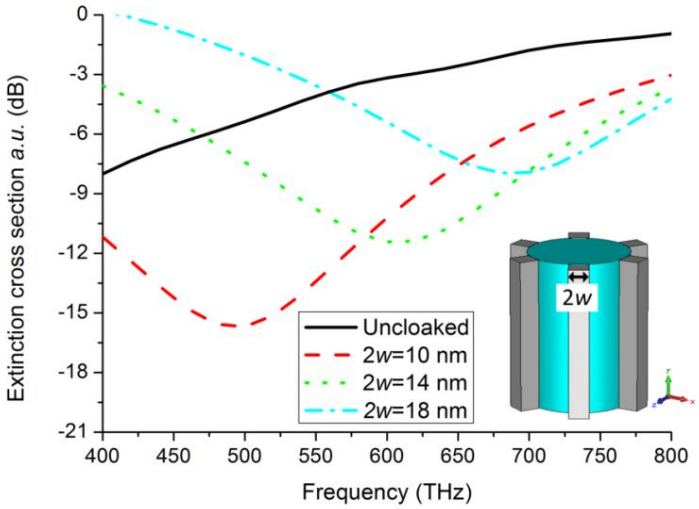

Fig. 88: Total ECS of the cylinder surrounded by the nanorods for different values of the rod side.

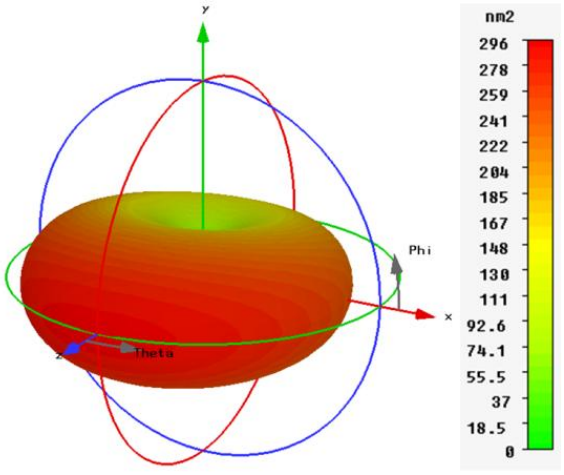

Fig. 89: 3D SCS pattern at 620 THz in the uncloaked case. The SCS is expressed in nm^2.

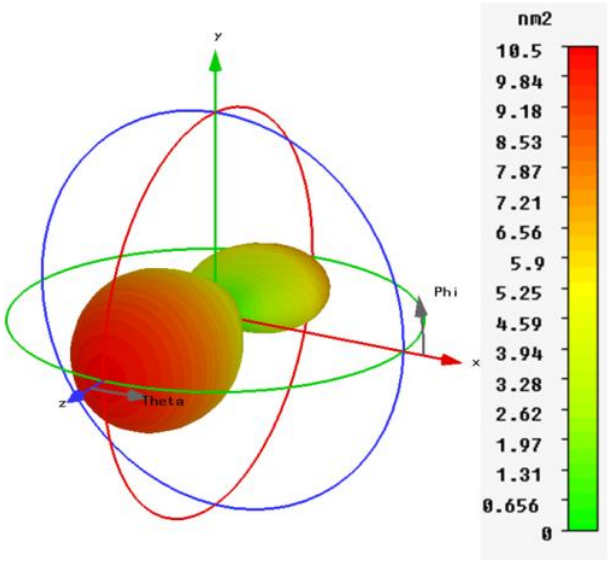

Fig. 90: 3D SCS pattern at 620 THz in the cloaked case for the cloaking devices with . The SCS is expressed in nm^2.

I conclude observing that the structures described in this Section remind, in a certain way, the plasmonic satellites appeared in the early cloaking literature [56]. In that case, the idea of using antiphase discrete scatterers along a cylinder has been theoretically investigated, and cloaking conditions for the real part of the scatterer permittivity have been derived. In our case, on the contrary, I design these structures based on their average surface impedance, suggesting a practical implementation with realistic materials working at optical frequencies. The proposed approach, therefore, allows interpreting the plasmonic satellite approach, as long as they are dense enough to be homogenized into a surface, as a particular case of mantle cloaking.

3.3 References

[1] A. Alù, N. Engheta, A. Ersentok, R.W. Ziolkowski, *IEEE Antennas Propag. Mag.*, vol. 49, 23, 2007.

[2] A. Alù, M.G. Silveirinha, A. Salandrino, N. Engheta, *Phys. Rev. B*, vol. 75, 155410, 2007.

[3] R.W. Ziolkowski, *Phys. Rev.* E 70, 046608 (2004).

[4] S. Enoch, G. Tayeb, P. Sabouroux, N. Guerin, P. A. Vincent, *Phys. Rev. Lett*. 89, 213902 (2002).

[5] N. Engheta, *Sci*. 317, 1698 (2007).

[6] M.G. Silveirinha, N. Engheta, *Phys. Rev. B* 76, 245109 (2007).

[7] A. Alù, F. Bilotti, N. Engheta, L. Vegni, *IEEE Trans. Antennas Propagat*. 54, 1632 (2006).

[8] M. Silveirinha, N. Engheta, *Phys. Rev. Lett*. 97, 157403 (2006).

[9] B. Edwards, A. Alù, M. Young, M. Silveirinha, N. Engheta, *Phys. Rev. Lett*. 100, 033903 (2008).

[10] R. Liu, Q. Cheng, T. Hand, J. J. Mock, T. J. Cui, S. A. Cummer, and D. R. Smith, *Phys. Rev. Lett*. 100, 023903 (2008).

[11] M. Navarro-Cía, M. Beruete, M. Sorolla, N. Engheta, *IEEE AP-S Int. Symp*. (2011).

[12] M. Navarro-Cía, M. Beruete, I. Campillo, M. Sorolla, *Phys. Rev. B* 83, 115112 (2011).

[13] F. Bilotti, S. Tricarico, L. Vegni, *New J. Phys*. 10, 115035 (2008).

[14] F. Bilotti, S. Tricarico, L. Vegni, *IEEE Trans. Nanotech*. 9, 55 (2010).

[15] S. Tricarico, F. Bilotti, A. Alù, L. Vegni, *Phys. Rev. E* 81, 026602 (2010).

[16] A. Alù, N. Engheta, *Phys. Rev. Lett*. 102, 233901 (2009).

[17] A. Alù, N. Engheta, *Metamaterials* 4, 153 (2010).

[18] A. Alù, N. Engheta, *Phys. Rev. Lett.* 105, 263906 (2010).

[19] F. Bilotti, S. Tricarico, F. Pierini, L. Vegni, *Opt. Lett.* 36, 211 (2011).

[20] F. Bilotti, F. Pierini, L. Vegni, *Metamaterials* 5, 119 (2011).

[21] M. Silveirinha, N. Engheta, *Phys. Rev. B* 75, 075119 (2007).

[22] W.G. Spitzer, D. Kleinman, D. Walsh, *Phys. Rev. Lett.* 113, 127 (1959).

[23] M.G. Silveirinha, A. Alù, N. Engheta, *Phys. Rev. B* 78, 075107 (2008).

[24] S.M. Rytov, Sov. *Phys.—JETP* 2, 466 (1955).

[25] B.Wood, J.B. Pendry, D.P. Tsai, *Phys. Rev. B* 74, 115116 (2006).

[26] S. Mühlig, M. Farhat, C. Rockstuhl, F. Lederer, *Phys. Rev. B* 83, 195116 (2011).

[27] J.C. Maxwell-Garnett, *Phil. Trans. Soc*. 203, 385 (1904).

[28] P.B. Johnson, R. W. Christy, *Phys. Rev. B* 6, 4370 (1972).

[29] T.G. Mackay, *J. Nanophotonics* 2, 029503 (2008).

[30] E. Prodan, C. Radloff, N. J. Halas, P. Nordlander, *Sci*. 302, 419 (2003).

[31] A. Sihvola, Progr, *Electromag. Res*. 66, 191 (2006).

[32] A. Sihvola, Subsurf. *Sensing Technol. Appl*. 1, 393 (2000).

[33] X.-X. Liu, A. Alù, *Metamaterials* 5, 56 (2011).

[44] A. Alù, *Phys. Rev. B* **80**, 24115 (2009).

[45] P. Y. Chen and A. Alù, *Phys. Rev. B* **84**, 205110 (2011).

[46] C. Saeidi and D. van der Weide, *Opt. Expr*. **21**, 16170 (2013).

[47] C. Saeidi and D. van der Weide, *Opt. Expr*. **22**, 12499 (2014).

[48] A. Alù and N. Engheta, "Optical Wave Interaction with Two-Dimensional Arrays of Plasmonic Nanoparticles," in *Structured Surfaces as Optical Metamaterials*, A. A. Maradudin, ed. Cambridge University Press, Ch. 3 (2011).

[49] C. Noguez, *J. Phys. Chem*. C **111**, 3806 (2007).

[50] V. P. Drachev, U. K. Chettiar, A. V. Kildishev, H.-K. Yuan, W. Cai, and V. M. Shalaev, *Opt. Expr.* **16**, 1186 (2008).

[51] C. Noguez, *Opt. Mat*. **27**, 1204 (2005).

[52] N. I. Grigorchuk and P. M. Tomchuk, *Phys. Rev. B* **84**, 085448 (2011).

[53] A. Hilger, M. Tenfelde, and U. Kreibig, *Appl. Phys. B* **73**, 361 (2001).

[54] W. A. Kraus and G. C. Schatz, *J. Chem. Phys*. **79**, 6130 (1983).

[55] S. Mühlig, A. Cunningham, J. Dintinger, M. Farhat, S. B. Hasan, T. Scharf, T. Bürgi, F. Lederer, and C. Rockstuhl, arXiv 1310.5888 (2013).

[56] M. G. Silveirinha, A. Alù, and N. Engheta, *Phys. Rev. B* **78**, 205109 (2008).

4 Other research activities

In this Chapter, I discuss some of the results ([J06]-[J07], [C04]-[C05], [C18], [C20]-[C22]) that I have obtained in research areas different to the cloaking science. First, I focus my attention on the design of actively loaded magnetic inclusions by investigating the use of non-Foster active elements to increase the operation bandwidth of a split-ring resonator (SRR). In particular, I design the circuit topology of the active load required to compensate the intrinsic reactance of the SRR and get a broadband response. Then, I show that the same procedure can be successfully applied to the case of a SRR-based monopole antenna and, in principle, to any metamaterial-inspired device employing SRRs. Finally, integrating an electromagnetic and a circuit simulator, I propose a possible realistic implementation of the active load, based on the employment of commercially available circuit elements. The obtained results (seven times improvement of the impedance bandwidth of the SRR-based monopole antenna) prove that non-Foster active loads can be successfully used to overcome the inherent narrow-band operation of SRR-based passive metamaterials and metamaterial-inspired components. The implementation issues related to circuit element dispersion, parasitic effects, and stability of the active circuit are fully considered in the proposed design.

Secondly, I propose a simple and low-cost technique for realizing resistive sheets. This approach, requiring only easy-to-find and inexpensive materials, consists in the deposition of graphite powder on ultrathin plastic sheet substrates. By controlling the deposition time and the mass of the deposited powder, I show that it is possible to realize resistive sheets exhibiting a desired surface resistance in a wide range of values. The proposed procedure is validated by means of both DC characterization and waveguide measurements that are in excellent agreement with the full-wave simulations.

4.1 Design of broadband actively loaded MTM-inspired components

Metamaterials (MTMs) represent a recent and ever growing research field in electromagnetics [1]-[3]. A MTM can be defined as an artificial engineered material, whose electromagnetic properties are not available in nature at the frequencies of interest.

In this Section, I focus my attention on the split ring resonator (SRR), which is a miniaturized inclusion useful to obtain artificial magnetism at microwave frequencies [4]. Exploiting its geometrical features, the resonant dimensions of the SRR are usually of the order of $\lambda/10$. Several different magnetic inclusions have been introduced to achieve a higher degree of miniaturization, remove the inherent bi-anisotropy characterizing the electromagnetic behavior of the SRR or obtain an isotropic response [4]-[9]. Tunable inclusions loaded with active elements have been also proposed [10]-[11]. Besides these modeling efforts, several innovative components and devices based on artificial magnetic materials have been proposed [12]-[21].

However, artificial magnetic materials exhibit some intrinsic limitations. Due to energy considerations, in fact, any passive MTM is necessarily a dispersive medium [22], meaning that the desired values of the electromagnetic parameters are typically reached only in a narrow frequency range and, consequently, the operation bandwidth of MTM-based components is limited. Moreover, as it is clear from Kramers-Kronig causality relationships, the dispersion phenomenon is always related to loss mechanisms [22] that further reduce the potentials of the designed MTMs.

Nevertheless, as shown in [23], it is in principle possible to widen the operation bandwidth of a passive MTM by loading it with an active circuit. In particular, in [23] a short dipole (or a small loop) antenna loaded with an ideal two-port electronic circuit has been considered and it has been shown that, in order to get negative and frequency-independent values of the permittivity (or permeability), it is necessary to use a negative capacitance (or inductance). In [23] it has been also suggested that this kind of reactive elements can be obtained using negative impedance converters (NICs), i.e. two-port

devices exhibiting at the input port an impedance that is the opposite of the load one [24].

This class of active circuits, violating Foster's theorem [25], has been introduced in the last century to compensate resistive losses [26] and their first transistor-based implementations are due to Linvill [27]. Recently, due to their unique and interesting properties, NIC circuits have been extensively applied to widen the operational bandwidth of electromagnetic components. For instance, as far as antennas are concerned, NICs have been used to design active external matching networks for both microstrip [28] and electrically small dipole/monopole/loop antennas [29]-[31] able to overcome Bode-Fano criterion, while a different conceptual approach, based on internal non-Foster matching circuits, has been proposed in [32]-[33]. Moreover, NICs have been used to synthesize ultra-wideband artificial magnetic conductors (AMCs) and electromagnetic band gap structures [34] and superluminal waveguides for broadband leaky-wave antennas [35]-[36].

In the last few years, some groups have focused their efforts to investigate the possibility of using NICs to overcome the limitations of passive MTMs. In particular, non-Foster elements have been used to increase the bandwidth of several types of broadband and electrically small MTM-inspired antennas [37]-[40] and to obtain an almost dispersionless epsilon-near-zero MTM, useful for cloaking applications [41]-[42]. Finally, in [43] an active broadband effective MTM has been proposed.

It is important to observe that, despite the potentials of such NIC circuits, their practical use is still limited, due to the fact that the design and the proper use of a NIC is not a trivial task. One of the main issues concerns the theoretical evaluation of the NIC stability [22] and the related technological aspects. As clarified in [44], where several circuits including negative lumped elements have been investigated, in fact, the correct evaluation of the stability depends also on the evaluation approach used and the uncritical use of classical stability methods may result in assessment mistakes.

In this work, inspired by the aforementioned papers, I propose to load a SRR with a proper NIC-based active circuit, in order to increase its operation bandwidth and make it useful for the application in broadband MTM-inspired components. In order to show the potentials of the proposed broadband SRR, I analyze the performance improvement of

the SRR-based antenna presented in [45], suitably scaled to work within the RF band, where NIC implementation is not critical by using discrete circuit elements.

4.1.1 Design of a broadband split-ring-resonator (SRR)

Magnetic MTMs at microwave frequencies are typically realized with metallic resonant inclusions embedded in a host material. The most common inclusion used to obtain a magnetic response is the SRR. A squared SRR consists of two concentric metallic rings with gaps at two opposite sides (Fig. 91 (a)). Due to the electrically small dimensions of the structure, it is possible to study its electromagnetic behaviour using a quasi-static approach [5]. Following this concept, and considering a magnetic excitation, a possible and quite accurate model of the SRR is given by an equivalent parallel *LC* lumped circuit. The angular resonant frequency ω_0 of the SRR, thus, can be expressed as:

$$\omega_0 = \frac{1}{\sqrt{LC}}, \tag{3.19}$$

where *L* and *C* are related to the geometrical dimensions of the SRR [6]. By definition, at the resonant frequency of the LC parallel circuit susceptance is zero. However, due to the high electromagnetic energy storage in proximity of the resonator, susceptance remains close to zero only in a very narrow frequency range around ω_0. The consequence of this phenomenon is the strong dispersive behaviour of the SRR, resulting in its narrow operation bandwidth.

On the basis of this consideration, it is easy to understand that a simple way to broaden the bandwidth of the SRR is to compensate its intrinsic susceptance by loading the inclusion with a proper circuit, whose susceptance is, for each frequency, the opposite of the SRR one. In this way, the overall susceptance of the loaded SRR becomes zero in a large frequency range around the resonant frequency.

In order to determine the load impedance required to satisfy the previous condition, I have theoretically loaded the SRR with an ideal impedance Z_L. Clearly, the circuit design

depends on where the non-Foster load is placed. For the sake of simplicity, I have decided to place it across the gap of the external ring (see Fig. 1(a)). In circuital terms, such physical connection corresponds to connect the ideal load in parallel to the *LC* equivalent circuit modeling the SRR (Fig. 91(b)). Under these assumptions, the overall admittance of the loaded resonator can be written as:

$$Y_{tot} = -j\frac{Z_L + j\omega L - \omega^2 LCZ_L}{\omega L Z_L}. \tag{3.20}$$

Imposing the cancellation of Y_{tot}, from (2) I obtain:

$$Z_L = j\frac{\omega L}{\omega^2 LC - 1}, \tag{3.21}$$

that can be expressed in admittance form as:

$$Y_L = -j\frac{\omega^2 LC - 1}{\omega L} = -j\omega C + j\frac{1}{\omega L}. \tag{3.22}$$

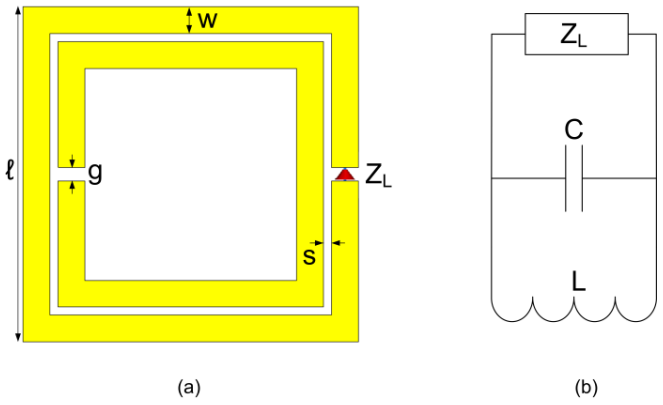

Fig. 91: (a) Geometry of a SRR loaded with an arbitrary impedance ZL and (b) its lumped element equivalent circuit representation.

Thus, the ideal load to be used to compensate the SRR reactance is a parallel combination of a negative inductance and a negative capacitance, whose values are equal, but opposite, to those of the lumped equivalent circuit of the SRR. Negative

reactive elements exhibit a negative slope of the reactance versus frequency. Therefore, a circuit with such features violates Foster's theorem [25] and cannot be a passive one [23].

As a first approximation, one can estimate the values of *L* and *C* from the geometry of the SRR. In the open technical literature, there are several analytical expressions [4]-[7] that allow deriving the values of *L* and *C* (and, then, of the resonant frequency of the resonator) from the SRR geometry. However, after a first set of simulations, I noticed that the desired bandwidth enhancement effect is rather sensitive to the circuital values of the load, and that better results can be obtained determining the required *L* and *C* values through full-wave numerical simulations.

For this purpose, I have simulated the behavior of a rectangular SRR employing CST Microwave Studio [46], a full-wave commercial software based on the finite integration technique. The simulated structure consists of a two-port ideal waveguide with a SRR placed in its center. The waveguide walls have been realized using perfect electric conductor (PEC) and perfect magnetic conductor (PMC) boundary conditions, so that the SRR is excited by a TEM mode, whose magnetic field is parallel to the axis of the SRR. I note here that waveguide dimensions have been chosen in such a way that the mutual coupling between SRR replicas due the boundary conditions is negligible and, thus, the results are the same as for a single SRR under an ideal TEM excitation. The magnitude of the S_{11} parameter in the case of an unloaded SRR with geometric dimensions (in mm) $\ell = 5,\ g = 0.2,\ w = 0.4,\ s = 0.12,$ is shown in Fig. 92 (solid line). As expected, in a narrow frequency band around the resonant frequency of the SRR most of the incoming signal is reflected back at the input port.

In order to obtain the loading element values to compensate the intrinsic reactance of the SRR and improve the bandwidth performance, I have followed the procedure described in [32] and [37]. In CST Microwave Studio, the SRR has been loaded with a discrete port placed in the gap of its external ring. The gap can be replaced by an arbitrary circuit (in our case a simple test capacitance C_{test}) designed in CST Design Studio, that is a schematic design tool directly interfaced to CST Microwave Studio. By changing the test capacitance value, the SRR resonates at different frequencies, as shown in Fig. 93. Please note that the same plot could be obtained by adding a lumped element in the gap of the SRR and performing a parametric sweep in CST Microwave Studio with

respect to the capacitance value. With our method, however, after the first full-wave microwave analysis, it is possible to realize the same sweep directly in CST Design Studio that, being a circuital tool, allows a dramatic simulation time saving.

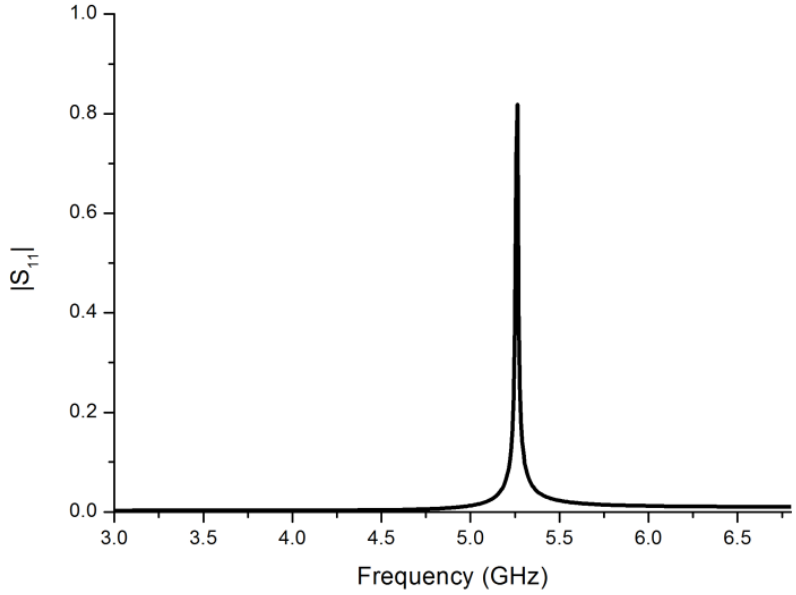

Fig. 92: Magnitude of the S_{11} parameter of the unloaded SRR.

If I plot the values of the loading reactance as a function of the corresponding resonant frequencies (triangular symbols in), it is possible to retrieve point-by-point the non-Foster reactance compensating the intrinsic reactance of the SRR. In fact, if the reactance curve of the loading circuit passes through the points that describe the relationship between the SRR resonant frequency and the corresponding test loading capacitance, the SRR resonates over a wide frequency band. Assuming to load the SRR with a *LC* tank circuit (see the conclusions of the analytical analysis reported in the previous Section) and imposing that the analytical reactance of the loading circuit fits the required one in two points symmetric with respect to the resonant frequency of the unloaded SRR (f_1 = 5.24 GHz and f_2 = 5.28 GHz), the values of the non-Foster elements, L_t and C_t, can be easily derived solving a 2x2 algebraic linear system. In particular, I have obtained:

$$\begin{aligned} L_t &= -7.3\,nH \\ C_t &= -0.125\,pF \end{aligned} \tag{3.23}$$

Using these values, the curve of the reactive load well approximates the desired shape, as shown in Fig. 93 (dashed line). Moreover, as expected, the loaded SRR exhibits a wider bandwidth than the one of the unloaded SRR. Please note that the two frequency points used to determine (3.23) are chosen in close proximity of the resonance frequency in order to maximize the bandwidth enhancement effect. The simulations conducted revealed, in fact, that, when f_1 and f_2 are more far apart, a better overlap between the realized and the desired reactance curves is obtained around the selected points, resulting in a worse approximation around the resonant frequency. The described effect resulted in an unwanted split of the widened -10 dB bandwidth of the SRR in two narrower symmetric bands. Please note that the obtained bandwidth is, however, significantly larger than the range $f_2 - f_1$, as it is clear from Fig. 95.

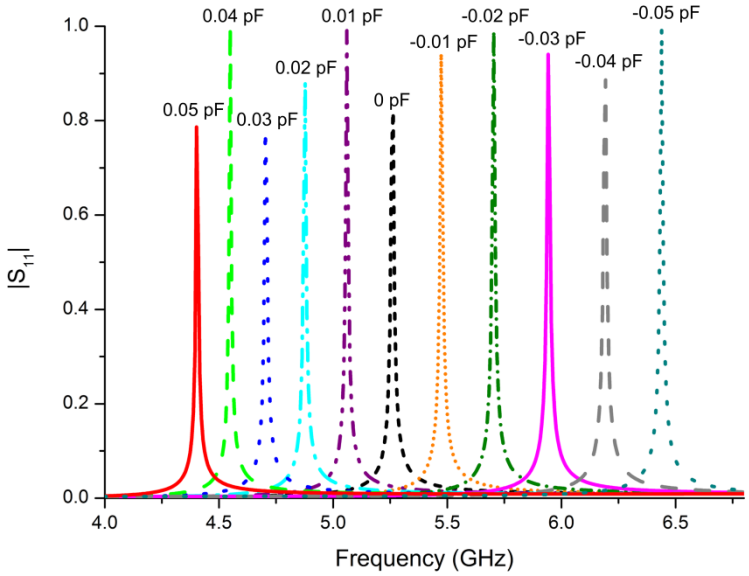

Fig. 93: Magnitude of the S_{11} parameter of a waveguide with a SRR loaded with different test capacitances (values in the range -0.05-0.05 pF).

However, the refinement of the model leads to ever more complex circuits, involving an increasing number of negative valued lumped elements, which, as it will be clear in the next Sections, are not of straightforward implementation. In the following, thus, I will limit my analysis to the first order approximation of the SRR reactance through the LC tank circuit, which leads to reasonable accuracy and keeps the circuit complexity rather moderate to be realistically implemented.

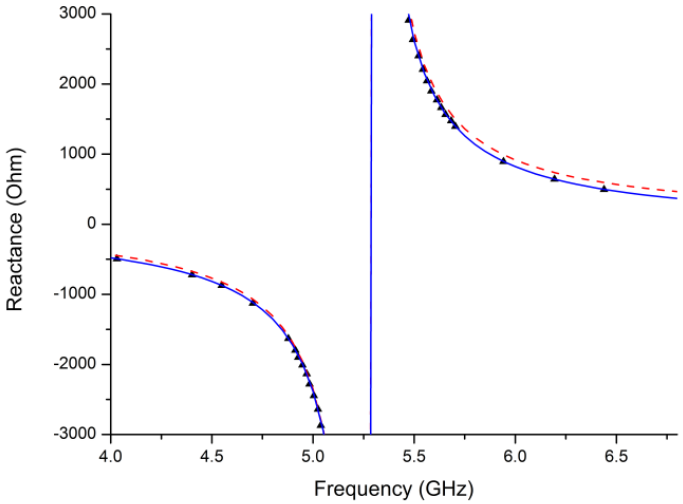

Fig. 94: Reactance of the loading capacitance as a function of the corresponding resonant frequency (triangular symbols), reactance of the *LC* tank non-Foster circuit (values in (5) have been used) (dashed line), and non-Foster reactance of a *LC* tank circuit in series with an inductor (values in (5) have been used) (solid line).

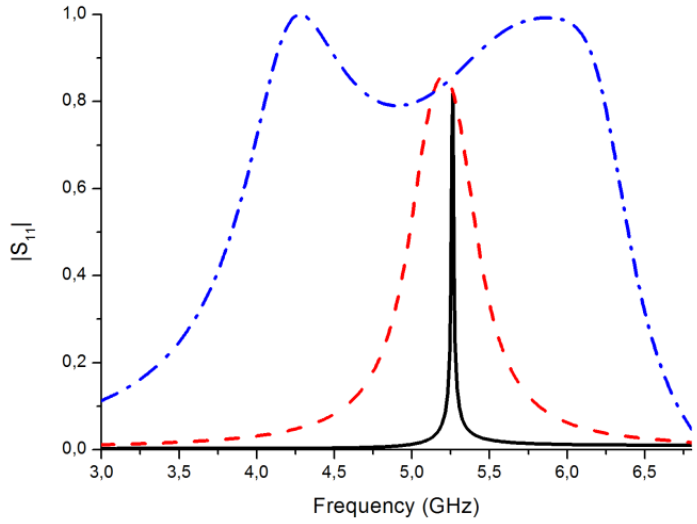

Fig. 95: Magnitude of the S_{11} parameter of the unloaded SRR case (solid line), of the SRR loaded with a *LC* tank circuit (dashed line), and of the SRR loaded with a *LC* tank circuit in series with an inductance (dot-dashed line).

4.1.2 Design of a broadband miniaturized monopole antennas

The design principles exposed in the previous Section can be used in any MTM-based application involving a magnetic resonator. In fact, once the equivalent circuit model of the chosen resonator is known, the extension of the aforementioned design principles to the specific application is a straightforward task.

As an example, I consider here the MTM-inspired SRR-based monopole antenna proposed in [45] and shown in Fig. 96. Please note that, due to the implementation issues discussed in the next Section, the structure reported here is scaled compared to the original one, in order to operate within the VHF band. This antenna consists of an electrically short monopole placed in close proximity of a SRR. The SRR is designed to resonate at a much lower frequency compared to the resonant frequency of the monopole and is excited through the near-field coupling with the monopole antenna. As shown in [45], thus, such an antenna operates at the resonant frequency of the SRR, radiating with a reasonable efficiency.

Since, as expected [45], the operation of this antenna is limited by the narrowband behavior of the SRR, it represents a proper example to demonstrate the usefulness of the approach proposed here to improve the bandwidth performance.

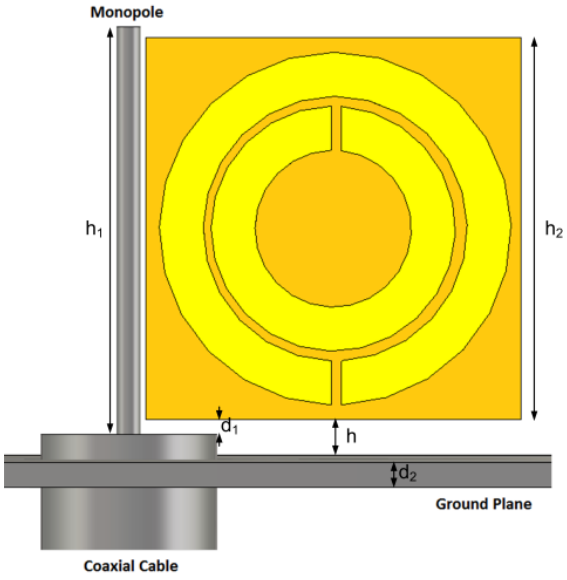

Fig. 96: Geometrical sketch of the SRR-based antenna proposed in [45]. Antenna dimensions in cm: h = 3.00, h_1 = 31.60, h_2 = 29.64, d_1 = 1.14, d_2 = 1.90. SRR dimensions in cm: w = 3.42, R = 13.70, g = 0.76, s = 0.76. Slab (FR-4): ε_r = 3.5, $tan\delta$ = 0.025 , thickness: 6.08 mm.

Following step-by-step the design procedure outlined in the previous Sections, I have determined the required circuital values of the non-Foster LC load circuit necessary to obtain a broadband antenna behaviour: L_t = -284.3 nH, C_t = -8.93 pF.

The magnitudes of the S_{11} parameter of the antenna in the unloaded and loaded cases are reported in Fig. 97. Such numerical results confirm the effectiveness of the design,

leading to a magnitude of the S_{11} parameter better than –10 dB within the frequency range 90-113.5 MHz and resulting in a bandwidth of operation more than 17 times larger than the one of the scaled SRR-based antenna (99.25-100.57 MHz).

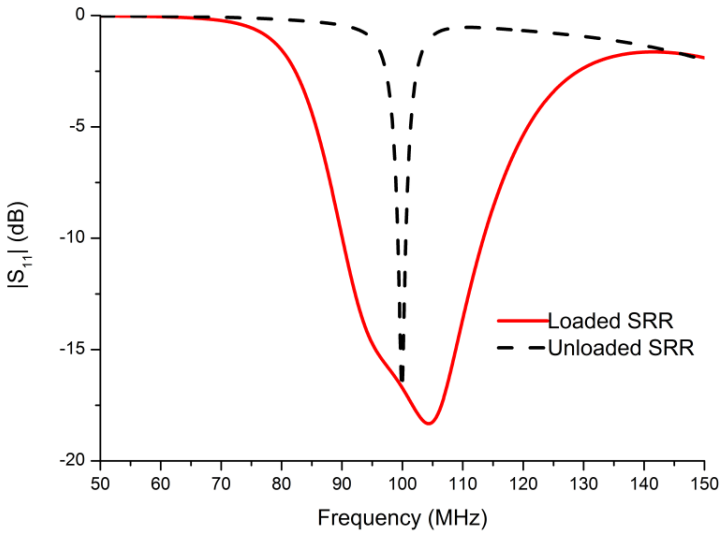

Fig. 97: Magnitude of the S_{11} parameter of the unloaded (dashed line) and loaded (solid line) antenna.

As previously anticipated, such negative lumped elements can be implemented with the aid of NICs. A NIC is a four-pole active circuit exhibiting a 180° phase shift between its input and output ports: this peculiar behaviour allows obtaining at the input port an impedance (admittance) that is the opposite to the one used to load the output port.

NICs can be realized using different active devices, such as operational amplifiers or transistors [31]. Though a straightforward choice would involve the use of op-amps, I should consider that the highest operation frequency is limited by the transit frequency of the used active elements [41] and, thus, proper operation of the circuit at VHF or higher frequencies is typically achieved by using transistors.

The design of a transistor-based NIC is not a straightforward task and special care to some critical aspects is needed. First of all, transistor technology (BJT, FET, etc.) and complexity of the polarization network represent key elements to determine appropriateness, performance, implementation easiness, and costs of the active circuit. Then, the response of the impedance converter must be checked against the sensitivity to the variation of the nominal values of the lumped elements used in the polarization networks and as loads, due to both frequency dispersion and parasitic effects. Finally,

the potential instability of the whole circuit (i.e. the combination of the loaded SRR and the antenna in our case) is a crucial issue, which should be properly considered at the design stage.

Before considering the cited issues one by one, I need first to choose the most appropriate NIC configuration. In the open technical literature, different circuit topologies have been proposed to obtain the required phase inversion (see [47] for some examples). In order to test their performances, I have used a circuital software (Advanced Design System – ADS), equipped with an extensive library of commercial elements. After having performed a number of simulations and comparisons, I have decided to adopt the circuit topology presented in [48], originally proposed to realize a negative capacitance and increase the tuning range of a varactor diode. In this configuration (see either of the circuits reported in Fig. 98), the two common-gate transistors of the ideal NIC scheme are powered by two current generators in cascode configuration. The reason of this choice resides in the high performance in terms of stability compared to the other configurations. The proposed topology, in fact, allows separating the input port from the output one, giving, thus, better performance in terms of Miller effect reduction and stability. On the other hand, this choice involves the use of more transistors (additional noise and higher costs are expected) and requires a higher DC voltage compared to regular configurations not involving cascode feeding.

In the following, I describe the design procedure I have adopted to optimize the performance of the circuit to properly work in the case of the SRR-based monopole antenna described in the previous Section. However, I remark here that the design procedure can be easily applied to any other device involving similar actively loaded SRRs.

First of all, I have exported into a s2p file the simulated (CST Microwave Studio has been used) S-parameters of a two-port dummy box placed across the gap of the external ring of the SRR excited by the monopole antenna. This file has been used to characterize the behaviour of the antenna within the circuital software. Basically, I replaced the discrete port located in the external gap of the SRR with the parallel connection of the NIC circuits giving the negative capacitance and the negative inductance. Please note that the circuit implementing the negative capacitance has been used in the form

proposed in [48], while the negative inductance implementation required slight modifications, as reported in Fig. 98.

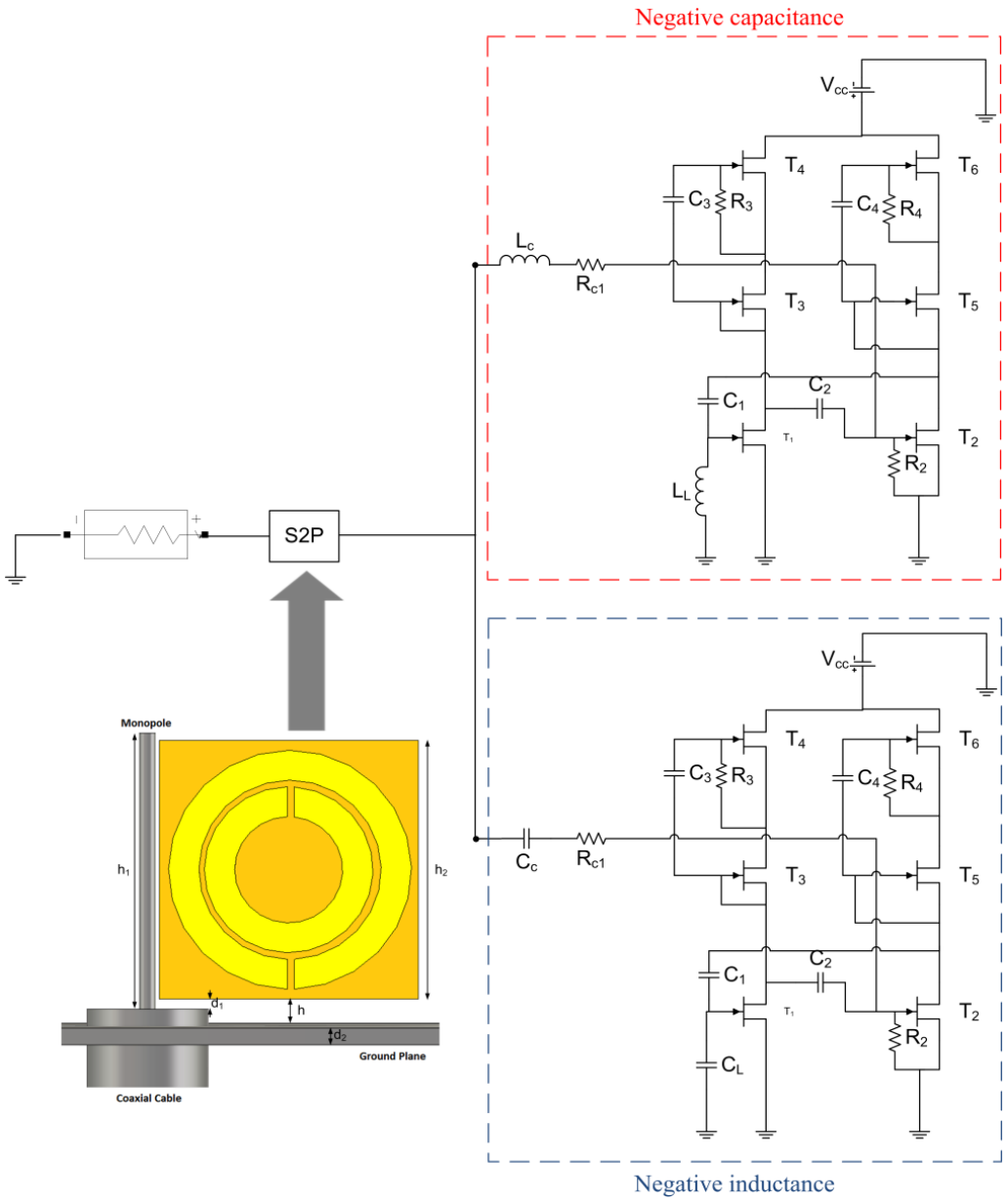

Fig. 98: SRR-based monopole antenna loaded with a parallel connection of two NIC circuits.

The first step to implement the NIC was the choice of a proper transistor. In the end, I have adopted the TSB JS8910AS, whose data sheets are present in the software library. Then, I have designed the polarization networks for the two branches of the circuit and optimized the overall circuit to produce the best bandwidth performance in terms of the antenna S_{11} parameter. The results, reported in Fig. 99 (dotted line), show a considerable

widening of the -10 dB bandwidth, that is only slightly reduced if compared to the one obtained in the ideal case (i.e. ideal negative lumped load).

In this design step I have used real circuital transistor models but ideal lumped elements (i.e. resistances, capacitances, and inductances). However, to consider a more realistic implementation, it is necessary to replace ideal elements with the corresponding real ones with the same nominal values available in the software libraries. Unfortunately, this procedure produces a dramatic deterioration of the antenna performance, because of the circuit sensitivity to the parasitic and frequency dispersive effects that always afflict real lumped elements.

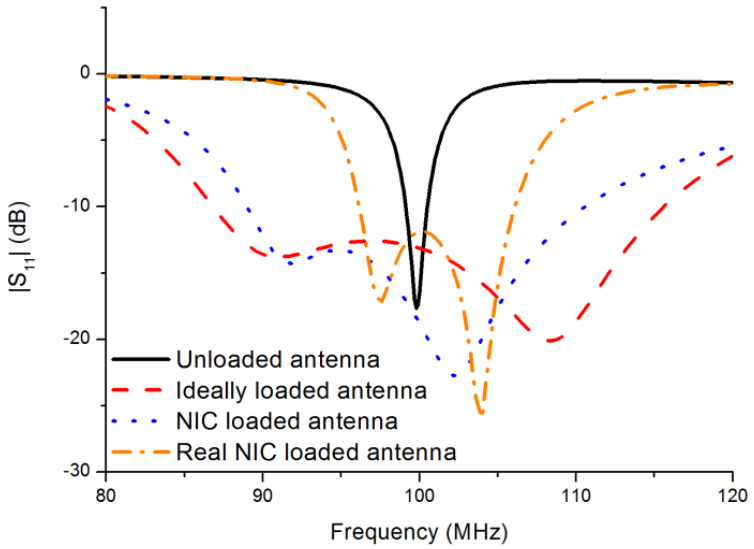

Fig. 99: Magnitude of the S_{11} parameter of the unloaded (solid line), ideally loaded (dashed line), NIC loaded (dotted line), and real NIC loaded (dot-dashed line) antenna.

In order to overcome this issue, as a second approach, I have performed a discrete optimization in which the whole set of ideal lumped elements has been replaced by the commercial ones contained in the software library. After this optimization, the results are the ones shown in Fig. 99 (dot-dashed line), exhibiting a significant reduction of the performance with respect to the ideal load case. Nevertheless, I have obtained a significant widening of the bandwidth of about 7 times with respect to the unloaded antenna. The corresponding nominal values of all the real lumped elements are reported in Table 3.

Please note that, in the circuit simulator, all the components are modeled with an accurate equivalent circuit (depending on the vendor's data sheet) that takes into account the parasitic effects and the frequency dispersion of the lumped values. Moreover, a probability density function is associated to each components to consider the corresponding tolerances available from the manufacturer. In all the cases, the chosen density function is the uniform one, which represents a worst case compared to the Gaussian distribution of the manufacturing process. For these reasons, the simulated results can be considered robust against almost of the critical issues that arises in the realization of a real circuit.

Table 3: Nominal values of the real lumped elements of the circuits.

Element	Nominal Value (Negative Capacitance Circuit)	Nominal Value (Negative Inductance Circuit)
R_{c1}		787 Ω
R_2	3.16 kΩ	453 Ω
R_3	309 Ω	71.5 Ω
R_4	3.4 kΩ	2.37 kΩ
C_1	13 pF	0.5 pF
C_2	24 pF	1.6 pF
C_3	270 pF	1.2 pF
C_4	24 pF	27 pF
C_c		6.2 pF
C_L		130 pF
L_c	1.8 nH	
L_L	2 nH	

For the sake of completeness, in Fig. 100 I show the input impedances of the unloaded and realistic loaded antennas, and, in Fig. 101, the directivity patterns of the loaded electrically small SRR antenna at 100 MHz and at the edge frequencies of the impedance bandwidth. The reference patterns of the unloaded SRR monopole antenna working at 100 MHz are not reported here, being almost the same as the ones of the loaded SRR antenna at the same frequency. Please note that the efficiency of the realistic loaded SRR

antenna is, within the operation bandwidth, comparable to the one of the unloaded SRR-based antenna at 100 MHz (about 40%).

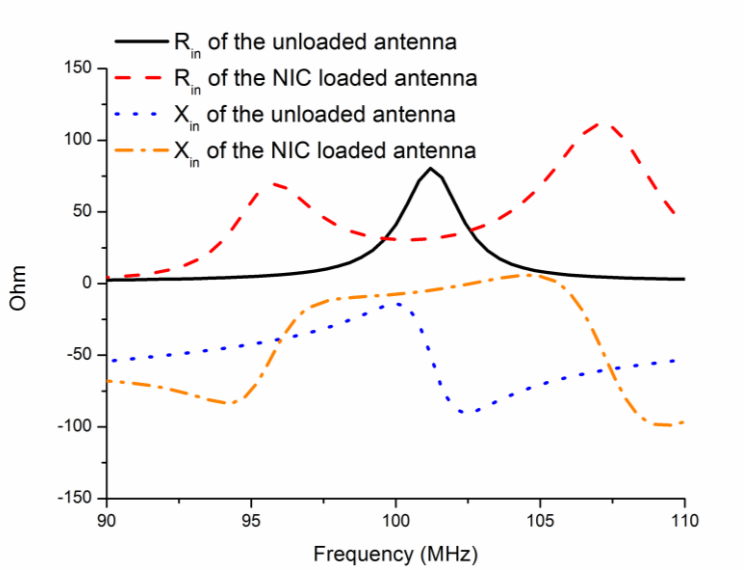

Fig. 100: Input impedance of the unloaded and real NIC loaded antennas in real (solid and dotted line, respectively) and imaginary (dashed and dot-dashed line, respectively) part.

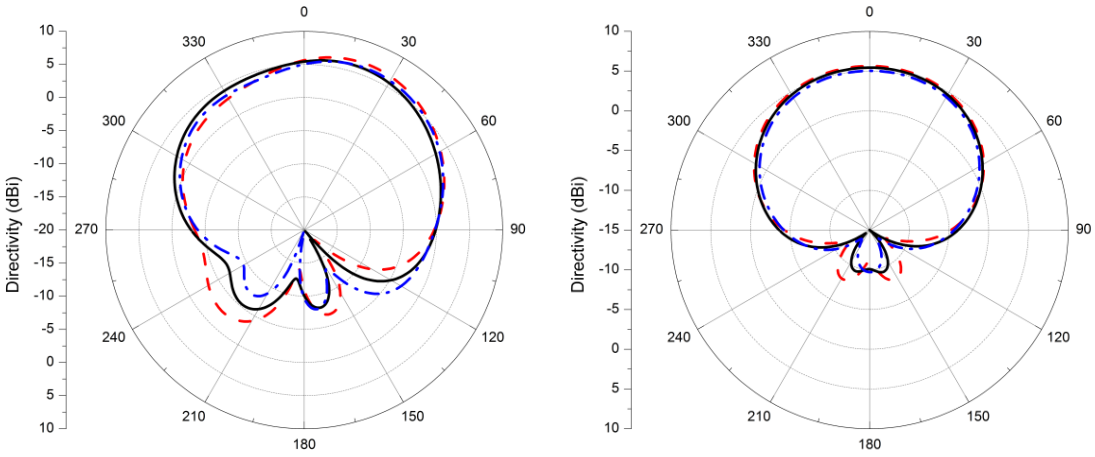

Fig. 101: Directivity patterns of the real NIC loaded antenna in the (left) E-plane and (right) H-plane at 100 MHz (solid line), 96.1 MHz (dashed line) and 106.1 MHz (dot-dashed line).

4.1.3 Stability issues

As mentioned before, when I design a device involving active circuits with positive feedback as NICs are, it is essential to perform a proper analysis to verify the stability of the overall system. This analysis, however, requires special care. In fact, as exhaustively

discussed in [41], the frequency domain methods typically employed in the field of RF and microwave active devices cannot be used for NIC components since they assume implicitly that Nyquist's criterion is fulfilled, which may not be the case. Alternative methods, as the one presented in [49] providing the evaluation of the system stability by using an ideal circulator, cannot be used, as well. In fact, as clarified in [50], this method is applicable in all the cases in which the circuit can become unstable only after its connection to the resonator. In our case, however, I cannot ensure the inherent stability of the circuit before I connect it to the antenna. For these reasons, only a time domain analysis, or a frequency one based on Nyquist's criterion, allows evaluating in an unambiguous way if the system is stable or not [41], [44].

Based on the previous discussion on the correct approaches used to check stability, in order to analyze the behaviour of the actively loaded antenna, I have decided to adopt a time-domain analysis using the tools offered by the circuit simulator. In particular, I have fed the realistic NIC loaded antenna with several time domain sources (e.g. sine wave, square wave, two sided exponential decay, Gaussian, etc.) and monitored the time-behaviour of the current at the ends of the coaxial cable feeding the antenna system. In all the tested cases the overall system was stable. Just as an example, in Fig. 102 andFig. 103, I show the responses of the unloaded and loaded antennas, respectively, in the case of a source signal with a Gaussian spectrum in the range 96-106 MHz (slightly wider than the -10 dB bandwidth of the loaded antenna). For comparison, in these figures I report also the current signal obtained closing the source on an ideal 50 Ohm load. From Fig. 103, I see that current in the loaded antenna remains bounded and maintains the same envelope of the signal in the ideal 50 Ohm load.

Please note that, in light of the considerations made in Section V about the circuit model of the lumped components, the stability of the system is guaranteed against all the parasitic effects and the variation of the lumped values (frequency dispersion ant tolerances). Moreover, from all the set of my simulations, I have noticed that the system is not at the edge of stability, so further eventual variations of the component values should not affect the stability.

Finally, as expected, in Fig. 102 it is possible to note a signal distortion and a considerable reduction of the signal amplitude, caused by the reflection of a significant

amount of spectral components due to the narrowband operation of the unloaded antenna. On the contrary, the signal in Fig. 103 is not affected by distortion and exhibits a smaller reduction of the amplitude, since the impedance bandwidth of the loaded antenna is approximately the same as the bandwidth of the source signal. Therefore, the comparison between the two plots provides a further confirmation of the effective widening of the bandwidth achieved in the actively loaded case.

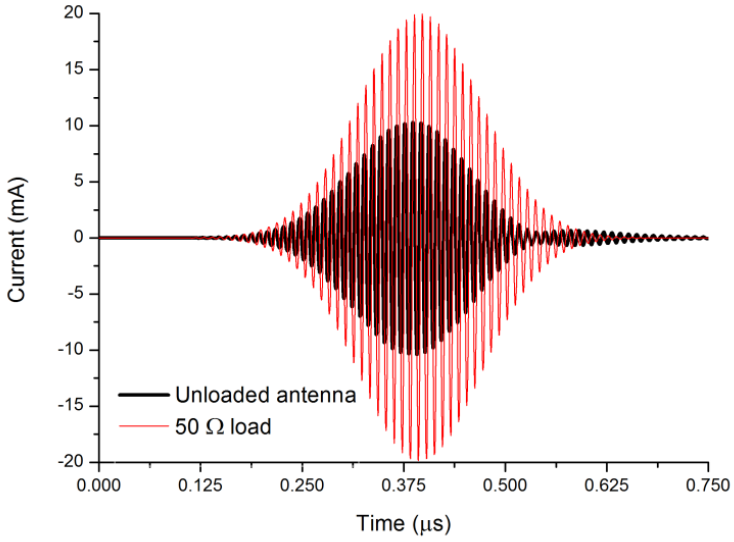

Fig. 102: Time-domain behavior of the current for the case of the unloaded antenna (thick black line) and for the case of an ideal 50 Ohm load (thin red line).

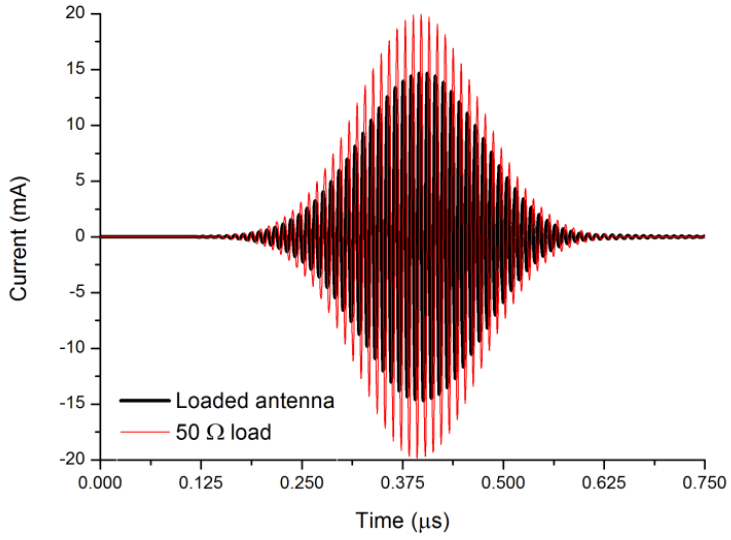

Fig. 103: Time-domain behavior of the current for the case of the loaded antenna (thick black line) and for the case of an ideal 50 Ohm load (thin red line).

4.2 Fabrication and characterization of resistive sheets

4.2.1 Realization of graphite-based resistive sheets

Due to their inherent low weight and low space occupancy, the use of engineered surfaces has experienced a great development in the last decade [51]. These surfaces, also known as *reactive sheets*, exhibit ideally a zero real part and a tunable imaginary part of their intrinsic surface impedance and can be employed for many intriguing applications as the cloaking ones discussed in the previous Chapter. On the contrary, *resistive sheets*, which exhibit a zero imaginary part and a tunable real part R_s (Ω/sq), are typically used for the reduction of the radar cross section of a target [52] and/or for the reduction of the antenna edge effects [53], due to their ability to dissipate the electromagnetic energy.

From a conceptual viewpoint, resistive sheets simply consist of a thin layer of a lossy material. Nevertheless, their practical realization still remains a not straightforward task. In fact, since the surface resistance of a sheet is equal to $R_s=1/(\sigma t)$, being σ the conductivity of the lossy material and t its thickness, the fabrication of a sheet exhibiting a desired value of R_s requires a strict control of both the thickness and the conductivity of the lossy material constituting the sheet.

In this Section, I propose an easy realization procedure of resistive sheets made of graphite powder. Graphite powder has been proposed as an element to realize electromagnetic shielding devices [54] or to design artificially synthesized dry phantom material [55] but, to the best of my knowledge, the use of graphite powder for the realization of resistive sheets has not been investigated yet, especially for what concerns the design procedure and the actual implementation. The aim of this Section is to propose a procedure allowing the fabrication of resistive sheets exhibiting a desired surface resistance within a wide range of values using low-cost and easily available materials.

As already clarified above, the main issue in the realization of a resistive sheet is the choice of a proper lossy material. After an accurate analysis, I have found that, due to its peculiarities, powdered graphite can be considered as an excellent candidate for this purpose. In fact, graphite powder is a low-cost material available in spray bottles as an

anti-adhesive and lubricant (see Fig. 104(a)). The availability of a spray product dramatically simplifies the deposition process of the lossy material. Moreover, its electrical conductivity can be tuned in a wide range by controlling the powder volume fraction [56]. As I will show below, the possibility to control the graphite conductivity during the powder deposition process allow us achieving a fine control of the surface resistance exhibited by the sheet.

Taking into control the deposition time, the graphite powder has been deposited onto a square semi-rigid plastic sheet with thickness 0.2 *mm* and relative electric permittivity equal to $\varepsilon_r = 2.7$ [57]. To guarantee the homogeneity of the samples, sheet dimensions are chosen to be small compared to the emission cone of the graphite spray. Following this procedure, I have realized 18 samples progressively increasing the deposition time. A picture of a realized sample is shown Fig. 104(b).

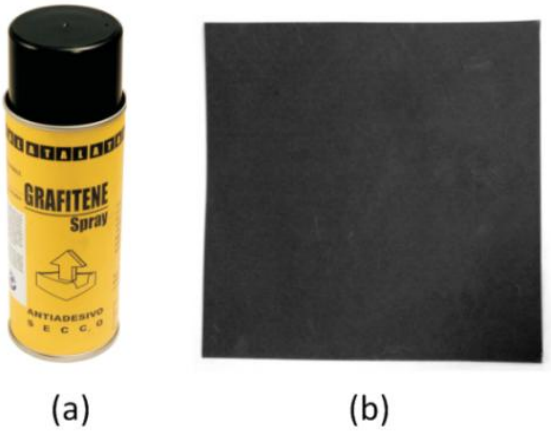

Fig. 104: (a) Commercial graphite powder spray produced by ATAL SrL; (b) A realized resistive sheet composed by a plastic sheet covered by a proper amount of graphite powder. The two images are not in scale.

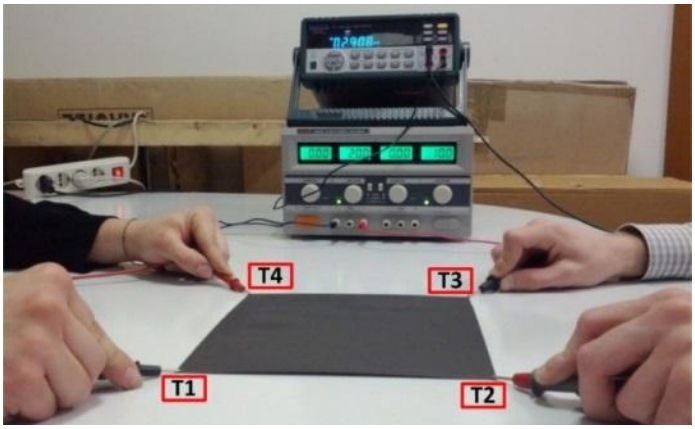

Fig. 105: Application of the Van der Pauw method for the resistive sheet characterization.

The realized resistive sheets have been characterized using the well-known Van der Pauw method [58]. This method allows retrieving the surface resistance R_s of a resistive sheet by using a set of four DC voltage measurements. For these measurements I have used the regulated power supply Life 41.5D1731SB3A and a digital multimeter EuroTEK DM50. The DC measurement setup is shown in Fig. 105.

First, the sample is excited by a DC current I_{23} at one side (delimited by the points T2-T3) and the output voltage V_{14} is measured at the opposite side (T1-T4). The resistance $R_{23,14}$ is equal to $R_{23,14}= V_{14} / I_{23}$. The procedure is then repeated to calculate $R_{14,23}$ by inverting the input and the output sheet side. According to the Van der Pauw method, the vertical resistance R_v is equal to the average value of the two resistances, *i.e.*,

$$R_v = \frac{R_{23,14} + R_{14,23}}{2}. \tag{3.24}$$

A similar procedure can be performed to calculate the vertical resistance R_h. Once R_v and R_h have been calculated, the surface resistance R_s of the resistive sheet can be computed by numerically solving the following equation for R_s:

$$e^{-\pi R_v/R_s} + e^{-\pi R_h/R_s} = 1. \tag{3.25}$$

In Fig. 106, I report the measured surface resistance values of the 18 realized samples as a function of the surface density of the graphite powder deposited on each sample. The surface density is defined as the ratio between the mass of the graphite powder and the area of the plastic sheet. The powder mass has been retrieved by measuring the mass of the resistive sheet with a professional scale (Nahita series 5023 100 *g*/1 *mg*) and subtracting to it the mass of the bare plastic sheet. As expected, as the mass of the deposited graphite powder increases, the relative surface resistance of the sheet decreases. In particular, the surface resistance is almost inversely proportional to the graphite powder mass. This is a non-surprising result since the surface resistance of a lossy material is inversely proportional to its thickness and to its conductivity that, in the case of the graphite powder, increases with its volume fraction [56]. The curve in Fig. 106

can be considered as the calibration curve of the graphite spray and can be easily exploited to estimate the mass of the graphite powder able to return a desired value of the surface resistance. It is worth noticing that, by finely controlling the amount of the deposited graphite powder, it is possible to achieve surface resistance values ranging from 50 Ω/sq to 800 Ω/sq.

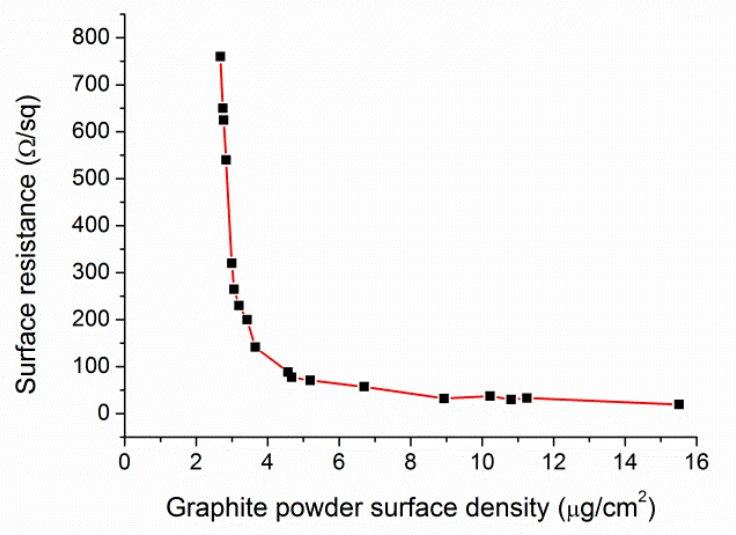

Fig. 106: Surface resistance exhibited by the 18 realized samples compared to the relative graphite powder surface density.

To experimentally verify the effectiveness of both the realization procedure and the characterization process, I have used the experimentally setup schematized in Fig. 107 consisting of a coax–to–waveguide adapter connected to a Rohde Swartz R&S®ZVA40, a WR90 waveguide, and a matched load. A properly shaped portion of the resistive sheet under test, supported by a sample holder, is placed between the matched load and the WR90 waveguide (see the inset of Fig. 107). This setup allows to measure the reflection coefficient of the resistive sheet that can be compared to the one returned by a full-wave simulator when a resistive sheet of the value retrieved in the previous section is used. The comparison between the measured and simulated reflection coefficients is shown in Fig. 108 for two resistive sheets with surface resistance equal to 41.5 Ω/sq and 141.5 Ω/sq, respectively. The agreement between simulations and measurements is excellent, confirming the effectiveness of the proposed procedure to realize a resistive sheet with a desired value of surface resistance.

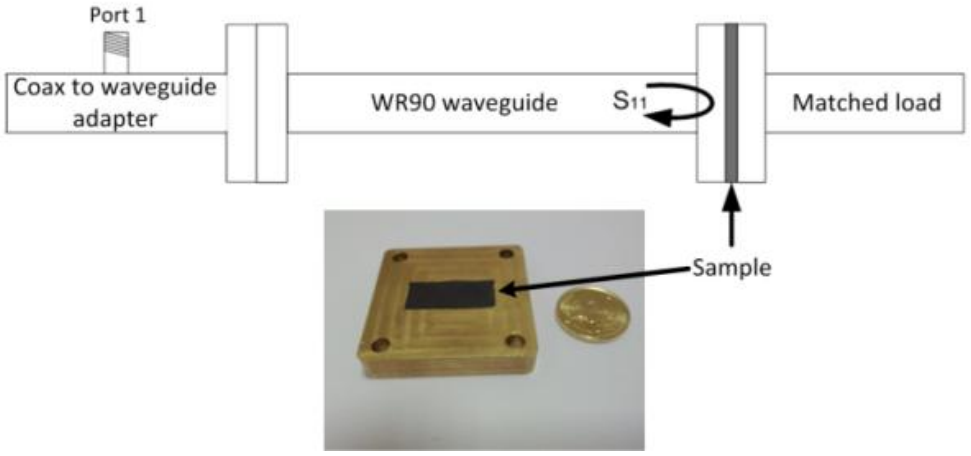

Fig. 107: Experimental setup used to measure the reflection coefficient of the realized resistive sheets. In the inset, it is shown a properly shaped resistive sheet supported by a sample holder.

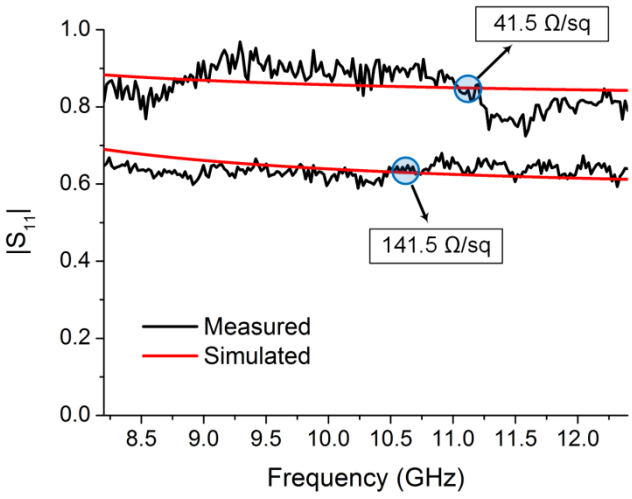

Fig. 108: Comparison between the measured and the simulated amplitude of the S_{11} parameter for two resistive sheets with R_s = 41.5 Ω/sq and R_s = 141.5 Ω/sq, respectively.

4.2.2 *Realization of a MTM-inspired electromagnetic absorber without a metallic backing*

Radar absorbing structures (RAS) play a key-role in different application fields, and, particularly, in the reduction of the radar cross section (RCS) of civil or military platforms (e.g. aircraft, ships, tanks, and other objects). Although several RAS configurations have been proposed in the literature [52], most of them require, as it happens also for the first radar absorbers (*i.e.*, the Dallenbach absorber and the Salisbury

screen), the use of a metallic ground plane, allowing both cancellation of the transmitted field beyond the absorber and introduction of a proper boundary condition useful to cancel the reflected wave. However, the use of a metallic plate entails also some inherent disadvantages, e.g. when a non-metallic object has to be hidden, a metallic cover may significantly increase the weight as well as the RCS of the object itself outside the operating band of the absorber.

Reducing both the out-of-band reflection and the weight of the absorber is possible exploiting the unusual properties of metamaterials. For instance, in [59] a metamaterial absorber without a metallic backing is proposed by using a perfect magnetic conductor made of a proper array of magnetic inclusions. In [60], *Landy et al.* propose to use only two metamaterial resonators to design an absorbing structure with near unity absorption. Another similar approach has been proposed in [61], consisting of two resonators and a metal wire. However, all these approaches are limited by the narrow frequency bandwidth characterizing the operation of metamaterial-based components.

In order to overcome this issue, I propose here to move from a metamaterial-based approach to a metamaterial-inspired one. In particular, in this Section I introduce a new low-cost and wideband absorber based on the use of a metasurface that is properly designed to act as a metallic plate in the X-band.

The structure of a traditional Salisbury screen, whose sketch is reported in Fig. 109, consists of a metallic backing and a resistive sheet placed $\lambda/4$ apart from it (where λ is the desired operational wavelength). In order to remove the metallic backing without affecting the behavior of the absorber, I need a proper metasurface that, in a specific range of frequencies, acts as a metallic plate.

Inspired by the reflection properties shown by metamaterial resonant inclusions, I have designed a simple resonating metamaterial-inspired structure consisting of a planar array of metallic rings printed on both sides of a 1.6 mm-thick dielectric substrate (FR4 with $\varepsilon_r = 4.3$ and $\tan\delta = 0.025$). For the sake of simplicity, I report in Fig. 110 only the transmission (S_{21} scattering parameter) and reflection coefficients (S_{11} scattering parameter) for a normally incident plane-wave with linearly *y*-polarized electric field. However, due to the isotropy of the inclusion on the array plane, the metamaterial-inspired surface is able to reflect any polarization of the incident electric field. The

spatial periodicity and the inner and outer diameter of the rings have been designed in order to have a PEC-like behavior (zero transmission and high reflection) in a broad frequency range centered at 10.2 GHz. As shown in Fig. 110, the EM wave is almost completely reflected by the metasurface and no transmission occurs in the entire X-band. Please note that this behavior has been obtained despite the significant reduction of metallic material (about 70% less than a full metal plate).

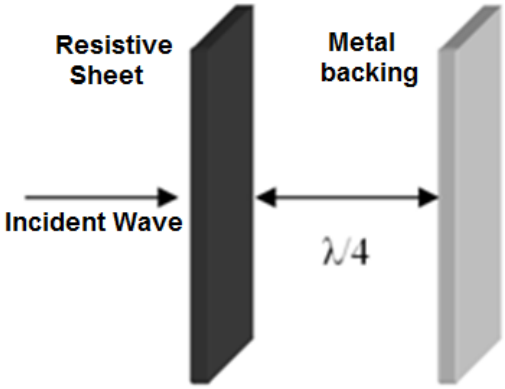

Fig. 109: Geometrical sketch describing the structure of a traditional Salisbury screen.

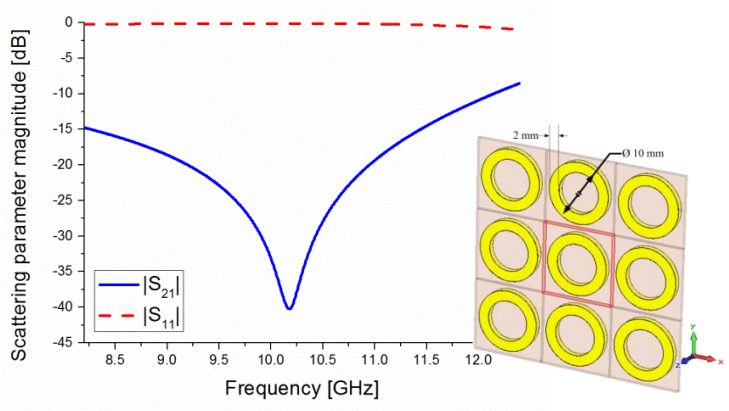

Fig. 110: Simulated amplitude of the transmission and reflection coefficients (for normal incidence) of the proposed metasurface (inset: geometrical sketch of the metasurface and dimensions of the metallic rings).

Implementation of the absorber: Since the metasurface emulates the behavior of a metal plate within the band of interest, it can be used to implement a metamaterial-inspired absorber. In particular, starting from the classical configuration of a Salysbury screen (see, e.g. Fig. 109), the metamaterial-inspired absorber here proposed consists of the metasurface presented in the previous Section, some foam sheets used as spacers, and a proper resistive sheet, as shown in Fig. 111(a). In order to achieve the impedance

matching between free-space and the resistive sheet and, at the same time, allow absorbing the reflected wave from the metasurface, the resistive sheet must exhibit a surface resistance around 377 Ω. The metasurface has been fabricated through the use of a LPKF Protomat-S milling machine (Fig. Fig. 111-b) and the resistive sheet has been realized by using the procedure described in [11], obtaining a surface resistance around 390 Ω (Fig. Fig. 111-c). Finally, I have assembled the overall structure, obtaining the planar absorber of dimensions $210\times210\times5\ \mathrm{mm}^3$ shown in Fig. Fig. 111a.

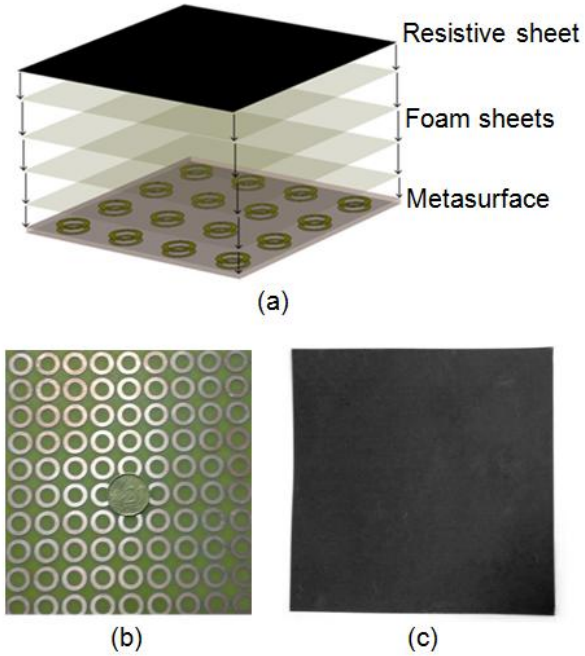

Fig. 111: (a) Geometrical sketch, (b) rear view and (c) front view of the proposed metamaterial-inspired absorber.

The performances of the absorber have been verified by using a measurement system consisting of two high-gain pyramidal horn antennas (one in TX mode and one in RX mode) and a vector network analyzer, as shown in Fig. 112. In order to emulate the illumination from a monostatic radar, the absorber has been placed in the far-field zone of both radiators and centered with respect to the joining between them, in order to illuminate the absorber with a normally incidence plane-wave. Such configuration tests the performances of the absorber in the worst case, i.e. normal incidence, because for different incidence angles the energy is reflected back in opposite direction with respect to the transmitter and the captured reflected energy is much lower. Please note that the

fabricated prototype has lateral dimensions of $210\times210\ \text{mm}^2\ (7\lambda_0\times7\lambda_0)$, which are large enough to perform a reliable measurement in free-space conditions.

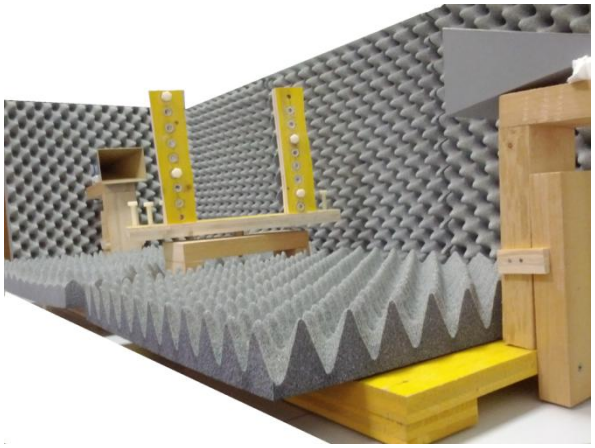

Fig. 112: Photograph of the measurement system consisting of two high-gain pyramidal horn antenna and the sample holder.

The corresponding measured and simulated absorption (defined as $A=1-\left|S_{11}\right|^2-\left|S_{21}\right|^2$) is reported in Fig. 113. From this figure, it is possible noticing that the combined operation of the metasurface and the resistive sheet significantly reduces the reflection from and the transmission through the metasurface, being the energy delivered by the incident field almost completely dissipated by the resistive sheet. In fact, the measured absorption values are greater than 0.9, i.e., more than 90% of the energy is absorbed in the entire X-band, confirming the wideband behavior of the proposed absorber.

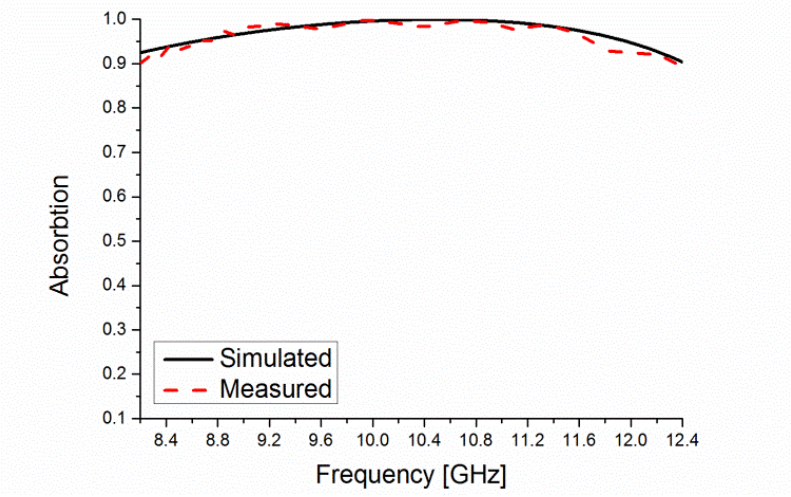

Fig. 113: Absorption of the metamaterial-inspired absorber shown in Fig. 111.

4.3 References

[1] G.V. Eleftheriades, and K.G. Balmain, *Negative Refraction Metamaterials: Fundamental Principles and Applications*. Hoboken, NJ: Wiley-IEEE Press, 2005.

[2] N. Engheta, and R.W. Ziolkowski, *Electromagnetic Metamaterials: Physics and Engineering Explorations*. Hoboken, NJ: Wiley-IEEE Press, 2006.

[3] F. Bilotti, and L. Sevgi, "Metamaterials: definitions, properties, applications, and FDTD-based modeling and simulation," *Int. J. RF Microw. CAE*, Vol. 22, pp. 422-438, 2012.

[4] R. Marqués, F. Medina, and R. Rafii-El-Idrissi, "Role of bi-anisotropy in negative permeability and left handed metamaterials," *Phys. Rev. B*, Vol. 65, 144441, 2002.

[5] R. Marqués, F. Mesa, J. Martel, and F. Medina, "Comparative analysis of edge and broadside coupled split ring resonators for metamaterial design. Theory and experiment," *IEEE Trans. Antennas Propagat*., Vol. 51, pp. 2572–2581, 2003.

[6] F. Bilotti, A. Toscano, and L. Vegni, "Design of spiral and multiple split ring resonator for the realization of miniaturized metamaterial samples," *IEEE Trans. Antennas Propagat*., Vol. 55, pp. 2258-2267, 2007.

[7] F. Bilotti, A. Toscano, L. Vegni, K. Aydin, K.B. Alici and E. Ozbay, "Equivalent-circuit models for the design of metamaterials based on artificial magnetic inclusions," *IEEE Trans. Microwave Theory Tech*., Vol. 55, pp. 2865-2873, 2007.

[8] J. D. Baena. R. Marqués, F. Medina, and J. Martel, "Artificial magnetic metamaterial design by using spiral resonators," *Phys. Rev. B*, Vol. 69, 014402, 2004.

[9] P. Gay-Balmaz, and O. J. F. Martin, "Efficient isotropic magnetic resonator," *Appl. Phys. Lett*., Vol. 81, pp. 939–941, 2002.

[10] I. V. Shadrivov, A. B. Kozyrev, D. W. van der Weide, and Y. S. Kivshar, "Nonlinear magnetic metamaterials," *Opt. Expr*., Vol. 16, pp. 20266-20271, 2008.

[11] K. E. Hannam, D. A. Powell, I. V. Shadrivov, and Y. S. Kivshar, "Tuning the nonlinear response of coupled split-ring resonators," *Appl Phys Lett.*, Vol. 100, 081111, 2012.

[12] P. Belov, R. Marques, S. Maslovski, I. Nefedov, M. Silverinha, C. Simovski, and S. Tretyakov, "Experimental study of the subwavelength imaging by a wire medium slab," *Phys. Rev. B*, Vol. 67, 113103, 2003.

[13] W. Zhang, H. Chen, and H.O. Moser, "Subwavelength imaging in a cylindrical hyperlens based on S-string resonators," *Appl. Phys. Lett*., Vol. 98, 073501, 2011.

[14] F. Bilotti, A. Alù, and L. Vegni, "Design of miniaturized metamaterial patch antennas with μ-negative loading," *IEEE Trans. Antennas Propagat*., Vol. 56, pp. 1640-1647, 2008.

[15] M. Barbuto, F. Bilotti, and A. Toscano, "Design of a multifunctional SRR-loaded printed monopole antenna," *Int. J. RF Microw. CAE*, Vol. 22, pp. 552-557, 2012.

[16] F. Bilotti, L. Scorrano, E. Ozbay, and L. Vegni, "Enhanced transmission through a sub-wavelength aperture: Resonant approaches employing metamaterials," *J. Opt. A*, Vol.11, 114029, 2009

[17] K. Aydin, A.O. Cakmak, L. Sahin, Z. Li, F. Bilotti, L. Vegni, and E. Ozbay, "Split-ring-resonator-coupled enhanced transmission through a single subwavelength aperture," *Phys. Rev. Lett*., Vol. 102, pp. 013904, 2009.

[18] K.B. Alici, F. Bilotti, L. Vegni, and E. Ozbay, "Optimization and tunability of deep subwavelength resonators for metamaterial applications: complete enhanced transmission through a subwavelength aperture," *Opt. Expr*., Vol. 17, pp. 5933-5943, 2009.

[19] A.O. Cakmak, K. Aydin, E. Colak, Z. Li, F. Bilotti, L. Vegni, and E. Ozbay, "Enhanced transmission through a sub-wavelength aperture using metamaterials," *Appl. Phys. Lett*., Vol. 95, 052103, 2009.

[20] J. Martel, R. Marques, F. Falcone, J.D. Baena, F. Medina, F. Martin, and M. Sorolla, "A new LC series element for compact bandpass filter design," *IEEE Microwave Wireless Compon. Lett.*, Vol. 14, pp. 210-212, 2004.

[21] F. Bilotti, L. Nucci, and L. Vegni, "An SRR based microwave absorber," *Microw. Opt. Technol. Lett*., Vol. 48, pp. 2171-2175, 2006.

[22] S. A. Tretyakov, and S. I. Maslovski, "Veselago materials: What is possible and impossible about the dispersion of the constitutive parameters," *IEEE Antennas Propag. Mag*., Vol. 49, pp. 37-43, 2007.

[23] S.A. Tretyakov, "Meta-materials with wideband negative permittivity and permeability," *Microw. Opt. Technol. Lett*., vol. 31, no. 3, pp. 163-165, 2001.

[24] W. K. Chen, *The Circuit and Filters Handbook*. Boca Raton, FL: CRC Press, 2005.

[25] R.M. Foster, "A reactance theorem," *Bell Syst. Tech. J*., Vol. 3, pp. 259–267, 1924.

[26] J. L. Merill, "Theory of the negative impedance converter," *Bell Syst. Tech. J*., Vol. 30, pp. 88–109, 1951.

[27] J. G. Linvill, "Transistor negative impedance converters," *Proc. IRE*, Vol. 41, pp. 725–729, 1953.

[28] L. Kaya, and E.Y. Yuksel, "Investigation of a compensated rectangular microstrip antenna with negative capacitor and negative inductor for bandwidth enhancement," *IEEE Trans. Antennas Propagat*., Vol. 55, pp. 1275-1282, 2007.

[29] G. Skahill, R.M. Rudich, and J. Piero, "Electrically small, efficient, wide-band, low-noise antenna elements," *1998 Antenna Application Symposium*, pp. 214-231.

[30] S.E. Sussman-Fort, and R.M. Rudish, "Non-Foster Impedance Matching of Electrically-Small Antennas," *IEEE Trans. Antennas Propagat*., Vol. 57, pp. 2230-2241, 2009.

[31] J.T. Aberle and R. Loepsinger-Romak, *Active Antennas with Non-Foster Matching Networks*. San Rafael, CA: Morgan and Claypool Publishers, 2007.

[32] I. Di Nallo, G. Bit-Babik, and A. Faraone, "Wideband antenna using non-foster loading elements," *2007 IEEE AP-S Int. Symp*., pp. 4501-4504.

[33] G. Bit-Babik, C. Di Nallo, J. Svigelj, A. Faraone, "Small wideband antenna with non-Foster loading elements," *2007 ICEAA*, pp. 105-107.

[34] J. Kern, D. H. Werner, and M. J. Wilhelm, "Active negative impedance loaded EBG structures for the realization of ultra-wide band artificial magnetic conductors," *2003 IEEE AP-S Int. Symp*., Vol. 2, pp. 427-430.

[35] D. Sievenpiper, "Superluminal Waveguides Based on Non-Foster Circuits for Broadband Leaky-Wave Antennas," *IEEE Antennas Wireless Propag. Lett*., Vol. 10, pp. 231 - 234, 2011.

[36] D. Sievenpiper, M. Jacob, and J. Long, "Active electromagnetic structures, metamaterials, and antennas," *2012 IEEE iWAT*, pp. 289-292.

[37] P. Jin, and R.W. Ziolkowski, "Broadband, efficient, electrically small metamaterial-inspired antennas facilitated by active near-field resonant parasitic elements," *IEEE Trans. Antennas Propagat*., Vol. 58, pp. 318-327, 2010.

[38] R.W. Ziolkowski, and P. Jin, "Introduction of internal matching circuit to increase the bandwidth of a metamaterial-inspired efficient electrically small antenna," *2008 IEEE AP-S Int. Symp*., pp. 1-4.

[39] H. Mirzaei, and G.V. Eleftheriades, "A wideband metamaterial-inspired compact antenna using embedded non-Foster matching," *2011 IEEE APS-URSI Int. Sym*., pp. 1950-1953.

[40] H. Mirzaei, and G.V. Eleftheriades, "Antenna applications of non-Foster elements," *2012 IEEE iWAT*, pp. 281-284.

[41] S. Hrabar, I. Krois, and A. Kiricenko, "Towards active dispersionless ENZ meta-material for cloacking applications," *Metamaterials*, Vol. 4, pp. 89-97, 2010.

[42] S. Hrabar, I. Krois, I. Bonic, and A. Kiricenko, "Negative capacitor paves the way to ultra-broadband metamaterials," *Appl. Phys. Lett*., Vol. 99, 254103, 2011.

[43] K. Z. Rajab, Y. Hao, D. Bao, C. G. Parini, J. Vazquez, and M. Philippakis, "Stability of active magnetoinductive metamaterials," *J. Appl. Phys*., Vol. 108, 054904, 2010.

[44] E. Ugarte-Muñoz, S. Hrabar, D. Segovia-Vargas, and A. Kiricenko, "Stability of non-Foster reactive elements for use in active metamaterials and antennas," *IEEE Trans. Antennas Propagat*., Vol. 60, pp. 3490-3494, 2012.

[45] K.B. Alici and E. Ozbay "Electrically small split ring resonator antennas," *J. Appl. Phys*., Vol. 101, pp. 08314, 2007.

[46] Computer Simulation Technology, CST Studio Suite 2011, http://www.cst.com.

[47] S.E. Sussman-Fort, "Gyrator-based biquad filters and negative impedance converters for microwaves," *Int. J. RF Microw. CAE*, Vol. 8, pp. 86-101, 1998.

[48] S. Kolev, B. Delacressonière, and J.L. Gautier, "Using a negative capacitance to increase the tuning range of a varactor diode in MMIC technology," *IEEE Trans. Microw. Theory Tech*., Vol. 49, pp. 2425-2430, 2001.

[49] R.W. Jackson, "Criteria for the onset of oscillation in microwave circuits," *IEEE Trans. Microw. Theory Tech.*, Vol. 40, pp. 566–569, 1992.

[50] R. W. Jackson, Comments on "Criteria for the onset of oscillation in microwave circuits," *IEEE Trans. Microw. Theory Tech.*, Vol. 40, pp. 1850-1851, 1992.

[51] C.L. Holloway, E.F. Kuester, J.A. Gordon, J. O'Hara, J. Booth, and D.R. Smith, 'An Overview of the Theory and Applications of Metasurfaces', *IEEE Ant. Propag. Mag*., vol. 54, pp.10-35, 2012.

[52] Knott, E.F.: 'Radar Cross Section' (SciTech Publishing, Raleigh, NC, USA, 2004, second edition).

[53] J.L. Volakis, A. Alexanian, and J.M. Lin. "Broadband RCS reduction of rectangular patch by using distributed loading," *Electronics Letters*, vol. 28, pp. 2322-2323, 1992.

[54] C. Morari, I. Balan, J. Pintea, E. Chitanu, and I. Iordache "Electrical conductivity and electromagnetic shielding effectiveness of silicone rubber filled with ferrite and graphite powders," *PIER M*, vol. 21, pp. 93-104, 2011.

[55] H. Tamura, T. Nishikawa, T. Kobayashi, and T. Nojima, "A dry phantom material composed of ceramic and graphite powder," *IEEE Trans. Electromagn. Compat.*, vol. 39, pp. 132-137, 1997.

[56] N. Deprez, and D.S. McLachlan, "The analysis of the electrical conductivity of graphite conductivity of graphite powders during compaction," *J. Phys. D: Appl. Phys.*, vol. 21, pp. 101-107, 1988.

[57] B. Riddle, J. Baker-Jarvis, and J. Krupka, "Complex permettivity measurements of common plastics over variable temperatures," *IEEE Trans. Microwave Theory Tech.*, vol. 51, pp. 727-733, 2003.

[58] L.J. Van der Pauw, "A method of measuring specific resistivity and Hall effect of discs of arbitrary shape", *Philips Research Reports*, vol. **13**, pp. 1–9, 1985.

[59] F. Bilotti, A. Toscano, K.B. Alici, E. Ozbay, and L. Vegni, "Design of miniaturized narrowband absorber based on resonant-magnetic inclusions," *IEEE Trans. Electromagn. Compatibility.*, vol. 53, pp. 63–72, 2011.

[60] N.I. Landy, S. Sajuyigbe, J.J Mock, D.R. Smith, W.J. Padilla, "Perfect metamaterial absorber," *Phys. Rev. Lett*., vol. **100**, 207402, 2008.

[61] Y. Cheng, and H. Yang, "Design, simulation and measurement of metamaterial absorber," *J. Appl. Phys.*, vol. 108, 034906, 2010.

List of Figures and Tables

Fig. 1: Schematic representation of the operation of a transformation electromagnetic-based cloaking device [2]. 21

Fig. 2: Schematic representation of the operation of a scattering cancellation-based cloaking device. 22

Fig. 3: Some examples of mantle cloaking devices for a spherical object [8]. 23

Fig. 4: Infinitely long cylinder surrounded by a conformal metasurface. 24

Fig. 5: (left) First and (right) second interface of the coated cylinder. 27

Fig. 6: SCS contribution of several scattering modes of a dielectric cylinder with relative permittivity equal to ε = 4 and ε = 10, respectively, as the cylinder radius changes. The operation frequency is f_0 = 3 GHz. 28

Fig. 7: Variation of the scattering width gain with the surface reactance of a mantle cloak for an infinitely long dielectric cylinder with permittivity $\varepsilon = 10$ and radius $a = \lambda_0/10$. 28

Fig. 8: Normalized SCS of a dielectric cylinder with relative permittivity $\varepsilon = 10$ at 3 GHz for both TM and TE incidence as the cylinder radius changes. 30

Fig. 9: Section of a multilayer mantle cloaking in the cylindrical geometry. 32

Fig. 10: (Top panel) Scattering profile targeting the monopolar mode at 2 GHz and the dipolar at 3 GHz. (Bottom panel) Scattering profile targeting the monopolar mode at 2 and 3 GHz. 33

Fig. 11: SCS contribution of the first three scattering modes for a dielectric cylinder with relative permittivity $\varepsilon = 10$ at a frequency $f_0 = 3$ GHz for both TM (left) and TE (right) incidence. 34

Fig. 12: SCS contribution of the first three scattering modes for a dielectric cylinder with relative permittivity $\varepsilon = 10$ at a frequency $f_0 = 3$ GHz coated with a bi-layer mantle cloak device as the cylinder radius changes for both TM (left picture) and TE (right picture) incidence. 35

Fig. 13: SCS contribution of the first three scattering modes for a dielectric cylinder with relative permittivity $\varepsilon = 10$ at a frequency $f_0 = 3$ GHz coated with a tri-layer mantle

cloak device as the cylinder radius changes for both TM (left picture) and TE (right picture) incidence. 35

Fig. 14: Unit-cell (inside the dashed line) of an array of metallic strips (grid). 37

Fig. 15: (a) Unit-cell of a rectangular metasurface. w_1 and w_2 are the widths of each parallel segment of the metasurface. (b)-(c) Its equivalent circuit model for the TM and TE polarization, respectively. 39

Fig. 16: (a) Metasurface characterized by a rectangular unit-cell with horizontal slits able to exhibit a negative and a positive value of surface reactance for TM and TE polarization, respectively; (b)-(c) Its equivalent circuit model for the TM and TE polarization, respectively. 40

Fig. 17: (a) Metasurface characterized by a rectangular unit-cell with vertical slits able to exhibit a positive and a negative value of surface reactance for TM and TE polarization, respectively; (b)-(c) Its equivalent circuit model for the TM and TE polarization, respectively. 42

Fig. 18: (a) Metasurface characterized by a rectangular unit-cell with both horizontal and vertical slits able to exhibit a negative value of surface reactance for both TM and TE polarization; (b)-(c) Its equivalent circuit model for the TM and TE polarization, respectively..... 42

Fig. 19: Magnitude of the reflection and transmission coefficients for a cloaked slab with thickness $t = \lambda_0/100$ (shown in the inset) in the case of TM and TE incident polarizations. The mantle cloaking cover is realized with the rectangular unit cell metasurface..... 46

Fig. 20: Magnitude of the reflection and transmission coefficients for a cloaked slab with thickness $t = \lambda_0/10$ (shown in the inset) in the case of TM and TE incident polarizations. The mantle cloaking cover is realized with the rectangular unit cell metasurface with both horizontal and vertical slits. 47

Fig. 21: Reflection coefficient of the cloaked slab for different incidence angles. Solid lines refer to TM polarization whereas dashed lines are obtained for TE polarization. ... 48

Fig. 22: Theoretical SW gain as the surface impedance of the cover changed for the case of TE incidence on a 2D metallic cylinder. 50

Fig. 23: Simulated SW gain for both TM and TE polarization compared to the one derived from Mie theory for a cloaked infinitely long metallic cylinder. 50

Fig. 24: Comparison between the SCS suppression performance of a dual polarized mantle cloak (solid line) and a single polarized mantle cloak (dashed line) in the case of normally incident left-handed circularly polarized plane wave. The scattering of the bare cylinder is represented using the dot-dashed line. 53

Fig. 25: 3D SCS at the cloaking frequency for TM polarization in the (a) uncloaked and (b) cloaked case. Picture (c) and (d) represents the same quantities for TE polarization.. 54

Fig. 26: (Left) Geometry of a conducting cylinder covered by a bilayer mantle cloak under a TM plane wave illumination. (Top) dual band operation and (bottom) wideband. 55

Fig. 27: Bilayer cloak for broadband operation as in Fig. 26. 55

Fig. 28: Unit cells of the two designed dual-polarized metasurface working for a non-electrically small dielectric cylinder. 56

Fig. 29: Performance of the by-layer dual-polarized mantle cloaking device working for a non-electrically small dielectric cylinder. 56

Fig. 30: Geometry of interest: a loaded dipole antenna coated with a mantle cloak. ... 63

Fig. 31: Absorption efficiency versus absorption for a bare $\lambda/4$ receiving dipole antenna loaded by an impedance $Z_L = R_L + jX_L$. The black (darker) contours are generated keeping X_L constant while sweeping R_L over all positive values (solid black: $X_L = -X_{in}$; dashed black: $X_L = -4X_{in}$). The blue (lighter) contours are generated keeping R_L constant and sweeping X_L over all real values (blue dots: $R_L = R_{in}$; dashed blue: $R_L = 100R_{in}$). The grey shaded area is forbidden to passive dipolar scatterers. Full-wave simulations are shown in circles. 65

Fig. 32: Variation of the absorption efficiency at resonance with the load resistance, comparing the bare (black line, white dots) and cloaked (blue line, blue dots) $\lambda/4$ sensor of Fig. 31. Solid lines show the analytical results, dots indicate full-wave simulations. The inset shows the corresponding dispersion on a plot consistent with Fig. 31. 67

Fig. 33: Geometry of the proposed inductive metascreen over the two arms of the dipole antenna, leaving the small gap open to free space. 68

Fig. 34: Comparison of the open circuit far-field scattering of the bare (a) and covered dipole (b). 69

Fig. 35: Absorption efficiencies versus absorption of the bare and covered $\lambda/2$ dipole antennas at 3 GHz. 69

Fig. 36: Open-circuit scattering suppression considering several realistic material covers, including dielectric and metal losses. 70

Fig. 37: 3D gain patterns of (a) the isolated first dipole at f_{01}, (b) the isolated second dipole at f_{02}, (c) the first dipole at f_{01} in presence of the second dipole, and (d) the second dipole at f_{02} in presence of the first dipole. 72

Fig. 38: Amplitude of the reflection coefficient at the input port of the first and second dipole in the isolated case (continuous and dashed line, respectively) and in the reference scenario (dotted line and dash-dotted line, respectively). 73

Fig. 39: The two dipole antennas cloaked with two metasurfaces consisting of N vertical metallic strips printed on thin, flexible, commercial substrates (DuPont 951 with ε_r = 7.8, $tan\delta$ = 0.0015 at 2 GHz and Roger TMM4 with ε_r = 4.5, $tan\delta$ = 0.002 at 10 GHz, respectively). The geometrical parameters are: (a) N = 11, d_v = 1.07 mm, d_m = 0.3 mm and (b) N = 3, d_v = 0.99 mm and d_m = 4 mm. The cover radii are a_c = 1.2a and a_c = 1.2a, respectively, a being the antenna radius. 74

Fig. 40: Gain patterns of the first antenna at 3.298 GHz on the (a) H-plane and (b) E-plane in the case of isolated dipoles (continuous line), the uncloaked scenario (dashed line), and the cloaked one (dotted line). Figures (c) and (d) show the same quantities for the second antenna at 2.970 GHz. 74

Fig. 41: Amplitude of the reflection coefficient at the input port of the first and second dipole in the uncloaked case (continuous and dashed lines, respectively) and of the first and second dipole in the cloaked case (dotted and dash-dotted lines, respectively). 75

Fig. 42: (a) Gain pattern of the first antenna at 3.298 GHz on the H-plane and (b) gain pattern of the second antenna at 2.970 GHz in the isolated, uncloaked and cloaked scenario for a separation distance equal to $\lambda/15$. 75

Fig. 43: Gain patterns on the H-plane of the (a) first and (b) second dipole around their respective resonance frequencies. 76

Fig. 44: Magnitude of S_{11} of a horn antenna in presence of bare and cloaked array of cylinders for different values of d_{horn} (with $d_{array} = \lambda_0/3$) and d_{array} (with $d_{horn} = \lambda_0/5$). 77

Fig. 45: Testing scenarios: (Top left: TM-pol array), (Top right: TE-pol array), (Bottom left: TM-pol triangle), and (Bottom right: ultraconformal cover). 78

Fig. 46: A dense TM-polarized array. (Top) Snapshot in time of the transverse electric field distribution (bare, covered, free-space) at 3.1 GHz. (Bottom) Input impedance improvement as seen by the S-band microwave horn used in the near field images. The inset also shows the polarization and testing geometry in the measurements. 79

Fig. 47: A dense TE-pol array. (Top) Snapshot in time of the transverse electric field distribution (bare, covered, free-space) at 3.2 GHz. (Bottom) Input impedance improvement as seen by the S-band microwave horn used in the near field images. 80

Fig. 48: A dense TM-polarized triangular array. (Top) Snapshot in time of the transverse electric field distribution (bare, covered, free-space) at 3.0 GHz. (Bottom) Input impedance improvement as seen by the S-band microwave horn used in the near field images. 80

Fig. 49: (a) Geometry of a traditional Yagi-Uda antenna; (b) Geometry of a cloaked Yagi-Uda antenna in which the three metallic rods are surrounded by as many generic mantle cloaking devices. γ is the ratio between the cover and the cylinder radius.....82

Fig. 50: Magnitude of the reflection coefficient of the bare Yagi-Uda antenna (continuous line), of the not optimized cloaked Yagi-Uda antenna (dashed line) and of the optimized cloaked Yagi-Uda antenna (dotted line). 83

Fig. 51: Forward and backward gain of the bare Yagi-Uda antenna compared to the ones achieved with a not optimized and an optimized cloaked Yagi-Uda antenna. 84

Fig. 52: Forward and backward gain of the cloaked Yagi-Uda antenna at the center frequency of BW_a as the director and reflector lengths change (once fixed $L_r = 140\ mm$ and $L_d = 60\ mm$, respectively.....85

Fig. 53: Input resistance and reactance of the cloaked Yagi-Uda antenna at the center frequency of BW_a as the director and reflector lengths change (once fixed $L_r = 140\ mm$ and $L_d = 60\ mm$, respectively). 86

Fig. 54: Forward and backward gain of the cloaked Yagi-Uda antenna at the center frequency of BW_a as the distances d_{cd} and d_{cr} change (once fixed $d_{cr} = 98\ mm$ and $d_{cd} = 74\ mm$, respectively). 86

Fig. 55: Input resistance of the cloaked Yagi-Uda antenna at the center frequency of BW_a as the distances d_{cd} and d_{cr} change (once fixed $d_{cr} = 98\ mm$ and $d_{cd} = 74\ mm$, respectively). 87

Fig. 56: Retrieved surface reactance as the frequency changes of the three designed vertical strips metasurfaces. 89

Fig. 57: Total scattering cross section of the Yagi-Uda antenna in the uncloaked case (continuous line) and in the cloaked one (dashed line) under a TM plane wave illumination. 89

Fig. 58: Magnitude of the reflection coefficient of the horn antenna in the isolated case (continuous line), in the uncloaked one (dotted line) and in the cloaked one (dashed line). 91

Fig. 59: Radiation pattern of the horn antenna on the horizontal plane at 3.1 *GHz* in the isolated (continuous line), in the uncloaked (dotted line) and in the cloaked case (dashed line). 91

Fig. 60: Radiation pattern of the horn antenna on the horizontal plane at 3.6 *GHz* in the isolated (continuous line), in the uncloaked (dotted line) and in the cloaked case (dashed line). 92

Fig. 61: Antenna scenario in which a Yagi-Uda antenna operating at *3.2 GHz* is placed between the director and the driven element of the cloaked Yagi-Uda antenna (that operates a 0.93 *GHz*). 93

Fig. 62: Directivity on the *x-z* plane of the two Yagi-Uda antennas system shown in Fig. 61. The directivity of the second Yagi-Uda is shown both in the uncloaked and in the cloaked scenario. 93

Fig. 63: Forward and backward gain of the two Yagi-Uda antennas shown in Fig. 61. 93

Fig. 64: Real part of the effective permittivity for an array of gold nano-spheres embedded in a silica matrix for different values of the filling volume fraction. 102

Fig. 65: Imaginary part of the effective permittivity for an array of gold nano-spheres embedded in a silica matrix for different values of the filling volume fraction. 102

Fig. 66: Real part of the effective permittivity for an array of silver nano-spheres embedded in a silica matrix for different values of the filling volume fraction. 103

Fig. 67: Imaginary part of the effective permittivity for an array of silver nano-spheres embedded in a silica matrix for different values of the filling volume fraction. 103

Fig. 68: Unit-cell of the designed artificial material slab. The thickness of the slab along the *z*-axis is $d = 0.17\ \lambda_0$ at the design frequency. 104

Fig. 69: Real and imaginary part of the effective permittivity for an array of core-shell nano-spheres embedded in a silica matrix with $\beta=0.296$ and $f=0.3$ 104

Fig. 70: Transmittance spectrum of the ENZ slab with thickness $d = 0.17\ \lambda_0$ versus the incidence angle at three different frequencies: *600 THz* (red solid line), *715 THz* (black dash line), and *800 THz* (blue dash-dot line). 106

Fig. 71: Transmittance spectrum for different thicknesses *d* of the slab at *715 THz*. Each curve is normalized to the respective normal incidence transmittance value. 107

Fig. 72: Distribution of the electric field at (a) *600 THz*, (b) *715 THz*, and (c) *800 THz* for three different incidence angles (*0°*, *30°*, and *45°*) for an ENZ slab with thickness $d = 0.27\ \lambda_0$. 108

Fig. 73: Bare (left) and cloaked (right) cone. Geometrical parameters: $h = 484\ nm$, $R_B = 50\ nm$ and $R_b = 30\ nm$. 109

Fig. 74: Total scattering cross-section of the bare cone (black solid line) and of the cloaked one for different values of the volume filling fraction *f*. 109

Fig. 75: Amplitude (up) and phase (down) distributions of *y*-component of the electric field for the cases of the bare (a) and cloaked cone (b). The plots show the field distribution at the cloak frequency of *740 THz* on a plane parallel to the *x*-*z* plane placed at the half height of the cone. 110

Fig. 76: Required surface reactance within the visible range, calculated using (1) for a cylinder of infinite length made of silica. 112

Fig. 77: Single layer of lossless plasmonic nanoparticles arranged in a squared lattice. 114

Fig. 78: (a) Unit cell of the optical metasurface implemented in a full-wave simulator; (b) Equivalent circuit model of the structure. 115

Fig. 79: Comparison between the retrieved values of surface reactance (red scatters) and the ones given by the 2D analytical model (continuous lines) for an array of silver spherical nanoparticles. In the inset the considered array of spherical nanoparticles is shown. 116

Fig. 80: Comparison between the retrieved values (red scatters) of the surface reactance values and the ones provided by the 2D analytical model (continuous lines) for two arrays of spherical core-shell nanoparticles. In the inset, it is shown a single core-shell nanoparticle 117

Fig. 81: y-component of the surface reactance at f_0 = 600 THz for an array of prolate spheroids as a function of the eccentricity of the nanoparticles. The limit case e = 0 corresponds to spherical nanoparticles. 119

Fig. 82: Pictures (a) and (b) show, respectively, the real and imaginary parts of the x- and y-components of the silver electric permittivity for an elongated spheroidal nanoparticle taking into account the size-correction term. The corrected permittivity is compared to the bulk one presented in the literature [28]. 121

Fig. 83: Performance of the three nanoparticle-based cloaks in terms of minimization of the total scattering cross section 123

Fig. 84: Performance of the three designed cloaks in terms of minimization of the total extinction cross section. 124

Fig. 85: (a)-(b) Amplitude of the electric field on a plane orthogonal to the cylinder axis and passing through its centre in the uncloaked and cloaked case, respectively; (c)-(d) Phase pattern of the y-component of the electric field on the same plane in the uncloaked and cloaked case. 125

Fig. 86: Performance of the second nanoparticle-based cloak towards the alignment tolerances. In the inset, it is shown the structure for the case Δ=13 nm. 125

Fig. 87: Total SCS of the cylinder surrounded by the nanorods for different values of the rod side. 127

Fig. 88: Total ECS of the cylinder surrounded by the nanorods for different values of the rod side. 127

Fig. 89: 3D SCS pattern at 620 THz in the uncloaked case. The SCS is expressed in nm^2. 127

Fig. 90: 3D SCS pattern at 620 THz in the cloaked case for the cloaking devices with . The SCS is expressed in nm^2. 128

Fig. 91: (a) Geometry of a SRR loaded with an arbitrary impedance ZL and (b) its lumped element equivalent circuit representation. 135

Fig. 92: Magnitude of the S_{11} parameter of the unloaded SRR. 137

Fig. 93: Magnitude of the S_{11} parameter of a waveguide with a SRR loaded with different test capacitances (values in the range -0.05-0.05 pF). 138

Fig. 94: Reactance of the loading capacitance as a function of the corresponding resonant frequency (triangular symbols), reactance of the *LC* tank non-Foster circuit (values in (5) have been used) (dashed line), and non-Foster reactance of a *LC* tank circuit in series with an inductor (values in (5) have been used) (solid line). 139

Fig. 95: Magnitude of the S_{11} parameter of the unloaded SRR case (solid line), of the SRR loaded with a *LC* tank circuit (dashed line), and of the SRR loaded with a *LC* tank circuit in series with an inductance (dot-dashed line). 139

Fig. 96: Geometrical sketch of the SRR-based antenna proposed in [45]. Antenna dimensions in cm: $h = 3.00$, $h_1 = 31.60$, $h_2 = 29.64$, $d_1 = 1.14$, $d_2 = 1.90$. SRR dimensions in cm: $w = 3.42$, $R = 13.70$, $g = 0.76$, $s = 0.76$. Slab (FR-4): $\varepsilon_r = 3.5$, $tan\delta = 0.025$, thickness: 6.08 mm. 140

Fig. 97: Magnitude of the S_{11} parameter of the unloaded (dashed line) and loaded (solid line) antenna. 141

Fig. 98: SRR-based monopole antenna loaded with a parallel connection of two NIC circuits. 143

Fig. 99: Magnitude of the S_{11} parameter of the unloaded (solid line), ideally loaded (dashed line), NIC loaded (dotted line), and real NIC loaded (dot-dashed line) antenna. 144

Fig. 100: Input impedance of the unloaded and real NIC loaded antennas in real (solid and dotted line, respectively) and imaginary (dashed and dot-dashed line, respectively) part. 146

Fig. 101: Directivity patterns of the real NIC loaded antenna in the (left) E-plane and (right) H-plane at 100 MHz (solid line), 96.1 MHz (dashed line) and 106.1 MHz (dot-dashed line). 146

Fig. 102: Time-domain behavior of the current for the case of the unloaded antenna (thick black line) and for the case of an ideal 50 Ohm load (thin red line). 148

Fig. 103: Time-domain behavior of the current for the case of the loaded antenna (thick black line) and for the case of an ideal 50 Ohm load (thin red line). 148

Fig. 104: (a) Commercial graphite powder spray produced by ATAL SrL; (b) A realized resistive sheet composed by a plastic sheet covered by a proper amount of graphite powder. The two images are not in scale. 150

Fig. 105: Application of the Van der Pauw method for the resistive sheet characterization..... 150

Fig. 106: Surface resistance exhibited by the 18 realized samples compared to the relative graphite powder surface density. 152

Fig. 107: Experimental setup used to measure the reflection coefficient of the realized resistive sheets. In the inset, it is shown a properly shaped resistive sheet supported by a sample holder..... 153

Fig. 108: Comparison between the measured and the simulated amplitude of the S_{11} parameter for two resistive sheets with R_s = 41.5 Ω/sq and R_s = 141.5 Ω/sq, respectively. 153

Fig. 109: Geometrical sketch describing the structure of a traditional Salisbury screen. 155

Fig. 110: Simulated amplitude of the transmission and reflection coefficients (for normal incidence) of the proposed metasurface (inset: geometrical sketch of the metasurface and dimensions of the metallic rings). 155

Fig. 111: (a) Geometrical sketch, (b) rear view and (c) front view of the proposed metamaterial-inspired absorber. 156

Fig. 112: Photograph of the measurement system consisting of two high-gain pyramidal horn antenna and the sample holder. 157

Fig. 113: Absorption of the metamaterial-inspired absorber shown in Fig. 111..... 157

Publications

Journal paper

[J01] J. Soric, **A. Monti**, A. Toscano, F. Bilotti, and A. Alù, "Antenna Blockage Reduction Using Metasurface Cloaks," submitted to *IEEE Transactions on Antennas and Propagation* (under review).

[J02] J. C. Soric, **A. Monti**, A. Toscano, F. Bilotti, and A. Alù, "Multiband and Wideband Bilayer Mantle Cloaks," accepted for publication in *IEEE Transactions on Antennas and Propagation*.

[J03] **A. Monti**, A. Alù, A. Toscano, and F. Bilotti, "Optical invisibility through metasurfaces made of plasmonic nanoparticles," *Journal of Applied Physics*, vol. 117, *123103*, 2015.

[J04] **A. Monti**, J. Soric, A. Alù, A. Toscano, and F. Bilotti, "Anisotropic mantle cloaks for TM and TE scattering reduction," *IEEE Transactions on Antennas and Propagation*, vol. 63, (in press), doi: 10.1109/TAP.2015.2396532, 2015.

[J05] J. Soric, R. Fleury, **A. Monti**, A. Toscano, F. Bilotti, A. Alù, "Controlling scattering and absorption with metamaterial covers," *IEEE Transactions on Antennas and Propagation*, vol. 62, pp. 4220-4229, 2014.

[J06] **A. Monti**, L. Scorrano, S. Tricarico, F. Bilotti, A. Toscano, and L. Vegni, "Achieving PMC boundary conditions through metamaterials with extreme values of permittivity and permeability," *COMPEL - The International Journal for Computation and Mathematics in Electrical and Electronic Engineering*, vol. 32, pp. 1876-1890, 2013.

[J07] M. Barbuto, **A. Monti**, F. Bilotti, and A. Toscano, "Design of a non-Foster actively loaded SRR and application in metamaterial-inspired components," *IEEE Transactions on Antennas and Propagation*, vol. 61, pp. 1219-1227, 2013.

[J08] **A. Monti**, J. Soric, A. Alu, F. Bilotti, A. Toscano, and L. Vegni, "Overcoming Mutual Blockage between Neighboring Dipole Antennas using a low-profile Patterned

Metasurface," *IEEE Antenna and Wireless Propagation Letters*, vol. 11, pp. 1414-1417, 2012.

[J09] **A. Monti**, F. Bilotti, and A. Toscano, and L. Vegni, "Possible implementation of epsilon-near-zero metamaterials working at optical frequencies," *Optics Communications*, vol. 285, pp. 3412-3418, 2012.

[J10] **A. Monti**, F. Bilotti, and A. Toscano, "Optical cloaking of cylindrical objects by using covers made of core-shell nano-particles," *Optics Letters*, vol. 36, pp. 4479-4481, 2011.

Conference paper

[C01] L. Tenuti, G. Oliveri, F. Viani, A. Massa, A. **Monti**, F. Bilotti, and A. Toscano, "A System-by-Design Approach for the Synthesis of Multi-Layer Mantle Cloaks," Proceedings of the 2015 IEEE International Symposium on Antennas and Propagation and USNC-URSI National Radio Science Meeting, Vancouver, Canada, 19-25 July, 2015.

[C02] A. **Monti**, J. Soric, A. Alù, A. Toscano, and F. Bilotti, "Mantle cloaking: Antenna applications," Proceedings of the 2015 IEEE International Symposium on Antennas and Propagation and USNC-URSI National Radio Science Meeting, Vancouver, Canada, 19-25 July, 2015.

[C03] D. Ramaccia, A. Verrengia, F. Bilotti, A. Toscano, A. **Monti**, M. Barbuto, F. Trotta, D. Muha, S. Hrabar, "Experimental Verification of Broadband Antennas loaded with Metamaterials," Proceedings of the 2015 IEEE International Symposium on Antennas and Propagation and USNC-URSI National Radio Science Meeting, Vancouver, Canada, 19-25 July, 2015.

[C04] **A. Monti**, M. Barbuto, D. Ramaccia, A. Toscano, and F. Bilotti, "Broadband Enhanced Transmission through a Single Aperture based on Actively Loaded SRR," Proceedings of the 12th International Conference of Numerical Analysis and Applied Mathematics – ICNAAM 2014, Rhodes, Greece, 22 – 28 September, 2014.

[C05] M. Barbuto, **A. Monti**, D. Ramaccia, F. Bilotti, and A. Toscano, "Design and realization of MTM-inspired absorbers using graphite resistive sheets," Proceedings of the 12th International Conference of Numerical Analysis and Applied Mathematics – ICNAAM 2014, Rhodes, Greece, 22 – 28 September, 2014.

[C06] **A. Monti**, J. Soric, A. Alù, A. Toscano, and F. Bilotti, "Advances in Mantle Cloaking Design," Proceedings of the 17th European Microwave Week conference, Rome, Italy, 5 – 10 October, 2014.

[C07] M. Barbuto, F. Bilotti, **A. Monti**, D. Ramaccia, and A. Toscano, "Use of metamaterials to improve electrical and radiating performances of horn antennas," Proceedings of XX RiNEm, Padua, Italy, 15 - 18 September, 2014.

[C08] **A. Monti**, L. Tenuti, G. Oliveri, A. Alù, A. Massa, A. Toscano, and F. Bilotti, "Design of multi-layer mantle cloaks," Proceedings of the 8th International Congress on Advanced Electromagnetic Materials in Microwaves and Optics – Metamaterials 2014, Copenhagen, Denmark, 25– 28 August, 2014.

[C09] **A. Monti**, J. Soric, R. Fleury, A. Alù, A. Toscano, F. Bilotti, "Mantle cloaking and related applications in antennas," Proceeding of the International Conference on Electromagnetic in Advanced Applications, Palm Beach, Aruba, 3 – 8 August, 2014.

[C10] **A. Monti**, M. Barbuto, D. Ramaccia, A. Toscano, and F. Bilotti, "Use of plasmonic nanoparticles to achieve mantle cloaking at optical frequencies," Proceedings of the Plasmonica 2014 workshop, Rome, Italy, 30 June – 2 July, 2014 (poster presentation).

[C11] D. Ramaccia, M. Barbuto, **A. Monti**. F. Bilotti, and A. Toscano, "Horn Nano-antenna: Efficient Wideband Radiator at Near-infrared and Optical frequencies," Proceedings of the Plasmonica 2014 workshop, Rome, Italy, 30 June – 2 July, 2014.

[C12] **A. Monti**, A. Toscano, and F. Bilotti, "Optical mantle cloaking using plasmonic nanoparticle arrays," Proceedings of the Nanoplasm 2014 symposium, Cetraro, Italy, 16 – 20 June, 2014.

[C13] G. Bella, F. Fortuna, M. Barbuto, R. Conti, R. Cozzolino, S. Di Francesco, A. Donno, V. Duraccio, O. Giannini, V. Montesarchio, **A. Monti**, L. Tribioli, and F. Trovalusci, "Virtual academic teaching for next generation engineers," Proceedings of the 12th

Biennial Conference on Engineering Systems Design and Analysis – ESDA 2014, Copenhagen, Denmark, 25 – 27 June, 2014.

[C14] **A. Monti**, A. Alù, A. Toscano, and F. Bilotti, "Design and simulations of dual-polarized mantle cloaking devices," Proceedings of the 7th International Congress on Advanced Electromagnetic Materials in Microwaves and Optics – Metamaterials 2013, Bordeaux, France, 16 – 19 September, 2013.

[C15] **A. Monti**, J. Soric, A. Alù, F. Bilotti, and A. Toscano, "Mantle cloak devices for TE and TM polarizations," Proceedings of the 2013 IEEE International Symposium on Antennas and Propagation and USNC-URSI National Radio Science Meeting, Orlando, Florida, USA, 07-13 July, 2013.

[C16] **A. Monti**, A. Alù, and F. Bilotti, "Cloaked half-wave dipole antennas using the mantle-cloaking approach," Proceedings of the 6th International Congress on Advanced Electromagnetic Materials in Microwaves and Optics – Metamaterials 2012, St. Petersburg, Russia, 17 – 22 September, 2012 (this contribution has been awarded with the second place of the student paper competition of the conference).

[C17] M. Barbuto, **A. Monti**, D. Ramaccia, F. Bilotti, A. Toscano, and L. Vegni, "Metamaterial activities at microwave and optical frequencies at "Roma Tre" University," Proceedings of XIX RiNEm, Rome, Italy, 10-14 September, 2012 (poster presentation).

[C18] M. Barbuto, **A. Monti**, A. Toscano, and F. Bilotti, "Design of a Non-Foster Actively Loaded Metamaterial-Inspired Antenna," Proceedings of the 2012 IEEE International Symposium on Antennas and Propagation and USNC-URSI National Radio Science Meeting, Chicago, IL, USA, 08-14 July, 2012.

[C19] **A. Monti**, A. Toscano, and F. Bilotti, "Metasurface Mantle Cloak for Antenna applications," Proceedings of the 2012 IEEE International Symposium on Antennas and Propagation and USNC-URSI National Radio Science Meeting, Chicago, IL, USA, 08-14 July, 2012 (this contribution has been selected as a finalist of the student paper competition of the conference).

[C20] D. Ramaccia, **A. Monti**, M. Barbuto, F. Bilotti, and A. Toscano, "Realizzazione e caratterizzazione di fogli resistivi a base di grafite," Convegno su Campi elettromagnetici e innovazione tecnologica in ambito Difesa, Industria e Ricerca, C.I.S.A.M., Pisa, Italy, 2012.

[C21] M. Barbuto, **A. Monti**, F. Bilotti, and A. Toscano, "Employment of non-Foster active loads to improve the operation bandwidth of SRR loaded monopole antennas," Proc. of the 8th IEEE International Workshop on Antenna Technology (iWAT 2012), pp. 285-288, Tucson, AX, USA, 5-7 March, 2012 (invited paper).

[C22] M. Barbuto, A. **Monti**, F. Bilotti, and A. Toscano, "Some applications of MTMs based on non-Foster active loads," Proceedings of the Fifth International Congress on Advanced Electromagnetic Materials in Microwaves and Optics – Metamaterials 2011, Barcelona, Spain, 10 – 15 October, 2011.

Ph.D. candidate profile

February 16, 1987	Born date (Rome, Italy)
October 08, 2008	B.S. Electronic Engineering
October 25, 2010	M.S. Telecommunication Engineering
September, 2011	Engineering license
January 2011 – December 2014	PhD Student in Applied Electromagnetics

Alessio Monti (S'12, M'15) was born in Rome, Italy, on February 16, 1987. He received the B.S. degree (summa cum laude) and the M.S. degree (summa cum laude) in electronic and ICT engineering both from Roma Tre University, Rome, in 2008 and 2010, respectively. From 2011 to 2014, he attended the doctoral school in electronic engineering at Roma Tre University.

Alessio Monti is a member of the secretarial office of the International Association "Metamorphose-VI" and of the Technical Program Committee (TPC) of the 8th and 9th International Congress on Advanced Electromagnetic Materials in Microwaves and Optics. He has also been serving as a Technical Reviewer of the many high-level international journals related to electromagnetic field theory, metamaterials and plasmonics.

His research interests include the design and the applications of microwave and optical artificially engineered materials and metasurfaces, the design of cloaking devices for scattering cancellation operating at microwave and optical frequencies and the study of the electromagnetic properties of the plasmonic nanoparticles arrays.

Alessio Monti received 2nd place in the student paper competition at the Metamaterials 2012 in St. Petersburg, Russia, and was selected as a finalist for the student paper completion for the 2012 IEEE International Symposium on Antennas and Propagation and USNC-URSI National Radio Science Meeting in Chicago, IL.